University of Reading

School of Mathematical, Physical and Computational Sciences
Department of Meteorology

Fast, approximate methods for electromagnetic wave scattering by complex ice crystals and snowflakes

Karina McCusker

A thesis submitted for the degree of
Doctor of Philosophy in Atmosphere, Ocean and Climate
December 2019

Declaration

I confirm that this is my own work, and the use of all material from other sources has been properly and fully acknowledged.

The work in chapter 3 has been published in the Journal of Quantitative Spectroscopy and Radiative Transfer (JQSRT) [1]. I was the primary author of the article, implementing the numerical method, performing DDA calculations, and writing the paper. The coauthors contributed to the conception and design of the study. Some of the work in the introductory chapters of this thesis is also included in the publication.

Karina McCusker

Abstract

Improvements to scattering models are important for accurate retrievals of cloud ice. This thesis involves analysing the internal electric fields of ice particles and using the findings to develop and test new scattering approximations.

The discrete dipole approximation (DDA) is used to explore the internal fields and far-field scattering properties of ice particles. We show that the field is relatively uniform for size parameter $x = 2$, but for monocrystals of $x = 10$ there is a complex internal structure, with focussing of the field towards the forward side. As particle complexity is increased due to aggregation, the field becomes smoother and less focussing is seen. For complex aggregates, the individual monomers act almost independently of one another, suggesting simplified methods of calculating scattering. We find that the Rayleigh-Gans approximation (RGA) and soft spheres provide a poor representation of the internal and far fields.

A logical elaboration on RGA is a formulation permitting higher scattering orders. This technique is evaluated, however we find convergence is restricted to a limited subset of size parameter and shape. A new approximation for aggregates called the Independent Monomer Approximation (IMA) is presented, where interactions between different monomers of an aggregate are ignored. This enables time and memory reductions compared to using DDA. The IMA results are superior to RGA.

A microwave closure experiment is performed. Aggregate models are generated to match measurements. The IMA method is used to perform scattering calculations that are input into a radiative transfer model. Simulations are compared to measurements from the ISMAR radiometer. Unlike RGA, the new method can reproduce the measured brightness temperature depressions and polarimetric signal, but results are sensitive to choice of particle shape. These findings are useful to guide preparations for the Ice Cloud Imager which will measure ice in clouds and snowfall from space following launch in 2023.

Acknowledgements

First and foremost, I am eternally grateful to my supervisors Chris Westbrook, Andrea Moiola, Anthony Baran, and Simon Chandler-Wilde, along with my monitoring committee members - Joy Singarayer and Keith Shine.

During my PhD, I have had the great pleasure of working with many leading scientists in the field. I would like to express gratitude to everyone at the UK Met Office who helped with the project, including Stuart Fox and Richard Cotton who processed the observational data. Thanks to Patrick Eriksson and his team for providing me with invaluable help with the setup and testing of the ARTS software, along with Pawel Stasiak and Maria Broadbridge at the University of Reading for assisting when things went wrong. I am grateful to Jani Tyynelä and Sam Groth for their help and guidance, and to my colleagues in radar group. I also thank the three reviewers of my first publication for their constructive comments.

I thank EPSRC and the UK Met Office for funding the project.

Last but not least, I am extremely grateful to my family and friends for their support and encouragement over the past 4 years. Special thanks to Christine, who played an invaluable role in helping me to get the ball rolling in the first few weeks.

Contents

List of Tables

List of Figures

Abbreviations

ARTS: Atmospheric Radiative Transfer Simulator

BEM: Boundary Element Method

CIP: Cloud Imaging Probe

CoSSIR: Compact Scanning Submillimeter Imaging Radiometer

DDA: Discrete Dipole Approximation

ESA: European Space Agency

EUMETSAT: EUropean organisation for the exploitation of METeorological SATellites

FAAM: Facility for Airborne Atmospheric Measurements

GCM: Global Climate Model

GRaCE: G-band Radar for Cloud Evaluation

HALO: High Altitude LOng range research aircraft

HAMP: HAlo Microwave Package

ICI: Ice Cloud Imager

IMA: Independent Monomer Approximation

ISMAR: International Sub-Millimeter Airborne Radiometer

IWC: Ice Water Content

IWP: Ice Water Path

MADA: Modified Anomalous Diffraction Approximation

NAWDEX: North Atlantic Waveguide and Downstream impact EXperiment

NWP: Numerical Weather Prediction

OAP: Optical Array Probe

PSD: Particle Size Distribution

RAL: Rutherford Appleton Laboratory

RASTA: Radar Aéroporté et Sol de Télédétection des propriétés nuAgeuses

RGA: Rayleigh Gans Approximation

RTDF: Ray Tracing with Diffraction on Facets

SAFIRE: Service des Avions Francais Instrumentions pour la Recherche en Environnement

VRTE: Vector Radiative Transfer Equation

Chapter 1

Introduction and project background

1.1 Motivation

It is well established that clouds have a substantial influence on climate, but there are large uncertainties associated with the radiative effects of different cloud types. Using satellite-based remote sensing, Matus and L'Ecuyer [6] document that clouds exert a net cooling effect on the climate over most of the planet, with net cooling from both liquid and mixed-phase clouds. The research suggests that cirrus clouds, comprising ice crystals and aggregate snowflakes, have an overall warming effect. However, as shown by Zhang et al. [7], simulations of the radiative forcing of ice clouds are highly sensitive to representation of particle size and shape. Since it is estimated that cirrus clouds cover approximately 30% of the surface of the earth (e.g. Wylie et al. [8]), developing our understanding of ice clouds is fundamental to improving future climate predictions.

Important quantities for climate studies include ice water content and ice water path. The ice water content (IWC) of a cloud is defined as the mass of ice per unit volume of air. The integral of this quantity over a column is referred to as the ice water path (IWP) and is considered one of the essential climate variables by the World Meteorological Organisation. Li et al. [9] showed that there remains a large disagreement

between observed globally averaged IWP, and IWP modelled using different global climate models (GCMs). Factors of 2-10 differences were found for a majority of the GCMs used, some of which were used for the IPCC 5th Assessment Report.

Ice particles in clouds also have important hydrological impacts, contributing to rainfall in the midlatitudes [10], and snowfall at high latitudes. CloudSat [11] has provided our best estimates thus far of global snowfall, using a 94 GHz cloud radar to profile cloud vertical structure and obtain information on the constituent ice and water particles. However, there are still substantial uncertainties in converting the backscatter from snow at this frequency into a snowfall rate, and part of this uncertainty is due to the assumptions and approximations made about how natural snowflakes scatter electromagnetic waves [12].

Improvements to ice cloud retrievals are required in order to gain more precise information on cloud and hydrometeor profiles, and thus address the above uncertainties. Comparing 5 different satellite products, Refs. [13, 14] have shown that there are large inconsistencies between retrieved IWP from the different datasets. Improved retrievals of such properties are integral to the development of ice cloud microphysics schemes, which will allow advancements in the representation of different processes in both Numerical Weather Prediction (NWP) and climate models. Retrievals from remote sensing instruments are sensitive to scattering by ice particles which are comparable to or larger than the wavelength. The scattering behaviour becomes more complicated in such cases, and approximations like a Mie sphere become poor [15]. Therefore, the development of more sophisticated scattering methods for realistic, non-spherical particles is needed. This will aid accurate detection of cloud ice and snowfall from space, which remains an area of great difficulty.

1.2 Atmospheric ice particles

There are many different crystalline phases of ice, but the most common phase obtained when water is frozen at atmospheric pressure is ice Ih. This has a basic hexagonal ar-

rangement, and is the reason why the thermodynamically favoured equilibrium shape for atmospheric ice is a hexagon. The constituent particles of ice clouds vary in size and shape depending on the temperature and supersaturation of the surrounding environment. Different growth processes complicate the crystal habits, such as diffusion, accretion, and aggregation. Diffusion is the mechanism by which individual crystals grow, as water vapour molecules are deposited onto the ice surface. As ice particles grow by diffusion, new molecules will try to maintain the equilibrium shape by moving into the hexagonal structure. At low to moderate vapour densities, the vapour can be quickly distributed over the crystal surface and incorporated into the lattice, and the crystal habit will not change. However, at higher vapour densities there may not be enough time for molecules to arrange themselves in the energetically favoured way. In such cases, convergent diffusion towards the corners may result in more complex particle structures such as dendrites or stellar plates. More detail on ice particle habits may be found in books such as Refs. [16, 17]. As ice particles fall they may experience riming, which is the process describing accretion of supercooled liquid droplets by the crystals. Aggregation can occur when ice crystals fall at different speeds, resulting in them colliding and sticking together to form complex snowflake clusters.

We will investigate a number of different idealisations of single and aggregated ice crystals. These are:

- Hexagonal plates: Horizontally aligned hexagonal plates are frequently found in mixed-phase layer clouds [18], and at the top of cirrus clouds [19,20], particularly in anvil cirrus [21]. These studies found plate-like crystals with D_{max} reaching almost 1 mm, where D_{max} is the maximum distance between any 2 points within the particle.

- Hexagonal columns: Collating data from three different cloud campaigns, Um et al. [21] concluded that hexagonal columns exist at all temperatures explored, between -87 and $0\,^{\circ}\mathrm{C}$. However, growth is favoured between -4 and $-8\,^{\circ}\mathrm{C}$ [22]. During the campaigns, columns of projected D_{max} values between approximately 0.025 and 1 mm were observed. In this study we look at short columns of solid

ice, which usually occur at low ice supersaturations [23].

- Chain aggregates of plates: Aggregates of plate-like crystals occur in regions of high electric field, such as within deep convective clouds [24–26]. These observations support laboratory measurements which recorded an increase in aggregation efficiency due to the presence of electric fields [27,28]. Vonnegut [29] showed that polarisation due to the external field orients the individual plates such that they align with the electric field lines. This increase in contact time results in greater adhesion efficiency by enhancing the occurrence of sintering at the points of contact of the monocrystals. This particle shape is a logical elaboration on single plates and is useful to study the transition from single crystals to complex aggregates.

- Irregular aggregates of ice crystals: These are a more complex representation of realistic aggregates found in stratiform ice clouds and snowfall. Hobbs et al. [30] observed dendritic aggregates of D_{max} up to 1.4 cm. Such large aggregates play a significant role in microwave scattering as they dominate radar reflectivity when present, thus proving important for snowfall retrievals. Hence it is useful to explore their scattering properties. In chapter 3 we present results for two aggregates of fernlike dendrites modelled by Tyynelä et al. [3]. We also explore aggregates generated specifically for this work in chapters 4 to 6, comprising monomers of plates, columns, and dendrites.

1.3 Remote sensing of ice particles

Validation and testing of the capabilities of NWP and climate models relies on high-quality global measurements of atmospheric cloud ice. This is made possible using both active and passive remote sensing instruments. Active sensors emit electromagnetic radiation and measure the returned signal, while passive sensors measure radiation emitted from the earth's surface and from hydrometeors in the atmosphere. The intensity of the detected radiation is diminished from its original state due to scattering

and absorption by particles in the atmosphere, such as the water droplets and ice crystals that constitute clouds. Depending on the wavelength or frequency of operation, remote sensors may be sensitive to different regions of a cloud. A brief overview of some commonly used instruments is provided below.

1.3.1 Active instruments

Lidars operate at high frequencies within the visible or near-infrared region of the electromagnetic spectrum, and thus have the capability to sample small particles. This means the instrument can detect thin cirrus, along with providing useful information on cloud boundaries. However, strong attenuation at these frequencies means a lidar fails to see deep into the cloud.

Cloud radars provide an important tool for probing the cloud structure and enabling detection of tiny water droplets and ice crystals, along with larger particles. The instruments operate at wavelengths between about 1 mm and 1 cm. They transmit waves with wavelengths about 10 times shorter than precipitation radars, in order to detect the smaller sizes. Such instruments are beneficial for determining particle size and shape, and deriving the IWC within a cloud. The two cloud radars at Chilbolton observatory have frequencies of 35 GHz and 94 GHz, i.e. wavelengths of 8.6 mm and 3.2 mm. Exploitation of higher frequency radars for meteorological applications is becoming increasingly possible, and Battaglia et al. [31] found that retrievals could be significantly improved from using G-band radar with frequencies of 110 to 300 GHz. A new 200 GHz instrument called GRaCE (G-band Radar for Cloud Evaluation) has recently been built by RAL Space, and is currently being tested. The corresponding shorter wavelength of approximately 1.5 mm will allow measurements of even smaller atmospheric particles, thus facilitating more accurate estimations of IWC.

1.3.2 Passive instruments

Passive radiometry allows for accurate measurements of the column mass of atmospheric ice, since radiometers operate at a wide range of frequencies which are very sensitive to scattering by ice. Efforts have been made to improve airborne and spaceborne retrievals of IWP by measuring sub-millimetre brightness temperatures using radiometers such as the Compact Scanning Submillimeter Imaging Radiometer (CoSSIR), the Ice Cloud Imager (ICI), and the International Sub-Millimeter Airborne Radiometer (ISMAR) [32–35]. CoSSIR was one of the pioneering airborne sub-mm radiometers, and promising retrieval capabilities have been demonstrated using measurements from the instrument [36]. Following on from this success, ICI will be the first operational instrument to cover sub-mm wavelengths, with frequencies ranging from 183 to 664 GHz. The instrument has been specifically designed for measuring cloud ice from space, and is due for launch on-board the MetOp-SG satellite "B" in 2023. ICI was developed by ESA but is operated by EUMETSAT. It is expected that the combination of frequencies available will allow for more accurate estimations of IWP and cloud ice effective radius. Moreover, the instrument has the capability of measuring simultaneous horizontal and vertical polarisation states from some channels, providing valuable insight into the shape and alignment of cloud particles. The UK Met Office and ESA have developed an airborne demonstrator instrument for ICI, named ISMAR. The ISMAR radiometer flies on the Facility for Airborne Atmospheric Measurements (FAAM) BAe-146 research aircraft and is useful for testing ice scattering models that could be used within retrieval algorithms for ICI. At present the instrument covers a frequency range of 118 to 664 GHz, but a new 874 GHz channel is currently in development. The frequency range covered by ISMAR and ICI corresponds to wavelengths of $0.3 - 2.5$ mm.

1.4 Aims and outline of thesis

The irregular habits of realistic ice particles make scattering calculations difficult. In the past, radiative transfer models have employed drastic simplifications of cloud ice,

such as approximating particles by spheres or spheroids of equivalent size. However, as particle size increases with respect to the wavelength, the particle shape and material play a significant role in different interference patterns that are found within the particle. Recently there have been advances in using more realistic habits for single scattering calculations e.g. the Atmospheric Radiative Transfer Simulator (ARTS) database (Eriksson et al. [37]). With the advent of high frequency observations, accurate retrievals require continued efforts to improve our understanding of the scattering properties of realistic ice cloud particles. This will enable better interpretations of scattered electromagnetic waves, in turn allowing more precise retrievals of cloud properties from both radars and radiometers.

The overall purpose of this thesis is to develop new methods to approximate electromagnetic wave scattering by ice crystals and snowflakes, and test their performance. The goal is that the methods will be computationally cheap, but accurate enough to be used along with radar and radiometer data. Thus, for the purpose of this work I focus on the mm and sub-mm region of the electromagnetic spectrum, with relevant wavelengths ranging from $0.3 - 8.6$ mm. Ideally the approximations may be used with particles with a range of sizes, from those that are much smaller than the wavelength e.g. frozen cloud droplets of approximately 10 µm, to particles larger than the wavelength. Considering the previously mentioned plate-like particles with D_{max} up to 1 mm, this means the method would ideally be accurate for size parameters up to approximately 10, where the size parameter x is defined as $x = kD_{max}/2$, and k is the wavenumber. However, we note that snowflake aggregates often exceed these sizes, with in-situ aircraft based measurements revealing the presence of very large aggregates of dendritic crystals with diameters of $4 - 5$ cm (Lawson et al. [38]). This discovery is important as these particles are not included in the particle size distribution (PSD) parameterisations currently used in NWP and climate models, such as the one developed by Field et al. [39]. Baran et al. [40] point out that these large particles must be considered for accurate ice cloud remote sensing in the microwave region. Thus it may be necessary to consider scattering calculations at larger size parameters, but we do not explore such sizes in this thesis.

By using one of the newly developed methods to perform scattering calculations that are input into radiative transfer simulations, comparisons may be done with remote sensing observations from ISMAR. This allows validation of cloud ice retrievals that may be used to guide ICI preparations and provide recommendations on required retrieval parameters. It may provide information on the ways in which the multi-frequency capabilities of ICI could be exploited to reduce uncertainties and improve retrievals.

The outline of the thesis is as follows. Chapter 2 summarises the basic electromagnetic theory relevant to this study. The Maxwell equations are introduced, and descriptions of how different scattering quantities are calculated are provided. In chapter 3 we explore the scattering of mm and sub-mm electromagnetic waves by ice particles and snowflakes through an investigation of their internal electric fields. As we will show, this allows us to identify different physical effects, which in turn control different aspects of the far-field scattering; in addition it allows us to test at a more fundamental level the realism of approaches like RGA, by comparing the true internal field with the incident plane wave. Chapter 4 explores the use of iterative methods to calculate scattering, while a new approximation called the Independent Monomer Approximation (IMA) is introduced and tested in chapter 5. The newly developed IMA method is used to perform scattering calculations which are input into radiative transfer simulations in chapter 6. Results are compared to observations from ISMAR. Conclusions of the work are provided in chapter 7, along with plans for future work.

Chapter 2

Electromagnetic scattering theory

2.1 Maxwell's equations

The four fundamental Maxwell equations describe the properties of electromagnetic fields, and how they interrelate with each other. Following Liou and Yang [41], the equations are given in Gaussian (cgs) units as:

Gauss' Law for Electricity:

$$\nabla \cdot \mathbf{D} = 4\pi\rho \tag{2.1}$$

Gauss' Law for Magnetism:

$$\nabla \cdot \mathbf{B} = 0 \tag{2.2}$$

Faraday's Law:

$$\nabla \times \mathbf{E} = -\frac{1}{c}\frac{\partial \mathbf{B}}{\partial t} \tag{2.3}$$

Ampere-Maxwell Law:

$$\nabla \times \mathbf{H} = \frac{1}{c}\frac{\partial \mathbf{D}}{\partial t} + \frac{4\pi}{c}\mathbf{J} \tag{2.4}$$

In the above equations, $\mathbf{E}$ represents the electric field vector, $\mathbf{H}$ is the magnetic field

vector, ρ is the charge density, $\mathbf{J}$ is the current density, and c is the speed of light in vacuum. The remaining quantities are related to $\mathbf{E}$ and $\mathbf{H}$ via the constitutive equations. In a linear, homogeneous, isotropic medium, these are given by:

$$\mathbf{J} = \sigma\mathbf{E} \tag{2.5}$$

$$\mathbf{D} = \epsilon\mathbf{E} \tag{2.6}$$

$$\mathbf{B} = \mu\mathbf{H} \tag{2.7}$$

The quantities ρ and $\mathbf{J}$ are from external charges and may be thought of as the sources of the electromagnetic field. $\mathbf{D}$ is the electric displacement, and $\mathbf{B}$ is the magnetic induction vector. The electrical conductivity is denoted by σ. The electric permittivity and magnetic permeability are given by ϵ and μ. A dielectric is a substance with negligibly small conductivity, so its electric and magnetic properties are determined by ϵ and μ. For non-magnetic substances, such as ice and air, we may assume they are insulators with $\mu \approx 1$. This means the materials are defined by the complex permittivity $\epsilon = \epsilon_r + i\epsilon_i$, which we assume is constant throughout the medium. We can also write $\epsilon = m^2$, where m is the complex index of refraction of the particle. As recommended by Eriksson et al. [42], the permittivity parameterisation introduced by Mätzler [43] has been used to calculate the dielectric properties of the ice particles modelled in this study. The authors of Ref. [42] outline that the Mätzler model consolidates a number of earlier models, and as such is currently the most accurate parameterisation available for the microwave region. The real part of the permittivity ϵ_r, which represents phase velocity, varies weakly with temperature. The imaginary part ϵ_i, which represents absorption of the wave in the particle, varies more strongly with temperature, and also with frequency. In the majority of the calculations presented here, we have assumed a temperature of $-20°$C. For the ice particles in chapter 3, this results in a value of 3.1702 for ϵ_r, while ϵ_i varies between approximately 0.0002 and 0.0075. In chapter 6, rather than assuming a temperature of $-20°$C, the temperature data is obtained from observations.

Equations (2.1) to (2.4) show that separated positive and negative charges give rise to an electric field. If there is a charge, there is an electric field. As this electric field changes with time it will give rise to a rotating and therefore time-changing magnetic field. The time-changing magnetic field gives rise to a rotating and therefore time-changing electric field. Hence the result is a self-propagating electromagnetic wave that does not require a medium and can travel through a vacuum. The coupled electric and magnetic fields oscillate perpendicular to each other, and both are perpendicular to the direction of propagation of the wave, i.e. the wave is transverse. Electromagnetic waves can be classified by their wavelengths, and the complete range is known as the electromagnetic spectrum.

2.2 Electromagnetic wave equation

From Maxwell's equations we can derive the electromagnetic wave equation. If we consider a source-free region with no charges or currents, $\rho = 0$ and $\mathbf{J} = \mathbf{0}$, and the equations reduce to:

$$\nabla \cdot \mathbf{E} = 0 \tag{2.8}$$

$$\nabla \cdot \mathbf{H} = 0 \tag{2.9}$$

$$\nabla \times \mathbf{E} = -\frac{\mu}{c}\frac{\partial \mathbf{H}}{\partial t} \tag{2.10}$$

$$\nabla \times \mathbf{H} = \frac{\epsilon}{c}\frac{\partial \mathbf{E}}{\partial t} \tag{2.11}$$

Taking the curl of both sides of Eq. (2.10)

$$\nabla \times (\nabla \times \mathbf{E}) = -\frac{\mu}{c}\frac{\partial}{\partial t}(\nabla \times \mathbf{H}) \tag{2.12}$$

and using Eq. (2.11)

$$\nabla \times (\nabla \times \mathbf{E}) = -\frac{\epsilon\mu}{c^2}\frac{\partial^2 \mathbf{E}}{\partial t^2}. \tag{2.13}$$

Using the vector identity $\mathbf{a} \times (\mathbf{b} \times \mathbf{c}) = \mathbf{b}(\mathbf{a} \cdot \mathbf{c}) - \mathbf{c}(\mathbf{a} \cdot \mathbf{b})$ we can write Eq. (2.13) as:

$$\nabla(\nabla \cdot \mathbf{E}) - (\nabla \cdot \nabla)\mathbf{E} = -\frac{\epsilon\mu}{c^2}\frac{\partial^2 \mathbf{E}}{\partial t^2}. \tag{2.14}$$

Using Eq. (2.8) and rearraging, we obtain:

$$\frac{\partial^2 \mathbf{E}}{\partial t^2} = \frac{c^2}{\epsilon\mu}\nabla^2 \mathbf{E} \tag{2.15}$$

or

$$\frac{\partial^2 \mathbf{E}}{\partial t^2} = \frac{c^2}{\epsilon\mu}\left(\frac{\partial^2 \mathbf{E}}{\partial x^2} + \frac{\partial^2 \mathbf{E}}{\partial y^2} + \frac{\partial^2 \mathbf{E}}{\partial z^2}\right), \tag{2.16}$$

Thus the electric field satisfies the three-dimensional wave equation, and the velocity of the wave is given by $v = c/\sqrt{\epsilon\mu}$. In a vacuum, $\epsilon = \mu = 1$ and $v = c$. In a non-magnetic dielectric, $v = c/\sqrt{\epsilon} = c/m$. In other words, the wave gets slowed down by a factor of the refractive index. A similar equation could be obtained for the magnetic field $\mathbf{H}$, if required, but we only focus on the electric field here.

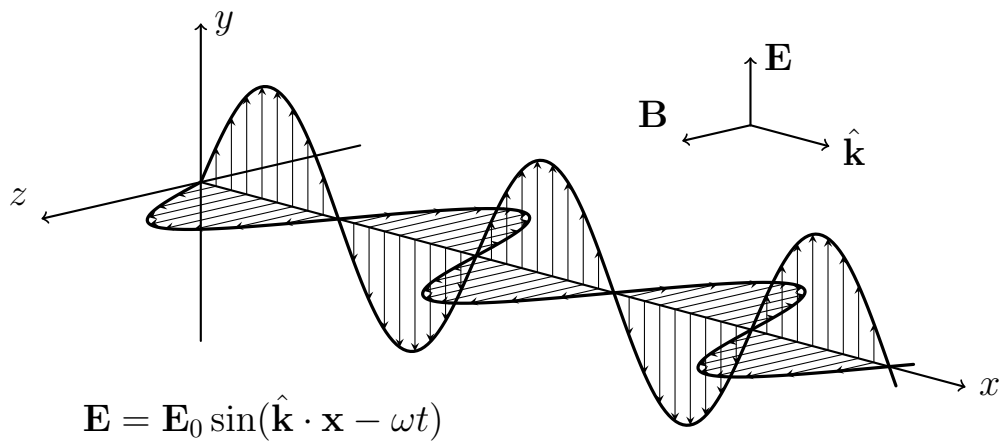

$$\mathbf{E} = \mathbf{E}_0 \sin(\hat{\mathbf{k}} \cdot \mathbf{x} - \omega t)$$

$$\mathbf{B} = \mathbf{B}_0 \sin(\hat{\mathbf{k}} \cdot \mathbf{x} - \omega t)$$

The wave equation has a large number of solutions, such as plane waves, spherical waves, and standing waves. The simplest solutions are plane waves, where $\mathbf{E}$ is uniform over every plane perpendicular to the direction of propagation, i.e. everywhere on the surface with constant phase $\phi = \mathbf{k}\cdot\mathbf{x} - \omega t$, where $\mathbf{k}$ is the wave vector, whose magnitude $k = |\mathbf{k}| = 2\pi/\lambda$ is the wavenumber corresponding to an incident wave of wavelength λ, and whose direction $\hat{\mathbf{k}} = \mathbf{k}/k$ is the direction of propagation of the wave. The angular frequency is given by $\omega = ck$, i.e. a point moves in direction $\hat{\mathbf{k}}$ with speed ω/k.

$\mathbf{E}_0 = E_0\hat{\mathbf{e}}$ is the polarisation vector for the electric field, where E_0 is the amplitude and $\hat{\mathbf{e}}$ is the unit vector in the direction of polarisation.

2.3 Scattering of electromagnetic waves

A variety of atmospheric particles cause scattering of radiation, including small gas molecules, aerosols, water droplets, and ice particles. Let us consider a volume of air, and introduce an applied incident wave, such as a radar pulse. If an ice particle is inserted into the volume, the total electric field will be modified due to the presence of that particle. Scattering is the term given to describe the modification of the incident field due to the presence of a particle. Hence we may express the total field as a combination of the incident and scattered fields, i.e. $\mathbf{E} = \mathbf{E}^{inc} + \mathbf{E}^{sca}$.

The field at an observation point $\mathbf{r}$ can be related to all other fields using an electric field volume integral equation of the form (e.g. Refs. [41, 44, 45]):

$$\mathbf{E}(\mathbf{r}) = \mathbf{E}^{inc}(\mathbf{r}) + \int_V d^3\mathbf{r}'\bar{\mathbf{G}}(\mathbf{r},\mathbf{r}')\chi(\mathbf{r}')\mathbf{E}(\mathbf{r}'), \tag{2.17}$$

where V is the particle volume. The free-space dyadic Green's function is the solution due to a point source excitation at $\mathbf{r}'$, and is given by:

$$\bar{\mathbf{G}}(\mathbf{r},\mathbf{r}') = [k^2\mathbf{1}_3 + \nabla\nabla]g(\mathbf{r},\mathbf{r}'). \tag{2.18}$$

The scalar Green's function $g(\mathbf{r},\mathbf{r}')$ is:

$$g(\mathbf{r},\mathbf{r}') = \frac{\exp(ikR)}{R}, \tag{2.19}$$

where $\mathbf{R} = \mathbf{r} - \mathbf{r}'$ and $R = |\mathbf{R}|$. Eq. (2.18) can be expanded out to give:

$$\bar{\mathbf{G}}(\mathbf{r},\mathbf{r}') = \frac{\exp(ikR)}{R}\Big[k^2(\mathbf{1}_3 - \hat{\mathbf{R}}\hat{\mathbf{R}}) - \frac{1-ikR}{R^2}(\mathbf{1}_3 - 3\hat{\mathbf{R}}\hat{\mathbf{R}})\Big], \tag{2.20}$$

where $\hat{\mathbf{R}} = \mathbf{R}/R$, and $\hat{\mathbf{R}}\hat{\mathbf{R}}$ is a dyadic whose element $(\hat{\mathbf{R}}\hat{\mathbf{R}})_{J,J'} = \hat{\mathbf{R}}_J\hat{\mathbf{R}}_{J'}$ for $J, J' = 1, 2, 3$. $\bar{\mathbf{G}}(\mathbf{r}, \mathbf{r}')$ has a singularity at $\mathbf{r} = \mathbf{r}'$, and for numerical calculations this must be treated with care. One approach is to consider a small volume V_0 surrounding point $\mathbf{r}$, with bounding surface denoted by S_0. Then Eq. (2.17) may be split into different parts and rewritten using integrals $\bar{\mathbf{M}}$ and $\bar{\mathbf{L}}$, associated with the small volume:

$$\mathbf{E}(\mathbf{r}) = \mathbf{E}^{inc}(\mathbf{r}) + \int_{V\setminus V_0} d^3\mathbf{r}'\bar{\mathbf{G}}(\mathbf{r}, \mathbf{r}')\chi(\mathbf{r}')\mathbf{E}(\mathbf{r}') + [\bar{\mathbf{M}}(\mathbf{r}) - \bar{\mathbf{L}}(\mathbf{r})]\chi(\mathbf{r})\mathbf{E}(\mathbf{r}). \tag{2.21}$$

The integrals $\bar{\mathbf{M}}$ and $\bar{\mathbf{L}}$ are given by:

$$\bar{\mathbf{M}}(\mathbf{r}) = \int_{V_0} d^3r' \Big(\bar{\mathbf{G}}(\mathbf{r}, \mathbf{r}') - \bar{\mathbf{G}}^{st}(\mathbf{r}, \mathbf{r}')\Big), \tag{2.22}$$

$$\bar{\mathbf{L}}(\mathbf{r}) = -\int_{V_0} d^3r'\bar{\mathbf{G}}^{st}(\mathbf{r}, \mathbf{r}'), \tag{2.23}$$

where $\bar{\mathbf{G}}^{st}(\mathbf{r}, \mathbf{r}')$ is the static limit of $\bar{\mathbf{G}}(\mathbf{r}, \mathbf{r}')$:

$$\bar{\mathbf{G}}^{st}(\mathbf{r}, \mathbf{r}') = \nabla\nabla\frac{1}{R} = -\nabla\Big(\frac{\hat{\mathbf{R}}}{R^2}\Big) = -\frac{1}{R^3}(\mathbf{1}_3 - 3\hat{\mathbf{R}}\hat{\mathbf{R}}). \tag{2.24}$$

$\bar{\mathbf{L}}$ can be converted from a volume integral to the following surface integral:

$$\bar{\mathbf{L}}(\mathbf{r}) = \int_{V_0} d^3r'\nabla\Big(\frac{\hat{\mathbf{R}}}{R^2}\Big) = \oint_{S_0} d^2r'\frac{\hat{n}'\hat{\mathbf{R}}}{R^2}, \tag{2.25}$$

where $\hat{n}'$ is the unit normal to the surface S_0 at point $\mathbf{r}'$.

$\bar{\mathbf{M}}$ is a volume integral which converges to 0 as the volume of V_0 decreases. The surface integral $\bar{\mathbf{L}}$ is referred to as the "depolarisation" dyadic (Ref. [46] chapter 3.9), and is a term which depends on the geometry of the volume V_0, but not on its size. In other words, $\bar{\mathbf{L}}$ approaches a constant value as V_0 tends to 0. As discussed in Ref. [47], $\bar{\mathbf{L}}$ can be shown to equal $4\pi\mathbf{1}_3/3$ for cubical or spherical volumes.

2.4 Far-field scattering

We illuminate the particle with a plane wave of unit amplitude, $E_0 = 1$, recalling that $\mathbf{E}_0 = E_0\hat{\mathbf{e}}$ is the polarisation vector:

$$\mathbf{E}^{inc}(\mathbf{r}) = \mathbf{E}_0 \exp(i\mathbf{k}\cdot\mathbf{r} - i\omega t). \tag{2.26}$$

It is well known that if the distance r between the detector and scatterer is large, we can make the following far-field approximations (e.g. see Jackson [48] chapter 9, or Mishchenko et al. [49] chapter 2):

$$R = |\mathbf{r} - \mathbf{r}'| \approx r - \mathbf{r}'\cdot\hat{\mathbf{n}} \tag{2.27}$$

$$\frac{1}{R} \approx \frac{1}{r}. \tag{2.28}$$

Combining the above approximations with Eqs. (2.17) and (2.20), and taking the limit $r \to \infty$, the scattered far field can be approximated by:

$$\mathbf{E}_{sca}(\mathbf{r}) = \frac{\exp(ikr)}{r}\mathbf{F}(\hat{\mathbf{n}}), \tag{2.29}$$

where the scattering amplitude $\mathbf{F}(\hat{\mathbf{n}})$ can be written:

$$\mathbf{F}(\hat{\mathbf{n}}) = k^2(\mathbf{1}_3 - \hat{\mathbf{n}}\hat{\mathbf{n}})\int_V \chi(\mathbf{r}')\mathbf{E}(\mathbf{r}')\exp(-ik\mathbf{r}'\cdot\hat{\mathbf{n}})d^3\mathbf{r}'. \tag{2.30}$$

The unit vector in the scattering direction is $\hat{\mathbf{n}} = \mathbf{r}/r$, and $\hat{\mathbf{n}}\hat{\mathbf{n}}$ is a dyadic. $\mathbf{1}_3$ is the identity dyadic, and $\mathbf{1}_3 - \hat{\mathbf{n}}\hat{\mathbf{n}}$ represents the transversality of the scattered wave. The electric susceptibility, $\chi(\mathbf{r}) = (\epsilon(\mathbf{r}) - 1)/4\pi$, is a complex-valued quantity which describes the degree to which charges align within a medium as a result of an electric field.

From a detector, we can measure waves polarised parallel to the unit vector $\hat{\mathbf{e}}_{det}$, so the

field we sample is $\mathbf{E}_{det}(\mathbf{r}, \hat{\mathbf{e}}_{det}) = \mathbf{E}_{sca}(\mathbf{r}) \cdot \hat{\mathbf{e}}_{det}$. The normalised differential scattering cross section $\sigma(\hat{\mathbf{n}}, \hat{\mathbf{e}}_{det})$ for one direction and polarisation can be calculated such that it is independent of distance r. The vector $\hat{\mathbf{e}}_{det}$ is chosen to be perpendicular to $\hat{\mathbf{n}}$, so $\hat{\mathbf{n}} \cdot \hat{\mathbf{e}}_{det} = 0$, and we have:

$$\sigma(\hat{\mathbf{n}}, \hat{\mathbf{e}}_{det}) = r^2 |\mathbf{E}_{det}(\mathbf{r}, \hat{\mathbf{e}}_{det})|^2. \tag{2.31}$$

The total scattering cross section σ_s represents a sum of waves scattered in all directions in the far field, and thus may be obtained by integrating over all scattering angles:

$$\sigma_s = \int_{4\pi} \sigma(\hat{\mathbf{n}}, \hat{\mathbf{e}}_{det}) d\Omega, \tag{2.32}$$

where $d\Omega = \sin\Theta d\Theta d\Phi$ is the differential solid angle for zenith and azimuthal angles Θ and Φ.

Absorption is when the energy of the field is converted into a different form, such as heat. The absorption cross section is:

$$\sigma_a = 4\pi k \int_V \Im(\chi(\mathbf{r}')) |\mathbf{E}(\mathbf{r}')|^2 d^3\mathbf{r}'. \tag{2.33}$$

Extinction is the removal of energy from an incident beam of light. This is caused by a combination of scattering and absorption. Thus, the extinction cross section σ_e may be written as:

$$\sigma_e = \sigma_s + \sigma_a. \tag{2.34}$$

However, extinction may also be calculated using the optical theorem which states that σ_e is proportional to the imaginary part of the scattering amplitude at zero scattering angle, i.e. in the forward direction only. Derivations are available in books such as Jackson [48]. We use the formulation of Draine [50]:

$$\sigma_e = \frac{4\pi}{k} \Im(\mathbf{F}(\hat{\mathbf{n}}_{inc}) \cdot \mathbf{E}_0^*), \tag{2.35}$$

where $\mathbf{F}(\hat{\mathbf{n}})$ was defined in Eq. (2.30).

The phase function is given by:

$$p(\Theta, \Phi) = \frac{4\pi}{\sigma_s} \left|\mathbf{F}(\hat{\mathbf{n}})\right|^2, \tag{2.36}$$

and is usually averaged over Φ so that the result is a function of the scattering angle only. The asymmetry parameter, g, is a related quantity, but with the inclusion of a $\cos\Theta$ factor:

$$g = \langle \cos\Theta \rangle = \frac{1}{\sigma_s} \int_{4\pi} \left|\mathbf{F}(\hat{\mathbf{n}})\right|^2 \cos\Theta d\Omega. \tag{2.37}$$

It is used as a measure of how much a particle scatters in the forward or backward direction. The values are between 1 and -1, where 1 means total forward scattering, -1 means total backscatter, with values around 0 obtained when there is equal forward and backscatter. This is the case for isotropic scatterers which distribute radiation evenly in all directions, and also for Rayleigh scatterers which have equal forward and backward scattering but are not isotropic.

2.5 Remote sensing theory and quantities

Radiative transfer simulations can be done with different models, such as the Atmospheric Radiative Transfer Simulator (ARTS) (Eriksson et al. [51]). ARTS version 2 is an open-source software program which supports polarised radiative transfer calculations. A single-scattering database is available to use with the software [37], but inputs of pre-calculated scattering properties are also accepted. This flexibility means it is possible to use arbitrary particle sizes and shapes, depending on the requirements of the study.

Polarimetry is an important concept in remote sensing. Radiation is said to be polarised when there is a preferred direction of the electric and magnetic field vectors of an electromagnetic wave. It is customary to describe the direction of polarisation as the direction of oscillation of the electric field vector. Sunlight is an example of unpo-

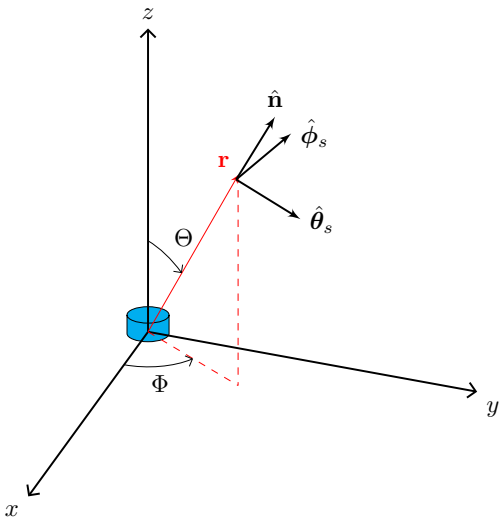

Figure 2.1: Scattering geometry for an incident wave in the direction of the z-axis, scattered at an angle (Θ, Φ).

larised radiation, i.e. the electric and magnetic field vectors have no preferred direction. Scattering is one method by which unpolarised light becomes polarised, with others including reflection and refraction. Polarimetric measurements aid characterisation of objects in the atmosphere. For example, coincident measurements at two orthogonal polarisation states can help to determine particle shape and orientation.

To specify the polarisation states of the incident and scattered fields in this study, we may introduce the unit vectors $\hat{\boldsymbol{\theta}}_i, \hat{\boldsymbol{\phi}}_i$ and $\hat{\boldsymbol{\theta}}_s, \hat{\boldsymbol{\phi}}_s$. The direction of incidence is $\hat{\mathbf{k}}_i = \hat{\boldsymbol{\theta}}_i \times \hat{\boldsymbol{\phi}}_i$, and the scattering direction is described by $\hat{\mathbf{n}} = \hat{\boldsymbol{\theta}}_s \times \hat{\boldsymbol{\phi}}_s$. The scattering setup for a point $\mathbf{r} = (r, \Theta, \Phi)$ in the far field is depicted in Fig. 2.1 for an incident wave in the z-direction. In that case $\hat{\boldsymbol{\theta}}_i$ and $\hat{\boldsymbol{\phi}}_i$ are equivalent to $\hat{\mathbf{x}}$ and $\hat{\mathbf{y}}$.

2.5.1 Amplitude scattering matrix

In order to input our own scattering calculations into ARTS, it is necessary to compute the 2×2 amplitude scattering matrix, $\mathbf{S}$. The matrix linearly transforms the electric field vector components of the incident plane wave into the electric field vector components of the scattered spherical wave:

$$\begin{bmatrix} \mathbf{E}_s \cdot \hat{\boldsymbol{\theta}}_s \\ \mathbf{E}_s \cdot \hat{\boldsymbol{\phi}}_s \end{bmatrix} = \frac{\exp(ikr)}{r} \begin{bmatrix} S_{11} & S_{12} \\ S_{21} & S_{22} \end{bmatrix} \begin{bmatrix} \mathbf{E}_i \cdot \hat{\boldsymbol{\theta}}_i \\ \mathbf{E}_i \cdot \hat{\boldsymbol{\phi}}_i \end{bmatrix}. \tag{2.38}$$

In this thesis, the convention of Mishchenko et al. [49] is adopted. Different notations are found in the literature, e.g. Bohren and Huffman [52] refer to parallel and perpendicular polarisation, where $\hat{\boldsymbol{\theta}} = \hat{\mathbf{e}}_{\parallel}$ and $\hat{\boldsymbol{\phi}} = -\hat{\mathbf{e}}_{\perp}$. Other authors such as Bringi and Chandrasekar [53] refer to horizontal and vertical polarisation states, which is common when considering radar applications. The amplitude of the outgoing spherical wave decreases as $1/r$. Different references commonly include a factor of ik in the denominator of Eq. (2.38), e.g. [52, 54]. It is explained in the text of van de Hulst [54] that the k is included to make $\mathbf{S}$ dimensionless, and the i may make certain scattering calculations more convenient.

Once $\mathbf{S}$ is calculated for a particle, it is possible to compute any other scattering quantities required. ARTS requires the phase matrix, $\mathbf{Z}$, the extinction matrix, $\mathbf{K}$, and the absorption vector, $\mathbf{a}$. Definitions for $\mathbf{Z}$ and $\mathbf{K}$ are available in Ref. [49], while the equations used for $\mathbf{a}$ are given by Evans and Stephens [55].

2.5.2 The radiative transfer equation

Once scattering calculations are performed and input into the model, ARTS solves the vector radiative transfer equation (VRTE). The VRTE expresses the change in intensity of radiation along the viewing path in terms of three contributions (Eriksson et al. [51]):

$$\frac{d\mathbf{I}(f, \mathbf{r}, \hat{\mathbf{n}})}{ds} = -\mathbf{K}(f, \mathbf{r}, \hat{\mathbf{n}})\mathbf{I}(f, \mathbf{r}, \hat{\mathbf{n}}) + \mathbf{a}(f, \mathbf{r}, \hat{\mathbf{n}})B(f, \mathbf{r}) + \int_{4\pi} d\hat{\mathbf{n}}' \mathbf{Z}(f, \mathbf{r}, \hat{\mathbf{n}})\mathbf{I}(f, \mathbf{r}, \hat{\mathbf{n}}'). \tag{2.39}$$

In Eq. (2.39), $\mathbf{I}$ is the radiance vector, ds is the pathlength element measured along the scattering direction $\hat{\mathbf{n}}$, f is the frequency, $\mathbf{r}$ is the position vector, B is the Planck function, and $\hat{\mathbf{n}}'$ represents the directions from which illumination is received. Thus, the first term on the right hand side of Eq. (2.39) represents attenuation of radiation

due to extinction, the second term describes the gain due to thermal emission, and the third term describes the radiation gain due to scattering from all directions $\hat{\mathbf{n}}'$ into the line of sight $\hat{\mathbf{n}}$. After solving Eq. (2.39), the radiances are converted to brightness temperatures within ARTS. These may then be compared to observations, such as those obtained from ISMAR.

2.6 Existing approaches to calculate scattering

A wide variety of methods to calculate electromagnetic wave scattering are available, but each have their pros and cons. Some methods are accurate but too expensive, and others are more efficient but inaccurate. Moreover, the amount of scattering that occurs varies depending on a measure of particle size relative to the wavelength of radiation. Mie scattering may be used to describe scattering by particles of any size, but unfortunately is only valid for spherical particles. There currently does not exist a single method that may be applied to scattering problems for arbitrarily shaped particles at all sizes.

As introduced in chapter 1, we define the size parameter of a particle as $x = kD_{max}/2$. Rayleigh scattering, which is the small particle limit of Mie theory, occurs when the scatterer is much smaller than the wavelength of the applied wave, i.e. if $x \ll 1$. The geometric-optics approach may be employed for large particles with $x \gg 1$. In this model, light propagation is described using ray tracing, while diffraction and internal interactions are ignored. Variations of the method, such as ray tracing with diffraction on facets (RTDF; [56]), have provided accurate results for size parameters as small as $x = 18$. For non-spherical particles approximately equal to the wavelength, neither of these approaches are valid, and analytical scattering solutions are only available for a limited number of simple shapes, such as spheres, spheroids, and infinite circular cylinders. Thus to compute scattering properties of non-spherical particles within this size range, such as ice crystals and snowflakes, different numerical methods are required. Here we briefly outline the main ideas behind some of the scattering methods that have been applied to atmospheric particles, but an extensive summary can be found in

Kahnert [45], and Liou and Yang [41].

The finite-difference time domain method (FDTD) is a differential equation method whereby a particle and the surrounding region are discretised into cells. The electromagnetic characteristics are represented by assigning values of permittivity, permeability, and conductivity to each cell. The FDTD algorithm involves replacing the derivatives in Maxwell's curl equations by finite differences, and simulating the propagation of scattered waves using a time-marching procedure. An advantage of FDTD is that it can be used for arbitrary particle geometries. However, the method can be very time and memory intensive as calculations must be performed over a spatial domain that is larger than the particle.

In the T-matrix approach, the incident and scattered fields are expanded in terms of suitable vector spherical wave functions. A transmitting matrix (or T-matrix) contains the full information on the single-scattering characteristics of the particle, i.e. it relates the scattered expansion coefficients to the incident coefficients. The advantage of a T-Matrix formalism is that once the matrix is calculated, scattering properties can be obtained for any orientation. Thus, averaging over random orientations can be done relatively quickly, compared to other methods that require new solutions to be calculated for each orientation. A T-matrix can be computed using many different numerical methods, but any scattering method using this approach is generally referred to as a T-matrix method. The original method used for this setup is the extended boundary condition method (EBCM) introduced by Waterman [57, 58]. T-matrix methods are usually applied to spheroids, but can be applied to other shapes with well-defined surfaces, such as cylinders. They are less frequently applied to non-symmetric particles due to convergence issues.

Another branch of numerical methods reformulates the scattering problem using integral equations. In the boundary element method (BEM), the problem is formulated as a system of boundary integral equations which may be solved to obtain the electric field. The advantages of the method are that it can be used with complicated geometries, and only the boundary of the particle needs to be discretised. However,

the method has been found to be more memory intensive than T-matrix methods [59].

The discrete dipole approximation (DDA) is a volume integral equation technique, i.e. it is a particular discretisation of the volume integral equation introduced in Eq. (2.17). The starting point of the method is to discretise the particle into small volume elements, each of which is excited by an electric field. Interactions between different volume elements are calculated, enabling accurate calculations using DDA. However, including all the interactions means the technique is computationally expensive. Researchers such as Westbrook et al. [60] have employed the less expensive Rayleigh-Gans approximation (RGA) in an attempt to calculate scattering properties in a more efficient manner. The problem can be set up in the same manner as DDA, but the field at each element in RGA is approximated by the applied field, with no interactions experienced between volume elements. Hence RGA is applicable for cases where interactions are negligible, i.e. when the relative refractive index is close to unity, and the phase shift across the particle is small. DDA and RGA are described in more detail in sections 2.8.2 and 2.8.4.

2.7 Previous studies of internal fields

The volume integral equation introduced in section 2.3 expresses the total electric field in terms of the incident field and the field inside a particle, while in section 2.4, the far-field scattering quantities are related to the internal field. Thus, it is useful to explore the internal fields of particles in order to obtain information on how different physical effects influence scattering properties in the far-field.

Comparing DDA results of the far-field scattering properties of snowflakes, Tyynelä et al. [61] found that RGA can lead to relative biases of -65%. Leinonen et al. [62] also found that even larger biases can occur for ice particles with elevated density due to riming. These findings suggest that the electric field inside the snowflake may be systematically larger in magnitude than the incident wave, and we are interested in exploring this further.

Internal fields of spheres, spheroids and cylinders have been explored in other disciplines, such as nanophotonics [63,64]. In these studies, complex internal field structures are seen, with constructive interference within the particles leading to a region of high electric field magnitude at the shadow-side of the particle, similar to the characteristic focussing nature of a lens. Owen et al. [65] describe the internal fields in infinitely long dielectric cylinders with size parameters of order 40. They observed enhanced electric fields in the forward portion of the cylinder which they ascribe to geometrical focussing; in addition, they noted the existence of a partial standing wave pattern close to the boundary of the scatterer. These surface waves are present over a range of size parameters: they are greatly enhanced in magnitude at very specific size parameters corresponding to resonances, or whispering gallery modes, where waves are internally reflected around the perimeter of the cylinder and repeat themselves (matched phase) after each trip; but they are also present as "partial standing waves" in the off-resonant case. Tyynelä [66] also modelled similar extrema in wavelength-scale spherical particles. Interference features connected to these internal waves could lead to enhancement and reduction of intensity at certain far-field scattering angles. Improved knowledge of these processes may prove useful in the development of scattering approximations.

Some research has been done on the internal field of more irregular particles [67, 68]. Similar focussing behaviour of the field was observed for Gaussian random spheres and debris particles, with the amount of focussing decreasing with increased shape complexity [67]. It was shown by Barton [68] that internal field variations with particle geometry lead to significant differences in far-field scattering properties. Lu et al. [69] studied the field inside a dendritic ice crystal, using their findings to modify RGA in such a way that scattering calculations are improved by including short-range interactions between volume elements. However, few other researchers have studied the problem for realistic ice particles to explore how these complex internal field structures differ with shape, and the role these variations play in far-field scattering. We hope to address the problem at a fundamental level to acquire understanding of how scattering at radar and radiometer frequencies works.

2.8 Methods used in this thesis

2.8.1 Effective medium approximations

Because aggregate snowflakes are not composed of solid ice, they are sometimes approximated by simpler shapes such as spheres or spheroids, comprised of a homogeneous ice-air mixture. This is achieved by changing the permittivity value of the particle. Such an approach has the potential to simplify scattering calculations as it means analytic solutions such as Mie theory can be used. Various effective medium approximations exist, and there are no clear guidelines to determine which is the best choice. For modelling snowflakes, the two best known and most widely used methods are those of Bruggeman [70] and Maxwell-Garnett [71], which are discussed in section 8.5 of Ref. [52]. Johnson et al. [72] compared the two methods by performing microwave calculations of brightness temperature and radar reflectivity, and found only minor differences in the results. For the irregular aggregates of crystals studied in chapter 3, comparisons have been done using the Maxwell-Garnett effective medium approximation. Using that method, the value of ϵ for the simplified model is adjusted to match the mass of the realistic particles they are approximating. In this study we have used spheres of equal D_{max} to the aggregate, and the reduced value of effective permittivity is determined based on the volume fraction of ice within the sphere:

- Calculate volume of aggregate v_{agg}
- Divide by volume that sphere of equal D_{max} would have, to obtain a volume fraction $f = 6v_{agg}/\pi D_{max}^3$
- Calculate average permittivity ϵ_{av} using that volume fraction in the Maxwell-Garnett equation, where ϵ is the permittivity of solid ice, and β is related to the shape of the ice inclusions (I use spherical inclusions, so $\beta = 0.58$, as discussed on pg. 217 of Ref. [52]):

$$\epsilon_{av} = \frac{1 - f + f\beta\epsilon}{1 - f + f\beta}$$

- Calculate scattering properties using the new permittivity value

2.8.2 Discrete dipole approximation

The discrete dipole approximation (DDA) is a method involving the discretisation of the volume integral equation in section 2.3. The DDA method is known to be an accurate method for computing scattering calculations, and thus is commonly used in atmospheric science to approximate the scattering properties of arbitrarily shaped particles. The most widely used publicly available codes are DDSCAT [73] and ADDA [74]. The idea behind DDA is that a particle may be discretised into an array of N homogeneous volume elements. It is assumed that the elements can be replaced by set of polarisable dipoles, i.e. the point scatterers are much smaller than the incident wavelength, such that they behave as radiating dipoles. Each dipole j $(= 1, \ldots, N)$ has a polarisation $\mathbf{P}_j = \alpha_j \mathbf{E}_j^{exc}$, where α_j is the polarisability and $\mathbf{E}_j^{exc}$ is the electric field incident on each dipole (the "exciting" field). The aim is to solve for $\mathbf{P}_j$ at every dipole.

The original idea behind DDA (also referred to as coupled dipole approximation) has been attributed to DeVoe [75,76], and later Purcell and Pennypacker [77]. The dielectric polarisability, α, determines how polarised the material becomes as a result of the applied field, representing the ease at which the positive and negative charges within a particle are distorted. There are different ways to prescribe the polarisability α_j of the dipoles that represent the particle. The polarisability can be written in terms of $\bar{\mathbf{L}}$ and $\bar{\mathbf{M}}$ from section 2.3 as $\alpha_j \mathbf{1}_3 = V_j \chi_j (\mathbf{1}_3 + (\bar{\mathbf{L}}_j - \bar{\mathbf{M}}_j)\chi_j)^{-1}$. By neglecting $\bar{\mathbf{M}}$ (sometimes referred to as the weak form of DDA - [78]) and using $\bar{\mathbf{L}} = 4\pi \mathbf{1}_3/3$, the Clausius-Mossoti polarisability is obtained. Purcell and Pennypacker employed the Clausius-Mossoti polarisability, which was derived for homogeneous, isotropic particles:

$$\alpha_{CM} = \frac{3d^3}{4\pi} \frac{m^2 - 1}{m^2 + 2}, \tag{2.40}$$

where d^3 is the volume of the cubic dipole.

Draine [50] outlined that a radiative correction is required for finite frequencies, pre-

senting a modified version of the polarisability as:

$$\alpha_{RR} = \frac{\alpha_{CM}}{1 - (2/3)ik^3\alpha_{CM}}. \tag{2.41}$$

Various improvements have since been made to calculate the polarisabilities in a more accurate way. In this work we use the lattice dispersion relation (LDR) formulation of Draine and Goodman [79], which is also used in DDSCAT:

$$\alpha_{LDR} = \frac{\alpha_{CM}}{1 + (\alpha_{CM}/d^3)[(b_1 + m^2 b_2 + m^2 b_3 S)(kd)^2 - (2/3)i(kd)^3]}, \tag{2.42}$$

where $b_1 = -1.891531$, $b_2 = 0.1648469$, $b_3 = -1.7700004$, $S = \sum_{j=1}^{3} (\hat{\mathbf{k}}_j \hat{\mathbf{e}}_j)^2$.

We illuminate the particle with a plane wave of unit amplitude, $E_0 = 1$:

$$\mathbf{E}_j^{inc} = \mathbf{E}_0 \exp(i\mathbf{k} \cdot \mathbf{r}_j - i\omega t). \tag{2.43}$$

The position vector is given by the central position of dipole j, i.e. $\mathbf{r}_j = [x_j, y_j, z_j]$. The time-dependent factor is represented by $e^{-i\omega t}$, but since the quantities of physical interest are always real, the factor could alternatively be chosen as $e^{i\omega t}$ provided the same choice is used consistently. From here on in, we assume all fields are time-harmonic, thus leaving out the $\exp(-i\omega t)$ component. The "exciting" electric field $\mathbf{E}_j^{exc}$ is given by $\mathbf{E}_j^{inc}$, plus the contributions from each of the other dipoles in the particle:

$$\mathbf{E}_j^{exc} = \mathbf{E}_j^{inc} - \sum_{j' \neq j} \mathbf{A}_{jj'} \mathbf{P}_{j'}. \tag{2.44}$$

$\mathbf{A}$ is a $3N \times 3N$ array commonly referred to as the interaction matrix. From Eq. (2.20) it is clear that the interaction matrix $\mathbf{A}$ is equivalent to $-\bar{\mathbf{G}}$. Each entry $\mathbf{A}_{jj'}$ is a 3×3 matrix which can be calculated for $j \neq j'$ by:

$$\mathbf{A}_{jj'} = \frac{\exp(ikR)}{R}\left[k^2(\hat{\mathbf{R}}\hat{\mathbf{R}} - \mathbf{1}_3) + \frac{ikR - 1}{R^2}(3\hat{\mathbf{R}}\hat{\mathbf{R}} - \mathbf{1}_3)\right], \tag{2.45}$$

for $j, j' = 1, \ldots, N$. The distance between points $\mathbf{r}_j$ and $\mathbf{r}_{j'}$ is given by $R = |\mathbf{R}|$, where $\mathbf{R} = \mathbf{r}_j - \mathbf{r}_{j'}$, and $\hat{\mathbf{R}} = \mathbf{R}/R$ is the directional unit vector between the two points. As

in Ref. [73], we make the standard assumption that $\mathbf{A}_{jj} = \alpha_j^{-1}\mathbf{1}_3$, where $\mathbf{1}_3$ is the 3×3 identity matrix. Thus we can write $\mathbf{E}_j^{exc} = \mathbf{A}_{jj}\mathbf{P}_j$ and rearrange Eq. (2.44) as:

$$\mathbf{E}_j^{inc} = \mathbf{A}_{jj}\mathbf{P}_j + \sum_{j' \neq j} \mathbf{A}_{jj'}\mathbf{P}_{j'}. \tag{2.46}$$

Hence the scattering problem can be reduced to a system of $3N$ linear equations to solve for the unknown dipole polarisations $\mathbf{P}_{j'}$:

$$\sum_{j'=1}^{N} \mathbf{A}_{jj'}\mathbf{P}_{j'} = \mathbf{E}_j^{inc}. \tag{2.47}$$

Once the value of $\mathbf{P}_j$ is known for each dipole, it is straightforward to compute the macroscopic electric field inside the volume elements (Liou and Yang [41]):

$$\mathbf{E}_j = \frac{\mathbf{P}_j}{V_j \chi_j}, \tag{2.48}$$

where $V_j = d^3$ is the volume of the dipole. This should not be confused with the exciting electric field $\mathbf{E}_j^{exc} = \mathbf{P}_j/\alpha_j$ mentioned previously, which includes the field resulting from the incident wave and contributions from the other $N-1$ dipoles, but not the field induced by the dipole on itself. For the particles in this study, the ratio $\alpha_j/V_j\chi_j$ between $\mathbf{E}_j$ and $\mathbf{E}_j^{exc}$ is approximately 0.58.

Calculation of $\mathbf{P}$ requires solving a large linear system $\mathbf{AP} = \mathbf{E}^{inc}$, where each element of $\mathbf{P}$ and $\mathbf{E}^{inc}$ are vectors of size 3×1:

$$\underbrace{\begin{bmatrix} \alpha^{-1}\mathbf{1}_3 & \mathbf{A}_{1,2} & \dots & \mathbf{A}_{1,N} \\ \mathbf{A}_{2,1} & \alpha^{-1}\mathbf{1}_3 & \dots & \mathbf{A}_{2,N} \\ \vdots & \vdots & \vdots & \vdots \\ \mathbf{A}_{N,1} & \mathbf{A}_{N,2} & \dots & \alpha^{-1}\mathbf{1}_3 \end{bmatrix}}_{\mathbf{A}=3N\times 3N} \underbrace{\begin{bmatrix} \mathbf{P}_1 \\ \mathbf{P}_2 \\ \vdots \\ \mathbf{P}_N \end{bmatrix}}_{\mathbf{P}=3N\times 1} = \underbrace{\begin{bmatrix} \mathbf{E}_1^{inc} \\ \mathbf{E}_2^{inc} \\ \vdots \\ \mathbf{E}_N^{inc} \end{bmatrix}}_{\mathbf{E}^{inc}=3N\times 1}$$

This can be done numerically using direct or iterative methods. The direct method involves matrix inversion, i.e. $\mathbf{P} = \mathbf{A}^{-1}\mathbf{E}^{inc}$. The problem with this approach is that the $3N \times 3N$ matrix $\mathbf{A}$ has to be stored and this requires a large amount of memory,

along with taking considerable time to solve. For a particle of N dipoles, the time taken to solve the standard DDA linear system is between $\mathcal{O}(N^2)$ and $\mathcal{O}(N^3)$, and the memory requirement is proportional to N^2. To reduce memory requirements, we have implemented a row-wise matrix-vector multiplication rather than assembling the full matrix. As outlined in Yurkin and Hoekstra [47], many iterative solvers exist that could be used for the computations; in this study we use the generalized minimal residual solver (GMRES; [80]). Our implementation means we only need to store one row of size $3\times3N$ at a time, and the memory scales as $\mathcal{O}(NM)$, where M is the number of GMRES iterations, rather than $\mathcal{O}(N^2)$. In previous literature, the fast Fourier transform (FFT) has been employed to accelerate calculations for larger size parameters, e.g. Goodman et al. [81]. However, in order to use this method, one must discretise a complete periodic lattice surrounding the particle, e.g. a cubic lattice, and do calculations for the total number of volume elements in the bounding box. This means the potential benefits of using this method are only realised for more dense particles that occupy the majority of the surrounding lattice. For particles of lower density, many of these volume elements are empty. Calculations for the empty elements would not need to be done if conventional DDA techniques were employed. The overheads of including FFT calculations in such cases would cost more than the savings.

Iterative methods have also been employed in the literature to increase speed of calculations and reduce memory requirements, and an overview can be found in Yurkin and Hoekstra [47]. A classical iterative procedure to solve linear equations is the Jacobi method. Details of the method can be found in numerical mathematics books such as Quarteroni et al. [82]. It is also discussed further in chapter 4 of this work. Singham and Bohren [83, 84] refer to this as a scattering order formulation of the DDA, and provide a physical interpretation of the method. The zeroth order approximation is equivalent to the Rayleigh-Gans approximation, where only the incident field is considered and interactions between dipoles are ignored. The first order approximation describes the field at the i^{th} dipole resulting from single scattering from all the other dipoles in the particle. The second order approximation describes the field resulting from double scattering, and so on.

A successive over-relaxation iterative method was used by Purcell and Pennypacker [77], i.e. a Jacobi iterative method with a relaxation parameter to improve convergence. The optimal value to use for the relaxation parameter is not trivial. The authors of Ref. [77] state that in the calculations they presented, a value of 0.5 was 'usually' used.

The far-field scattering properties of a particle may be derived by formulating the relationships outlined in section 2.4 in terms of the DDA method. The quantity $\mathbf{A}_{jj'} \cdot \mathbf{P}_j$ represents the electric field at dipole j' radiated by the j^{th} dipole. The scattered electric field is calculated by summing the power radiated by the array of N oscillating dipoles. Using Eq. (2.29) and Eq. (2.30), the scattering amplitude can now be written:

$$\mathbf{F}(\hat{\mathbf{n}}) = k^2(\mathbf{1}_3 - \hat{\mathbf{n}}\hat{\mathbf{n}}) \sum_{j=1}^{N} \mathbf{P}_j \exp(-ik\mathbf{r}_j \cdot \hat{\mathbf{n}}). \tag{2.49}$$

The differential scattering cross section in Eq. (2.31) is:

$$\sigma(\hat{\mathbf{n}}, \hat{\mathbf{e}}_{det}) = k^4 \left| \sum_{j=1}^{N} \mathbf{P}_j \cdot \hat{\mathbf{e}}_{det} \exp(-ik\mathbf{r}_j \cdot \hat{\mathbf{n}}) \right|^2. \tag{2.50}$$

If $\hat{\mathbf{n}} = -\mathbf{k}/|\mathbf{k}|$, then we obtain backscattering and $\sigma(\hat{\mathbf{n}}, \hat{\mathbf{e}}_{det})$ coincides with Eq. (7) in Ref. [85].

The absorption cross section may be calculated as:

$$\sigma_a = 4\pi k \sum_{j=1}^{N} [\Im(\mathbf{P}_j \cdot \mathbf{E}_j^{exc*}) - (2/3)k^3 \mathbf{P}_j \cdot \mathbf{P}_j^*]. \tag{2.51}$$

Combining the optical theorem in Eq. (2.35) with the scattering amplitude in Eq. (2.49), the extinction cross section is given by:

$$\sigma_e = 4\pi k \sum_{j=1}^{N} \Im(\mathbf{P}_j \cdot \mathbf{E}_{inc,j}^*). \tag{2.52}$$

For use within ARTS, the chosen numerical method is used to solve for the dipole

moment $\mathbf{P}$ using 2 orthogonal incident polarisations $\hat{\boldsymbol{\theta}}_i$ and $\hat{\boldsymbol{\phi}}_i$. These solutions are then used to obtain the individual components of $\mathbf{S}$, as described in Draine [50]:

$$S_{ml} = k^2 \sum_{j=1}^{N} \mathbf{P}_j^l \cdot \hat{\mathbf{e}}_m \exp(-ik\mathbf{r}_j \cdot \hat{\mathbf{n}}). \tag{2.53}$$

$l = 1, 2$ represents the 2 different polarisation states of the incident wave, i.e. $\mathbf{P}_j^1$ and $\mathbf{P}_j^2$ are the solutions for $\hat{\boldsymbol{\theta}}_i$ and $\hat{\boldsymbol{\phi}}_i$, respectively. $m = 1, 2$ represents the scattered polarisation states, such that $\hat{\mathbf{e}}_1$ and $\hat{\mathbf{e}}_2$ correspond to $\hat{\boldsymbol{\theta}}_s$ and $\hat{\boldsymbol{\phi}}_s$. This solution is valid for the azimuthally random particles considered in this study, and is calculated for scattered polar and azimuthal angles of $\Theta \in [0°, 180°]$ and $\Phi \in [0°, 180°]$. It is noted that further transformations would be required if randomly oriented particles were of interest, and the range of azimuthal angles should be extended to 360°. Details of these transformations are found in Mishchenko et al. [49]. Once the amplitude scattering matrix elements are calculated, it is straightforward to obtain the phase matrix, extinction matrix, and absorption vector required by ARTS.

2.8.2.1 Accuracy of the DDA method

Two conditions are specified by Draine and Flatau [73] to minimize errors and ensure that the DDA formulation is valid:

1. The dipole spacing d must be sufficiently small compared to the internal wavelength of the particle. The condition given in their study is that the number of dipoles per internal wavelength, $n_\lambda = \lambda/(\Re(m)d)$, should exceed a value of 2π. Zubko et al. [86] showed that the DDA provides highly accurate results for irregular particles with this condition. However, a more restrictive value of $n_\lambda > 4\pi$ is recommended by Draine and Flatau for scattering phase function calculations such as radar cross sections [87]. This value has been employed in some scattering studies, e.g. Tyynelä et al. [67]. The most commonly used convention for discretisation is to prescribe at least 10 dipoles per internal wavelength, i.e. $n_\lambda \geqslant 10$. Yurkin and Hoekstra [47] state that this constraint is a good first guess

for many applications, but accuracy is not guaranteed, particularly for large size parameters. Comparisons with Mie theory for solid ice spheres have shown that in fact $n_\lambda > 42$ may be required for accurate values of the backscatter cross section, σ_b [85].

2. The shape of the particle must be described adequately by ensuring that N is sufficiently large, i.e. d is small enough for the results to converge. It is unclear from the literature how to quantify this condition, so the required N is calculated on a case-by-case basis.

2.8.3 Rayleigh scattering

Rayleigh scattering is generally applicable if the following conditions are met:

$$x \ll 1 \tag{2.54}$$

$$x|m| \ll 1 \tag{2.55}$$

In this case, the particle is small enough that the applied electric field may be considered uniform across the volume, and we can view it as an electrostatics problem. This means the scatterer behaves like an individual dipole, which oscillates at the same frequency as the incident field and radiates in all directions.

The most well known example of Rayleigh scattering is perhaps scattering of visible light with wavelengths of $0.4-0.7\,\mu m$ by atmospheric molecules. The sizes of these molecules are much smaller than the wavelengths of solar and infrared radiation. Rayleigh scattering of light varies strongly with wavelength, with the intensity decreasing as the inverse fourth power of the wavelength. Thus, shorter wavelength blue light is scattered more than longer wavelength red light, explaining why the sky appears blue. For a vertical column of atmosphere, approximately 40% of the light is scattered in the near ultraviolet while 1% is lost in the near infrared.

In the Rayleigh limit, the amplitude scattering matrix $\mathbf{S}$ for a scatterer can be written:

$$\begin{bmatrix} S_{11} & S_{12} \\ S_{21} & S_{22} \end{bmatrix} = k^2 V \alpha' \begin{bmatrix} \cos\theta & 0 \\ 0 & 1 \end{bmatrix}, \tag{2.56}$$

where $\alpha' = \alpha/d^3$ is the polarisability per unit volume. For lower frequency weather radars, such as those operating in the S-band ($2-4$ GHz) or C-band ($4-8$ GHz), Rayleigh theory is often valid due to particles being smaller in size than the wavelengths used by these instruments. However, for higher frequency cloud radars, ice particles and snowflakes are large enough that they do not scatter in the Rayleigh regime. Thus improvements to the method are required.

2.8.4 Rayleigh-Gans approximation

As the particle size increases such that the size is comparable to the incident wavelength, the Rayleigh approximation no longer holds. For larger spherical particles, scattering and absorption can be calculated using Mie theory. However, the non-spherical shapes of ice particles and snowflakes require that different scattering methods are employed. RGA provides better results for larger sizes, and is based on the assumption that the total amount of scattering from a particle can be calculated by dividing it into small volume elements, and treating each element as a Rayleigh point scatterer. The scattered incident wave can then be calculated simply by summing the individual scattered waves from each sub element. Near-field interactions between elements are neglected, but the far-field interference is taken into account through an appropriate phase factor. The method is also known as the first Born approximation [54].

RGA is applicable if the refractive index is close to that of the surrounding medium, i.e. it is "optically soft", and if the phase shift from one side of the particle to the other is small. In other words, the approximation is applicable if the internal interactions within the particle are so weak that the incident field remains almost unchanged within the particle, and thus the interactions can be neglected. It is generally accepted that

RGA may be applied to particles that meet the following conditions:

$$|m-1| \ll 1 \tag{2.57}$$

$$2x|m-1| \ll 1. \tag{2.58}$$

Using the refractive index of solid ice gives a value of $|m-1| \approx 0.78$. This is clearly less than 1, but perhaps not "much less than 1", as required in condition (2.57). Moreover, the phase shift condition given in (2.58) would only be satisfied for small values of x in the solid ice case. However, it is not clear whether the conditions could be relaxed if the particles were fluffy snow aggregates as opposed to solid ice spheres, for example. The lower effective refractive index of those particles may mean that RGA could provide good results even if conditions (2.57) and (2.58) are not strictly met.

Improvements to RGA are possible using methods such as the Wentzel-Kramers-Brillouin (WKB) approximation [88]. The WKB method is similar to RGA but with the inclusion of a local phase delay corresponding to the propagation of the wave from the particle penetration point to the interior location of the volume element. Allowing such a phase change means that the second RGA condition given in (2.58) is not required for WKB, and thus the method has a wider range of applicability. Klett and Sutherland [89] applied WKB to spheres and cylinders and found that the accuracy of phase functions with increased refractive index was better than with RGA. However, the method did not perform well for backscatter.

The RGA method is outlined as follows - For a single volume element at position $\mathbf{r}$ within the particle, it is necessary to account for the change of phase between the incident and scattered waves with direction vectors $\hat{\mathbf{e}}_z$ and $\hat{\mathbf{e}}_r$ respectively. Writing the phase differences as $\delta(\mathbf{r}) = k\mathbf{r} \cdot (\hat{\mathbf{e}}_z - \hat{\mathbf{e}}_r)$, we may introduce the form factor f which is an interference function accounting for the phase differences of the whole particle, i.e. how coherent or incoherent the scattered waves are:

$$f = \left| \frac{1}{V} \int \exp(i\delta(\mathbf{r}))d\mathbf{r} \right|^2. \tag{2.59}$$

Summing over the entire particle of volume V, we can then write:

$$\begin{bmatrix} S_{11} & S_{12} \\ S_{21} & S_{22} \end{bmatrix} = k^2 V \alpha' f(\theta, \phi) \begin{bmatrix} \cos\theta & 0 \\ 0 & 1 \end{bmatrix}. \tag{2.60}$$

Often the Clausius-Mossotti factor is employed with the Rayleigh-Gans approximation, but we use $\alpha = \alpha_{LDR}$ in any results shown in this thesis, in order to be consistent with the DDA calculations.

RGA is an example of a computationally cheap method which has limited accuracy. Tyynelä et al. [61] found that using RGA to approximate scattering by realistic snowflake shapes is an improvement to the traditional approach to parameterisation where particles are approximated by simple shapes and an effective medium approximation is employed. Since RGA doesn't include internal field interactions, the improvements to scattering by aggregates have been attributed to the fact that the spatial structure of ice in the particle is modelled in RGA calculations.

Rayleigh scattering of light occurs when the particle is much smaller than the wavelength of the incident wave, and in this case $\delta(\mathbf{r}) \to 0$ and $f \to 1$. As the particle size increases relative to wavelength and Rayleigh scattering no longer applies, $f < 1$ and the form factor changes depending on the shape of the particle, taking interference between volume elements into account. An analytical equation for the RGA form factor is known for a number of shapes, including spheres, spheroids, and circular cylinders [52]. It is also possible to derive expressions for hexagonal prisms, as outlined in the following sub-section.

2.8.5 Analytical RGA form factor equations for a hexagonal prism

In a homogeneous particle, each volume element in a given slice perpendicular to the direction of the incident wave has the same phase shift. As the RGA only includes the interference due to phase shift and ignores interactions between elements, the form

factor can be viewed as a summation of area integrals of thin slices of the shape. As outlined by [54], it is possible to derive form factors for simple shapes using this concept. Here we explore a hexagonal prism geometry. The form factor has been derived for the separate cases where the incident wave reaches the shape along the two axes of symmetry of the basal face. These directions are shown in Fig. 2.2.

2.8.5.1 x-direction

Consider a hexagonal prism geometry of side length r and height L, oriented as in Fig. 2.2a. The particle is illuminated by a plane wave propagating along the x-axis in the positive x direction. If we consider the backscatter direction, $\delta(\mathbf{r}) = 2k\mathbf{r} \cdot \hat{\mathbf{e}}_z$ and the interference function in Eq. (2.59) can be written:

$$f = \left| \frac{1}{V} \int \exp(2ki\mathbf{r} \cdot \hat{\mathbf{e}}_z) d\mathbf{r} \right|^2.$$

This can be re-expressed as:

$$\sqrt{f} = \frac{1}{V} \int_x A(x) \exp(i2kx) dx.$$

$A(x)$ is the area of the intersection of the prism with the plane perpendicular to the x-axis at a particular x coordinate. This integral can be computed by decomposing the hexagonal prism into two trapezoidal prisms, as in Fig. 2.2a, and evaluating the integral separately for the two segments:

$$\sqrt{f}V = \int_{-\sqrt{3}r/2}^{0} A(x) \exp(i2kx) dx + \int_{0}^{\sqrt{3}r/2} A(x) \exp(i2kx) dx.$$

Looking at the first integral, it is clear that the area of a slice at $x = -\sqrt{3}r/2$ is rL, and $A(x)$ increases linearly with x until $A(x) = 2rL$ at $x = 0$. Thus we can say $A(x) = (2x/\sqrt{3}r + 2)rL$ for the first trapezoidal prism. Applying the same method, we can determine that $A(x) = (-2x/\sqrt{3}r + 2)rL$ for the second prism. Using these

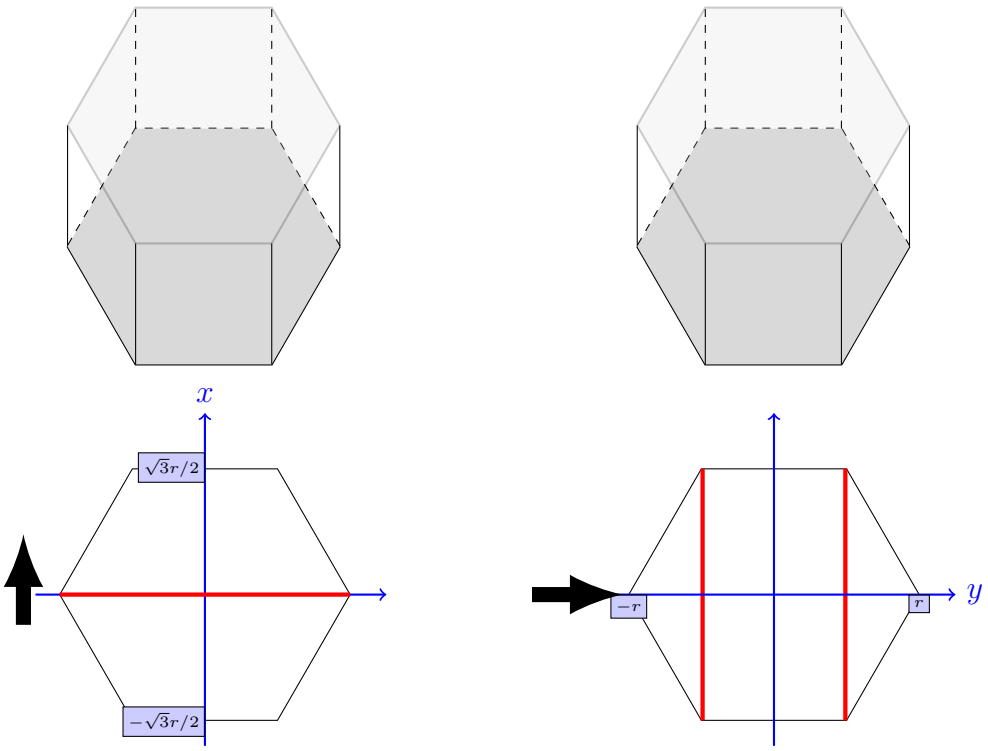

(a) x direction (b) y direction

Figure 2.2: Basal face of the hexagonal geometry. The thick black arrows show the direction of the incident wave in each case, travelling along the x-axis in the left panel, and along the y-axis in the right panel. The red lines indicate how the particle was divided up in each case, in order to perform the integral.

values, it can be shown that the form factor for the total hexagonal prism is:

$$f = \left(\frac{L}{kV}\left(\frac{r}{u}(1-\cos u) + r\sin u\right)\right)^2, \tag{2.61}$$

where $u = \sqrt{3}kr$.

2.8.5.2 y-direction

Now consider the same geometry but with the plane wave propagating along the y-axis in the positive y direction (Fig. 2.2b). In this case the integral is evaluated by splitting the shape into 2 triangular prisms and a rectangular prism:

$$\sqrt{f}V = \int_{-r}^{-r/2}(y+r)2\sqrt{3}L\exp(i2ky)dy + \int_{-r/2}^{r/2}\sqrt{3}rL\exp(i2ky)dy + \int_{r/2}^{r}(r-y)2\sqrt{3}L\exp(i2ky)dy.$$

Using the same method as before, it can be shown that when the incident wave travels in the y direction the form factor is given by:

$$f = \left(\frac{\sqrt{3}L}{k^2 V} (\cos kr - \cos 2kr \right)^2 . \tag{2.62}$$

In the following four chapters, the results of this this thesis are presented. We begin with a study of the internal electric fields of a variety of ice particles in the next section, relating these to scattering properties in the far-field.

Chapter 3

Analysis of the internal fields of pristine ice crystals and aggregate snowflakes, and their effect on scattering

The work in this chapter has been published in the Journal of Quantitative Spectroscopy and Radiative Transfer (JQSRT) [1].

3.1 Summary of the study

The discrete dipole approximation is used to explore the internal electric fields of plane-wave-illuminated ice particles. This is done for monocrystals and aggregates at two different frequencies for each particle, corresponding to size parameters of $x = 2$ and $x = 10$. For these properties the real part of ϵ has a value of 3.1702 for solid ice, and the imaginary part varies between 0.0002 and 0.0075. We also present calculations for some of the particles with a smaller size parameter of $x = 0.01$. The wavelength used in those cases results in an imaginary part of ϵ which is of order 10^{-6}.

The differential scattering cross sections of the particles are also explored. In the case of the complex aggregates, comparisons using DDA and RGA are presented, along with results obtained using a soft sphere approximation.

3.2 Validation of the numerical method

3.2.1 Verification of DDA internal field results using BEM++

As discussed in section 2.8.2.1, the accuracy of the DDA method is sensitive to both discretisation and shape errors. A detailed summary of previous attempts to quantify these errors is given by Yurkin and Hoekstra [47].

To do the calculations in this chapter, a version of the DDA method was implemented in Matlab, using the GMRES iterative solver. This was done to develop a deeper understanding of the DDA method, to have convenient control over input geometries and visualisation of results, and to have a basis to develop simplified approximate methods. We note that the code used here is not highly optimised, unlike popular open-source codes such as DDSCAT [73] and ADDA [90].

To verify the implementation of the DDA code and validate the findings presented here, we compared a number of results to those obtained using a fundamentally different numerical method. In the Boundary Element Method (BEM), the electric field is obtained by formulating the problem as boundary integral equations. Groth et al. [59] studied the performance of BEM for the problem of scattering by ice particles, using an open source boundary element library called BEM++, developed by Śmigaj et al. [91]. In that paper they show that by using 10 mesh elements per wavelength, BEM++ gives results for scattering and extinction efficiencies, and phase function that are accurate to within 1%. However, the accuracy of the internal fields was not investigated. The difference between the internal field obtained using our DDA code and the BEM++

setup used by Ref. [59] was calculated as:

$$\frac{\|\mathbf{E}_{DDA} - \mathbf{E}_{BEM}\|}{\|\mathbf{E}_{BEM}\|} \times 100\%, \tag{3.1}$$

where $\mathbf{E}_{DDA,j}$ and $\mathbf{E}_{BEM,j}$ are the solutions evaluated in the centre of the jth dipole, using DDA and BEM++ respectively. We clarify that this test is useful for validating the code, but does not validate either of the numerical methods.

This experiment was performed for a thin hexagonal plate of solid ice, with a size parameter of 2 and an aspect ratio of 0.1. For the calculations we use 17 elements per wavelength for BEM++, which is better than the required BEM++ resolution specified in Ref. [59]. The difference from Eq. (3.1) was calculated using different grid refinements for DDA. The dipole size was determined by specifying the number of dipoles along the smallest dimension of the particle. In the case of the thin plate, this means we specify the number in the vertical dimension (n_z). The difference obtained for various values of n_z, and their corresponding number of dipoles per internal wavelength, n_λ, was calculated. The results ranged from 1.2% for $n_z = 3$ ($n_\lambda = 26$), to 0.6% for $n_z = 7$ ($n_\lambda = 61$). This confirms that the DDA code is performing as expected, and thus we are confident that it can be used for the $x = 2$ calculations in this study.

Unfortunately we could not perform analogous comparisons for $x = 10$, as the resources we had available were insufficient to run BEM++ for that case. Therefore, we took an alternative approach to examine the accuracy of DDA calculations for $x = 10$, outlined in the following section.

3.2.2 Convergence of DDA internal field results with increasing n_λ

In this section we explore how the internal field calculations for $x = 10$ converge as the number of dipoles per internal wavelength is increased.

Fig. 3.1 examines the convergence of the DDA internal field with increased grid reso-

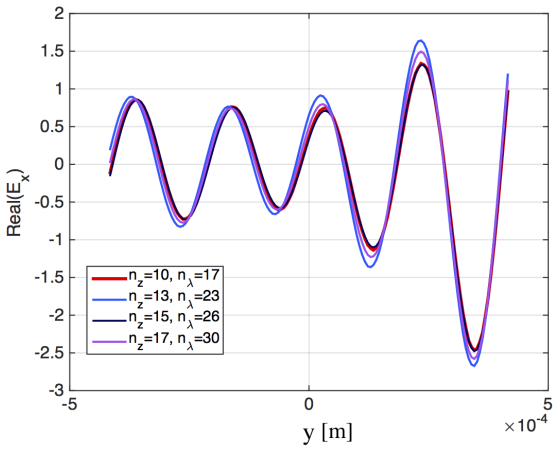

Figure 3.1: $\Re(E_x)$ through the centre of a hexagonal plate of $x = 10$ and aspect ratio 0.1. The colours show different grid refinements of $n_z = 10, 13, 15, 17$, corresponding to $n_\lambda = 17, 23, 26, 30$.

lution. The lines show the real part of the x component of the field though the centre of a hexagonal plate of $x = 10$ and aspect ratio 0.1. The results for different grid refinements of $n_z = 10, 13, 15$, and 17 have been plotted in the figure, corresponding to $n_\lambda = 17, 23, 26$, and 30. The curves are qualitatively similar for each of the different grid resolutions, with the main differences occurring in the field amplitudes.

We estimate the error in the internal fields by comparing our highest resolution case of $n_\lambda = 30$ to results of lower resolution, ranging from $n_\lambda = 8$ to 26. The calculations are done in an analogous manner to Eq. (3.1). We find that using a minimum of 17 dipoles per internal wavelength gives an error below 10% in the field for $x = 10$.

This experiment was also done for $x = 2$. It is noted that using the same discretisation for $x = 2$ results in higher values of n_λ, so greater accuracy is expected. The values tested range between $n_\lambda = 44$ and 124, uncovering much smaller errors below 0.5%. The accuracy estimated via these tests is sufficient for exploring the qualitative properties we are interested in here, i.e. the variation of internal field with particle size and shape, and the effects of these changes on far-field scattering.

It is worth noting that despite the fact we are well within the commonly prescribed criterion of $n_\lambda = 10$, convergence with increasing resolution is slow. Although the fields are very similar, the results in some regions of the particle have not completely converged, and the relative errors do not decrease monotonically as n_λ is increased.

Yurkin et al. [92] found a similar pattern, highlighting that the issue only occurs with shapes that cannot be modelled exactly by cubical cells. Inaccurate representation of boundaries leads to small variations in particle shape with discretisation, which in turn causes oscillating errors. However, this does not affect the conclusions we are drawing in the rest of the paper.

Comparisons of the corresponding scattering cross section results for these discretisations (not shown for brevity) reveals that the error in the far field is mainly concentrated in the backward direction. The backscatter cross section, σ_b, is very sensitive to particle discretisation, whereas scattering in other directions shows little variation with discretisation. This result is consistent with Petty and Huang [85] who show that smaller dipole spacing is required for accurate backscatter results. As pointed out in section 2.8.2.1, they suggest using a value of $n_\lambda > 42$ for accurate σ_b in the case of ice spheres, and with our highest resolution we are only using $n_\lambda = 30$. It is possible that a finer discretisation may be needed if accurate backscatter calculations are required.

3.3 Results and discussion - Pristine monocrystals

3.3.1 Hexagonal plate

3.3.1.1 Internal field

The aspect ratio of the monocrystals is defined as the ratio between the length of the particle in the z direction and the maximum width of the particle in the x-y plane. Fig. 3.2 shows the magnitude of the internal electric field through the central horizontal plane of a hexagonal plate of solid ice, with a maximum dimension (D_{max}) of 1 mm and an aspect ratio of 0.1. The plate is discretised with $n_z = 15$, resulting in approximately $n_\lambda = 132$ and $n_\lambda = 26$ for $x = 2$ and $x = 10$ respectively. The incident plane wave propagates in the y direction, i.e. from the top of the page to the bottom, and is polarised along the x-axis. Note that the color scales in Figs. 3.2a and 3.2b are not the same. The plots shown for $x = 2$ in this chapter have a smaller range than their

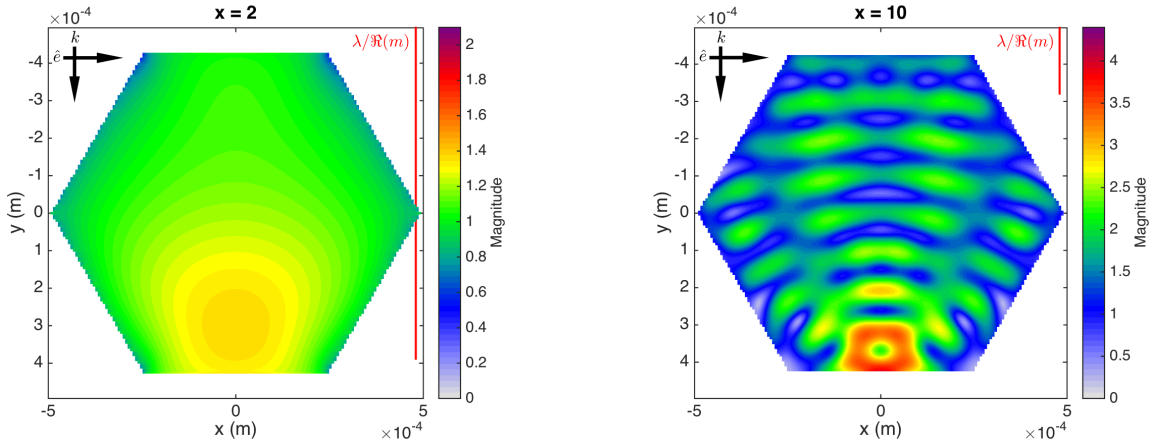

(a) $x = 2$ (b) $x = 10$

Figure 3.2: Magnitude of the internal field through the central horizontal plane of a hexagonal plate of aspect ratio 0.1 for (*a*) $x = 2$ and (*b*) $x = 10$. The arrows show the direction of propagation and polarisation, which are perpendicular to each other in the x-y plane. The particle is discretised with $n_z = 15$, resulting in (*a*) $n_\lambda = 132$; (*b*) $n_\lambda = 26$.

$x = 10$ equivalents, in order to show some detail for the smaller size parameter. This is the case for the majority of the internal field magnitude plots presented here, with the exception of the complex aggregate in Fig. 3.24.

The average and peak values of the field for both size parameters are given in Table 3.1, along with results for a smaller value of $x = 0.01$. For very small values of $x \ll 1$, particles are in the Rayleigh scattering limit. In this size regime, the internal field has approximately constant magnitude, with the maximum and average values varying by only a factor of 1.15. For $x = 2$ and $x = 10$, the largest value of electric field is observed close to the perimeter of the particle, at the opposite side from where the wave hits the plate. We refer to this as the forward region of the particle. For $x = 2$ there is a rather broad maximum centred at approximately 0.1 mm from the forward edge of the plate, with the peak magnitude reaching 1.3744. For $x = 10$, the focussing behaviour becomes more obvious, and the maximum magnitude also increases. There is an "O" shaped region where the field magnitude is largest, reaching a value close to 4. Figs. 3.3 to 3.5 shows how the field changes within the hexagonal plate geometry for intermediate size parameters between 2 and 10. The focussing pattern is a persistent feature, becoming more prominent with increased x. Therefore, this is not a resonant phenomenon. The maximum magnitude within the particle broadly increases with x. It is interesting to

	$x = 0.01$		$x = 2$		$x = 10$	
Geometry	Avg. $\|\mathbf{E}\|$	Max $\|\mathbf{E}\|$	Avg. $\|\mathbf{E}\|$	Max $\|\mathbf{E}\|$	Avg. $\|\mathbf{E}\|$	Max $\|\mathbf{E}\|$
1 hex plate	0.8169	0.9414	1.0969	1.3744	1.4108	3.9786
2 hex plates	0.8136	0.9173	0.9464	1.0949	1.6021	3.0049
5 hex plates	0.8583	1.2337	0.9111	1.3866	1.5049	2.3575
Aggregate 1	0.6503	1.2430	0.6593	1.2617	0.6986	1.4302
Aggregate 5	0.6593	1.2097	0.6650	1.2212	0.6879	1.2400

Table 3.1: Average and maximum internal field magnitudes for different geometries of $x = 0.01$, $x = 2$ and $x = 10$. The geometries included are the single hexagonal plate, aggregates of 2 and 5 plates, and 2 different arrangements of 10 "fernlike dendrite" monomers modelled by Tyynelä et al. [3]. "Aggregate 1" is the particle shown in Fig. 3.24; "Aggregate 5" is not shown for brevity. For reference, $|\mathbf{E}| \approx 0.58$ in the presence of the applied wave only.

note that for all size parameters shown, the magnitudes are considerably higher than the value of $|\mathbf{E}_j| = |\mathbf{E}_j^{inc}\alpha_j/V_j\chi_j| \approx 0.58$ that would result from the presence of the applied wave only. Hence there is a strong coupling between the dipoles across the crystal, and RGA provides a poor approximation to the field in this case.

Another interesting observation is that the inhomogeneity along the x-axis in Fig. 3.2b resembles diffraction and interference patterns, such as those resulting from Young's double-slit experiments. This suggests that we are entering a regime where physical optics approximations could be used. Geometric optics may be applied for size parameters much larger than the incident wavelength. However, improvements to geometric optics methods have been shown to be accurate for x as small as 18, e.g. using methods such as ray tracing with diffraction on facets (RTDF; [56]). Hence it is possible that for the larger size parameters considered here, physical or geometric optics methods may be suitable approximations to apply.

The concentration of the electric field is similar to the focussing nature of a convex optical lens, and is caused by a change in wavelength, due to m, that takes place inside the particle. The difference in wavelength is more pronounced through the centre of the particle than it is close to the boundaries, resulting in a curved wave front which focusses the field towards one side of the plate. Note that the symmetric structure and focussing behaviour of the field also occurs if the incident wave is propagating in the x direction, such that it encounters a corner of the plate rather than a flat side.

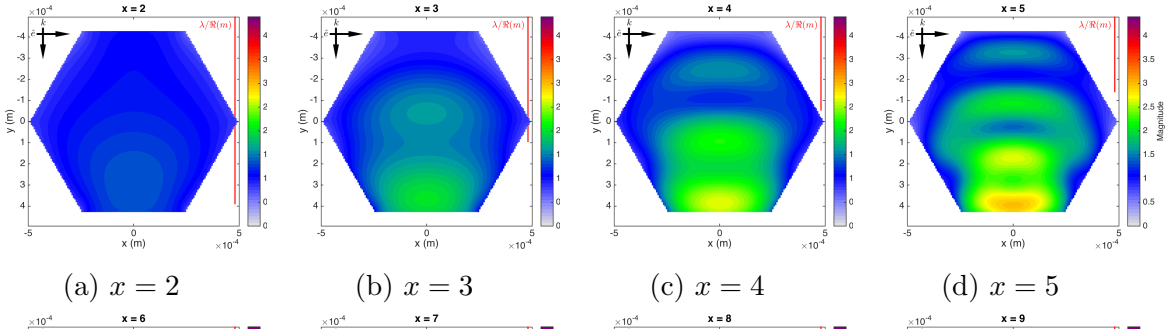

(a) $x = 2$ (b) $x = 3$ (c) $x = 4$ (d) $x = 5$

(e) $x = 6$ (f) $x = 7$ (g) $x = 8$ (h) $x = 9$

Figure 3.3: Magnitude of the internal field through the central plane of a hexagonal plate of aspect ratio 0.1 for different size parameters of $x = 2$ to $x = 9$. The incident wave is propagating in the y-direction and is polarised along the x-axis.

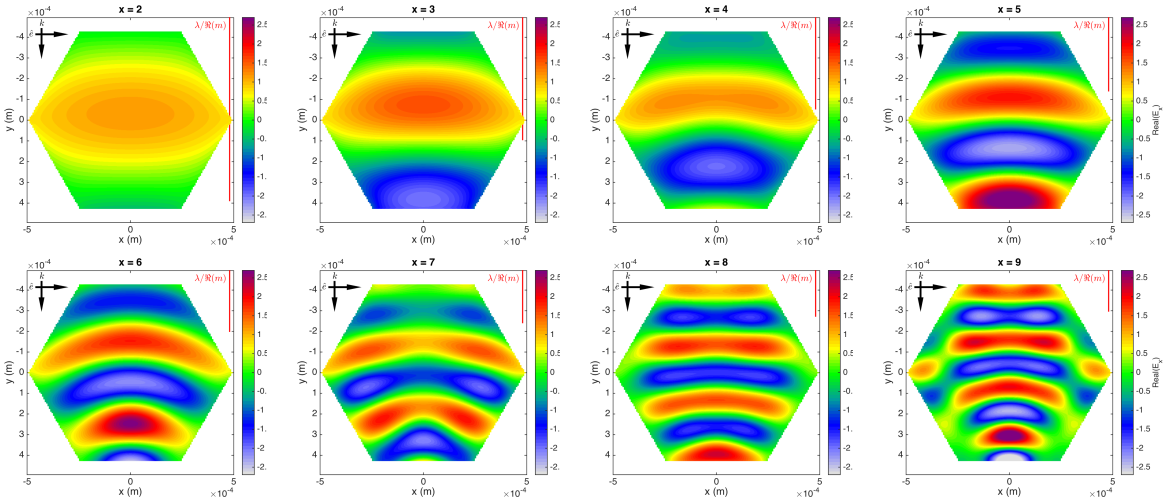

Figure 3.4: As in Fig. 3.3, but for $\Re(E_x)$.

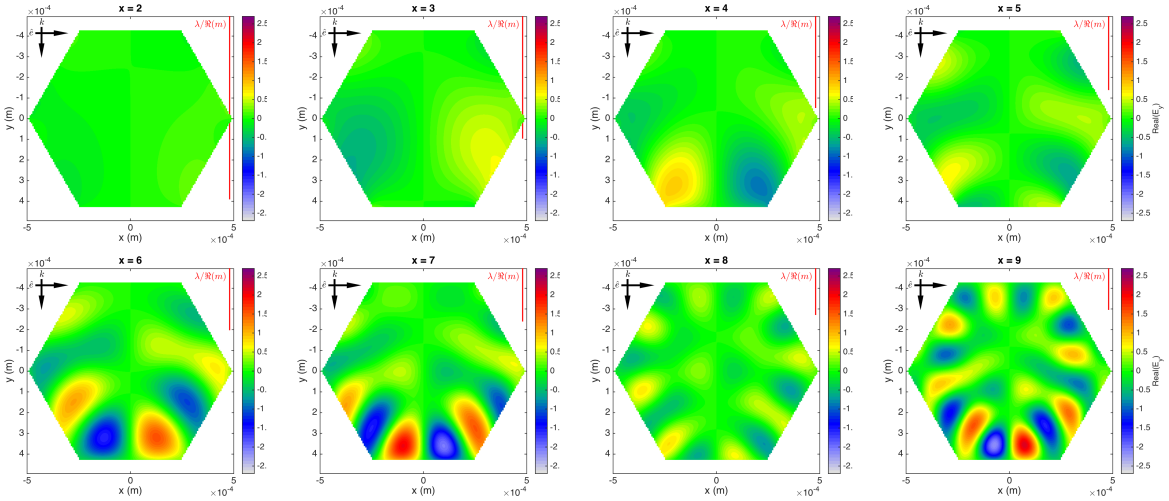

Figure 3.5: As in Fig. 3.3, but for $\Re(E_y)$.

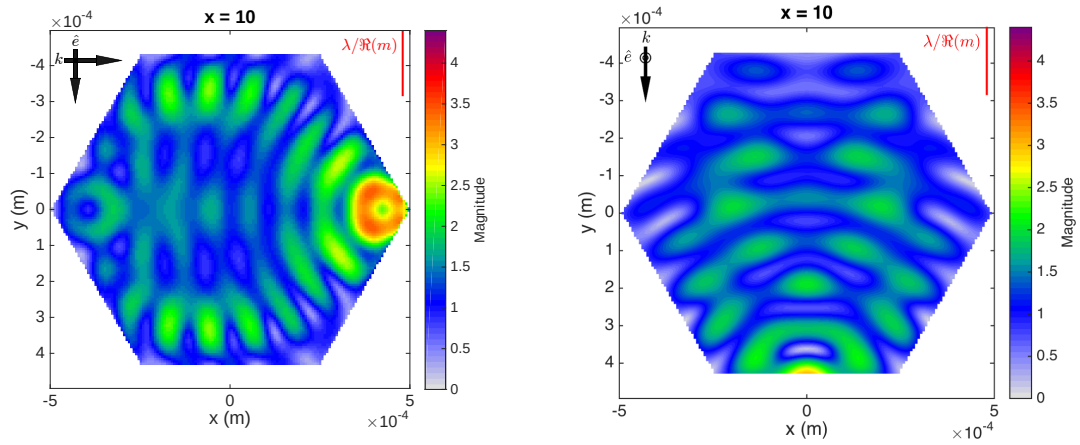

(a) x-direction; y-polarised.

(b) y-direction; z-polarised.

Figure 3.6: Magnitude of the internal field through the central plane of a hexagonal plate of aspect ratio 0.1 for $x = 10$. In the left panel, the incident wave is propagating in the x-direction and is polarised along the y-axis. In the right panel, the incident wave is propagating in the y-direction and is polarised along the z-axis.

Similarly, the symmetry and focussing remain when the wave is polarised orthogonal to the direction shown here, i.e. in the z direction. These results can be seen in Fig. 3.6. However, for the z polarised wave in Fig. 3.6b, the focussing occurs over a smaller region and is less prominent than in the x polarised case, showing a maximum magnitude that is 23% lower.

It is interesting to do some experiments to explore whether the phenomena above are a special case resulting from the symmetry of the setup, or whether they are part of a more general behaviour. We divide our sensitivity tests into 2 categories:

1. Experiments with $\hat{\mathbf{k}}$ in the x-y plane but not along an axis of symmetry of the hexagon.

2. Experiments where $\hat{\mathbf{k}}$ is rotated around the x-axis to lie at an angle in the y-z plane.

Fig. 3.7 shows the internal field when the incident wave is directed at an offset of 20° from the positive y-axis in the x-y plane. In this case the focussing behaviour is still prominent, but the symmetry of the field is lost as the incident wave is no longer directed along a particle axis of symmetry.

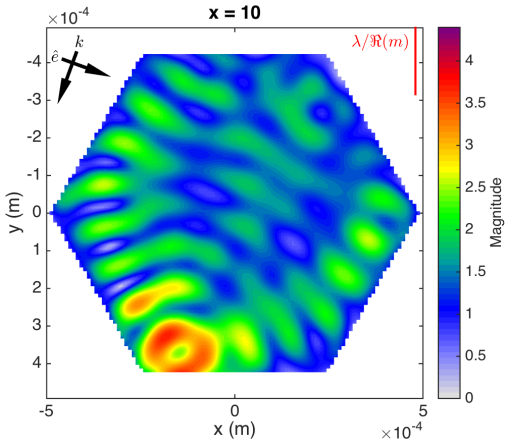

Figure 3.7: Magnitude of the internal field through the central plane of a hexagonal plate of aspect ratio 0.1 for $x = 10$. The incident wave is propagating in a direction at an angle of 20° in the clockwise direction from the y-axis, in the x-y plane. The polarisation direction is perpendicular to the incident wave, also in the x-y plane.

Fig. 3.8 shows the internal field magnitudes for incident angles of 20°, 70°, and 90° in the y-z plane. Focussing behaviour is still found for the smallest angle of 20° in the y-z plane (Fig. 3.8a), but the location of the focussing has moved slightly. There is a region at the bottom of the plate towards the forward side of the particle where the field values are large. An apparent internal reflection from the lower basal face results in the high field values being redirected towards the top of the particle. The field corresponding to this incident direction sees a decrease in maximum magnitude by approximately 10%, when compared to the case in Fig. 3.2b. Increasing the incident angle to 70° in the y-z plane diminishes much of the focussing behaviour. In this case the maximum magnitude decreases to a value approximately 50% lower than in Fig. 3.2b. Further increasing the angle to 90°, i.e. directing the incident wave from above a basal face, the maximum magnitude is found to occur close to the centre of the particle. Although the maximum is slightly larger than at 70°, it is still 42% lower than the horizontally directed case. Thus the largest fields are found when the incident wave is directed in a more horizontal direction, hitting the sides of the particle rather than the basal faces, even if the incident angle is not directed along an axis of symmetry. Lower field magnitudes result when the effective size parameter in the direction of propagation is small, as is the case for the incident wave directed at 70° and 90° in the y-z plane.

We explore the individual components of the field shown in Fig. 3.2b, where the incident

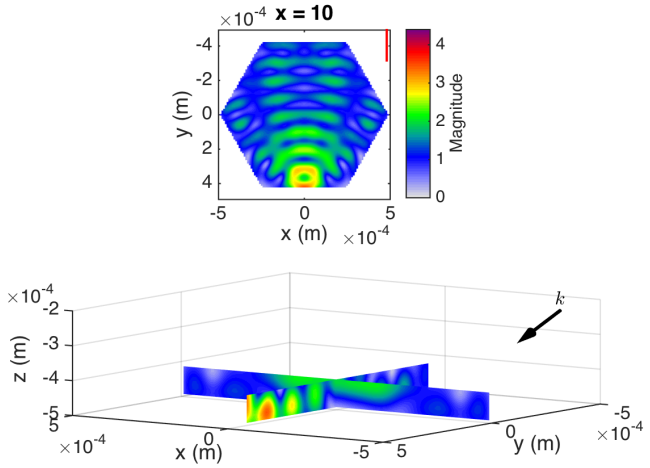

(a) Incident wave directed at 20° in the y-z plane.

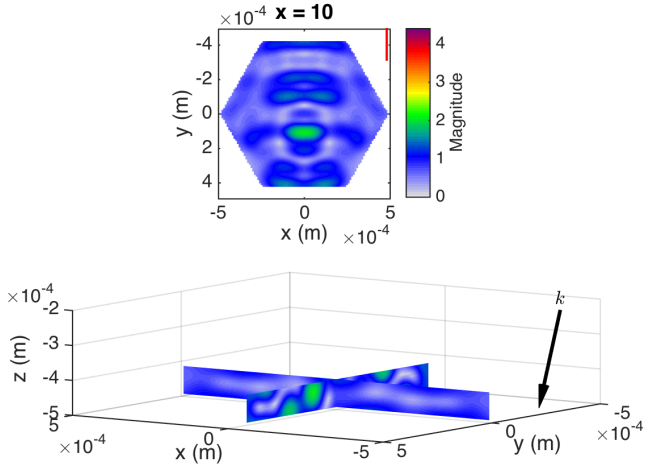

(b) Incident wave directed at 70° in the y-z plane.

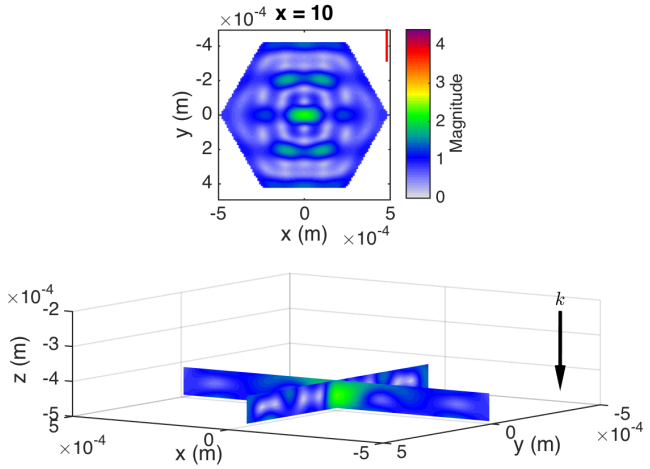

(c) Incident wave directed at 90° in the y-z plane.

Figure 3.8: Magnitude of the internal field through a hexagonal plate, when the incident wave is directed at different angles in the y-z plane. The top of each panel shows a slice through the central plane, and the bottom of each panel shows slices through $x = 0$ and $y = 0$. The incident wave is polarised along the x-axis.

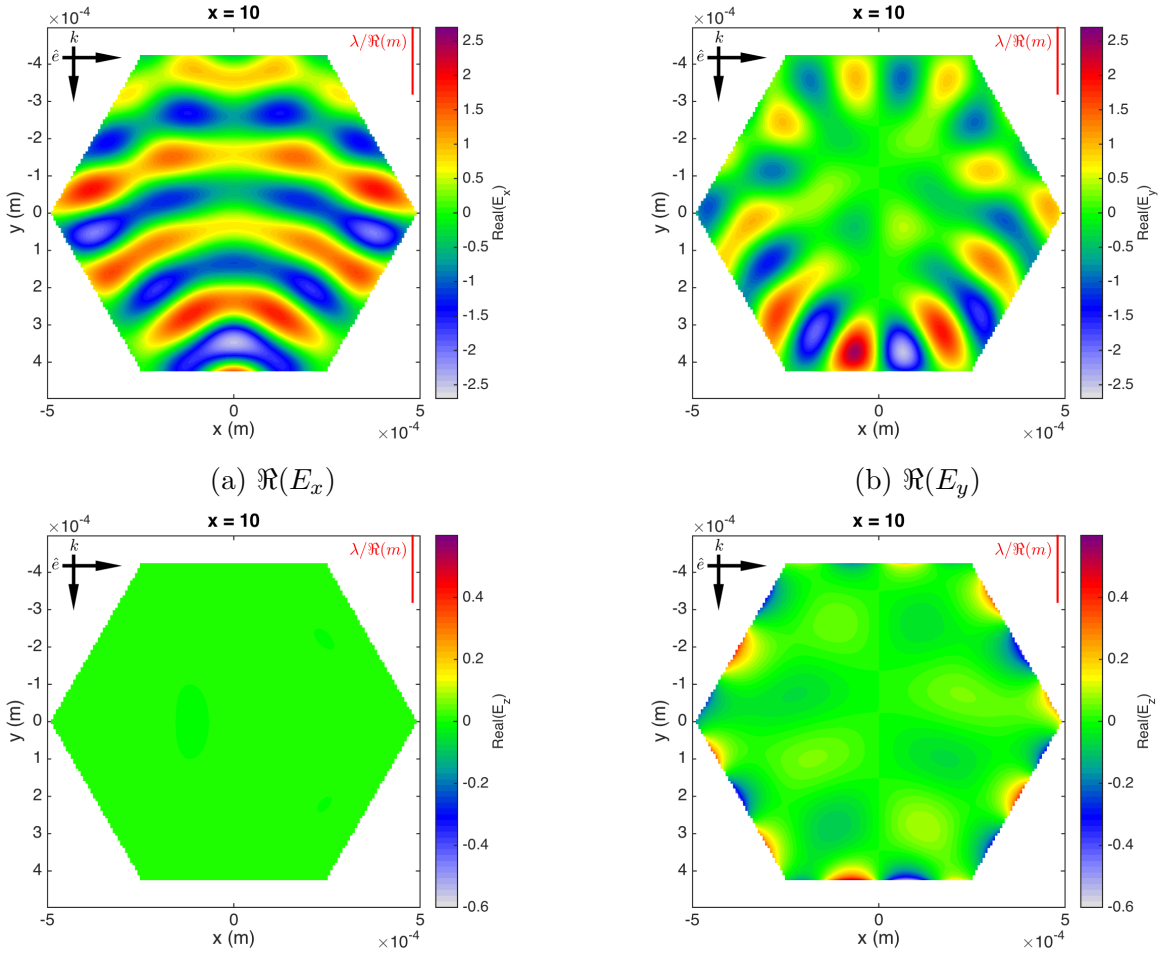

(a) $\Re(E_x)$

(b) $\Re(E_y)$

(c) $\Re(E_z)$: Central layer

(d) $\Re(E_z)$: Top layer

Figure 3.9: Real part of the (a) x component, (b) y component, (c, d) z component of the internal electric field of a plate of aspect ratio 0.1 for $x = 10$. The incident wave is propagating in the y-direction and is polarised along the x-axis. Panels (c) and (d) show slices through the central and top planes, respectively. Note that in these two panels a smaller range has been used for the colorbar.

wave is directed in the y direction and polarised in the x direction. Fig. 3.9 shows the real part of the components of the field which are perpendicular and parallel to the direction of propagation, i.e. the x (Fig. 3.9a) and y (Fig. 3.9b) components, for $x = 10$. This is what Tyynelä et al. [67] refer to as the transverse and longitudinal components of the field. The real part of the z component is also shown in the figure. Globally in L^2-norm E_z is 20 times smaller than E_x. Values of approximately 10^{-5} are found in the central plane of the particle, with a maximum of 0.55 on the top and bottom layers. Unlike the z component, the x and y components do not change much across the different layers within the plate. The fields are slightly larger in the central plane than on the top and bottom layers for the x and y components. For both E_x and

E_y, the field through the middle layer is approximately 30% larger than on the top and bottom layers. For E_z, the top and bottom layers have values which are 10^4 times larger than in the middle layer. The structure is concentrated on the particle boundary for E_z.

It is clear that the total field in Fig. 3.2b is a combination of two distinct waves. The x component in Fig. 3.9a shows a curved wave front extending through the bulk of the particle. The y component in Fig. 3.9b has a different structure resembling a standing wave around the perimeter of the plate, comprising a series of nodes (minima) and antinodes (maxima). It is seen in Fig. 3.9a that $\Re(E_x)$ has even symmetry, whereas the plot of $\Re(E_y)$ in Fig. 3.9b has odd symmetry. The focussing of a plane-like wave through the bulk of the crystal, plus a standing wave close to the boundary is similar to the behaviour found in spherical and cylindrical particles larger than the wavelength in Refs. [65,66,93]. As mentioned, we see this behaviour over a range of different values of x in the hexagonal plate, showing that this is an "off-resonance" phenomenon. Similar wave structures are observed for all size parameters, though it is less clear that a standing wave is present around the perimeter for smaller size parameters as there are fewer nodes and antinodes in these cases. Resonances may well exist at very specific values of x, however we have not found them, and unlike the case of spheres and infinite cylinders, there is no simple way to accurately predict the size parameters at which they would occur.

The different components of the field within the hexagonal plate of $x = 10$ for a z polarised wave have also been examined (not shown for brevity). $\Re(E_x)$ and $\Re(E_y)$ display fields with a node in the central plane of the particle, oscillating in sign between the top and bottom layers. $\Re(E_z)$ displays minimum values at the particle surface and reaches a maximum in the central plane, while the sign does not oscillate throughout the particle.

As expected, the wave extending through the particle in Fig. 3.9a has a shorter wavelength than in the exterior medium due to the refractive index, m, of the particle. For wavelength-scale spherical particles, analogous studies by Refs. [94,95] found the wave-

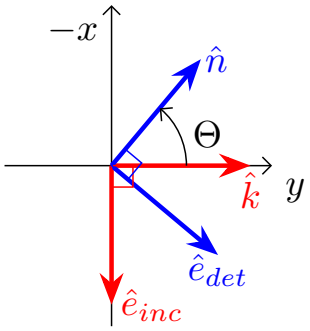

Figure 3.10: Coordinate system used for the far-field scattering calculations. The vectors corresponding to the incident field are shown in red, and those corresponding to the scattered field are in blue. The incident direction and polarisation ($\hat{\mathbf{k}}$ and $\hat{\mathbf{e}}_{inc}$) are in the y and x directions, respectively, while the scattered vectors $\hat{\mathbf{n}}$ and $\hat{\mathbf{e}}_{det}$ vary in the x-y plane according to the scattering angle Θ.

length through the central plane to be approximately equal to the material wavelength, i.e. $\lambda/\Re(m)$. In our case of a hexagonal plate with a wavelength smaller than the particle size, we have estimated that the external wavelength exceeds that inside the plate by a factor of 1.5 ± 0.2. This is slightly lower than the factor of approximately 1.78 that would result if the wavelength was dictated by the refractive index alone. This may be because we are looking at a flat geometry where even the central points are close to the particle boundary, so we don't see the material wavelength.

The standing wave around the perimeter has a longer wavelength that is more comparable to that of the incident wave, since it is located very close to the boundary. In this case, we have estimated that the incident wavelength is approximately 1.3 ± 0.2 times that of the standing wave. Again, this behaviour was observed in spherical particles by Refs. [94, 95], who also found that the number of maxima or minima around the perimeter was equal to the value of x. However, in our case we have found the number of maxima and minima to be less than x, counting a total of 9 each in Fig. 3.9b.

3.3.1.2 Far-field scattering

It is interesting to explore the effect the two different wave structures in Fig. 3.9 have on far-field scattering. To do this, Eq. (2.50) was used to calculate the differential scattering cross section, σ, computed at scattering angle intervals of 1°. Calculations

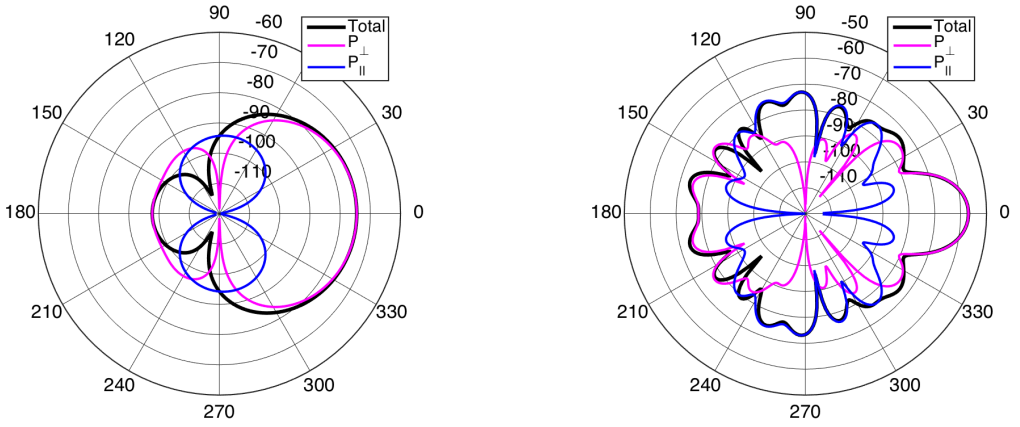

(a) $x = 2$ (b) $x = 10$

Figure 3.11: Polar plots of the differential scattering cross section of a hexagonal plate as a function of the propagation $\hat{\mathbf{n}}$ and polarisation $\hat{\mathbf{e}}_{det}$ directions of the scattered wave. This is calculated using all components of the field (black), only the perpendicular component ($P_\perp$; magenta), and only the parallel component ($P_\parallel$; blue). The value at 0° represents forward scattering, and 180° is backscatter.

of σ are displayed on a polar plot as a function of scattering direction $\hat{\mathbf{n}}$ using dB, i.e. $10\log_{10}(\sigma)$. Both $\hat{\mathbf{n}}$ and $\hat{\mathbf{e}}_{det}$ are in the x-y plane. The coordinate system used is shown in Fig. 3.10. Forward scattering is located at 0° on the plot, and backscatter is shown at 180°. It is noted that for $x = 0.01$ (not shown), scattering at different angles is less sensitive to particle shape, and scattering in the forward and backward directions is approximately equal.

Far from the source region, a scattered electromagnetic wave is transverse, i.e. the $\mathbf{E}$ and $\mathbf{H}$ fields are perpendicular to the direction of propagation of the scattered field. We investigate scattering calculated using different components of the internal field, which are defined relative to the direction of the incident field $\hat{\mathbf{k}}$. The cross sections for $x = 2$ and $x = 10$ are computed in 3 different ways: (i) using all components of the internal field; (ii) using only the component perpendicular to the incident wave ($P_\perp$), i.e. in the direction of $\hat{\mathbf{e}}_{inc}$; and (iii) using only the component parallel to the incident wave ($P_\parallel$), i.e. in the direction of $\hat{\mathbf{k}}$. In other words, there are geometric factors in the scattered far-field corresponding to the perpendicular and parallel components, which may be written as $|\hat{\mathbf{e}}_{inc} \cdot \hat{\mathbf{e}}_{det}| = \cos(\Theta)$ and $|\hat{\mathbf{k}} \cdot \hat{\mathbf{e}}_{det}| = \sin(\Theta)$, respectively. This means that the largest contribution to far-field scattering from the perpendicular component

will be in the forward and backward directions, while the largest contribution from the parallel component will be at intermediate scattering angles.

Fig. 3.11 shows the result for the hexagonal plate of $x = 2$ and $x = 10$. In both cases it can be seen that the transverse component, $P_{\perp}$, contributes more to scattering near the forward and backward directions, with a smaller contribution from $P_{\perp}$ at intermediate scattering angles close to 90° and 270°. Conversely, $P_{\parallel}$ contributes more to the total scattering at these angles, and less in the forward and backward directions. This is expected from Eq. (2.50), as the polarisation direction $\hat{\mathbf{e}}_{det}$ is perpendicular to the observation direction $\hat{\mathbf{n}}$.

The differential scattering cross section for the z polarised incident wave is shown in Fig. 3.12, this time plotting the results in the y-z plane. The same conclusions are drawn from this scenario - the transverse component (corresponding to the z component in this case) dominates forward and backward scattering, and the component in the direction of propagation (P_y) contributes mainly to sidescatter. Thus we deduce that the standing wave structure around the perimeter of the hexagonal plate contributes predominantly to sidescattering, and the wave extending through the centre is responsible for scattering at angles proximate to the forward and backward directions.

The results presented here help us to understand what controls the asymmetry parameter, g, which describes how much incident radiation is scattered in the forward and backward directions. Therefore, the finding could be useful for developing parameterisations of g for use in radiative transfer simulations.

3.3.2 Cylindrical disk and spheroid

Realistic ice particles have historically been approximated by simpler shapes such as spheres and spheroids in order to calculate their scattering properties. Much of the literature has shown that this method produces poor results for particles outside the Rayleigh regime [96]. It is interesting to explore whether it is possible to gain greater physical insight into why these methods fail to produce accurate results by modelling

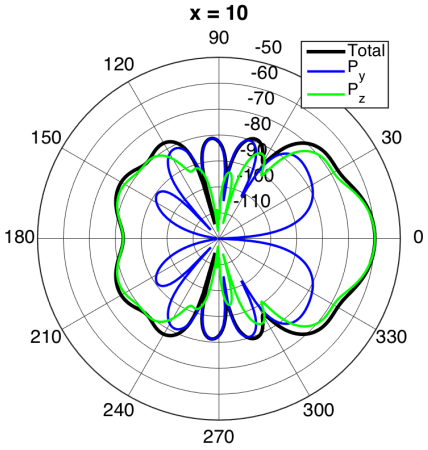

Figure 3.12: Polar plot showing the differential cross section of the plate in the y-z plane. The incident wave is propagating in the y-direction and is polarised along the z-axis. The value at 0° represents forward scattering. This is calculated using all components of the field (black line), only the y components (along direction of propagation; blue line), and only the z components (perpendicular to propagation direction; green line).

different approximations to the plate.

The magnitude of the internal field is plotted for a cylindrical disk of solid ice, with equivalent aspect ratio and D_{max} to the hexagonal plate in section 3.3.1. This allows us to look at the effect of particle shape on the structure of the field. We also look at a solid ice spheroid of equal aspect ratio and D_{max}. Fig. 3.13 shows the results for $x = 2$ and $x = 10$. The real parts of the x and y components of the field for $x = 10$ can be seen in Fig. 3.14c. Overall, there are clear similarities between the structure of the field within both of these particle shapes, compared to the hexagonal plate. The same phenomenology applies to both geometries, and the details of the perimeter of the particle are not critical to produce similar internal fields. The field is more uniform for $x = 2$, increasing in complexity for $x = 10$. The focussing behaviour in the forward region is also prominent for both the disk and spheroid. For $x = 2$, a slightly smaller amount of focussing is seen in the spheroid than in the disk and the hexagonal plate. Conversely, for $x = 10$, the spheroid exhibits more focussing than the other geometries. Within the spheroidal geometry, the wave crests (in green) appear to be more curved, extending to the the particle edge. This could be because the spheroidal shape is very thin close to the perimeter, resulting in less interference from different layers in these

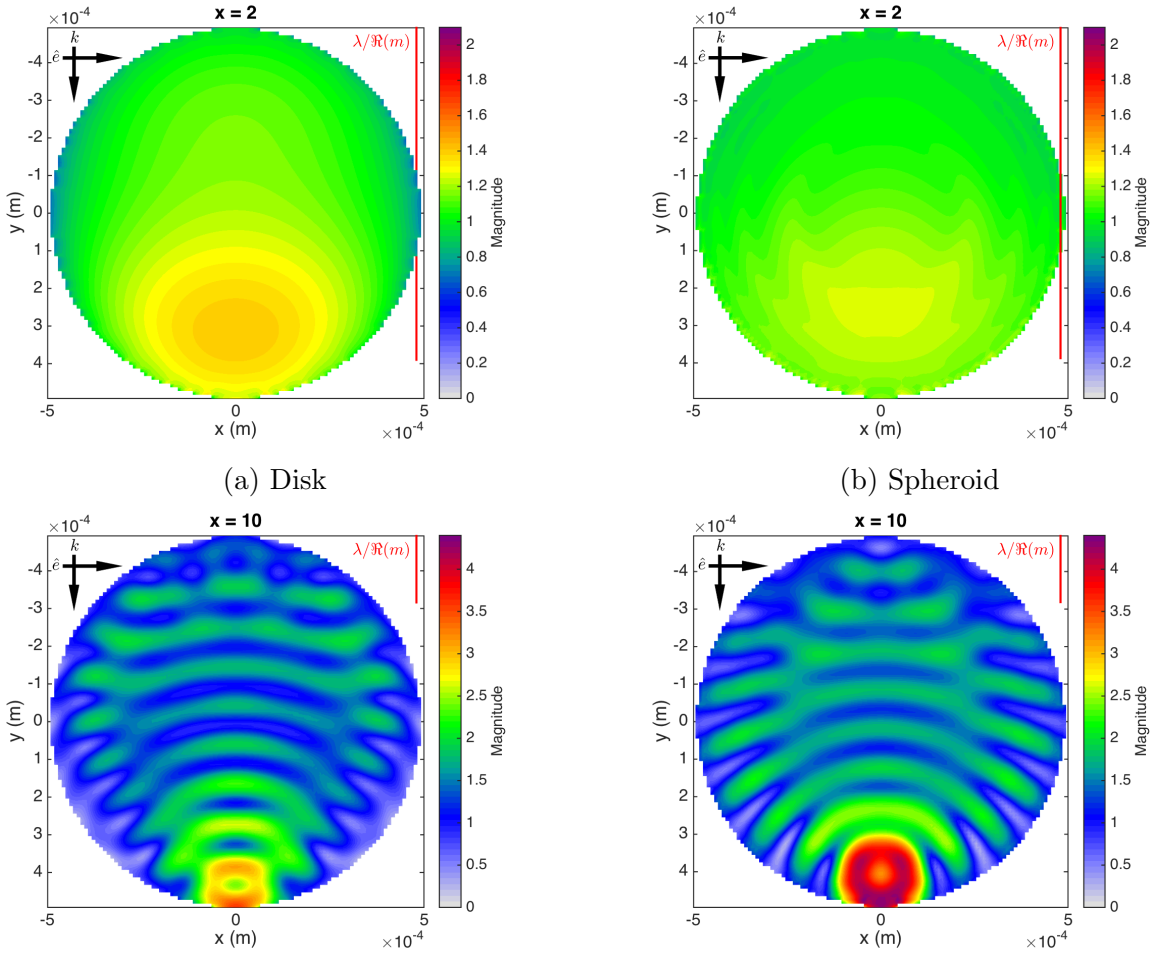

(a) Disk (b) Spheroid

(c) Disk (d) Spheroid

Figure 3.13: Magnitude of the internal field of (a, c) a disk and (b, d) a spheroid of $x = 2, 10$. Both particles have an aspect ratio of 0.1 and $D_{max} = 1$ mm, i.e. the same values as the hexagonal plate in section 3.3.1.

areas.

The structure of the fields within the cylindrical disk and the hexagonal plate exhibit clear resemblances, suggesting that in terms of approximations for a hexagonal geometry, a disk may provide superior results to a spheroid. However, in terms of the average magnitudes, the spheroid displays results that are closer to the plate, giving values within 1% for $x = 2$, and 3% for $x = 10$. The average values for the disk differ from the plate by approximately 4% and 13% for $x = 2$ and $x = 10$. For $x = 2$, the maximum magnitudes of the disk and spheroid are within 3% and 4% of the plate, respectively. For the larger size parameter of $x = 10$, both geometries have maximum values that differ from the plate by about 10%, but the spheroidal shape results in an overestimation while the disk gives an underestimation.

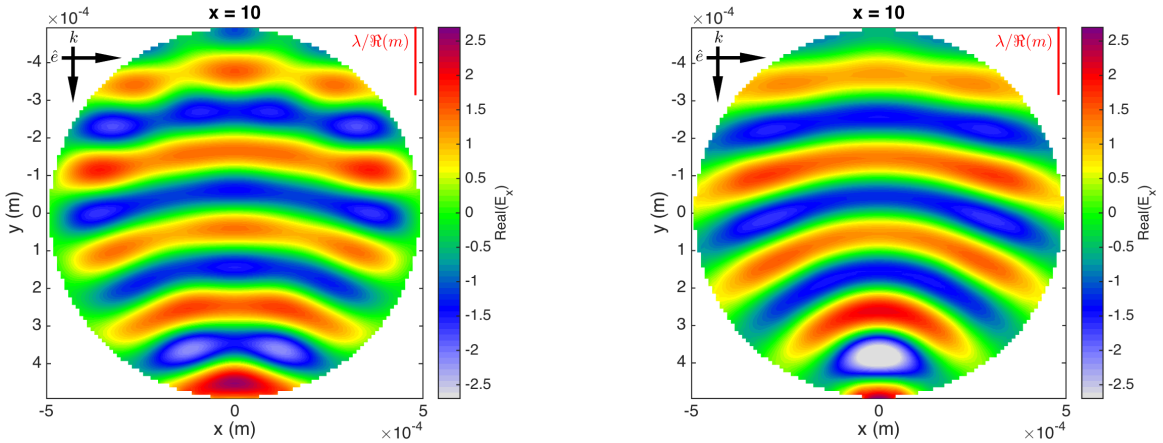

(a) Disk $\Re(E_x)$

(b) Spheroid $\Re(E_x)$

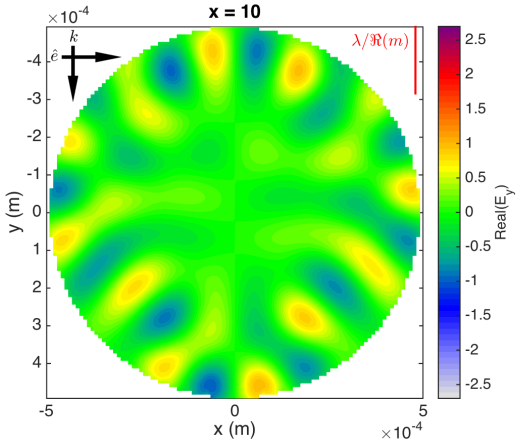

(c) Disk $\Re(E_y)$

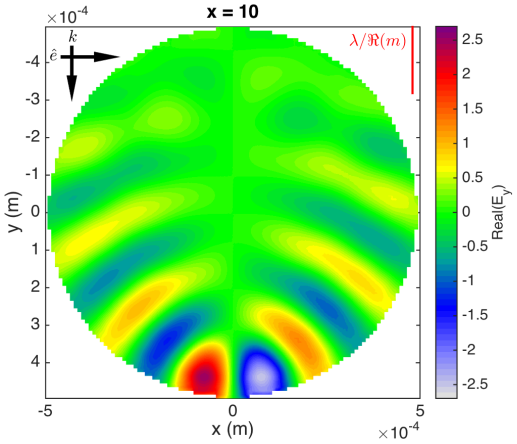

(d) Spheroid $\Re(E_y)$

Figure 3.14: Components of the internal field through the central plane of particles of $x = 10$ with aspect ratio and D_{max} equal to the hexagonal plate. (a) and (b) show the real part of the x components in a disk and spheroid, and (c) and (d) show the real part of the y components.

3.3.3 Hexagonal column

3.3.3.1 Internal field

Fig. 3.15 shows the field inside a hexagonal prism of aspect ratio 1 for $x = 2$ and $x = 10$. Slices have been plotted through the planes $x = 0$ m and $z = -1.2 \times 10^{-4}$ m, where $|\mathbf{E}|$ is at a maximum for $x = 10$. The particle has the same value of D_{max} as the plate. It can be seen that by increasing the aspect ratio, more focussing is seen for $x = 2$ compared to the plate, and the maximum field strength is approximately 20% larger. For $x = 10$, Fig. 3.15b shows that the increased aspect ratio results in 2 primary regions of focussing, but the maximum value of these is smaller than in the

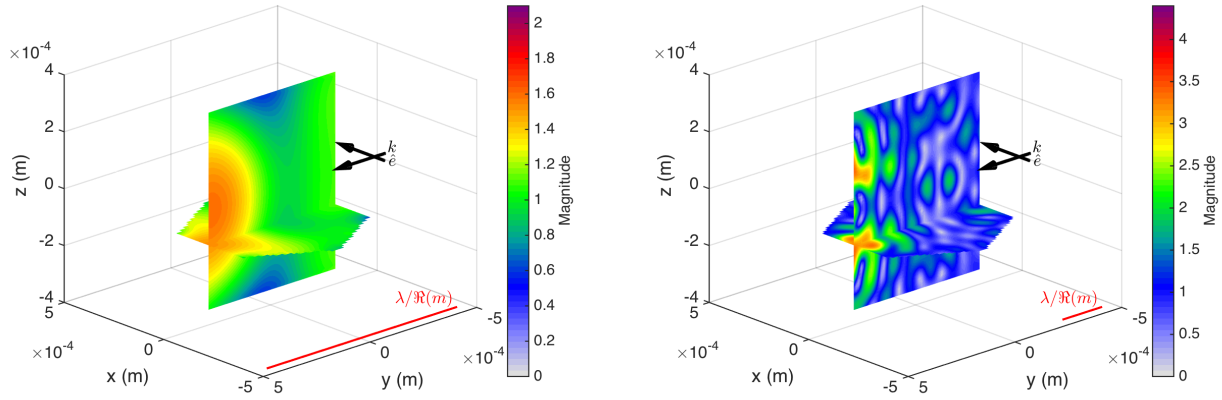

(a) $x = 2$ (b) $x = 10$

Figure 3.15: Magnitude of the internal field of a hexagonal column of aspect ratio 1 of (a) $x = 2$; (b) $x = 10$. Slices are shown through $x = 0\,\mathrm{m}$ and $z = -1.2 \times 10^{-4}\,\mathrm{m}$. These particles have a value of $n_\lambda = 62$ and 17, respectively.

flat plate. There appears to be more destructive interference in the prism, with the average magnitude in the plate exceeding that in the prism by a factor of 1.3.

Investigating the real part of the x and y components of the field for $x = 10$ shows that these are qualitatively very similar to the field components of the plate (not shown for brevity). The transverse component for the column exhibits a wave extending though the particle, and the component in the direction of propagation displays a well defined standing wave structure around the perimeter.

Fig. 3.16 shows the case equivalent to Fig. 3.15b, but with the incident wave along the z-axis, hitting the top basal face of the prism. This corresponds to an angle of 90°, as discussed for the plate in section 3.3.1. For the thin plate, it was found that this setup results in an internal field with lower maximum magnitudes than when the incident wave is directed in the x-y plane. For the prism of aspect ratio 1, this is not the case. Strong focussing behaviour is seen towards the forward region of the particle. Thus, the lower field value found for the plate when the incident angle is directed at 90° is a result of the aspect ratio of the particle. The effective size parameter in the direction of propagation is small for the thin plate, resulting in a diminished field, but this is not the case for the thick prism.

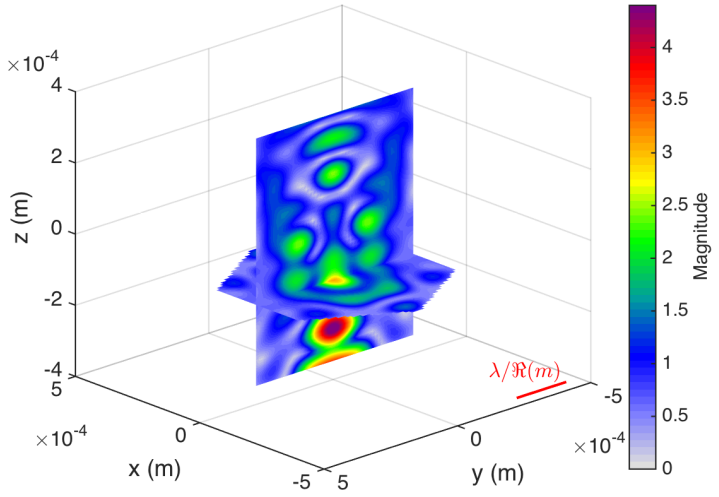

Figure 3.16: Magnitude of the internal field in a hexagonal prism of $x = 10$. The incident wave is directed along the z-axis and is polarised along the x-axis.

3.3.3.2 Far-field scattering

Polar plots of σ are displayed in Fig. 3.17 for a hexagonal column, to explore the effect of aspect ratio on the differential scattering cross section. The overall pattern resembles that of the thin plate with qualitatively similar $P_{\perp}$ and $P_{\parallel}$ contributions. Quantitatively, there are some large differences, particularly in the backscatter direction for $x = 10$. However, as mentioned in section 5.2, backscatter is very sensitive to discretisation. Therefore a finer mesh resolution would be required in order to make meaningful conclusions about changes in σ_b with aspect ratio.

3.3.4 Cylindrical column and sphere of same D_{max} as hexagonal prism

In section 3.3.2 we explored the differences between the internal field of the hexagonal plate and that of a cylindrical disk and spheroid. Analogous to this, we have compared the taller hexagonal prism to a sphere and right circular cylinder of equivalent aspect ratio and D_{max}. Fig. 3.18 shows the results for $x = 2$ and $x = 10$. For both values of x, it is observed that spheres have one principle region of focussing, rather than the two maxima we observed for the hexagonal column. The cylindrical column bears a closer

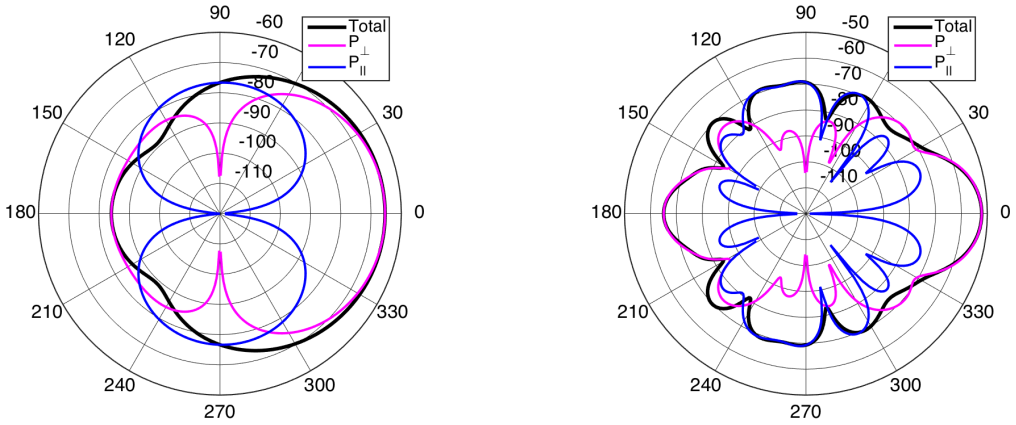

(a) $x = 2$ (b) $x = 10$

Figure 3.17: Differential scattering cross section, as in Fig. 3.11, but for a hexagonal prism of aspect ratio 1.

resemblance to the hexagonal prism geometry in that it displays multiple regions of large magnitude values for $x = 10$, although the maximum value is slightly larger for the cylindrical column, exceeding the hexagonal geometry by approximately 6%. However, the maximum magnitude of 6.6 found for the sphere of $x = 10$ overestimates the hexagonal case by 75%. It is noted that in order to enable clearer comparisons we fixed the range of the colour scale in Fig. 3.18d to be the same as the other shapes. Although the sphere displays a higher maximum value, the hexagonal and cylindrical prisms have larger average magnitudes than the sphere, by a factor of approximately 1.3. These results show that for the larger aspect ratio of 1 considered here, the cylindrical approximation to the hexagonal particle appears to be superior to the commonly used spherical or spheroidal approximations. In section 3.3.2, it was found that an equivalent aspect ratio spheroid gives a good approximation of the internal field for a smaller aspect ratio of 0.1. However, it is shown here that as the aspect ratio increases, the approximation becomes less accurate.

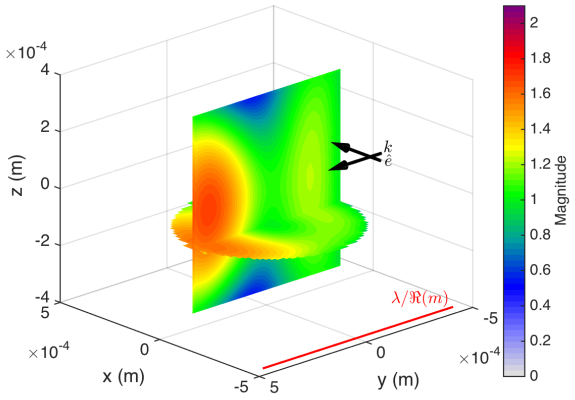

(a) Cylinder $x = 2$

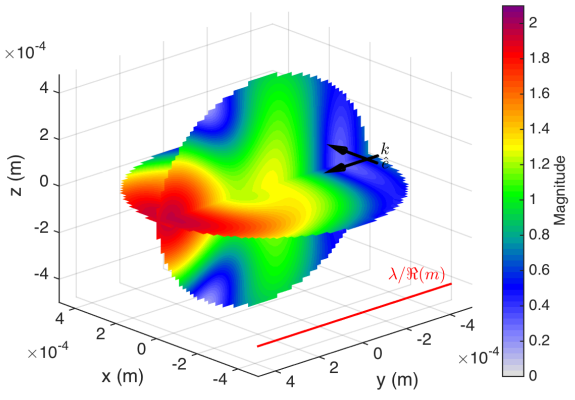

(b) Sphere $x = 2$

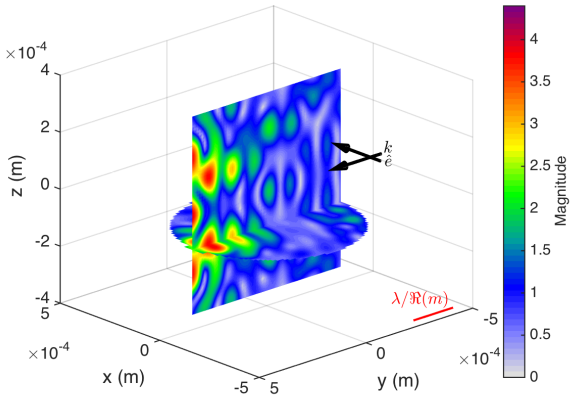

(c) Cylinder $x = 10$

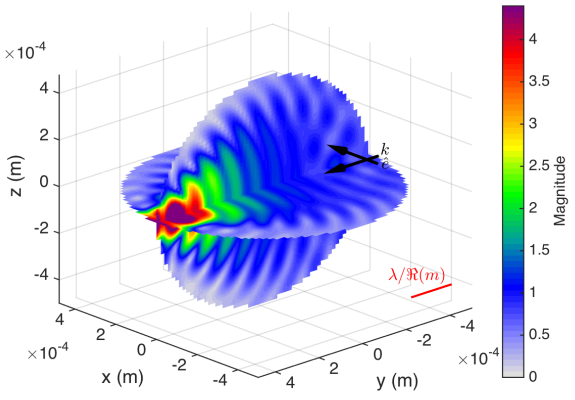

(d) Sphere $x = 10$

Figure 3.18: Magnitude of the internal field of (a, c) a cylindrical column and (b, d) a sphere of aspect ratio 1 for $x = 2, 10$.

3.4 Results and discussion - Aggregates

3.4.1 Chain aggregates of plates 1: 2 hexagonal plates

In the presence of an electric field, chain aggregates of plates can form. Connolly et al. [26] observed that these geometries form predominantly with the prism faces of individual crystals touching. Here we have studied two different aggregates of plates. The first is a simple aggregate of 2 plates, and the second is an aggregate of 5 plates. Both geometries are aligned with prism faces touching, and were generated by Ref. [97] using a stochastic algorithm.

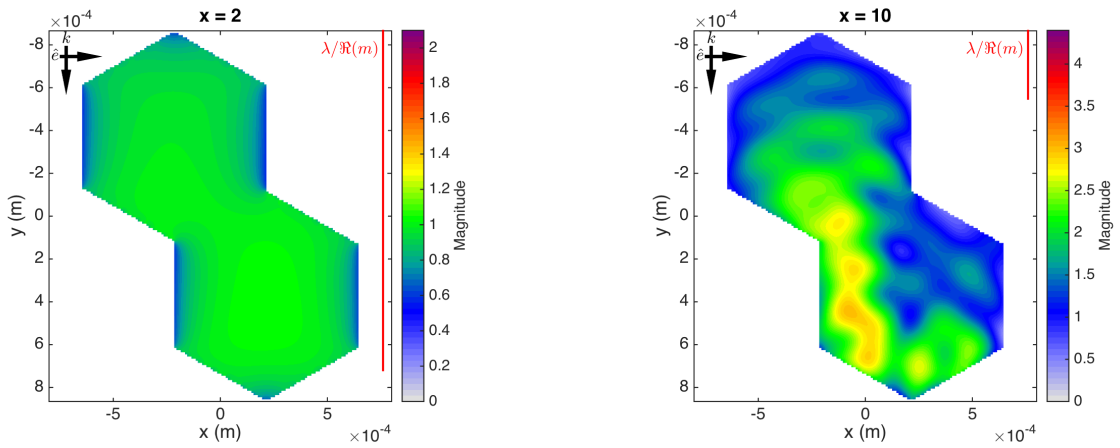

(a) $x = 2$ (b) $x = 10$

Figure 3.19: Magnitude of the internal field through the central plane of an aggregate of 2 hexagonal plates for (a) $x = 2$ and (b) $x = 10$. The number of dipoles per wavelength used in the calculations for these particles is $n_\lambda = 159$ and 31, respectively.

3.4.1.1 Internal field

First we look at an aggregate of 2 plate-like particles, where each monomer is the same height and D_{max} as the individual plate studied in section 3.3.1. Fig. 3.19 shows that the aggregates of 2 plates exhibit less defined regions of focussing with smaller maximum magnitudes than the previous geometries. For $x = 2$, there is very little focussing. In Fig. 3.19b, it can immediately be seen that for $x = 10$ interference between the two plates reduces the clear wavy structure and symmetry observed in the hexagonal, cylindrical, and spheroidal monocrystals. These interactions and the resulting field depend on the alignment of the 2 plates. If the arrangement is such that the aggregate of 2 plates is symmetric with respect to the incident wave, the internal field is also symmetric, as expected. An example of this can be seen in Fig. 3.20. Although the field has a symmetric structure in this case, the focussing is still less defined and the maximum magnitude is lower than that calculated for the single plate, suggesting that the complexity of the particle is integral to the loss of structure, rather than the alignment or orientation. We are interested in exploring more irregular aggregates which are frequently observed in clouds. The result in Fig. 3.19b suggests that the internal field within such particles may not exhibit any clear structure. To test this, the field inside an aggregate of 5 plates was examined, followed by the exploration of more complex aggregates in section 3.4.4.

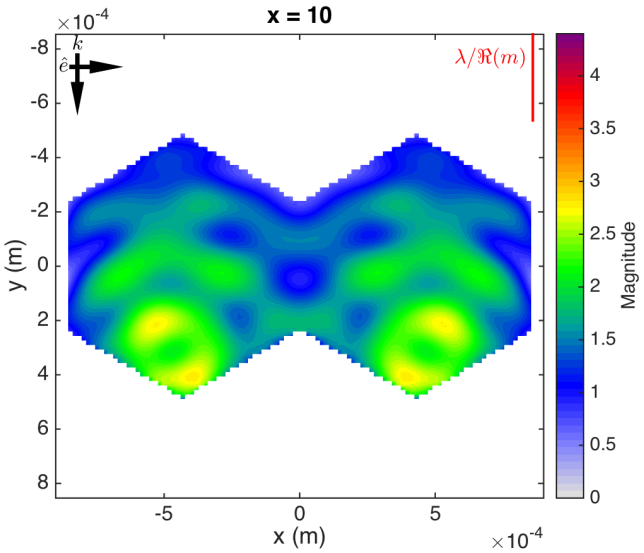

Figure 3.20: Magnitude of the internal field through the central plane of an aggregate of 2 hexagonal plates with $x = 10$. The incident wave is propagating in the y-direction and is polarised along the x-axis. The 2 plates are aligned such that the particle is symmetric with respect to the incident wave.

3.4.2 Chain aggregates of plates 2: 5 hexagonal plates

3.4.2.1 Internal field

Fig. 3.21 shows the field inside an aggregate of 5 hexagonal plates, where each plate has the same dimensions as the particle modelled in Fig. 3.2. Similarly to what was found for the aggregate of 2 plates, this particle has a field that shows less symmetry than the monocrystals. It is obvious that as the complexity of the geometry increases, there is a clear reduction in magnitude and further dampening of the wavy structure. The internal field magnitude becomes more smoothed and seems to lack the constructive interference that locally changes the magnitude in simpler particles such as the individual plate. However, upon closer inspection, the amount of focussing varies according to the orientation of the particle with respect to the incident wave. For example, directing the incident wave at an angle of 140° in the clockwise direction from that shown in Fig. 3.21b leads to a maximum magnitude which exceeds that shown here by almost 50%. This can be seen in Fig. 3.22. It is noted that this value is still less than that calculated for the single plate. Overall, the focussing effect appears to be more prominent in cases where the path length in the direction of propagation is longer. At 140°,

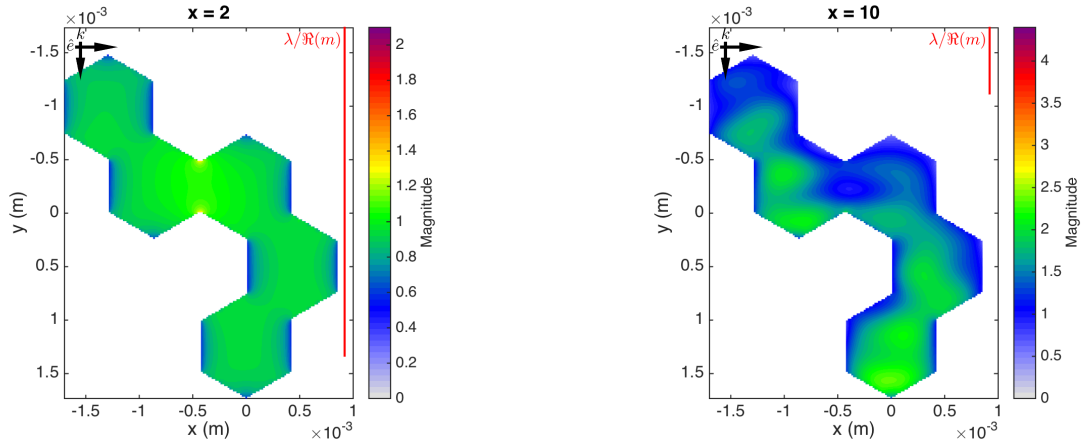

(a) $x = 2$ (b) $x = 10$

Figure 3.21: Magnitude of the internal field through the central plane of an aggregate of 5 hexagonal plates for (a) $x = 2$ and (b) $x = 10$. These particles have a value of $n_\lambda = 184$ and 36, respectively.

a large amount of focussing is seen as the incident wave is directed at an angle allowing passage through multiple plates with little deviation from the incident direction. This is similar to the results for the hexagonal monocrystals, with the incident wave directed along the z-axis. The shorter path length through the thin plate results in a lower maximum magnitude of the internal field, while the longer path length through the prism results in a larger field with prominent focussing behaviour.

For the orientation shown in Fig. 3.21, the average and maximum magnitudes for the aggregate of 5 plates are quantified in Table 3.1. Since remote sensors probe an ensemble of particle orientations, and details of the far-field patterns are sensitive to orientation, we consider orientationally averaged far-field scattering quantities in the following sections.

3.4.2.2 Far-field scattering

The far-field scattering results for the aggregate of 5 plates is shown in Fig. 3.23. As in previous cases, the incident plane wave propagates in the y direction, and is polarised perpendicular to the incident wave, along the x-axis. However, in this case we have considered an orientationally averaged example, for different orientations in the x-y plane. The particle is rotated at intervals of 10° about the z-axis, resulting

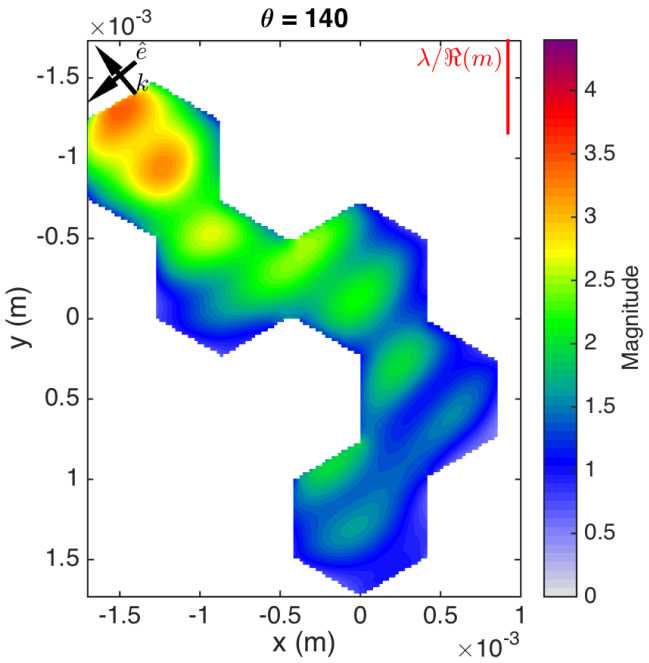

Figure 3.22: Magnitude of the internal field through the central plane of an aggregate of 5 hexagonal plates with $x = 10$. The incident wave is propagating in the x-y plane, at an angle of 140° in the clockwise direction from the y-axis. The polarisation direction is perpendicular to the incident wave, also in the x-y plane.

in scattering calculations being obtained for 36 different orientations. The results averaged over the 36 orientations are shown in Fig. 3.23. As before, the cross sections have been computed using all components of the internal field, and also using only the components perpendicular and parallel to the incident wave, $P_\perp$ and $P_\parallel$.

For $x = 2$, $P_\perp$ is responsible for the majority of the total scattering. The transverse component also has a larger contribution towards the total scattering value for $x = 10$. Similar to the results seen for the single plate with a fixed orientation in Fig. 3.11, $P_\perp$ contributes mainly to forward and backward scattering, and $P_\parallel$ contributes more to sidescatter. This pattern persists through orientation averaging, and is not limited to a single particle orientation.

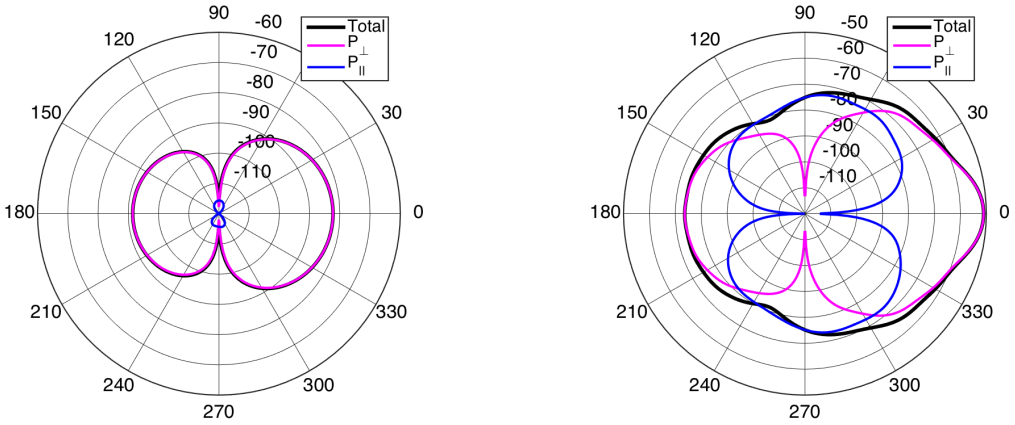

(a) $x = 2$ (b) $x = 10$

Figure 3.23: Scattering in different directions by chain-like aggregate of 5 plates for (*a*) $x = 2$ and (*b*) $x = 10$. In (*a*), the scattering due to $P_{\perp}$ (magenta line) almost entirely overlaps the total scattering (black), and the amount of scattering due to $P_{\parallel}$ (blue) is very small. For both size parameters, the results are averaged over 36 orientations in the x-y plane.

3.4.3 Spheroids of equal D_{max} and aspect ratio to plate-like aggregates, but with effective permittivity determined by volume fraction

Comparisons have been done with the internal field of spheroids of equal D_{max} and aspect ratio to the aggregates of plates. The permittivity of the spheroids have been reduced according to the Maxwell-Garnett formula in Ref. [71]. This mixing ratio determines the volume fraction of ice that such a spheroid has, and subsequently calculates the corresponding effective permittivity. Such soft sphere and spheroid approximations have been used extensively in previous literature, so we are interested in assessing the performance of this method.

For brevity, the internal field plots have not been included here; instead we summarise the results briefly. In all cases examined it is found that the Maxwell-Garnett approximation overestimates the average internal field value. This overestimation ranges between 5% and 11%. For the spheroidal approximation of 2 hexagonal plates of $x = 2$, the maximum field value is also overestimated. However, as the particle size or complexity is increased, the Maxwell-Garnett approximation results in underestimations

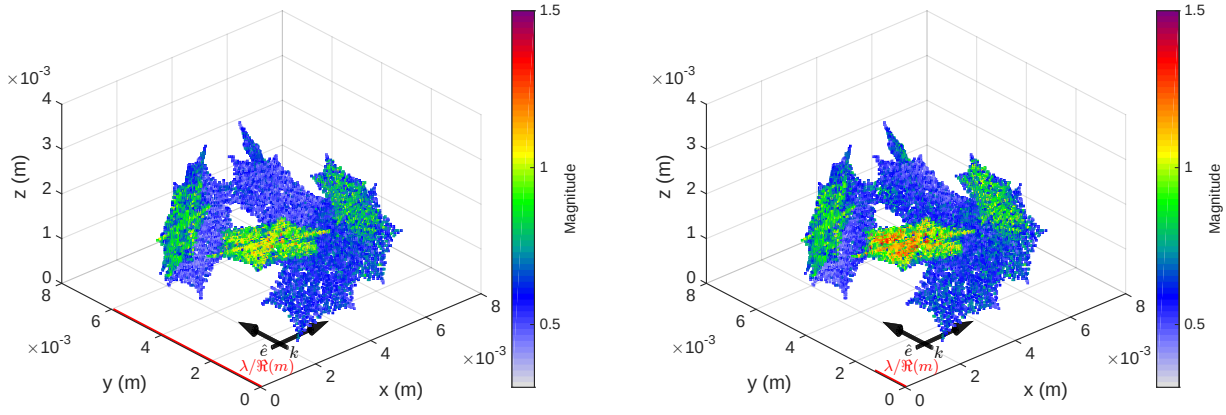

Figure 3.24: Magnitude of the internal field of an irregular aggregate of 10 "fernlike dendrite" monomers for (*a*) $x = 2$ and (*b*) $x = 10$. The dipole spacing is 47 µm, giving approximately $n_\lambda = 125$ for $x = 2$, and $n_\lambda = 25$ for $x = 10$. Note that the range of values in the colorbar is reduced, compared to previous cases.

of the maximum value. This is caused by the incapability of the spheroid to replicate complex interactions within realistic particles.

3.4.4 Irregular aggregates of 10 "fernlike dendrite" monomers

Realistic snowflakes modelled by Tyynelä et al. [3] have been used to examine the internal field of more complex geometries. These particles are composed of 10 "fernlike dendrite" monomers. Ten different arrangements of these particles were available to us, with values of D_{max} ranging from $6 - 9$ mm. We plot the field of one arrangement in Fig. 3.24, and include results for the average and peak fields of two different arrangements in Table 3.1.

3.4.4.1 Internal field

In Fig. 3.24, the internal field of one aggregate is plotted for $x = 2$ and $x = 10$. Note that the range of the colour scale has been reduced for these particles to observe more detail in the internal field. For both values of x, the average field value is very similar (approximately $0.65-0.7$, see Table 3.1), and the magnitudes are lower than in all other particles considered. The maximum field value is also considerably smaller than in the

different monocrystals of equal x. The same thing was found when these calculations were repeated for various different arrangements of 10 monomers. It can also be seen in Table 3.1 that calculations for $x = 0.01$ show almost identical average and maximum values to $x = 2$.

The values obtained for these particles are more similar to the value of $|\mathbf{E}| \approx 0.58$ you would see if only the applied field were present. This shows that for these fluffy aggregates, RGA is a more realistic approximation than for monocrystals. However, the true field is still systematically $15 - 20\%$ higher than that assumed by RGA, while peak values are at least a factor of 2 larger. These differences in the internal field strength lead to underestimates of scattering cross-sections by RGA, as observed by Tyynelä et al. [61].

No focussing behaviour is obvious for $x = 2$ or $x = 10$ in the complex aggregate. In fact, the individual crystals within each aggregate seem to be independent of each other, acting as if they are isolated. To test this, we calculated the field of the individual crystals detached from the rest of the aggregate. If we isolate crystals, we find the same field to within 5% of that calculated in the presence of the surrounding crystals. There is very little coupling between different monomers in the particle - only intramonomer. This may suggest a simplified method of computing scattering from large complex aggregates by considering interactions only within individual monomers. This implies that the "modified RGA" method developed by Lu et al. [98] is a reasonable approximation. In that method the range of interactions between dipoles is limited to some multiple of the minimum dimension of the particle. The method could provide good results for the fluffy aggregates considered here, provided that the range of interactions used is close to the scale of a monomer. This idea is developed further and tested for a range of aggregates in chapter 5.

Our results show that if the scattering by the monomer crystals can be computed individually, the net scattering by the aggregate can quickly be estimated using RGA, since coupling between the monomers is small. For monomers small compared to the wavelength, the monomer scattering could be calculated rapidly using the results

in Ref. [99]. For larger monomers, DDA calculations could be used (but on a much smaller scale than required to compute the scattering by the whole cluster). Our results support the assumptions made by Hogan et al. [100] who postulated that if an isolated monomer crystal scatters according to Gans theory with a particular dielectric factor (related to the internal field of the monomer), then a larger aggregate composed of several monomers could be described using RGA with that same value of dielectric factor - i.e. neglecting inter-monomer coupling.

3.4.4.2 Far-field scattering

For the complex aggregates, we have also considered a scenario averaged over 36 orientations, using the same methodology described in section 3.4.2.2 for the aggregate of 5 plates. The polar scattering plots in Fig. 3.25 show the orientationally averaged differential scattering cross sections. Panels (a) and (b) show the total amount of scattering, along with the contributions from the perpendicular and parallel components of the field, for $x = 2$ and 10. The results exhibit similar behaviour to the aggregate of 5 plates in Fig. 3.23. As before, a significant amount of scattering in the forward and backward directions is due to the component of the field perpendicular to the incident wave, with the parallel component contributing mainly to sidescatter. For the larger size parameter of $x = 10$, a comparison with the results for the aggregate of 5 plates in Fig. 3.23 shows that the influence of $P_{\parallel}$ on the total amount of scattering is getting weaker with particle complexity. In contrast to the aggregate of plates, there are now very few angles where $P_{\parallel}$ dominates the total. The cross sections for individual crystals isolated from the aggregate were also examined, showing the same results. Therefore we suggest that the decrease in contribution from the component in the direction of propagation occurs as a result of the reduction in homogeneity of the particle composition, i.e. the presence of regions of air between solid ice branches.

It is worth noting that in contrast to the example of a symmetric plate, the z component of the field for these fluffy aggregates is comparable to the y component. However, it is not significant for the scattering quantity considered here as in Eq. (2.50) we chose

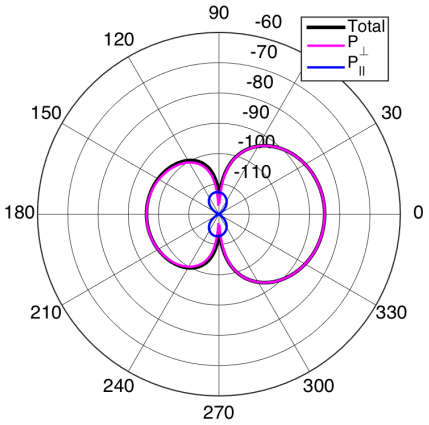

(a) $x = 2$

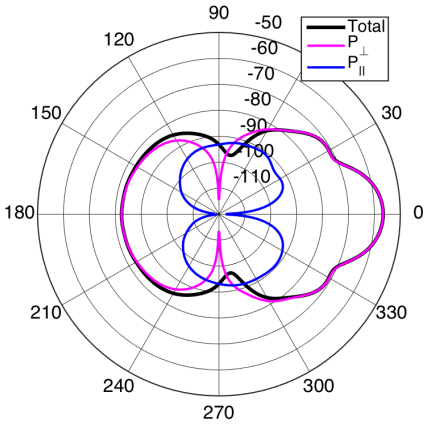

(b) $x = 10$

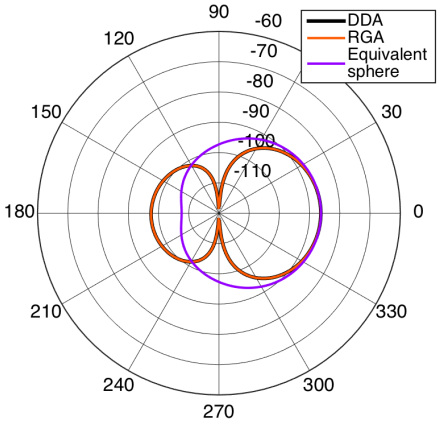

(c) $x = 2$

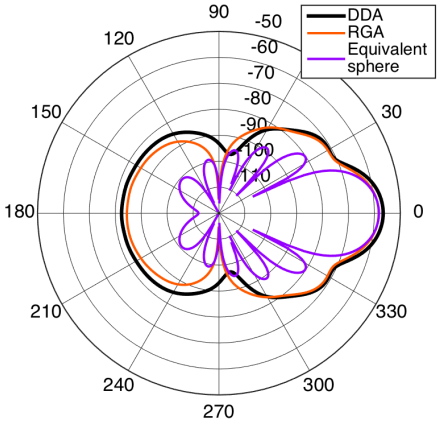

(d) $x = 10$

Figure 3.25: Orientationally averaged scattering cross section at different scattering angles by a complex aggregate for (a, c) $x = 2$ and (b, d) $x = 10$. The black lines in all plots show the total amount of scattering. The magenta lines in the top row show scattering due to $P_\perp$, and the blue lines show scattering due to $P_\parallel$. Panels (c) and (d) show comparisons of the total scattering with results obtained using RGA (orange), and an equivalent sphere approximation (purple) using the Maxwell-Garnett mixing ratio. The DDA and RGA results are almost identical for $x = 2$, with the orange line covering the black line in panel (c).

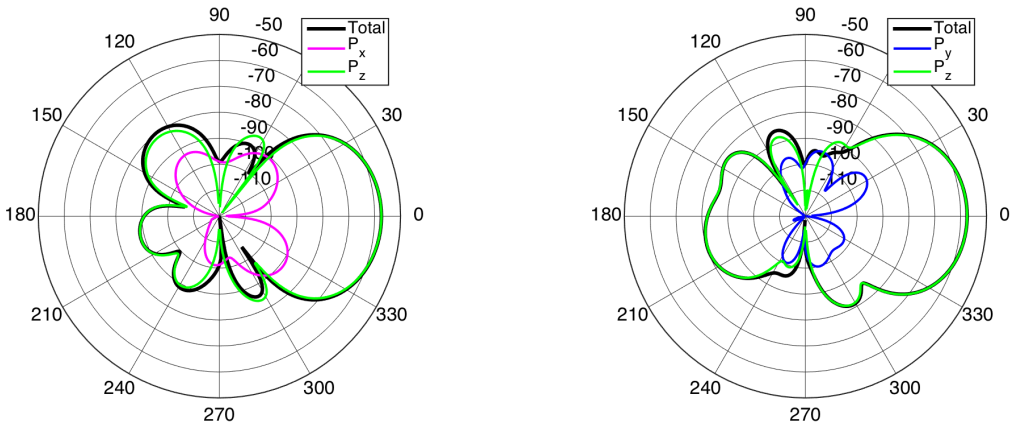

(a) x-z plane (b) y-z plane

Figure 3.26: Polar plot showing the differential cross section of the dendritic aggregate of $x = 10$ in the: (a) x-z plane. The incident wave is propagating in the x-direction and is polarised along the z-axis. The detector is polarised in the x-z plane. (b) y-z plane. The incident wave is propagating in the y-direction and is polarised along the z-axis. The detector is polarised in the y-z plane. The value at 0° represents forward scattering.

the detector to be polarised in the x-y plane.

We also note that as well as the results shown here, calculations were done for a z polarised incident wave travelling in the x and y directions, with the detector chosen to be polarised in the x-z and y-z directions, respectively. The corresponding results for $x = 10$ are shown Fig. 3.26. The same conclusion applies to these cases - the component parallel to the propagation direction is small and contributes to sidescatter, while the transverse component is responsible for the majority of the scattering in the forward and backward directions. Orientational averaging was not done for this case.

It is interesting to explore whether the diminishing contribution from the component parallel to propagation is a result of the inability of such low density structures to support a standing wave like that observed in the plot of $\Re(E_y)$ for the hexagonal plate in Fig. 3.9b. To test this, we plotted the parallel component of the field for some of the aggregate setups considered, i.e. for different incident directions and polarisations (not shown for brevity). It is found that there is no clear standing wave structure throughout the aggregate in any of the cases, suggesting that the standing wave may indeed play a key role in sidescatter. However, further work would be required to confirm whether the decreased influence of the field component parallel to the propagation direction

on the total amount of scattering within a complex aggregate is in fact caused by the inability to maintain a standing wave on the perimeter.

3.4.5 Sphere of equal D_{max} to aggregate, but with effective permittivity determined by volume fraction

In a similar manner to section 3.4.3, the Maxwell-Garnett formula is used to calculate the internal field of a sphere of equal D_{max} to the aggregate of fernlike dendrites. The plots of the field have been omitted in the interest of brevity. It is found that approximating the aggregate by a soft sphere results in a more uniform internal field. The symmetry of the particle leads to very slight focussing behaviour towards the forward region, but the magnitude of the field is close to 1 everywhere, meaning the average field value is larger than in the aggregate. The maximum magnitude value in the sphere is lower than in the aggregate, and the minimum value is higher.

In panels (c) and (d) of Fig. 3.25, the far field scattering by the complex aggregate is compared to the result calculated using the equivalent sphere, and also using RGA. For $x = 2$, the averaged differential cross section, σ, is accurately approximated by the equivalent sphere in the forward direction. However, the approximation overestimates sidescatter and underestimates backscatter for this size parameter. For $x = 10$, the DDA result is underestimated at almost all scattering angles by the equivalent sphere, particularly in the backscatter direction. Such underestimates in scattering properties as a result of soft sphere approximations are consistent with previous literature, e.g. [101, 102], with Ref. [102] showing that horizontally aligned soft spheroids provide better results for radar scattering by ice clouds. However, Tyynelä et al. [3] found that soft spheroids also underestimate the backscatter cross section of realistic aggregates.

The inaccuracies that result from soft sphere and spheroid approximations are due to a combination of 2 factors. As we just discussed, the first reason is that the internal fields are not represented correctly, with the Maxwell-Garnett approximation leading to a less structured field. The second reason is that the spatial structure of ice is incorrect

when approximating a realistic particle by a spherical or spheroidal equivalent. It has been suggested that for sparse structures such as the fluffy aggregates we are interested in, using RGA could result in more accurate scattering calculations than soft sphere or spheroid approximations, as in Ref. [61]. Since RGA doesn't include internal field interactions, these improvements to scattering by aggregates have been attributed to the fact that the spatial structure of the particle is modelled in RGA calculations. Fig. 3.25 (c) and (d) show σ for the aggregates of "fernlike dendrites" using RGA. It is clear that significant improvements are indeed seen for the irregular geometries used in this study by using RGA rather than soft sphere and spheroid approximations. Thus, a significant amount of the error caused by those approximations is due to the incorrect representation of the spatial structure of the particle. Internal coupling plays a smaller role, but nonetheless a notable one. Similar to the findings in Ref. [61], large errors between RGA and DDA are found in some directions. Underestimations of the backscatter cross sections become more prominent with size parameter, reaching -38% for $x = 10$, with errors increasing further towards sidescattering angles. Comparisons of the internal fields of these aggregates show that the average field strength is higher using DDA than it is using RGA. As the internal field is the same everywhere using RGA, the structure is also noticeably different. Hence it is worthwhile exploring whether improvements can be made to RGA in order to represent some internal structure and improve scattering calculations. Alternative methods are discussed in the following two chapters, starting with an iterative scattering order formulation of the DDA in the next chapter.

Chapter 4

Alternative scattering methods - Part 1: Iterative methods

Simplified methods such as the Rayleigh Gans Approximation may be applied to calculate the scattering properties of particles of small size parameter. RGA uses unphysical approximations and as such is limited in the range of sizes it can be used for. In the previous chapter, we showed that as x increases the method becomes less accurate, and large errors are found. As DDA is computationally expensive to use on scatterers of large x, particularly when calculations for many particles are required, we hope to develop a new approximation which is less expensive, but still sufficiently accurate. We begin by testing an iterative method that has been applied to arbitrary dielectric particles in previous literature. We test the applicability of the method to scattering by ice crystals, exploring both the internal electric fields and far-field scattering properties. We also perform tests using a newly derived parameter to improve convergence of the method. To our knowledge, none of these tests have been done before.

4.1 Overview of the iterative method

Recall from section 2.8.2 that in the DDA method we wish to solve a $3N \times 3N$ system of linear equations:

$$\sum_{j'=1}^{N} \mathbf{A}_{jj'} \mathbf{P}_{j'} = \mathbf{E}_j^{inc}, \tag{4.1}$$

where $\mathbf{A}_{jj'}$ describes the coupling between dipoles j' and j, $\mathbf{P}_j$ is the polarisation at dipole j, and $\mathbf{E}_{inc,j}$ is the electric field due to the incident wave.

This system may be solved using direct or iterative methods. The Jacobi method is a classical iterative procedure to solve a system of linear equations. More information on the iterative methods used here is available in numerical mathematics text books, such as section 4 of Quarteroni et al. [82]. Using the Jacobi method, the iterative approximation scheme corresponding to the DDA linear system may be defined as:

$$\mathbf{P}_j^{n+1} = \alpha_j (\mathbf{E}_{inc,j} - \sum_{j' \neq j} \mathbf{A}_{jj'} \mathbf{P}_{j'}^n), \quad \text{for } n = 1, 2, ..., \quad \mathbf{P}_j^1 = \alpha_j \mathbf{E}_{inc,j}, \tag{4.2}$$

where α_j is the polarisability, and $\alpha_j^{-1} \mathbf{1}_3 = \mathbf{A}_{jj}$. The iteration number is given by n.

Defining:

$$\mathbf{E}_j^{n+1} = \mathbf{E}_{inc,j} - \sum_{j' \neq j} \mathbf{A}_{jj'} \mathbf{P}_{j'}^n, \quad \text{for } n = 1, 2, ..., \tag{4.3}$$

the iterative method may also be written:

$$\mathbf{P}_j^{n+1} = \alpha_j \mathbf{E}_j^{n+1}, \quad \text{for } n = 1, 2, ..., \quad \mathbf{P}_j^1 = \alpha_j \mathbf{E}_{inc,j}. \tag{4.4}$$

The zeroth order solution of $\mathbf{P}_j^1 = \alpha_j \mathbf{E}_{inc,j}$ is an approximation saying that there is no coupling between the dipoles and each dipole behaves as a Rayleigh scatterer, responding to only the incident field. This is equivalent to the Rayleigh-Gans approximation of the internal field, also known as the Born approximation. A logical advancement of the RGA is to obtain higher order solutions by using $n \geq 1$ iterations. Thus, some authors have referred to the method as the iterative Rayleigh-Gans-Born approxima-

tion, e.g. de Hoop [103]. Singham and Bohren [84] relate the number of iterations to successive orders of scattering. With this physical interpretation, $n = 1$ corresponds to single-scattering between dipoles, i.e. the influence of scattering by each dipole on the remaining dipoles within a particle is considered once. For $n = 2$, double scattering is considered, and so on. Thus, this approach allows physical insight into the importance of multiple-scattering processes between volume elements. Note that this interpretation introduced in Ref. [84] refers to scattering orders *between dipoles*. If one were to consider the dipole response to the applied field as single-scattering, $n = 1$ may alternatively be interpreted as a double-scattering process, with $n = 2$ describing triple scattering etc. Either way, the expectation is that using higher orders will allow the RGA limits of size parameter and refractive index to be relaxed. Acquista [104] presented results using a second iteration and compared his findings to Mie scattering. The second iteration provided improvements to RGA, but results were only given for spheres of $x \leq 5$, and refractive indices of 1.55 and lower. The same approach has been taken by authors such as Chiapetta [105], and Singham and Bohren [83, 84], who applied Eq. 4.4 and referred to it as a scattering-order formulation of the DDA (SOF-DDA).

The authors of the above literature outline that SOF-DDA is beneficial in terms of time and memory requirements, when compared to a direct solve using DDA. A direct solve has a memory requirement which increases as $\mathcal{O}(N^2)$. As discussed in section 2.8.2, our row-wise implementation of DDA solved with GMRES has a smaller memory requirement of $\mathcal{O}(NM)$, where M is the number of GMRES iterations. It is possible to decrease the memory requirements by using restarted GMRES, but this may result in slow convergence, or even prevent convergence in some cases. The attraction of SOF-DDA is that it provides potential for further memory improvements. The memory required by SOF-DDA is independent of the number of iterations, increasing as $\mathcal{O}(N)$. This means that if M is large, SOF-DDA is more memory efficient than GMRES. Fig. 4.1 shows the number of iterations required by GMRES to obtain a solution for a hexagonal plate of solid ice. It is clear that GMRES requires more iterations with increased x, meaning there will be a corresponding increase in the memory requirement.

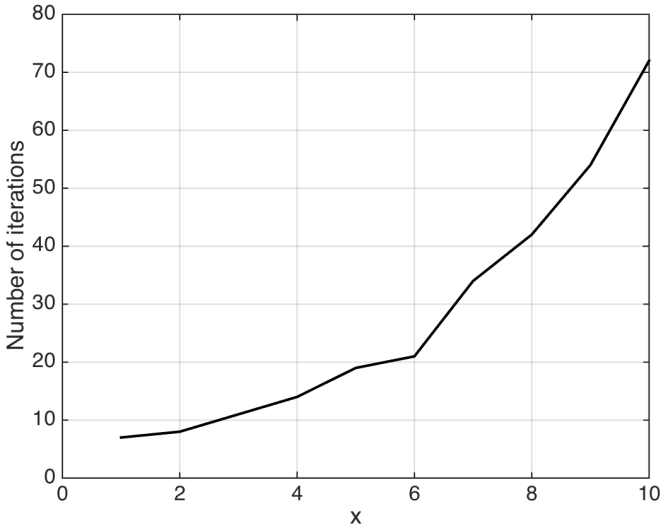

Figure 4.1: Number of iterations required to solve the DDA system using GMRES, for different size parameters, x. This example is for a hexagonal plate of solid ice.

Thus we hope that by using a scattering-order formulation, we can reduce memory requirements for larger x. The time taken to perform computations will increase as $\mathcal{O}(NM)$ for both SOF and GMRES. Since it is expected that the number of GMRES iterations required for convergence will be less than for SOF, a time improvement is not expected by using the iterative method.

However, it is well known that convergence is not guaranteed for series of this type. Ref. [84] outlines the reason for this issue. In the case of a particle with weak dipole-dipole interactions, the amplitude at a given dipole is close to that of the incident field, with much smaller contributions coming from interactions with the other dipoles. However, if the dipole-dipole interactions are strong, then summing the interactions at a dipole may result in field that is much larger than the incident field. The fields get larger and larger with each iteration, and the iterative method results in a divergent solution. Kleinman et al. [2] also point out that convergence of SOF-DDA is only guaranteed for weak scatterers, i.e. scatterers with a refractive index close to the surrounding medium, such that the phase shift does not vary considerably within the particle. Issues arise for large particle sizes and refractive indices. The authors of Refs. [83,84] compare the intensity of a sphere of $x = 2.23$ and show that there is a huge range in the number of scattering orders required for convergence using different refractive indices. Using a small refractive index of $m = 1.1 + 10^{-4}i$ allowed convergence within 8 orders, while

50 orders were required for the largest explored value of $m = 1.5 + 10^{-4}i$. For that refractive index, size parameters of 2.5 gave divergent results. Particle shape also plays a role in the convergence of the method. The authors of [83,84] look at different particle shapes, concluding that the method is more convergent for disk-like and filamentary particles, and less attractive for spheres and cubes.

Purcell and Pennypacker [77] use a similar equation to (4.4), but introduce a "numerical factor" $\eta > 0$ with the purpose of improving the convergence of the method. This is a Jacobi "over-relaxation" (JOR) scheme, and can be written as:

$$\mathbf{P}_j^{n+1} = \eta\alpha\mathbf{E}_j^{n+1} + (1-\eta)\mathbf{P}_j^n \quad \text{for } n = 0, 1, 2, ..., \quad \mathbf{P}^0 = 0. \tag{4.5}$$

Setting $\eta = 1$ gives the iterative method in Eq. (4.4), which is the standard Jacobi method and is equivalent to SOF-DDA. The physical interpretation of scattering orders is no longer valid when the value of η is changed. The optimal value to use for the relaxation parameter is not trivial to determine. Refs. [77] and [106] used a value of $\eta = 0.5$, but found poor convergence for spherical particles of $x > 1.5$ when using a refractive index of $m = 1.33$.

Eq. (4.5) is a stationary iterative method. Recalling that the diagonal part of matrix $\mathbf{A}$ is equivalent to $\alpha^{-1}\mathbf{1}_3$, we may replace $\sum_{k\neq j}\mathbf{A}_{jk}\mathbf{P}_k^n$ by $(\mathbf{A} - \alpha^{-1}\mathbf{1}_3)\mathbf{P}^n$, and Eq. (4.5) may be written:

$$\begin{aligned}\mathbf{P}^{n+1} &= \eta\alpha\mathbf{E}_{inc} - \eta\alpha(\mathbf{A} - \alpha^{-1}\mathbf{1}_3)\mathbf{P}^n + (1-\eta)\mathbf{P}^n \\ &= \eta\alpha\mathbf{E}_{inc} + (\mathbf{1}_3 - \eta\alpha\mathbf{A})\mathbf{P}^n.\end{aligned} \tag{4.6}$$

Convergence of an iterative method with the general form $\mathbf{x}^{n+1} = \mathbf{M}\mathbf{x}^n + \mathbf{y}$ depends on the iteration matrix $\mathbf{M}$. We may introduce the spectral radius of the iteration matrix, i.e. $\rho(\mathbf{M})$, defined as the maximum absolute eigenvalue of $\mathbf{M}$. Convergence of stationary iterative methods requires that $\rho(\mathbf{M})$ is less than 1, while if $\rho(\mathbf{M}) > 1$ the method will diverge:

$$\rho(\mathbf{M}) = \max|\lambda(\mathbf{M})| < 1. \tag{4.7}$$

In our case $\mathbf{M} = \mathbf{1}_3 - \eta\alpha\mathbf{A}$, and thus we require that $\rho(\mathbf{1}_3 - \eta\alpha\mathbf{A}) < 1$ in order to attain convergence of the stationary iterative method.

Computing the eigenvalues of a large matrix is very computationally expensive. However, calculating only the maximum eigenvalue may be done more efficiently using a numerical algorithm called the power method (e.g. section 5.3 of Ref. [82]). The method works by initialising an arbitrary vector $\mathbf{v}^{(1)}$, and performing the following steps for iterations $j = 1, 2, \ldots, n$:

for $j = 1 : n$

$\mathbf{v}^{(j+1)} = \mathbf{M}\mathbf{v}^{(j)}$

$\mathbf{v}^{(j)} = \mathbf{v}^{(j+1)} / \|(\mathbf{v}^{(j+1)})\|$

end

The value $(\mathbf{v}^{(j)})^* \mathbf{v}^{(j+1)}$ converges to the largest eigenvalue of $\mathbf{M}$, where the subscript * represents the conjugate transpose. Thus the spectral radius is calculated as $\rho(\mathbf{M}) = |(\mathbf{v}^{(j)})^* \mathbf{v}^{(j+1)}|$.

If the power method algorithm converges to the spectral radius within a small number of iterations, it may prove useful for determining whether convergence of the stationary iterative method will be achieved, rather than running for many iterations. However, the convergence rate of the power method depends on the ratio $|\lambda_2/\lambda_1|$ between the two largest eigenvalues λ_1 and λ_2, and the method may converge slowly if the two values are similar. In such a case, the required resources will increase while no useful information is gained. Note that a comparison of the computed norms will show that if $\|\mathbf{M}\mathbf{v}\| > \|\mathbf{v}\|$ at a given iteration of the power method, then the spectral radius is greater than 1, and the stationary iterative method will not converge.

We are interested in non-spherical particles such as hexagonal plates and irregular aggregates. We also wish to use larger refractive indices close to that of solid ice (e.g. $m = 1.7805 + 0.0021i$ for $x = 10$). From the results in the previous chapter, we know that as the size parameter of hexagonal plates increases, strong interactions occur between the dipoles. The dipoles tend to interact more weakly for aggregates. Thus we suspect that the iterative method may struggle to converge for compact scatterers

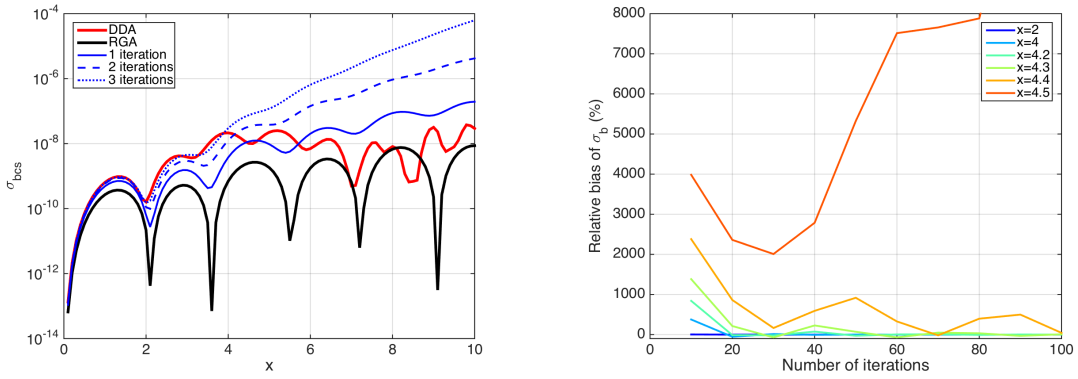

(a) σ_b (b) Bias in σ_b

Figure 4.2: (a) The backscatter cross section of a hexagonal plate of $n_z = 8$ and aspect ratio 0.1, using $\eta = 1$ (standard Jacobi/ SOF-DDA). The blue lines show results using SOF-DDA with 1, 2, and 3 iterations. Results using DDA and RGA are shown in red and black. (b) The bias in σ_b relative to the DDA solution for different values of x, as defined in Eq. (4.8).

such as plates, but converge more easily for aggregates. In this chapter we examine the performance of SOF-DDA for plates and aggregates, and explore whether any improvements to convergence are possible by using different values of η in Eq. (4.5). If convergence can be achieved, then it would be possible to avail of the memory improvements offered by using SOF rather than GMRES.

4.2 Results for hexagonal plates using SOF-DDA ($\eta = 1$)

4.2.1 Far-field scattering

Results for a hexagonal plate of aspect ratio 0.1 are shown in Fig. 4.2. The hexagonal plate used here has a value of $n_z = 8$, corresponding to 14 dipoles per wavelength at $x = 10$, thus satisfying the commonly used criterion of using at least 10 dipoles per internal wavelength (e.g. Yurkin and Hoekstra [47]). Fig. 4.2a shows the backscatter cross section, σ_b, for size parameters between 1 and 10, calculated using 1, 2, and 3 iterations of SOF-DDA. Results using DDA and RGA are also included on the plot, shown by the red and black lines respectively. It is clear that for small x, increasing the

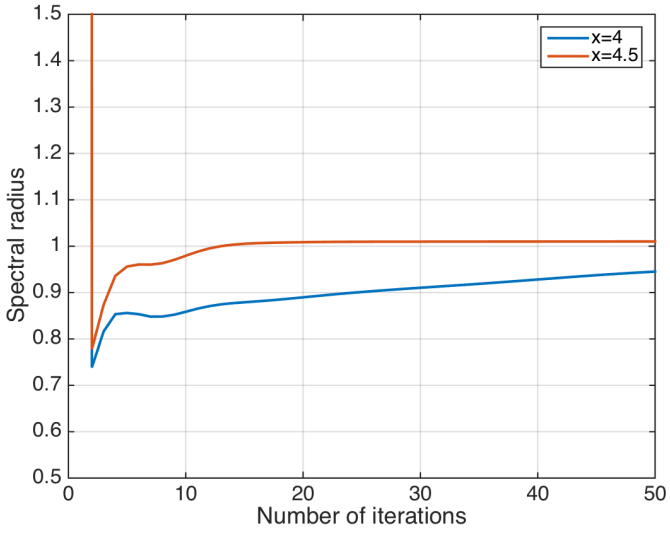

Figure 4.3: Spectral radius for different numbers of iterations of the power method algorithm, for the hexagonal plate of $x = 4$ (blue) and $x = 4.5$ (orange).

number of iterations provides improvements to the RGA solution, with results moving towards the DDA value. However, for $x \gtrapprox 4$ the results diverge, and large errors are found by using SOF-DDA.

The bias in σ_b compared to the DDA result is presented in Fig. 4.2b for different values of x. The bias is calculated as:

$$\frac{\sigma_{b,SOF} - \sigma_{b,DDA}}{\sigma_{b,DDA}} \times 100. \tag{4.8}$$

For values of x up to 4.3, the iterative result converges to the DDA solution with increased iterations, with more iterations required for convergence as x increases. For $x = 4.4$ the results have not converged within 100 iterations, but the solution does appear to be converging slowly. It is likely that convergence would be reached with more iterations. As x is increased further to 4.5, the solutions diverge rapidly. Fig. 4.3 shows that the spectral radius is consistent with these findings. For $x = 4$, ρ converges to a value below 1, but for $x = 4.5$, the spectral radius is greater than 1, and therefore the method is not convergent in this case. The lack of convergence for large size parameters is consistent with previous literature, as discussed in section 4.1. The results support the idea that the iterative method struggles to provide a convergent solution for particles comprising dipoles that interact strongly with each other. We

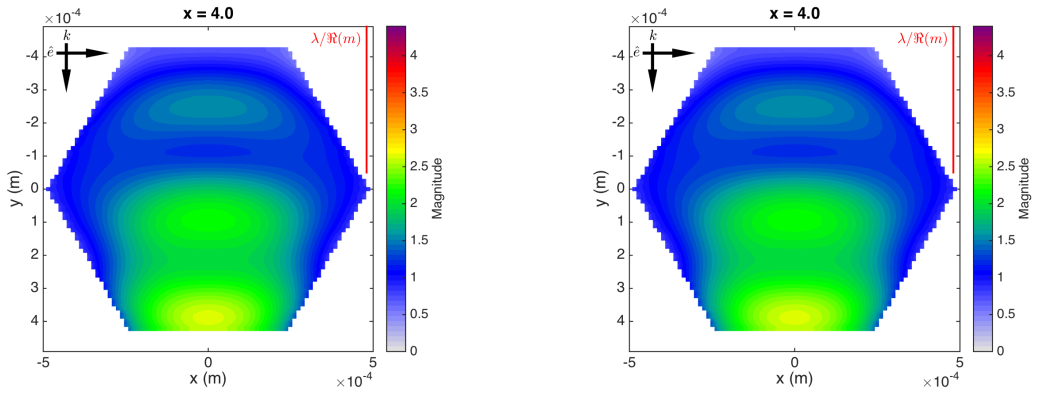

(a) DDA (b) SOF-DDA

(c) DDA (d) SOF-DDA

Figure 4.4: Magnitude of the internal field through the central plane of a hexagonal plate of $n_z = 8$ and aspect ratio 0.1. The top row shows results for $x = 4$, and the bottom row represents a slightly larger size parameter of $x = 4.5$. The fields shown in the left panels are calculated using DDA, and the right panels use SOF-DDA, i.e. $\eta = 1$, with 100 iterations.

explore this further by taking a closer look at the internal fields for different x.

4.2.2 Internal field

To understand why the method struggles to provide convergent far-field scattering solutions as the size parameter increases, we look at the internal fields. Fig. 4.4 shows the fields using DDA and SOF-DDA for two different size parameters of 4 and 4.5. For plates of $x = 4$ where convergent scattering solutions are obtained, there is no discernible difference between the internal field using DDA and SOF-DDA. The relative percentage error, calculated as in Eq. (3.1), has a value of less than 0.1%. Although not shown here, the errors are also very low for smaller values of x. Note that the relative internal field errors for the different cases shown are summarised in Table. 4.1 at the end

of the chapter. For $x = 4.5$ a much larger relative error of 167% is calculated, and the maximum field magnitude is overestimated in this case. The largest value in Fig. 4.4d is approximately 5.5, but the colorbar axis has been fixed such that it is consistent with the previous chapter. The overestimation of the maximum value computed with SOF-DDA is more extreme as size parameter is increased. This supports the explanation provided in Ref. [84] as to why the size parameter and refractive index for which SOF-DDA converges is limited. When interactions between dipoles are strong, the field at a given dipole resulting from summing the interactions may be larger than the incident field, continuing to increase with each iteration. It can be seen in Fig. 4.4d that along with overestimating the maximum field, the iterative method misrepresents the overall field structure. This combination of errors leads to divergent results for the far-field scattering quantities.

Increasing the resolution from $n_z = 8$ to $n_z = 12$ for the particle in Fig. 4.4 does not improve the representation of the field. This agrees with the results of Haspel and Tzabari [107], who found that increasing dipole resolution did not alleviate divergence when using SOF-DDA. Thus, although this method is useful because of the physical explanation of multiple scattering orders, it may not be practical for solid ice monomers at large size parameters due to convergence issues. Nonetheless, it may still have value at small x, because unlike RGA it can capture dipole coupling and hence polarisation effects, and therefore may be useful for polarimetric radar problems.

4.3 Results for aggregates using SOF-DDA ($\eta = 1$)

Results presented in chapter 3 showed that aggregates tend to have more weakly interacting dipoles and lower internal field magnitudes than single monomers, exhibiting structures that are less defined. To explore whether such fields are easier to simulate using the iterative method, we look at a variety of different aggregates. The particles used in this study were generated using the aggregation model of Westbrook et al. [108]. The monomer size distribution was chosen to be almost monodisperse, with only very slight variations such that differences in fall speeds allowed the aggregation

Figure 4.5: Examples of the generated particles of 3, 5, and 7 monomers. The top row shows aggregates of plates, the middle row shows columns, and the bottom row shows dendrites.

process to initiate. Aggregates were generated using three different monomer habits, as shown in Fig. 4.5. The habits used include plates of aspect ratio 0.15, columns of aspect ratio 3, and dendritic monomers of aspect ratio 0.25. The aspect ratios were chosen randomly, such that realistic particles were generated. For each of the monomer habits, we generated aggregates comprising 3, 5, and 7 monomers, storing 10 particles of each number. Each of the 10 aggregates have the same size and shape of monomers, but with different arrangements. This means that for the study we have 30 particles for each habit, and 90 particles in total. To our knowledge, the following results are the first to apply SOF-DDA to aggregates.

4.3.1 Far-field scattering

The SOF-DDA method is used to calculate the scattering properties of all 90 generated aggregates at size parameters of 2 and 10. At a small size parameter of $x = 2$, the iterative method provides a convergent solution for all particles considered. The details of those results are not shown here. Fig. 4.6 shows the bias in σ_b for all particles at $x = 10$. The top row shows results for plates, the middle row shows columns, and the bottom row shows dendrites. The three panels in each row represent aggregates of 3, 5, and 7 equal-sized monomers. It is clear that only the dendritic particles

converge for $x = 10$, with the rate of convergence increasing with the number of monomers. On top of that, the maximum positive bias tends to decrease with monomer number. In other words, an increased number of monomers means the SOF-DDA method is less likely to overestimate backscatter. This is most likely because the dipoles interact more weakly with increased monomers, resulting in a field with a lower magnitude, as seen in the results of the previous chapter. These lower magnitude fields are easier to reproduce using SOF-DDA, while the method overestimates larger fields, leading to overestimations of far-field scattering quantities. The method generally does not perform well for aggregates of plates and columns, with none of the 3 or 5-monomer particles showing convergence. For these particles, convergence also improves as the number of monomers is increased, and for 7 monomers some of the particles do converge. For a few of the aggregates of 7 plates, it is unclear whether they are oscillating around the correct answer and converging slowly to the solution, or if they are just not converging at all. Calculations of the spectral radius for those particles confirm that 5 of the 10 particles have divergent solutions.

We suspect that the SOF-DDA method overestimates the internal field for aggregates with more compact monomers such as plates and columns. We saw in the previous chapter that less compact dendritic monomers have lower magnitudes than plates, and the results here imply that the iterative method is capable of representing such fields. This is explored further in the following sub-section.

4.3.2 Internal field

The internal fields of three different aggregates are shown in Fig. 4.7. The incident wave is in the z-direction, travelling from below the particles, and is polarised in the x-direction. The top row shows the results using DDA, and the bottom row uses SOF-DDA. The particles shown include an aggregate of 7 dendrites, and two different aggregates of plates. These particles were chosen to represent the range of different convergence properties of the far-field solution. As with all the dendritic aggregates, the first particle has a convergent far-field scattering solution. The first aggregate of

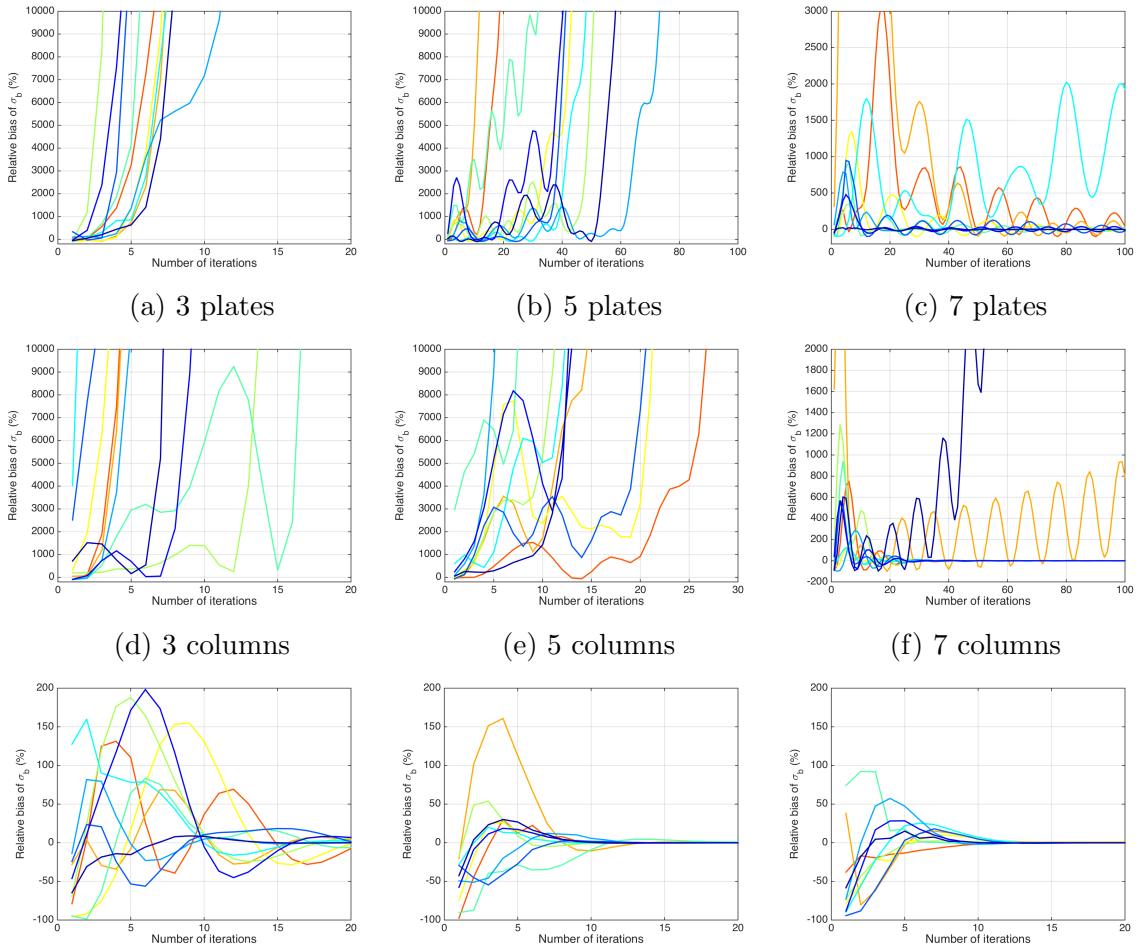

(a) 3 plates (b) 5 plates (c) 7 plates

(d) 3 columns (e) 5 columns (f) 7 columns

(g) 3 dendrites (h) 5 dendrites (i) 7 dendrites

Figure 4.6: Bias in σ_b in for the generated aggregates using SOF-DDA. The top row shows results for aggregates of plates, the middle row shows results for columns, and the bottom row is for the dendritic particles. Each of the colours represents a different particle, and calculations for 10 particles are shown in each panel.

plates shown (Figs. 4.7b and 4.7e) is a particle for which σ_b calculated using SOF-DDA converges very slowly. The second aggregate of plates (Figs. 4.7c and 4.7f) has a divergent far-field solution. These two aggregates of plates correspond to the darkest blue line and the cyan line in Fig. 4.6c, and are labelled "7 plates A" and "7 plates B" in Table. 4.1.

The SOF field shown for the dendritic particle is the result after 20 iterations, by which time σ_b has converged to the DDA solution. The results for the two aggregates of plates are plotted after 100 iterations. Comparisons of the DDA fields show that the maximum magnitude is lowest in the dendritic particle, with a value of 1.78. The field is higher within both of the aggregates of plates examined. As expected, the largest magnitude is found within the particle that has a divergent backscatter solution using SOF-DDA. The slowly convergent particle and the divergent particle have maximum magnitudes exceeding the dendritic aggregate by 18% and 50%, respectively. Visual inspection of the fields suggests that the large magnitude is due to the fact that the two monomers towards the left side of Fig. 4.7c are in close alignment with the incident wave. Recall from chapter 3 that such an alignment of plates leads to areas of enhanced coupling with large field values at the forward side of the particle.

Overall, the relative errors in the internal field for the three respective particles are 0.05%, 13.63%, and 131.98%. SOF-DDA accurately reproduces the maximum field magnitude of the dendritic particle, and the maximum magnitude of the first aggregate of plates is overestimated by only a small amount of 2%. However, Fig. 4.7f shows that SOF-DDA cannot reproduce the field within the particle with a divergent far-field solution, and the maximum magnitude of the second aggregate of plates is overestimated by a much larger 55%. This further supports the idea that SOF-DDA struggles when internal interactions become significant. In those cases, the field is overestimated by the iterative method, resulting in divergent far-field scattering solutions.

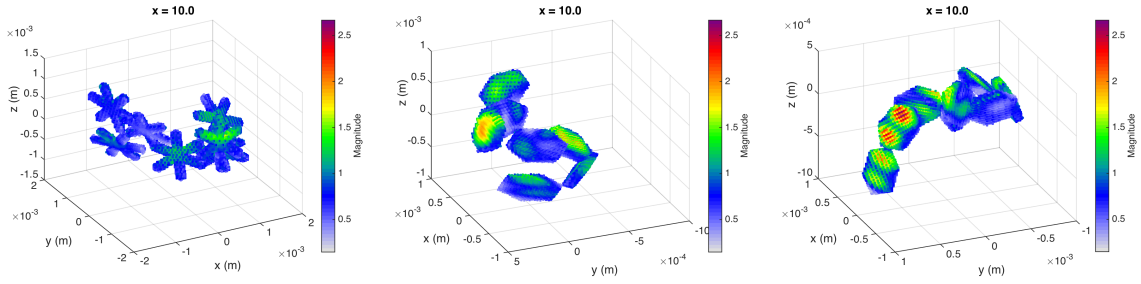

(a) Max($|\mathbf{E}|$) = 1.78 (b) Max($|\mathbf{E}|$) = 2.10 (c) Max($|\mathbf{E}|$) = 2.67

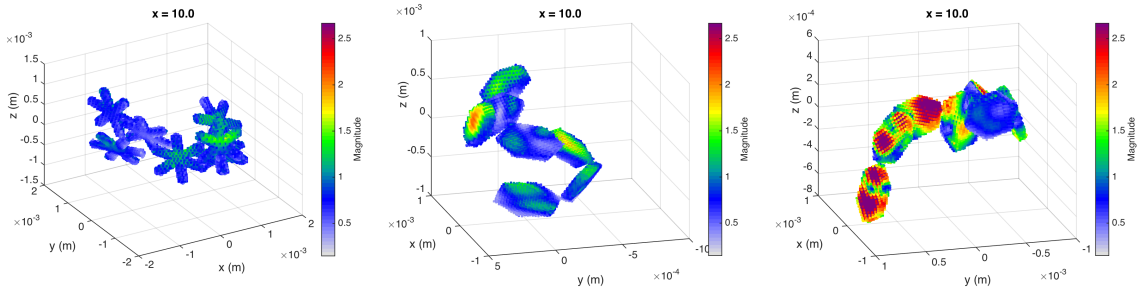

(d) Max($|\mathbf{E}|$) = 1.78 (e) Max($|\mathbf{E}|$) = 2.15 (f) Max($|\mathbf{E}|$) = 4.14

Figure 4.7: Fields of three different aggregates of 7 monomers, calculated using DDA (top row) and SOF-DDA (bottom row). In the order shown, the three aggregates represent particles with convergent, slowly convergent, and divergent backscatter cross section results using SOF-DDA. The corresponding relative errors in the internal field calculated using SOF-DDA are 0.05%, 13.63%, and 131.98%. The range of values in the colorbar are fixed to represent the DDA magnitudes, but note that case (f) exceeds those values.

4.4 Impacts on convergence of changing η

It is interesting to examine the effect of changing the relaxation parameter η introduced in Eq. (4.5) on the scattering properties of non-spherical particles. Fig. 4.2 shows results for the backscatter cross section of a hexagonal plate using SOF-DDA (i.e. $\eta = 1$), along with comparisons using DDA to see if increasing the number of iterations provides a solution that converges to the desired result. It is clear that using $\eta = 1$ provides good results for small x, but the results diverge for $x \geq 4$. This means that although the method may provide good results for particles in the radar regime, improvements to convergence are required in order to use it with higher frequency instruments such as ISMAR and ICI. We outlined that different values of η may be used in Eq. (4.5) to improve convergence, and this is explored further in the following sub-sections.

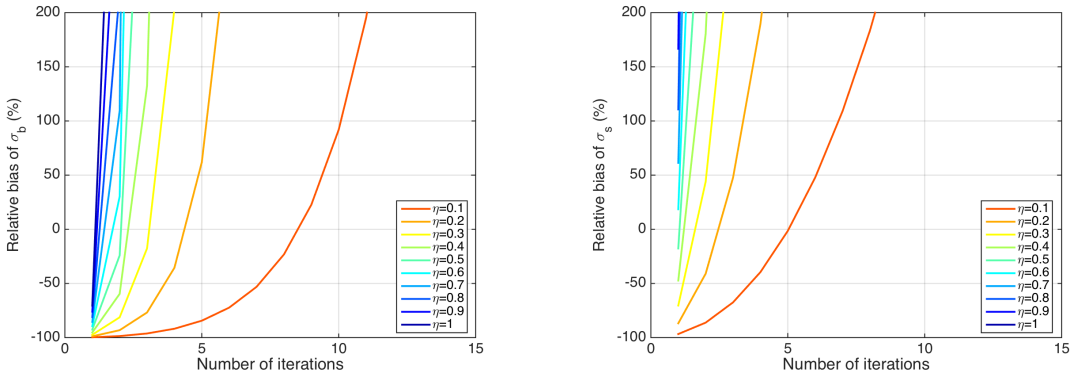

(a) σ_b (b) σ_s

Figure 4.8: Bias for the hexagonal plate with $x = 10$, using different values of η between 0.1 and 1.

4.4.1 Results for plates using $0.1 \leq \eta \leq 1$

To begin with, we compare results using different values of the relaxation parameter with values of $0.1 \leq \eta \leq 1$.

4.4.1.1 Far-field scattering

We calculate the bias in σ_b and σ_s using the JOR iterative method in Eq. (4.5) compared to the DDA solution. Fig. 4.8 shows the results for the hexagonal plate of $x = 10$, using different values of η between 0.1 and 1. It is clear that decreasing η improves the bias in both cases, but convergence is not achieved with any of the chosen values. It appears that if convergence is to be achieved at this size parameter, a value less than 0.1 would be required. It is possible that the values of η used here may result in convergent solutions for smaller values of x, but we have not explored this. Since the method fails for all values of η considered here, we do not explore the internal fields, and instead turn our attention to aggregates in the following section.

4.4.2 Results for aggregates using $0.1 \leq \eta \leq 1$

4.4.2.1 Far-field scattering

The far-field scattering properties of the three aggregates in Fig. 4.7 are explored, using values of η between 0.1 and 1. Fig. 4.9 shows results for the aggregate of 7 dendrites, and Figs. 4.10 and 4.11 show the results for the two aggregates of plates. In each case, the bias in σ_b is shown in the left panel, and the bias in σ_s is shown in the right panel.

Although the dendritic aggregate is convergent with SOF-DDA, it is interesting to examine the effect of using a relaxation parameter. It is clear from Fig. 4.9 that decreasing η results in a solution that converges more slowly towards the DDA solution, for both σ_b and σ_s. This is expected from the definition of the method, as the change in $\mathbf{P}$ at every step is proportional to η.

For both of the aggregates of plates, the magnitude of the backscatter bias is much larger than the total scattering bias. Backscatter is very sensitive to interference effects depending on the relative phases of waves scattered from different dipoles within the particle in a single direction. Although interference is also important for total scattering, the exact details in a given direction don't appear to be as critical.

The bias in both σ_b and σ_s generally decreases as η is reduced, along with the peak error decreasing. However, the solution is very sensitive to the choice of η. As with the dendritic aggregate, using the smallest values of $\eta = 0.1$ or 0.2 results in slower convergence than larger values of η. After 100 iterations the errors are still very large for most of the cases. The majority of the values of η result in a solution that oscillates around the DDA solution, and in fact none of them have provided a solution that has truly converged within 100 iterations. Nonetheless, using $\eta < 1$ does generally prevent the far-field solution from diverging when the number of iterations is increased.

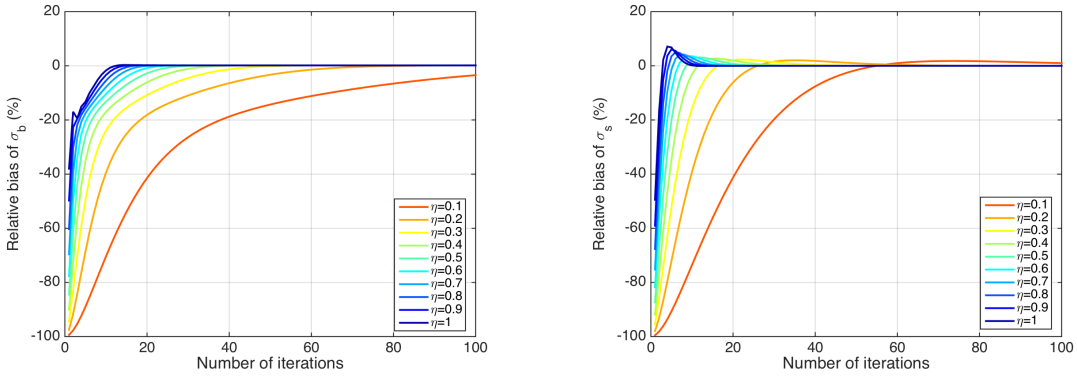

(a) σ_b (b) σ_s

Figure 4.9: Bias in σ_b and σ_s for one of the aggregates of 7 dendrites, using different values of η between 0.1 and 1.

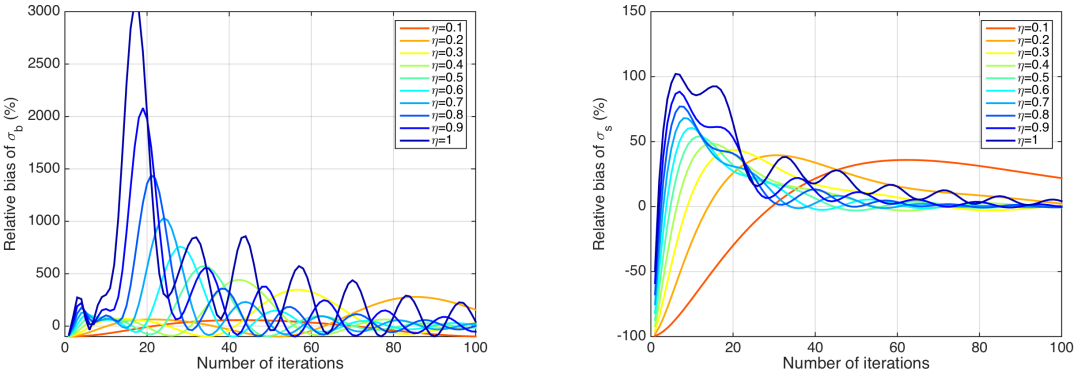

(a) σ_b (b) σ_s

Figure 4.10: Bias in σ_b and σ_s for one of the aggregates of 7 plates with $x = 10$ (i.e. dark blue line in Fig. 4.6c), using different values of η between 0.1 and 1.

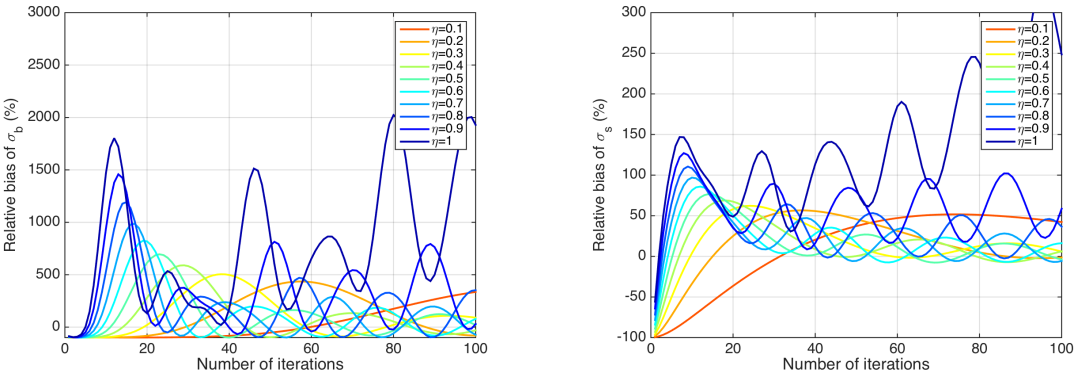

(a) σ_b (b) σ_s

Figure 4.11: Bias in σ_b and σ_s for one of the aggregates of 7 plates with $x = 10$ (i.e. cyan line in Fig. 4.6c), using different values of η between 0.1 and 1.

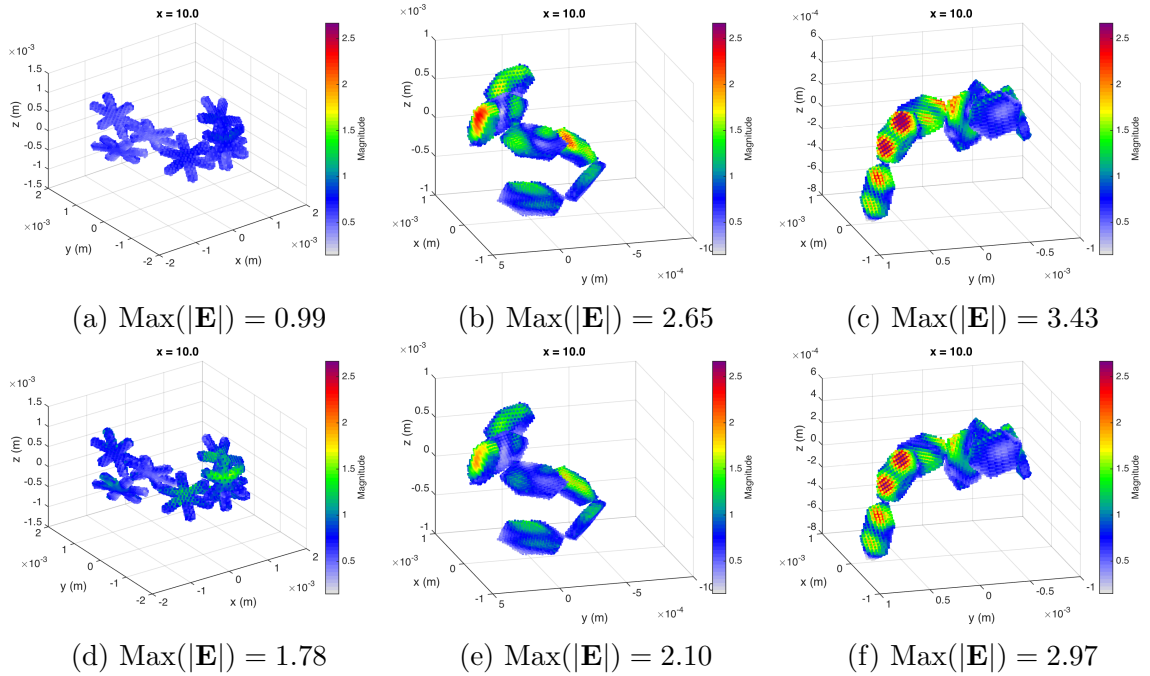

(a) Max($|\mathbf{E}|$) = 0.99 (b) Max($|\mathbf{E}|$) = 2.65 (c) Max($|\mathbf{E}|$) = 3.43

(d) Max($|\mathbf{E}|$) = 1.78 (e) Max($|\mathbf{E}|$) = 2.10 (f) Max($|\mathbf{E}|$) = 2.97

Figure 4.12: Fields of three different aggregates of 7 monomers, calculated using $\eta = 0.1$ (top row) and $\eta = 0.6$ (bottom row). The results are calculated using 20 iterations for the dendritic aggregate, and 100 iterations for the aggregates of plates.

4.4.2.2 Internal field

Fig. 4.12 shows the internal fields for the three aggregates using two different values of η. The top row shows results using $\eta = 0.1$ and the bottom row uses $\eta = 0.6$. The relative percentage errors for these cases are also provided in Table. 4.1.

The results presented for the dendritic particles were calculated using 20 iterations, since after 100 iterations the differences in the fields calculated using all values of η considered here are negligible. It is shown in Fig. 4.12a that the maximum field value calculated using DDA in Fig. 4.7a is underestimated after 20 iterations, when a value of $\eta = 0.1$ is used. Using a larger value of $\eta = 0.6$ reproduces the DDA field accurately (Fig. 4.12d). The relative errors corresponding to these two cases are 36.88% and 0.29%, respectively. The errors in the internal fields are correlated to the far-field biases in Fig. 4.9. The larger error and underestimated field magnitude using $\eta = 0.1$ results in a larger bias of -40% in the far-field calculations after 20 iterations, while the biases in σ_b and σ_s are very small for $\eta = 0.6$.

The internal fields of the aggregates of plates in Fig. 4.12 were calculated after 100

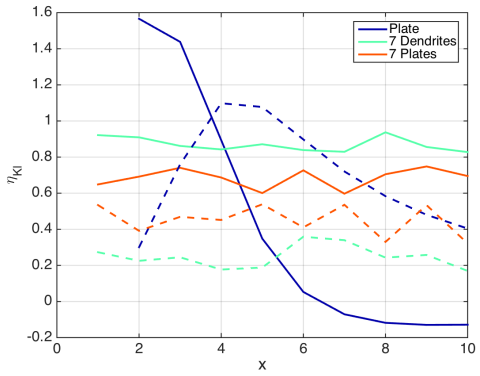

Figure 4.13: Examples of the real and imaginary parts of η_{Kl} computed at different size parameters, represented by the solid and dashed lines, respectively. Each colour represents a different particle, as indicated in the figure legend. Values are plotted for the single hexagonal plate, an aggregate of 7 dendrites, and an aggregate of 7 plates.

iterations. The relative error is over 30% for both aggregates when $\eta = 0.1$, and the maximum field is overestimated by slightly less than 30%. When $\eta = 0.6$, Fig. 4.12e shows that the field within the first aggregate of plates is accurately represented after 100 iterations, with an error less than 2%, and the same maximum value as the DDA result in Fig. 4.7b. The field within the second aggregate has an error of 17%, and the maximum value is still overestimated, but by a smaller amount of 11% (Fig. 4.12f). The faster rate of convergence for $\eta = 0.6$ gives an improved representation of the internal field for both aggregates of plates after a fixed number of 100 iterations. This results in more accurate far-field solutions, with smaller biases in both σ_b and σ_s in Figs. 4.10 and 4.11. Ideally we want to choose the optimum value of η to ensure convergence, but to approach the solution as quickly as possible. Thus in the following subsection we derive and test an expression to choose the optimal value of η.

4.4.3 Results for plates using the relaxation parameter of Kleinman et al. [2]

To explore the relaxation parameter η further, we look at other applications of the JOR method. Kleinman et al. [2] take a similar approach to solve a simpler Helmholtz scattering problem, i.e. the unknown is a scalar field rather than a vector field. They derive an expression for the relaxation parameter by choosing the value of η that

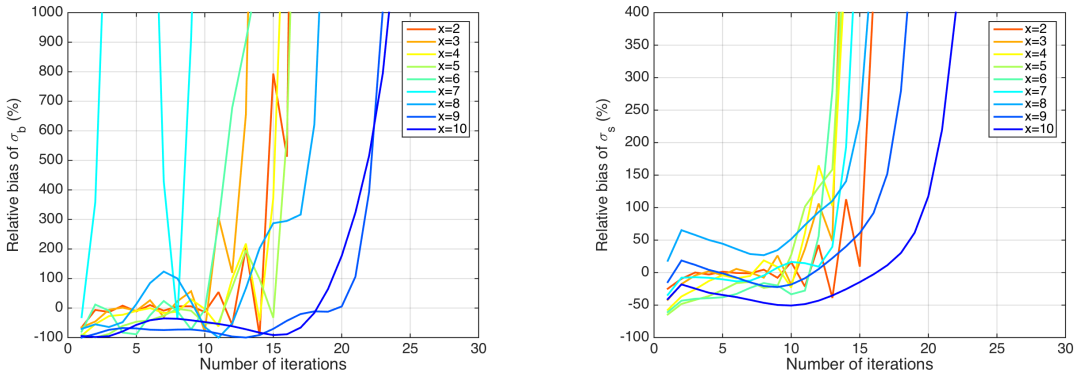

(a) σ_b (b) σ_s

Figure 4.14: Bias in σ_b and σ_s for the hexagonal plate, using η_{Kl}. The colours represent different size parameters, as labelled in the figure legend.

minimises the residual error after one iteration. We have determined the analogous specification for our Maxwell problem, in the hope that this technique can be applied to the type of problems we are interested in, improving the convergence of the iterative method. The derivation of the relaxation parameter in this case is given in appendix A, and the resulting expression which we will call η_{Kl} is:

$$\eta_{Kl} = \frac{(\mathbf{E}_{inc}, \mathbf{A}\mathbf{E}_{inc})}{\alpha \|\mathbf{A}\mathbf{E}_{inc}\|^2}. \tag{4.9}$$

4.4.3.1 Far-field scattering

Eq. (4.9) is used to calculate the relaxation parameter for the hexagonal plate. Up until now, we have only looked at real values of η, while the values of η_{Kl} used here are complex. The solid and dashed blue lines in Fig. 4.13 show the real and imaginary parts of η_{Kl} computed for the plate at different x. The real part is larger for small x, decreasing as x increases, while the imaginary part increases until $x = 4$, decreasing thereafter.

Fig. 4.14 shows the bias in σ_b and σ_s for the hexagonal plate, using $\eta = \eta_{Kl}$ in Eq. (4.5). It is immediately clear from the figure that convergence is not achieved as a result of this implementation. In fact, the method actually leads to divergence for small size parameters of $x \leq 4$ that showed convergence when SOF-DDA was used. As with previous results, the bias in σ_s is lower than σ_b, and exhibits behaviour that is less

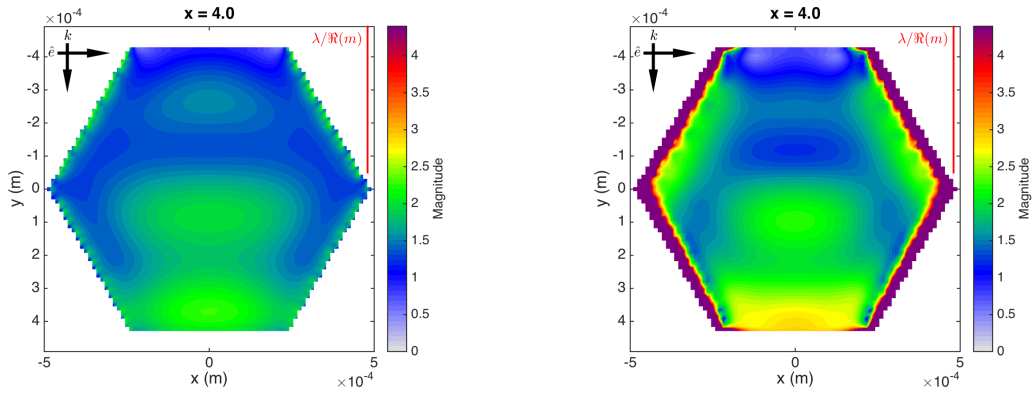

(a) 5 iterations (b) 10 iterations

Figure 4.15: Internal field of the hexagonal plate of $x = 4$, using η_{Kl}. The results are plotted after (a) 5 iterations; and (b) 10 iterations.

jumpy, particularly for $x = 7$. However, results at all size parameters still diverge after about 10 iterations. This result is not entirely unsurprising since the η_{Kl} convergence parameter is derived at the first iteration, meaning it may become less applicable as the number of iterations increases.

4.4.3.2 Internal field

Fig. 4.15 shows the internal field using the derived η_{Kl}, plotted for $x = 4$ after 5 and 10 iterations. After 5 iterations, the field looks like it may be converging towards the correct solution (plotted previously in Fig. 4.4a). However, after 10 iterations it is clear that the field magnitude is too high around the edges, resulting in a huge relative error of 450%. The range of the colorbar is limited for comparison with the other plots, but the maximum magnitude in Fig. 4.15b is approximately 40. It is unclear why the overestimations begin at the particle edge, but the maximum magnitude continues to rise with increased iterations, along with the overestimations moving throughout the particle rather than remaining on the edge. This is the case for all size parameters studied, i.e. $2 \leq x \leq 10$. The issue of the large field values around the particle edge is not improved by increasing the resolution from $n_z = 8$ to $n_z = 12$, i.e. increasing the number of dipoles per wavelength by 50%. Thus, this method of determining the optimal value of the relaxation parameter is not ideal for plates. We test the method on aggregates in the following section.

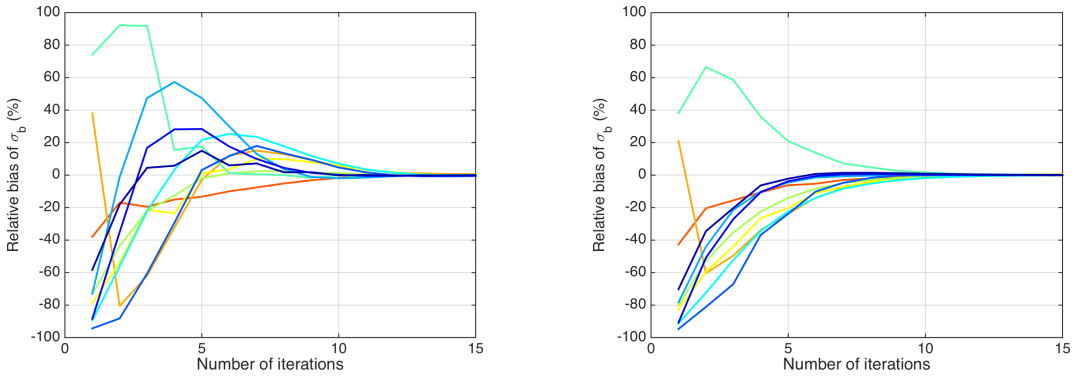

(a) $\eta = 1$ (b) η_{Kl}

Figure 4.16: Bias in σ_b for the 10 aggregates of 7 dendrites, using values of (a) $\eta = 1$ and (b) η_{Kl}. Each colour represents a different particle.

4.4.4 Results for aggregates using the relaxation parameter of Kleinman et al. [2]

4.4.4.1 Far-field scattering

Values of η_{Kl} for an aggregate of 7 dendrites and an aggregate of 7 plates are also shown in Fig. 4.13. Unlike for the single plate, η_{Kl} for the aggregates is approximately constant for different x. For the dendritic particle, $\Re(\eta_{Kl}) \approx 0.9$ and $\Im(\eta_{Kl}) \approx 0.2$. For the aggregate of plates, $\Re(\eta_{Kl}) \approx 0.7$ and $\Im(\eta_{Kl}) \approx 0.5$.

The bias in σ_b for aggregates of dendrites and plates calculated using η_{Kl} is plotted in Figs. 4.16 and 4.17, alongside the SOF-DDA results for comparison. Each panel includes results for the 10 different aggregates of each monomer type, at a size parameter of $x = 10$. Fig. 4.16 shows that for the aggregates of 7 dendrites, η_{Kl} results in decreased overestimations of σ_b. Use of the parameter also allows the rate of convergence to increase very slightly. However, such a small improvement is unlikely to be beneficial due to the added overhead of computing η_{Kl}.

It is interesting to see in Fig. 4.17 that using η_{Kl} results in improved convergence for the aggregates of plates. SOF-DDA results in very poor convergence for these particles, but using η_{Kl} allows solutions for almost all of the particles to converge within 20 iterations. However, it is clear that the solution for one of the particles is unstable, showing amplified approximation errors with increased iterations. In a

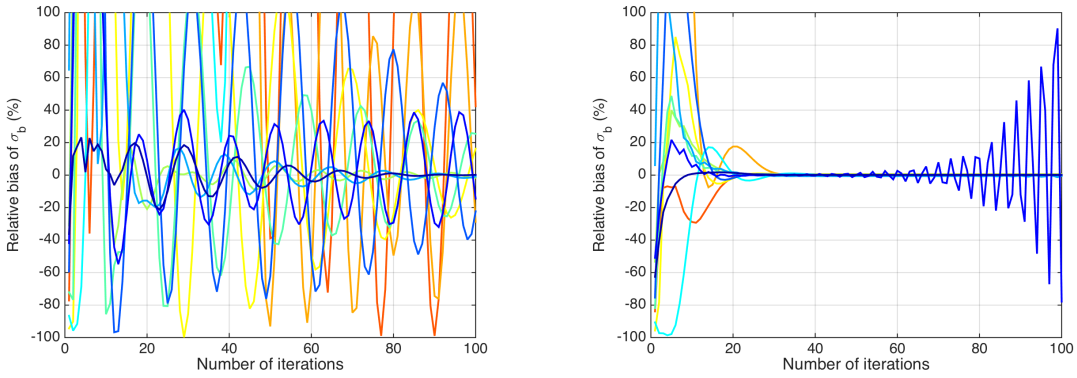

(a) $\eta = 1$ (b) η_{Kl}

Figure 4.17: Bias in σ_b for the 10 aggregates of 7 plates, using values of (a) $\eta = 1$ and (b) η_{Kl}. Each colour represents a different particle.

practical sense, the iterative method would generally continue until a given tolerance is reached. Thus, the approximation would have converged to the correct solution for the particles considered here. However, instability is not a desirable property, and it is unclear for this study whether instability may occur for other particles. Thus, although good results are obtained for the majority of the aggregates considered here, further experiments would be required to determine the full range of applicability.

4.4.4.2 Internal field

Fig. 4.18 shows the internal field of the aggregate of plates that has an unstable solution in Fig. 4.17b. The left panel represents the result after 20 iterations, when the far-field result appears to have converged. After 20 iterations, the internal field has a maximum magnitude of 2.4 and an average of 0.98.

The panel on the right side shows the internal field after 100 iterations, when the far-field result has become unstable. The relative error after 100 iterations compared to the DDA result is over 3000%. The field is greatly overestimated at some dipoles, and the colorbar shows that there are regions in Fig. 4.18b where the maximum magnitude reaches 153.7, and the average magnitude in that case is 21.4. This means the maximum and average values after 100 iterations exceed those after 20 iterations by over 6000% and 2000%.

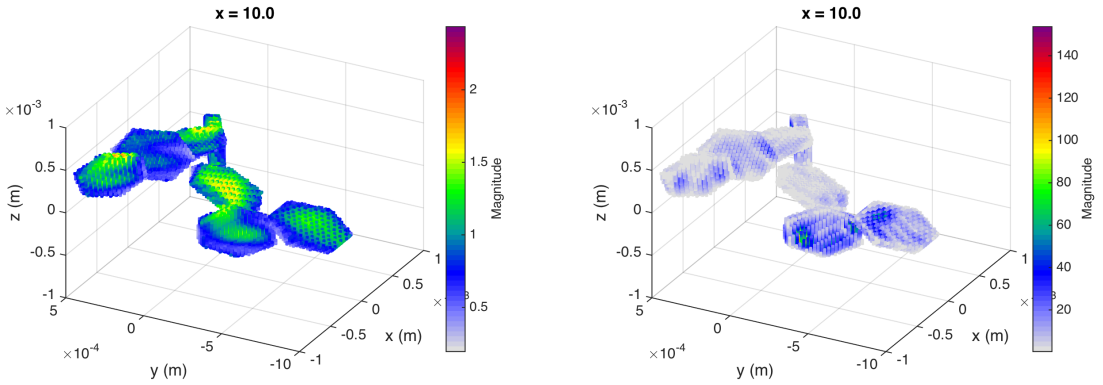

(a) 20 iterations (b) 100 iterations

Figure 4.18: Internal field of the aggregate of plates showing instability, plotted after (a) 20 iterations and (b) 100 iterations.

4.4.5 Summary of SOF and JOR methods

In this chapter we have attempted to improve convergence of SOF-DDA using a JOR iterative method. The idea behind this approach is that reductions to memory requirements may be possible, compared to solving DDA using the GMRES iterative method. Different values of the relaxation parameter, η, have been tested, but a method for determining the optimal value for convergence has not been achieved. An equation has been derived that shows promising results for some aggregates, but does not show good results for single hexagonal plates. Moreover, the results for the plate-like aggregates were shown to become unstable in one case. More tests are required to explore performance of the method with aggregates of different monomer shapes such as columns. Although memory savings are expected by using the JOR method, we have not presented any comparisons here since the desired convergence properties have not been attained. We leave that to future work, and instead turn our attention to an alternative scattering approximation in the next chapter.

Geometry	x	N	η	n	Relative error (%)	Figure
Plate	4	33504	1	100	0.07	4.4b
Plate	4.5	33504	1	100	167.45	4.4d
Plate	4	33504	η_{Kl}	10	450.87	4.15b
7 dendrites	10	11876	1	20	0.05	4.7d
7 dendrites	10	11876	0.1	20	36.88	4.12a
7 dendrites	10	11876	0.6	20	0.29	4.12d
7 plates A	10	19221	1	100	13.63	4.7e
7 plates A	10	19221	0.1	100	30.71	4.12b
7 plates A	10	19221	0.6	100	1.83	4.12e
7 plates B	10	19022	1	100	131.98	4.7f
7 plates B	10	19022	0.1	100	35.39	4.12c
7 plates B	10	19022	0.6	100	17.37	4.12f
7 plates (unstable)	10	19097	η_{Kl}	100	3124	4.18b

Table 4.1: Summary of the relative percentage errors in the internal field compared to DDA.

Chapter 5

Alternative scattering methods - Part 2: New IMA scattering method

In this chapter, we examine the applicability of a new method called the Independent Monomer Approximation (IMA). We investigate the accuracy and efficiency of the method by comparing calculations to benchmark DDA solutions. Comparisons with RGA solutions are also performed.

5.1 Overview of ideas and method

In previous chapters, results were presented using the DDA numerical method. In that method, the particle is divided into a cubical array of dipoles. The electric field at each dipole is calculated by summing the field due to the incident wave, and the field due to each of the remaining dipoles within the particle. In other words, interactions between all dipoles comprising the particle are considered. For large aggregates of multiple ice crystals, the DDA method is computationally expensive, because a large number of dipoles is needed to model the geometry and the variations in electric field across the particle. A direct solve of the standard DDA linear system has a computational cost

that grows quadratically with the number of dipoles, since coupling between all dipole pairs is represented. In fact, for a particle of N dipoles, the time taken to solve the system is between $\mathcal{O}(N^2)$ and $\mathcal{O}(N^3)$, and the memory requirement is proportional to N^2 [47]. However, as outlined in section 2.8.2, we implemented row-wise multiplication as an alternative to the full matrix assembly, meaning the required memory storage is reduced to $\mathcal{O}(N)$.

In chapter 6, we will utilise measurements from a case study to perform radiative transfer simulations. An important aspect of doing such simulations is to try and match the atmospheric state as closely as possible. In-situ measurements from cloud probes generally show that a wide variety of particle habits exist in clouds. Considering this large number of particles, computing the average scattering properties from an ensemble of aggregate geometries with DDA is problematic for current day computers, due to the time and memory requirements described above. As discussed in section 1.4, one way this has been addressed is by doing DDA calculations for different particles and storing them in publicly available databases. This is beneficial as it allows realistic geometries to be used, rather than assuming simpler shapes like spheres or spheroids. However, choices and assumptions still need to be made to do the calculations, for example particle size, shape, orientation, frequency, and temperature. The user is then limited to the calculations available, which may not be ideal for their case. Moreover, as discussed in chapter 2, different parameterisations exist to calculate refractive index. Refinements to these parameterisations may mean that the calculations in the scattering database would have to be regenerated. This task would be more feasible with efficient scattering methods, providing increased flexibility that would be useful as instruments and needs develop.

In section 3.4.4, DDA results for the internal electric fields within large aggregates were calculated. Individual monomers were then removed from the particle model and DDA calculations were performed on each of the isolated monomers. Examples of the resulting fields are shown in Fig. 5.1. The values of the field calculated in the two cases are within 5% of each other. The calculations reveal that the coupling between dipoles is almost entirely confined within individual monomer crystals, and inter-monomer

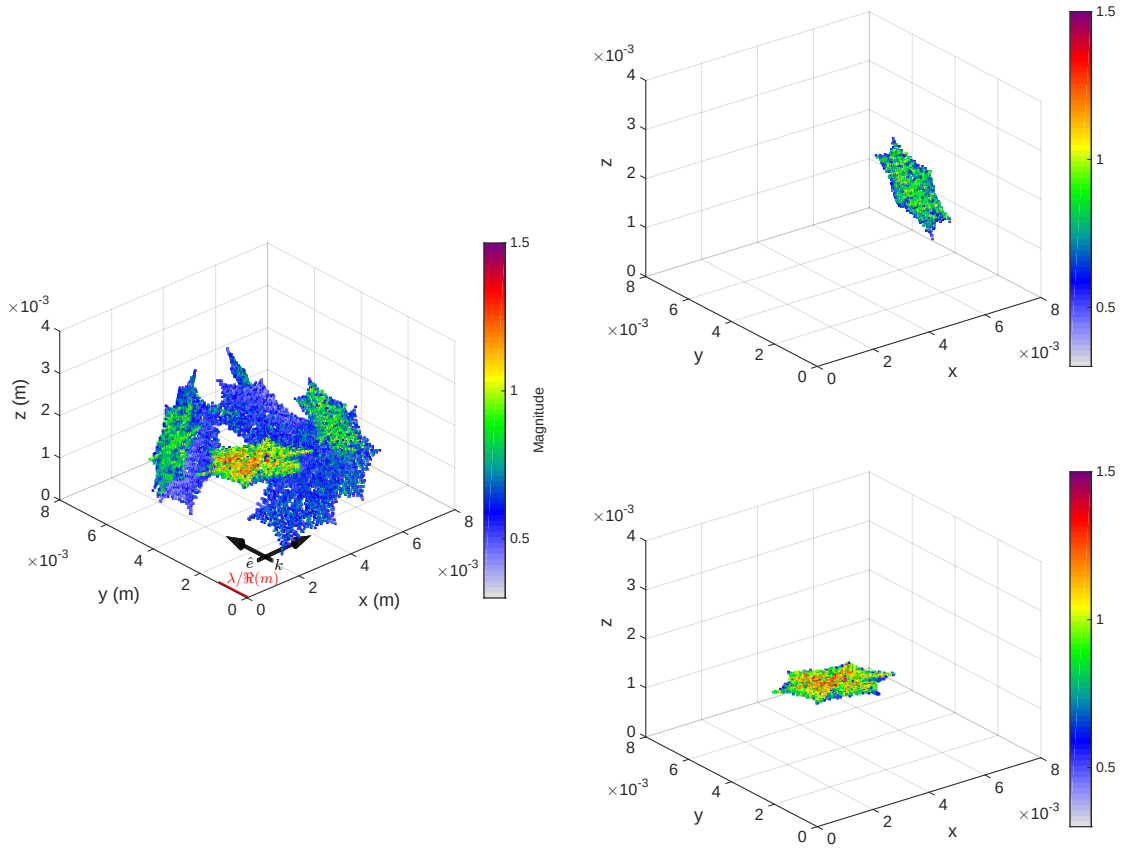

Figure 5.1: Examples of two monomers isolated from a complex aggregate. The left panel shows the field calculated using DDA for the full aggregate. Interactions between all dipoles within the aggregate are included. On the right, the field is calculated using DDA within individual monomers. This means any interactions that may result from other monomers are not included. The values of the resulting fields are within 5% of those calculated in the presence of the full aggregate.

coupling is weak. Thus we suggest a new approximate method in which we treat monomers independently.

Consider an aggregate of n monomers. The idea behind the IMA method for aggregates is that interactions are only considered within individual monomers, and inter-monomer interactions are ignored. The internal fields of the monomers are independent and do not influence each other. However, in the far field the scattering from the monomers may interfere constructively or destructively. Numerically, this involves considering each of the n monomers individually and independently, and performing DDA computations for each one. The dipole polarisations are saved, and the scattered fields from the dipoles in all n crystals are summed coherently, followed by computation of the net far field scattering. This approach enables significant improvements to the time and

memory requirements of scattering calculations for aggregates.

5.2 Time and memory requirements

Consider an aggregate comprising 10 identical monomers. Let's say the time taken to perform calculations using a given DDA implementation increases as $\mathcal{O}(N^2)$, where N is the total number of dipoles. Then calculations of an aggregate of 10 monomers would take 100 times longer than for one monomer on its own. However, if we take the IMA approach and do 10 calculations of one monomer each, this would only take 10 times longer than doing one monomer. This means that calculating the scattering for this particle using IMA would result in a potential saving of a factor of 10 in CPU time, compared to solving the whole particle using DDA. In other words, in the general case of an aggregate of n monomers, a time saving of a factor of n is possible. Thus, the saving increases with the number of monomers, and we expect the method to be particularly advantageous for aggregates of large n.

Improvements to the memory requirements are also expected. As outlined above, we implemented DDA in such a way that the memory usage increases as $\mathcal{O}(N)$. The memory required for an aggregate of 10 monomers will therefore be 10 times that of 1 monomer. Since the IMA method only considers 1 monomer at a time, we don't expect any difference in the peak memory usage as the number of monomers in an aggregate is increased. Thus, a memory saving of a factor of n could be achieved by using IMA instead of DDA.

5.3 Systematic study of IMA performance

Different experiments are performed using the new scattering method, and the main areas of interest are:

- How the accuracy of IMA changes with size parameter (x).

- How the accuracy of IMA changes when the shape of the individual monomers are changed: we consider the plate-like, dendritic, and columnar monomers shown in chapter 4.

- How the accuracy of IMA changes with effective density, which we examine by looking at particles with different numbers of monomers. Effective density is likely to be an important parameter because higher densities imply a strong coupling, and it is the coupling that we are simplifying in IMA.

Scattering calculations for an ensemble of particles are performed, using 10 different aggregate realisations for each experiment. The method used to generate the particles is described in chapter 4, and examples are shown in Fig. 4.5. Ensemble-averaged scattering quantities are calculated, i.e. averaging the results of a population of 10 different particles of a given monomer number and particle habit. For each x value considered in a given experiment, the wavelength is chosen by averaging the 10 different D_{max} values of the particles, and using the average value to calculate the wavelength as $\lambda = \pi\langle D_{max}\rangle/x$. Thus, the size parameters considered in Fig. 5.3 and Figs. 5.5 to 5.8 are essentially average values of x.

To ensure that the generated particles are realistic, their effective densities are plotted in Fig. 5.2. The values are calculated as the mass of the particle m divided by the volume of a sphere of equivalent size, i.e. $\rho_{eff} = m/\frac{4\pi R^3}{3}$, where $R = D_{max}/2$. For comparison, relationships derived from aircraft measurements by Brown and Francis [4], and Cotton et al. [5] have also been plotted.[1] Overall, the particles used in this study have realistic values of ρ_{eff}, following the general behaviour of the two previously derived relationships. The plate-like and columnar aggregates tend to have higher effective densities, while the long, thin arms of the dendrites result in particles with a lower density. Increasing the number of monomers in the aggregates also results in decreased particle effective density on average.

[1]Note that the original Brown and Francis relationship of $0.0185D^{1.9}$ relates mass to D_{mean}, where D_{mean} is the average of two orthogonal particle dimensions, measured in directions parallel and perpendicular to the direction of travel of the aircraft. Here we have used the relationship that was re-derived by Hogan et al. [102] to relate mass to D_{max}. In that paper, Hogan pointed out that the D_{mean} relationship is often mistakenly used in the literature, and could lead to overestimates in IWC by a factor of approximately 1.5.

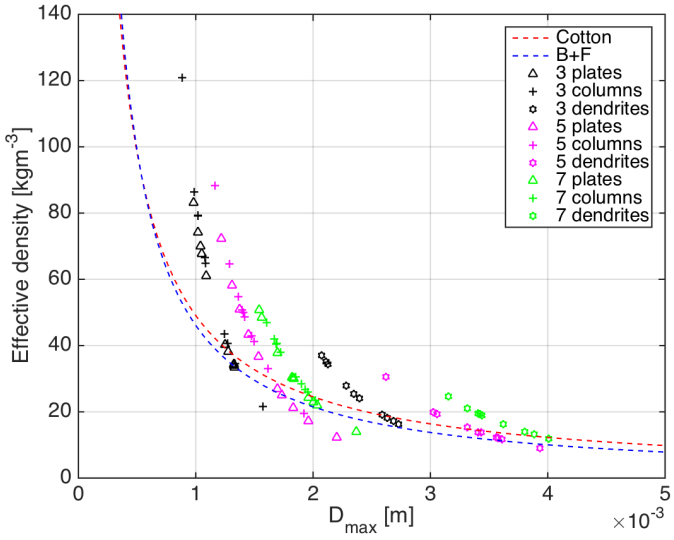

Figure 5.2: Effective densities of the particles generated for this study, along with dashed lines showing the values predicted using the relationships of Brown and Francis [4] and Cotton et al. [5]. The colours represent the different numbers of monomers used, and the marker shapes represent the different monomer habits, as described in the figure legend.

The accuracy of the IMA method is evaluated by comparing calculations with the DDA method. We calculate the percentage relative bias of each of the scattering parameters considered, e.g. $100(\sigma_{IMA} - \sigma_{DDA})/\sigma_{DDA}$. Equivalent calculations are also done with RGA in order to analyse the degree to which the IMA method provides an improvement to the simpler RGA approach.

Calculations for each particle are performed at one fixed orientation. The direction of travel of the incident wave is in the vertical z direction, and the wave is polarised in the x direction. However, each of the particles has a different orientation, since the aggregation model generates particles that are oriented randomly in space. As mentioned above, 10 different particles are used in each scenario for a given monomer number and particle habit. This means that although orientational averaging is not performed, we are integrating over multiple realisations, each in random orientations. This is similar to what would be sampled by a detector.

Four different quantities are analysed - the scattering cross section σ_s, absorption cross section σ_a, backscatter cross section σ_b, and the asymmetry parameter g. The extinction cross section σ_e was also calculated, but is not shown here due to the results being almost identical to σ_s. The parameter is discussed further in section 5.4. The results

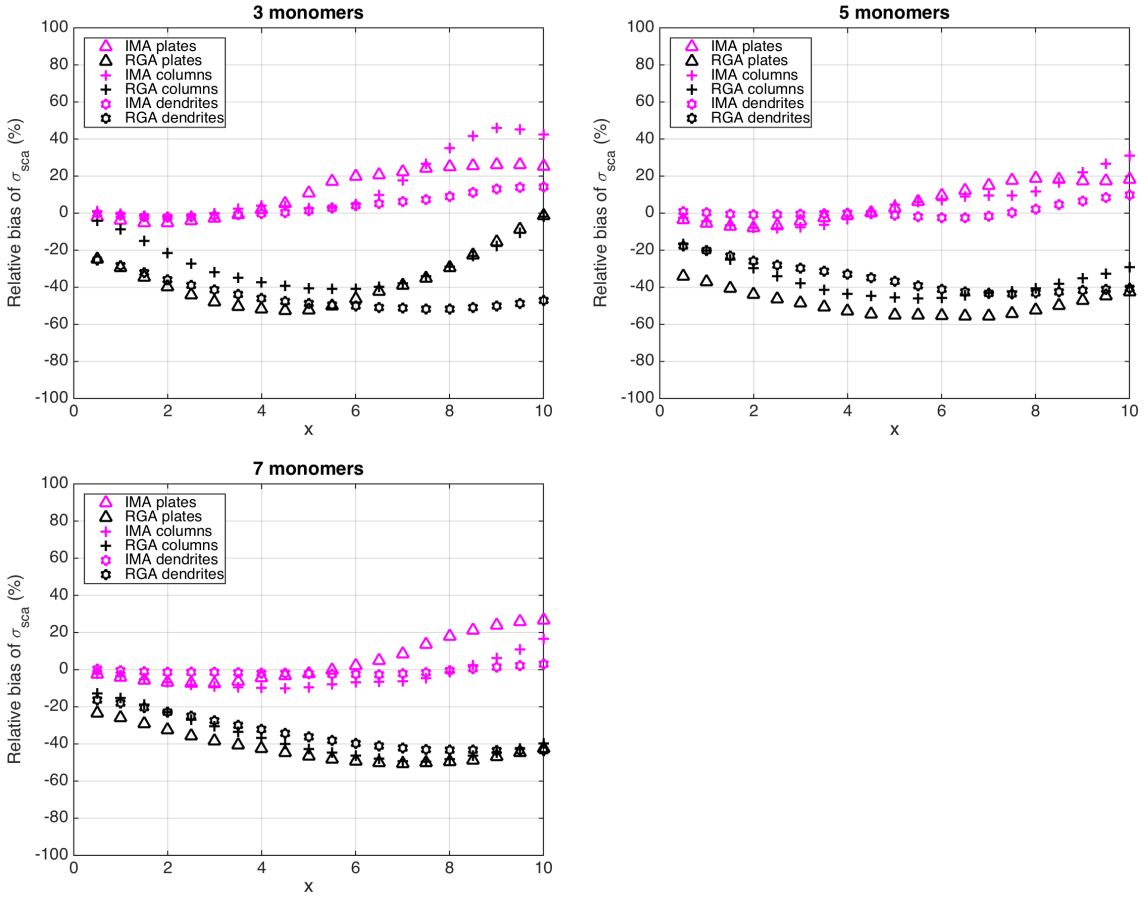

Figure 5.3: Relative bias in scattering cross section compared to reference DDA results, plotted as a function of size parameter. The three panels represent results for aggregates of 3, 5, and 7 monomers, respectively. IMA results are shown in magenta, and RGA results are shown in black. The results using different monomer habits are plotted using various markers; triangular markers represent plates, plus signs represent columns, and hexagrams represent dendrites. Each marker is an average of the results calculated for 10 particles comprising the same monomers, but with different arrangements.

are shown in Fig. 5.3, and Figs. 5.5 to 5.8. Each of the figures displays three panels, showing results for aggregates of 3, 5, and 7 monomers. In other words, the effective density of the particles decreases in consecutive panels. Within the panels, each of the particle habits are represented using different marker shapes, as detailed in the figure legend. IMA results are shown by the magenta markers, and RGA results are plotted in black.

5.3.1 Accuracy of the scattering cross section

First we consider the bias in the total scattering cross section. The cross section is given in Eq. (2.32). It is computed as an integral over a sphere, at different polar and

azimuthal angles of $\Theta \in [0°, 180°]$ and $\Phi \in [0°, 360°]$. A total of 800 different angles are used for the calculation. The first panel of Fig. 5.3 shows results for aggregates of 3 monomers. Using IMA produces a relative bias less than 10% for small size parameters of $x < 5$, for all monomer habits considered. The second and third panels show the results for aggregates of 5 and 7 monomers. As the number of monomers increases, the error incurred by using IMA generally decreases. Particles of $x < 6$ have errors below 10% when 5 monomers are considered, and this can be extended to $x < 7$ for 7 monomers. Even for the largest size parameters considered, the majority of the calculations remain within 20%.

With the IMA method, dendritic aggregates give the most accurate results out of the three different monomer habits. The bias in σ_s is generally within 10% of what DDA predicts, for all size parameters and numbers of monomers considered. The bias decreases with increased monomer number, i.e. with decreased effective density. The results for aggregates of plates and columns show more variation than the dendritic particles, with larger errors overall. As the number of monomers increases, the bias for columnar aggregates tends to decrease for $x \gtrsim 6$. For smaller x, the bias actually increases with monomer number. However, the increase is small and as mentioned the error remains within 10% for these size parameters. There is not a clear decreasing trend for the plate-like aggregates as monomer numbers are increased. At a range of size parameters between 5 and 8 the bias decreases, but for $x \gtrsim 8$ the error decreases for 5 monomers but increases again for 7 monomers. It is worth noting that this may be due to the differences in effective density not being defined enough to see the trend. For example, in Fig. 5.2 it may be seen that one of the particles of 5 plates in fact has a lower effective density than the aggregates of 7 monomers.

In chapter 3 we explored the internal fields of aggregates comprising solid ice particles such as plates, along with aggregates of more sparse structures such as dendrites. It was found that there is more focussing of the internal field when a particle has a greater amount of solid mass in the direction of travel. IMA would struggle to represent such behaviour, since the monomers act independently of one another in the approximation. Dendritic particles see less focussing due to the air gaps present in the particle structure.

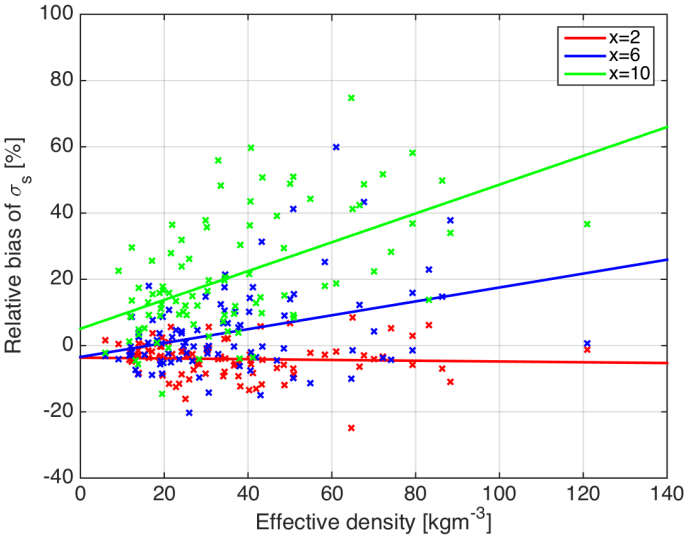

Figure 5.4: Variation in relative bias of σ_s with effective density. The different colours show results for size parameters of 2, 6, and 10. The crosses show the different particles, and straight lines have been fit to the points in order to see the trend.

The air gaps result in less significant interactions between dipoles, and subsequently a field that is more smoothed out. Such a field would be easier to reproduce using IMA, which may be why IMA calculations of σ_s for such particles have a lower bias than plate-like and columnar aggregates. It is likely that the metric of particle effective density is correlated with that property. We expect that increased effective density leads to increased dipole interactions, meaning a smaller IMA bias will occur for lower effective densities, with the error increasing with ρ_{eff}. It is worth exploring whether this is in fact the case.

Fig. 5.4 shows how the bias in σ_s using IMA changes with ρ_{eff}. Three different size parameters of 2, 6, and 10 are included in the plot. The crosses show the results for the individual particles, including all of the different monomer habits. Straight lines have been fit to the points for each value of x. It is seen that for small x, there is an almost constant bias, regardless of the effective density of the particle. As the size parameter is increased, a correlation between ρ_{eff} and bias can clearly be seen. It is not guaranteed that small values of ρ_{eff} result in low bias, and large ρ_{eff} means the bias will be large. Nonetheless, the general trend is that the bias in σ_s increases with ρ_{eff} for $x > 2$, with the relationship becoming more apparent as x increases.

As well as showing the bias in scattering cross section calculated using IMA, Fig. 5.3

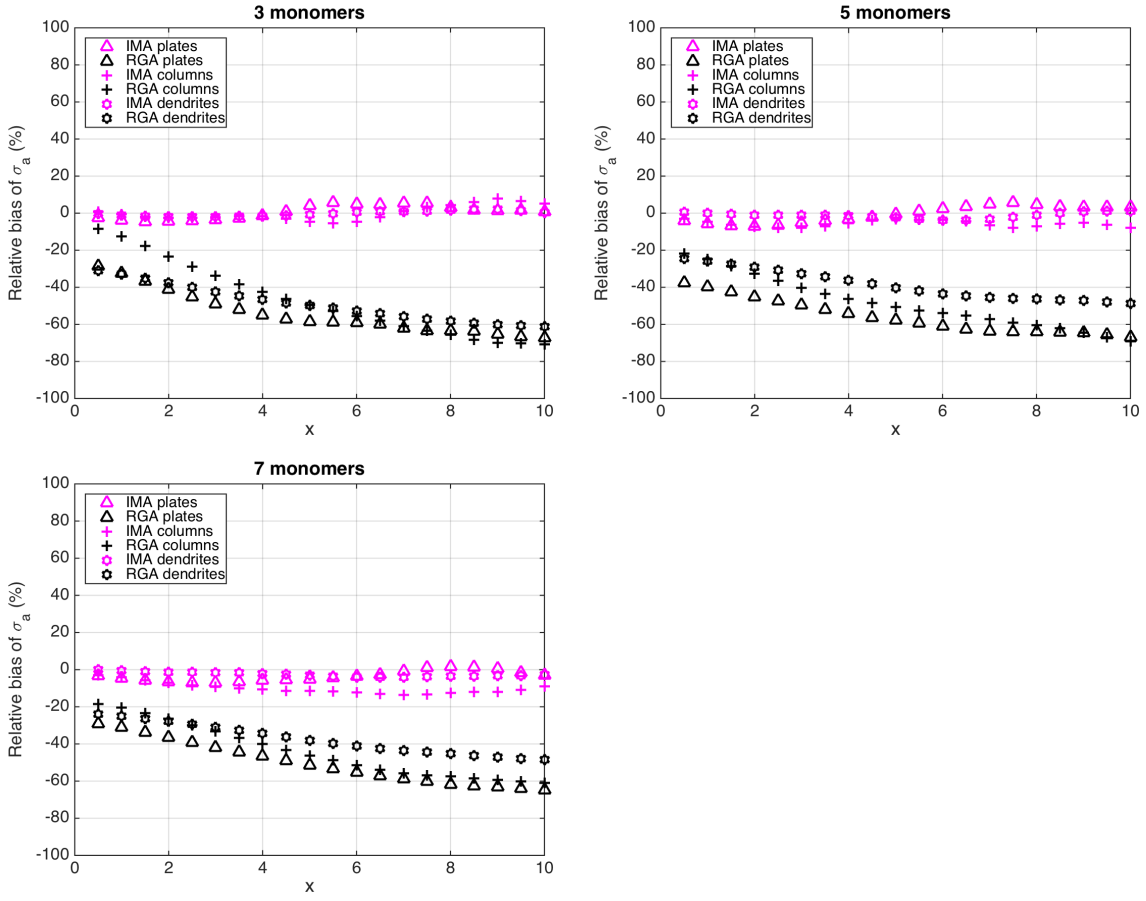

Figure 5.5: Same as in Fig. 5.3, but for the absorption cross section.

also shows results using RGA. Overall, RGA substantially underestimates scattering at all size parameters, with IMA providing a great improvement in the majority of the cases considered. It is interesting that the RGA biases tend to increase at intermediate size parameters, and then decrease again for larger size parameters. For aggregates of 3 columnar or plate-like monomers at $x \gtrsim 8$, the RGA bias decreases to values below IMA. Aside from these cases, RGA produces much larger errors than IMA, generally underpredicting σ_s by approximately 40%, and reaching almost 60% for some particles.

In section 2.8.4 we outlined that the RGA form factor describes the deviation from the Rayleigh regime, and $f \to 1$ when the particle is much smaller than the wavelength of the incident wave, i.e. in the Rayleigh regime. This is the case for the results for small x shown here, meaning we are using the Rayleigh approximation derived for spherical particles. It was pointed out by Refs. [61,62] that this results in a bias due to the non-sphericity of the particles in consideration. This may be the reason the RGA results show considerable inaccuracies even for small size parameters.

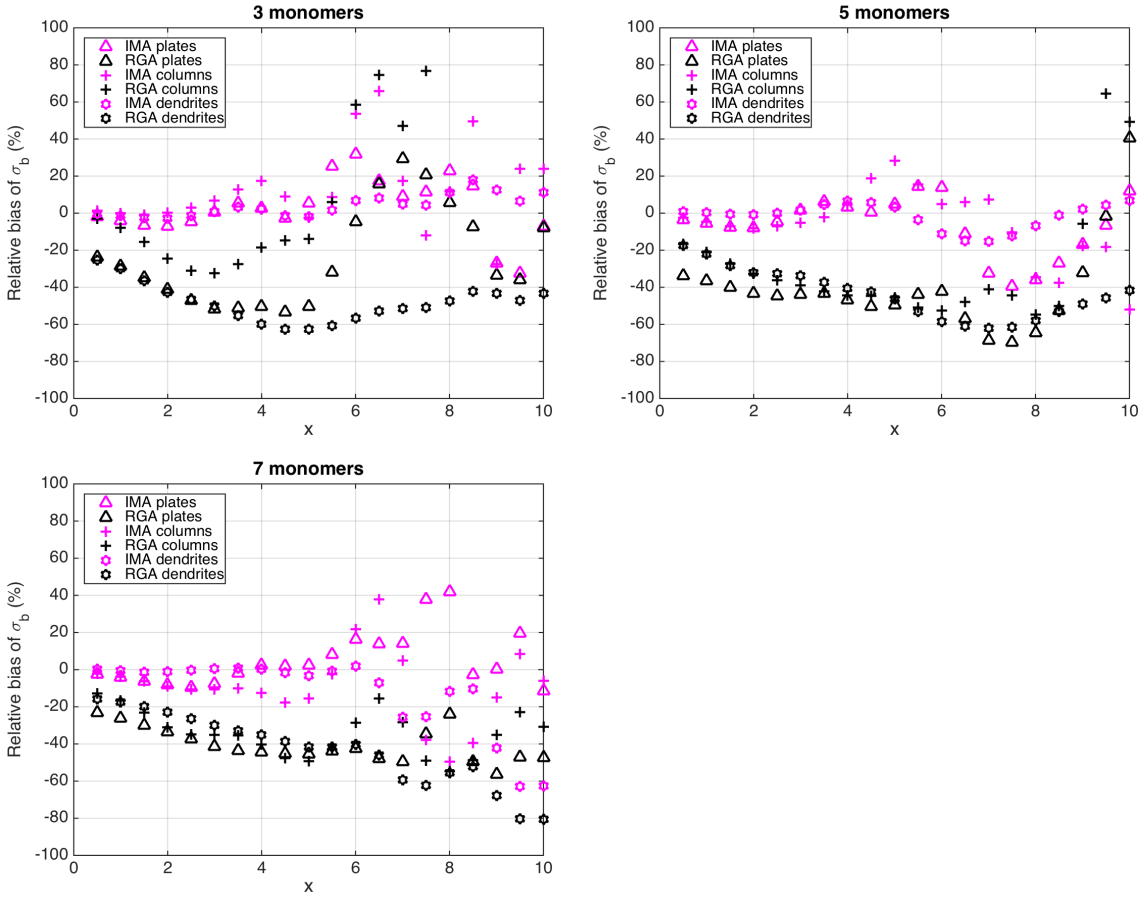

Figure 5.6: Same as in Fig. 5.3, but for the backscatter cross section.

5.3.2 Accuracy of other scattering quantities

The results for the absorption cross section are shown in Fig. 5.5. The bias in σ_a is very low using IMA, for all particles and sizes considered. The maximum bias found is for aggregates of 7 columns, but even in this case the error is within 20%. Using RGA, the absorption is significantly underestimated. The bias increases with size parameter, with large errors of 70% for most particles at $x = 10$. Aggregates of 5 and 7 dendritic particles of larger x have a slightly smaller error of approximately 50%.

Comparisons of the backscatter cross section provide a more sensitive test of the capabilities of IMA. It is expected that the quantity is more difficult to capture than σ_s, as an accurate representation of the internal field structure and interference in the far field are required to obtain good results. The results for σ_b are shown in Fig. 5.6. The error is generally less than 20% using IMA for $x < 5$. Larger underestimates of 60% are found for the equivalent cases using RGA. The errors for larger x are more unpre-

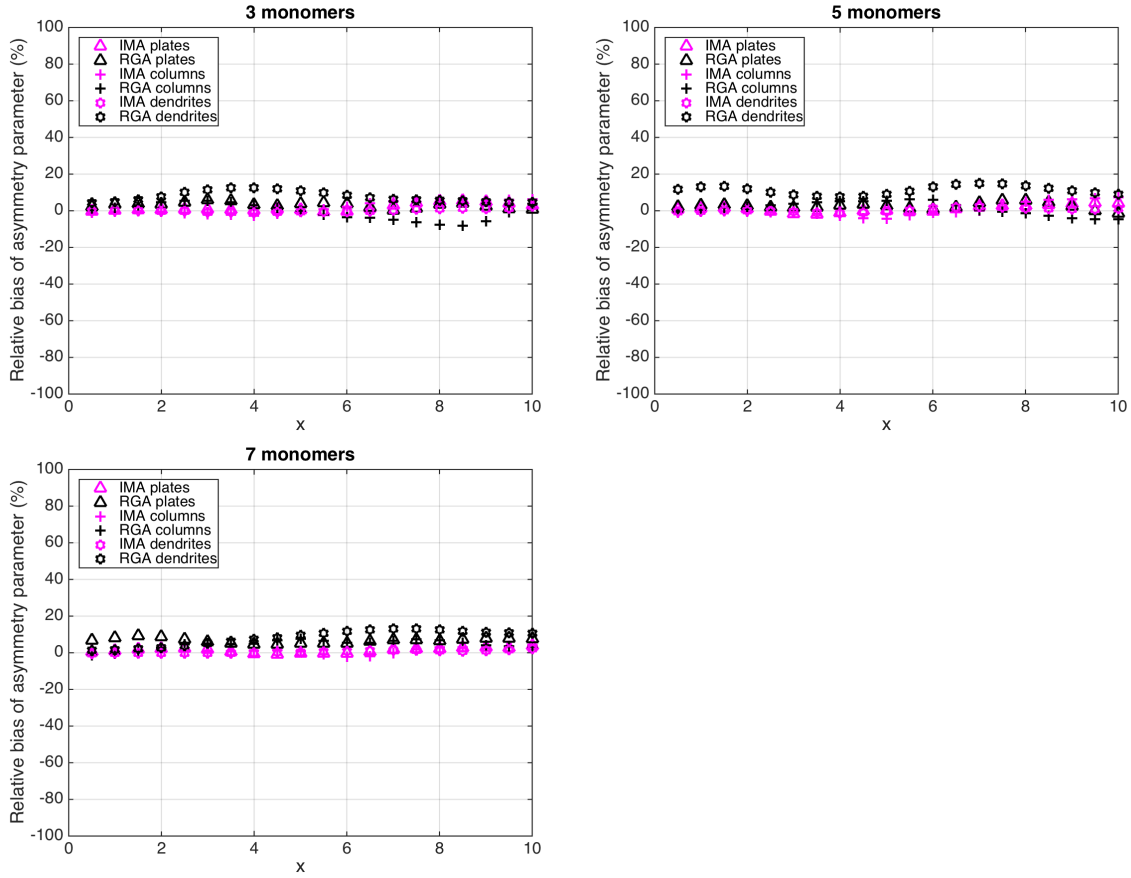

Figure 5.7: Same as in Fig. 5.3, but for the asymmetry parameter.

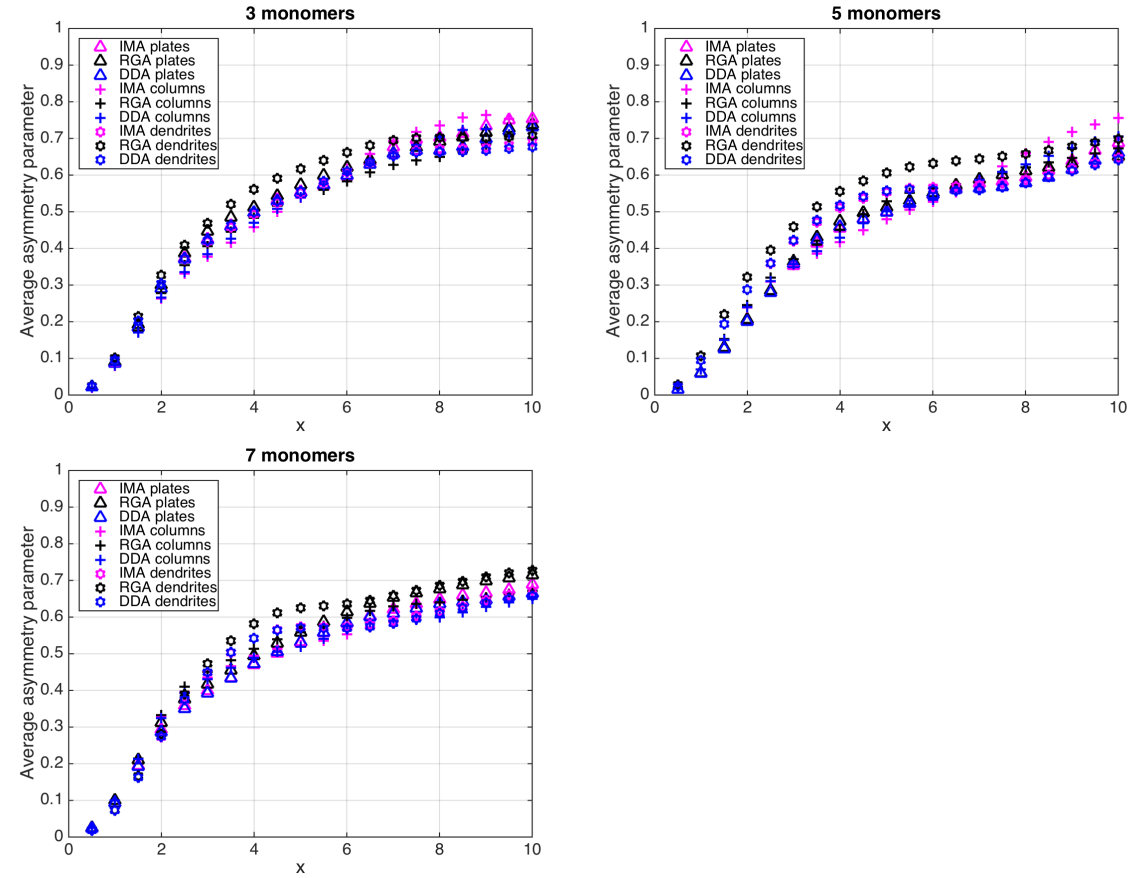

Figure 5.8: Asymmetry parameter plotted as a function of size parameter using IMA (magenta), RGA (black), and DDA (blue). Each marker represents the average value of g for the 10 particles used in each scenario.

dictable, particularly when the aggregate comprises columnar monomers. This shows that the backscatter is sensitive to monomer habit. However, we suspect that the large variation in bias would be smoothed out if orientation averaging was considered, or if a larger ensemble of particles was used. We plan to address these points in a future publication. Nonetheless, the promising result of small errors for $x < 5$ implies that the method could be used in the radar regime.

The asymmetry parameter g is defined in Eq. (2.37), and results showing the bias and the absolute values of g are shown in Figs. 5.7 and 5.8. It is clear that g is well captured by both IMA and RGA. The error using IMA is always within 10%. The error remains within 20% using RGA for all particles and values of x. RGA tends to overestimate forward scattering, as seen by the mainly positive biases in Fig. 5.7. This is also clear from Fig. 5.8, where in many cases the RGA results are larger than the values calculated using DDA. The exception to this is for columnar aggregates of 3 and 5 monomers, at a few larger values of x. It is encouraging that the general shape of the phase function is represented correctly using IMA. As g is an integral quantity evaluated by summing the phase function over all scattering directions, it makes sense that this quantity is not as prone to errors as the backscatter cross section.

In the next section we briefly explore what happens if the density of aggregates is increased via riming.

5.3.3 Rimed aggregates

It is known that particle density plays a role in the accuracy of RGA calculations, with more accurate results obtained for lower density aggregates. The low densities may be due to either increasing the number of monomers in an aggregate, or using lower density monomers such as dendrites rather than plates [61]. As discussed previously, the air gaps between dipoles result in less significant internal interactions in such examples. This means the RGA assumption of no interactions between dipoles is more applicable. We hypothesized that this was the reason the dendritic particles have a lower bias than plates and columns when the IMA method is used.

The process of accretion and freezing of supercooled water droplets on to the surface of ice particles is known as riming. Riming is a common mechanism of ice particle growth, and leads to the formation of rimed crystals or graupel. Low density aggregates may experience riming which increases the particle density, thus increasing the interactions within the aggregate. This means riming may make it more difficult for scattering approximations to perform well. Leinonen et al. [62] present results using RGA and SSRGA, which is an approximation based on RGA that may be used to calculate ensemble-averaged scattering properties [100, 109]. They show that significant deviations are found when the scattering properties of heavily rimed particles are compared to benchmark DDA solutions. It is interesting to test whether riming is also problematic for IMA.

From the particles generated for this study, one of the aggregates of dendrites where IMA performs well was chosen. A simplified algorithm to simulate riming, based on work done by Leinonen and Szyrmer [110], was used to generate rimed versions of the particle. The algorithm works by capturing stationary droplets on a particle as it falls vertically. This means the volume elements of ice representing rime are located at the bottom of the particle. The droplets are located at random positions within the square enclosing the horizontal projection of the particle. Unlike the authors of Ref. [110] who model both instantaneous and non-instantaneous freezing, we only consider droplets freezing immediately on contact with the particle.

On top of neglecting the terminal velocity of the droplet, we do not consider any properties of the surrounding environment that may influence the aerodynamics of the particle or the efficiency of riming. We simply specify the desired mass of the particle resulting from rimed droplets, then iterate the riming algorithm until that value is reached. We generate rimed versions of the aggregate where 10 to 50 % of the total particle mass is a result of rimed droplets. The particles are shown in Fig. 5.9.

Fig. 5.10 shows the bias in scattering cross section for each of the particles. The solid lines indicate the results using IMA, with the red line showing the values calculated for the particle without riming. In this case, IMA has a negative bias for $x \lesssim 4$, while for

Figure 5.9: The top left image shows a simulated unrimed aggregate of 7 dendrites. The following images show the simulated rimed versions of the particle, consecutively increasing the percentage of the final mass that is due to riming on the aggregate. The percentages range from 10% in the second image to 50% in the final image.

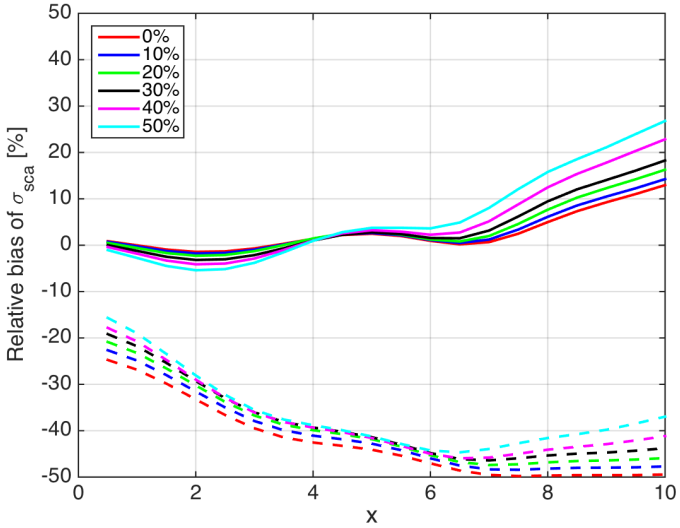

Figure 5.10: Relative bias in σ_s using different rime percentages on an aggregate of 7 dendrites. The solid lines show the results using IMA, while the dashed lines show the results using RGA.

$x \gtrsim 4$ the bias is positive. For almost all size parameters used here, the bias is enhanced by increasing the percentage of mass from rimed droplets. For $x \lesssim 4$ when IMA underestimates the scattering cross section, riming causes more of an underestimation, and for larger x when IMA overestimates σ_s, riming amplifies the overestimation. All rime percentages give a bias within 10% for $x \lesssim 7$ using IMA. The bias increases for larger size parameters, reaching almost 30% when 50% of the particle mass comes from rime.

The dashed lines in Fig. 5.10 show the equivalent results using RGA. Overall, it is clear that RGA is less accurate than IMA, showing a considerably greater bias in the scattering cross section. For $x \lesssim 7$ when the bias is within 10% using IMA, differences

as large as -50% are found using RGA. However, it is interesting to note that in this case the RGA method appears to improve slightly by riming. To try and understand this better, histograms of the internal field magnitudes using DDA and IMA are plotted in Fig. 5.11 for the unrimed and 50% rimed cases. Also included on the plots are lines showing the magnitude of 0.58 obtained using RGA. It is clear that the overall shape of the distribution changes due to riming. It can be seen in Fig. 5.11a that the unrimed particle has a more narrow distribution than the rimed version. The skewness of the distribution increases with rime, from a value of 0.6576 in the unrimed case, to 0.7298 when the particle is 50% rimed. It is worth noting that the IMA distribution is very similar to the DDA result in both cases. However, the IMA error in σ_s increases with riming. Therefore, the error is not limited to the overall distribution of magnitudes. The IMA bias must increase because the method struggles to correctly predict the locations of the magnitudes within the particle, leading to errors arising in far-field calculations.

Fig. 5.11a shows that in the unrimed case, the majority of dipoles within the particle have greater magnitudes than what RGA predicts. When the particle is rimed, Fig. 5.11b shows that there are more dipoles within the particle that have lower magnitudes, less than the RGA prediction. The median value of magnitude decreases slightly towards the RGA value. The shift in the overall distribution towards the RGA value is perhaps why the bias decreases, but it is difficult to draw meaningful conclusions by considering only one particle with a fixed orientation. It is possible that the increase in the number of dipoles with lower magnitudes is a manifestation of the particular riming algorithm used in this study. The rimed droplets are added to the base of the aggregate and tend to be quite isolated, meaning they experience only weak interactions with the rest of the particle. It is these low-magnitude dipoles that allow the DDA results to shift towards the RGA value. It may be that in reality the riming mechanism does not work in the same way as our model.

As mentioned, we have only considered riming of one particle with a fixed orientation, thus making it difficult to translate these findings into generalised conclusions. Nonetheless, it is sufficient to show that IMA is capable of reproducing the magnitude

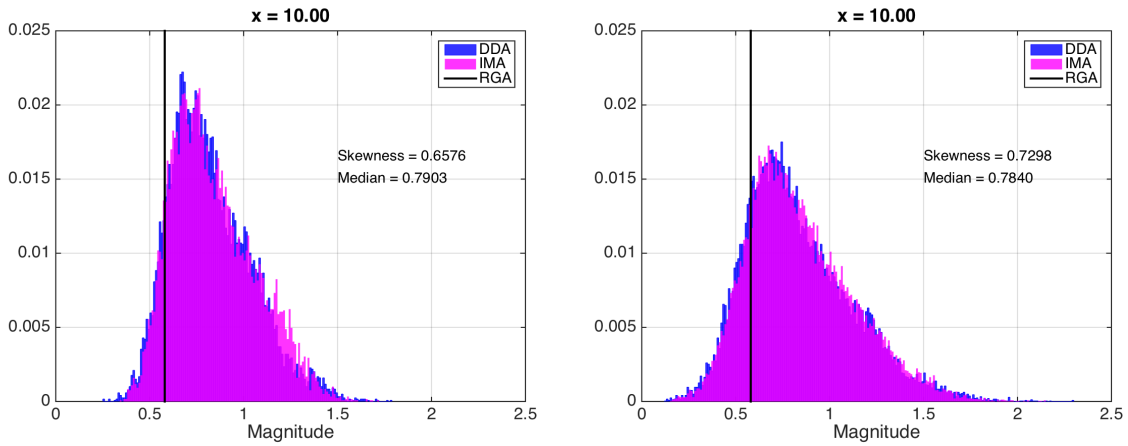

(a) Unrimed (b) 50% rimed

Figure 5.11: Probability density histograms of the magnitude of the internal fields within (a) the unrimed aggregate of 7 dendritic monomers, and (b) the 50% rimed aggregate. The results in blue are calculated using DDA, and results in magenta use IMA. A black line is also plotted in each panel to show the value of 0.58 that would result if RGA was used.

distribution of both unrimed and rimed aggregates, but at certain size parameters riming has an influence on the applicability of IMA to far-field scattering calculations.

5.4 IMA and the optical theorem

The extinction cross section was introduced in section 2.4, outlining that it may be calculated in two different ways. The first method is to calculate the total extinction by summing the scattering and absorption cross sections:

$$\sigma_e^{SA} = \sigma_s + \sigma_a \tag{5.1}$$

The calculation of the total scattering cross section is an integral over a far-field spherical surface (4π steradians) enclosing the particle, i.e. an integral of the differential scattering in all directions. This is a physically intuitive method to calculate extinction by a particle.

However, another common approach is to use the optical theorem. Using this method, σ_e may be calculated using the scattering amplitude in the forward direction only, i.e. in the same direction as the incident wave. This well-known, yet somewhat surprising

relationship is derived in Jackson [48]. We use the formulation of Draine [50]. For an incident plane wave, the extinction cross section is given by:

$$\sigma_e^{OT} = 4\pi k \sum_{j=1}^{N} \Im(\mathbf{P}_j \cdot \mathbf{E}^*_{inc,j}). \tag{5.2}$$

Application of the optical theorem requires that the scattering amplitude is known to sufficient accuracy (Tsang et al. [111]). The theorem is known to be invalid for the Rayleigh and Rayleigh-Gans approximations. One issue is obvious if we consider a non-absorbent particle, i.e. a particle with a real refractive index m. In this case the Clausius-Mossotti polarisability in Eq. (2.40) will also be real. This means that applying the optical theorem to such a particle will give $\sigma_e = 0$, implying that extinction depends only on absorption and not on scattering. This violates energy conservation. Van de Hulst [54] points out that if the optical theorem is to be used with non-absorbent particles, it is necessary to include the radiative reaction in calculations, as was introduced in Eq. (2.41). This causes a small phase lag relative to the incident field. However, Berg [112] points out that the main issue with RGA is the lack of refraction in the approximation caused by neglecting coupling between dipoles. This means the phase shift of the wave is not captured, and the optical theorem cannot be used. Thus, care must be taken to ensure the theorem is applicable before using it with approximate scattering methods.

The extinction cross section was calculated using both methods for the particles in this study, and comparisons of the results obtained using DDA and IMA were performed. We find that when DDA is used, excellent agreement is found between the two different extinction calculations in equations (5.1) and (5.2). However, this is not the case for IMA. The extinction calculated using the optical theorem (σ_e^{OT}) generally does not equal the value obtained by integrating over the sphere and adding absorption (σ_e^{SA}). The bias calculated for a single aggregate of 7 dendrites is shown in Fig. 5.12, i.e. $100(\sigma_e^{OT} - \sigma_e^{SA})/\sigma_e^{SA}$. Using the optical theorem results in underestimates of the extinction, with the exception of small particles in the Rayleigh regime where $x \to 0$. There is a very large bias at size parameters close to 1, with the error then decreasing

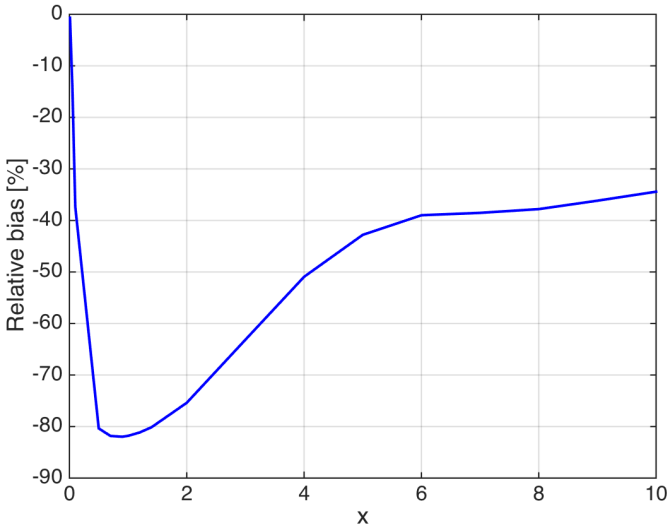

Figure 5.12: Relative bias (%) of the IMA extinction cross section calculated using the optical theorem in Eq. (5.2) compared to Eq. (5.1). This example is for an aggregate of 7 dendrites.

with increased x. Thus the IMA method does not satisfy the optical theorem, and the extinction cross section should be found by integrating the scattering over all angles of the sphere, and adding this to absorption using Eq. (5.1). Calculating extinction in this way matches results for σ_e^{SA} and σ_e^{OT} obtained using DDA.

5.4.1 Internal fields

It is interesting to consider possible sources of error in the IMA method, and relate these to the fact that the optical theorem is not satisfied. Looking at the equation for the optical theorem in Eq. (5.2), we are comparing the component of $\mathbf{P}_j$ in the forward direction, i.e. aligned with the incident field, against the incident field $\mathbf{E}_{inc}$ evaluated at that dipole. Thus any error found may arise from either the amplitude or the phase of $\mathbf{P}_j$. It has been discussed that the forward scattering amplitude calculated using RGA is not accurate enough for the method to satisfy the optical theorem [111]. We hypothesize that the most likely source of error in IMA is due to not capturing the internal phase shift correctly. Application of the optical theorem relies on capturing the phase shift within the particle, compared to applied field, as the wave moves through ice. The phase delay cannot be fully captured using the IMA method, since monomers only see the incident field. Thus it is possible that as more monomers are added to a

particle, the representation of the phase delay will become worse.

The internal fields represent combinations of the amplitude and phase at each dipole. We look at these individually below, using an aggregate of 7 plates.

5.4.1.1 Amplitude

To explore how well the IMA method reproduces amplitude, we plot the amplitude factor, i.e. $A = |\mathbf{P}_j \cdot \mathbf{E}^*_{inc,j}|$.

One arrangement from the 10 aggregates of 7 plate-like monomers has been chosen. The amplitude results are plotted for $x = 5$ and $x = 9$ in Fig. 5.13, using DDA and IMA. The incident wave is along the z-axis in the positive z direction, i.e. travelling from the bottom of the particle to the top, and it is polarised in the x-direction. Overall, the amplitudes are represented quite well using IMA. In terms of the regions of the aggregate where the field amplitude is largest, the IMA method generally places these regions within the correct monomer, although the exact location within the monomer is not always precisely captured. Unsurprisingly, larger errors are generally found where two monomers join. This can be seen clearly by the small red regions of large amplitude in Fig. 5.13a that are not reproduced by IMA in Fig. 5.13b. It is also seen in the central monomer in Fig. 5.13d, i.e. the fourth of the 7 monomers comprising the aggregate. The field within that monomer is clearly interacting with nearby monomers, exhibiting changes to the field close to those areas. The equivalent monomer does not show this behaviour in Fig. 5.13e for the IMA case. When the IMA method is used, we are ignoring interactions at those points that we know exist. The histograms in Figs. 5.13c and 5.13f show that the distribution is represented quite well using IMA, but the method slightly underestimates the full breadth of the distribution.

5.4.1.2 Phase

For a particle with a greater refractive index than the surrounding medium, the phase of a wave within the particle will be retarded when compared to the undisturbed applied

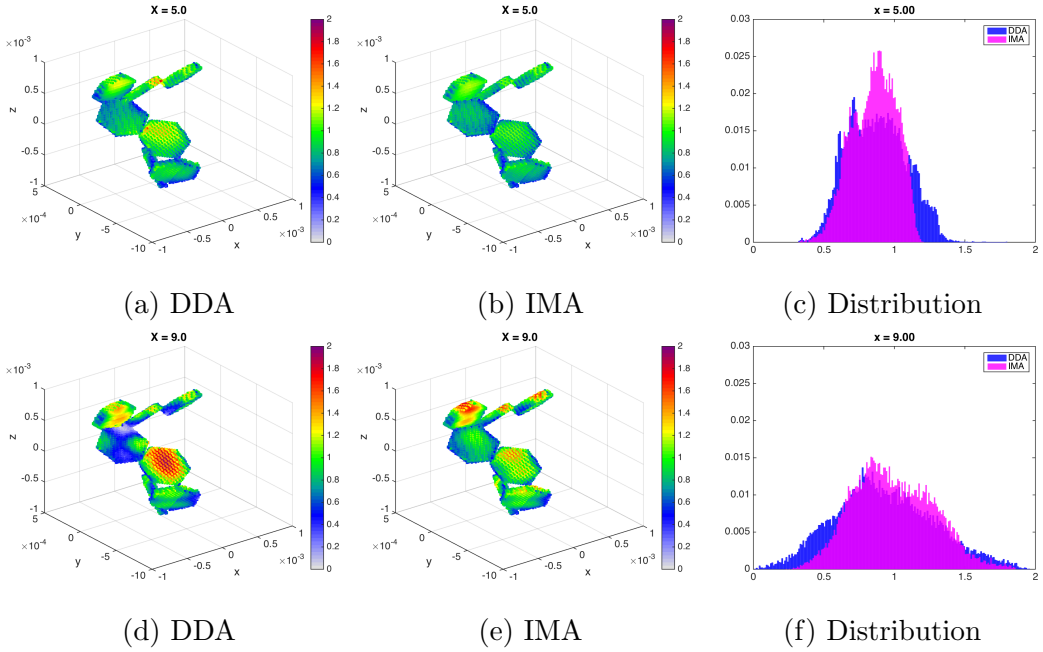

(a) DDA (b) IMA (c) Distribution

(d) DDA (e) IMA (f) Distribution

Figure 5.13: Amplitude within an aggregate of 7 plates for (a, b) $x = 5$ and (d, e) $x = 9$ using DDA and IMA. Panels (c) and (f) show probability histograms of the amplitude distribution within the aggregates.

wave outside the particle. The change in relative phase is known as the phase shift. Because IMA illuminates each monomer by the incident wave, any retardation of the phase by the other monomers is not captured. Therefore, it may be likely that the phases are very similar between DDA and IMA on the leading edge of the aggregate, diverging as the wave moves through to the far side. It is expected that the difference would be small for small size parameters, increasing as the size parameter gets bigger.

The vector $\mathbf{P}_j \cdot \mathbf{E}^*_{inc,j}$ represents the component of $\mathbf{P}_j$ in the direction of the incident wave, i.e. the parallel component. The phase of that vector can be used to see how much the phase changes inside the particle. This gives the phase shift of dipoles relative to the incident wave, and is calculated as:

$$Ph = \arctan\left(\frac{\Im(\mathbf{P}_j \cdot \mathbf{E}^*_{inc,j})}{\Re(\mathbf{P}_j \cdot \mathbf{E}^*_{inc,j})}\right)$$

Values of 0 indicate that the dipoles are oscillating in phase with the incident wave. Increasing values represent a greater phase delay within the particle.

To visualise this more clearly, an example showing the phase shift within a hexagonal plate is shown in Fig. 5.14. The incident direction is along the y-axis and the wave is

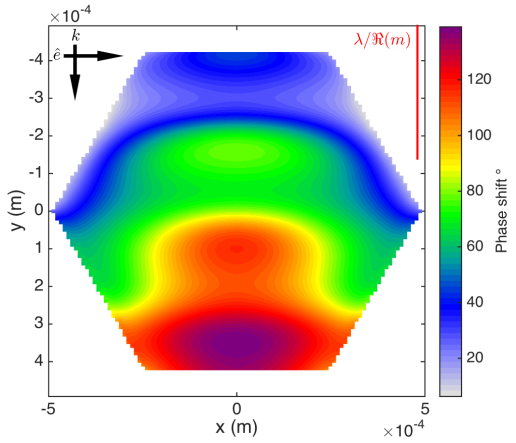

Figure 5.14: Phase shift (in degrees) relative to the incident field within a hexagonal plate of $x = 5$. The incident wave is in the y-direction and polarised along the x-axis. Increasing values with distance through the particle indicate that there is a phase delay with respect to the incident wave.

polarised along the x-axis. It is clear that the phase shift increases as the wave goes through the plate, i.e. there is more of a phase delay.

We now look at the behaviour of the phase shift for aggregates. Comparisons of results calculated using DDA and IMA allow us to examine how well the IMA method captures the phase shift through a particle.

Figs. 5.15a and 5.15b show the results for the aggregate of 7 plates with $x = 5$. The phase shifts are shown in degrees. The incident wave is along the z-axis in the positive z direction. The colour scale has been fixed to $[-180, 180]$ in order to easily compare the different cases. A histogram showing the distribution of the phase shifts can be seen in Fig. 5.15c. The equivalent results for $x = 9$ are shown in Figs. 5.15d to 5.15f.

For size parameters less than approximately 1, the dipoles oscillate in phase with the incident wave and no phase shift occurs within the particle. Fig. 5.15 shows that as x increases, the phase shift becomes more prominent. For $x = 5$, the phase shift calculated using DDA in Fig. 5.15a shows similar properties to the result using IMA in Fig. 5.15b, with differences in the phase shifts appearing quite insignificant. However, the histogram of the phase-shift distribution clearly shows that IMA does not incur as much of a phase lag as DDA. For $x = 9$, it is clear that the phase delay is larger, with more obvious red regions in Fig. 5.15d showing phase shifts reaching 163° when DDA is used. The behaviour captured using DDA is not represented by IMA, and the

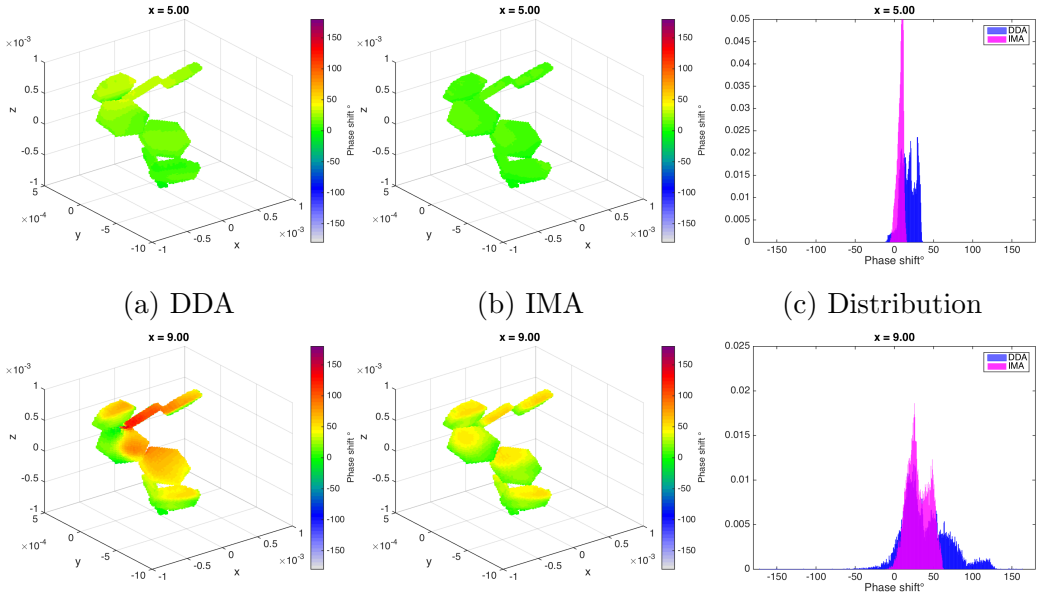

(a) DDA (b) IMA (c) Distribution

(d) DDA (e) IMA (f) Distribution

Figure 5.15: Phase shift in degrees within an aggregate of 7 plates for (a, b) $x = 5$ and (d, e) $x = 9$ using DDA and IMA. Panels (c) and (f) show probability histograms of the distribution of phase shifts within the aggregates.

maximum delay in Fig. 5.15e is only 62°. As hypothesized, the phase shifts calculated using the two methods are more comparable at the leading side of the particle along the direction of the incident wave, generally becoming less similar with distance through the particle.

A similar experiment is performed using dendritic aggregates of $x = 10$, as seen in Fig. 5.16. The colour scale has been reduced compared to Fig 5.15 in order to show more detail in the internal structure. The incident wave is in the z-direction, and polarised in the x-direction.

As in the case of the plate-like aggregates, there are red regions showing a phase lag in the DDA result in Fig. 5.16a that are not represented using IMA. However, considering we are looking at the $x = 10$ case, it is clear that the phase shift within dendritic particles is not as prominent as it is for plate-like aggregates. For a given size parameter, the phase retardation is greater within aggregates of plates and columns due to their larger densities, whereas the air gaps found in dendritic particles prevent the wave from experiencing such a large degree of retardation. The larger relative phase delay within more solid particles is not captured using IMA. The phase delay

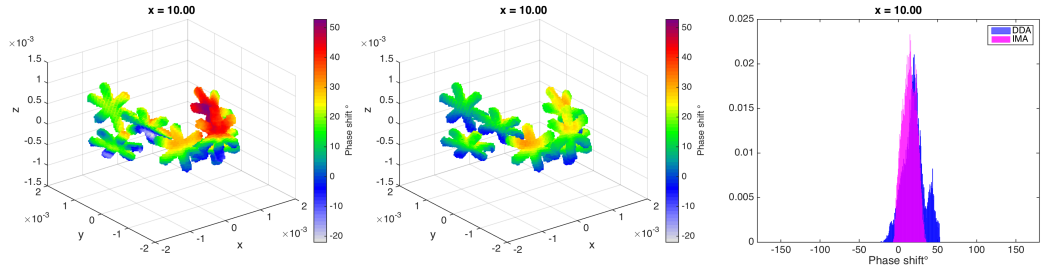

(a) DDA (b) IMA (c) Distribution

Figure 5.16: Phase shift in degrees within an aggregate of 7 dendrites for $x = 10$ using DDA and IMA. Note that in order to show more detail, the colour scale has been reduced compared to Fig 5.15. A probability histogram of the phase shift distribution is seen in panel (c).

within the dendritic particles is smaller, but Fig. 5.16c shows that IMA captures the peak of the distribution quite well. However, the method fails to capture details at the tails.

5.4.2 Relating the internal fields to far-field scattering

By examining the internal fields of different aggregates in the previous subsection, a weakness of the IMA method has become clear. Comparisons with DDA computations show that IMA underestimates the phase lag in the forward direction within different particles. The issue is more prominent for dense plate-like aggregates than for dendritic aggregates. We propose that it is possible to relate these findings to the biases in far-field scattering plotted in Fig. 5.10.

Fig. 5.15 shows that IMA underestimates the phase delay within aggregates of plates for both $x = 5$ and $x = 9$. However, the bias in σ_s is close to 0% for $x = 5$, and a much greater error of almost 50% is found for $x = 9$. This allows us to compare properties of the two cases, in order to determine the potential source of large error in the IMA method. The main difference between the internal field results for the two size parameters appears to be that the phase shift is smaller for $x = 5$ than for $x = 9$, as seen in the distribution plots in Figs. 5.15c and 5.15f. Using DDA, the phase shift reaches 36° for $x = 5$, whereas for $x = 9$ a considerably larger maximum phase shift of 163° is calculated. Thus, the scattering implications of underestimating the phase shift

depend on the absolute value of the phase shifts through the particle. In other words, underestimations of the phase shift do not have significant consequences if the overall phase shifts are small, while underestimations of the larger values found for $x = 9$ cause large errors in scattering. This is consistent with the findings of the dendritic aggregate of $x = 10$ in Fig. 5.16. A small maximum phase shift of 52° is calculated, and a small bias in σ_s of 13% is found.

The larger relative phase delay within more solid particles is not captured using IMA. We suggest that this is why IMA shows a lower bias when calculating scattering properties of dendrites compared to more solid plate-like and columnar aggregates. Thus we advise that the IMA method is only used if the phase shift within a particle is not too large.

5.5 Criteria for applicability of IMA - influence of refractive index

The two conditions of applicability for the RGA method are outlined in van de Hulst [54]. The conditions state that the refractive index should be close to 1, and that the "phase shift" within a particle, defined as $2x|m-1|$, should be much less than 1. As we found in section 5.4 that the IMA method struggles to represent phase lag, we now briefly consider whether a similar criterion could be used to diagnose the applicability of IMA. This would have particular relevance if we were to apply IMA to different types of aggregate particles in other physical problems- examples could include volcanic ash or soot particles.

All scattering quantities considered here remain within 20% bias for $x < 4$. For ice particles with $x = 4$ we obtain $2x|m-1| \approx 6.2$, suggesting that for errors within 20%, the IMA method should be limited to particles satisfying $2x|m-1| \lesssim 6$. To explore this further, equivalent computations were performed using different refractive indices with values both less than and greater than that of ice. Here we show results using $m = 0.7m_{ice}$ and $m = 2m_{ice}$, corresponding to values of $|m|$ of approximately 1.24

and 3.56, respectively. This allows us to determine whether the accuracy of the IMA method is determined by $2x|m-1|$.

Recall that the number of dipoles per internal wavelength, $n_\lambda = \lambda/(\Re(m)d)$, is generally required to be greater than 10 in order for the DDA method to be accurate. This means that when m is doubled, care must be taken to ensure that the DDA condition of applicability is still satisfied. However, as we are testing the condition of $2x|m-1| \lesssim 6$, it is sufficient to look at small size parameters when $m = 2m_{ice}$, and we do not do calculations for $x > 2$ in this case. For such values of x, we are using values of n_λ that are large enough to satisfy the DDA requirements.

Fig. 5.17 shows the error in scattering cross section as a function of $2x|m-1|$ for the aggregates of 3, 5, and 7 monomers. The magenta markers show the original results obtained using $m = m_{ice}$. The green and blue markers show results using $m = 2m_{ice}$ and $m = 0.7m_{ice}$, respectively. The monomer habits are represented using different marker shapes, synonymous with the previous results within this chapter. All results are calculated for x at intervals of 0.5, up to a maximum of $x = 10$. This means the abscissa points at which results are obtained vary for the three different values of m considered.

It is clear from Fig. 5.17 that the error is smaller for lower refractive indices, generally increasing with m. When $m = 2m_{ice}$, the error obtained for a given value of $2x|m-1|$ tends to be larger than for smaller m. This is particularly true for aggregates of plates and columns, while the error for dendritic particles remains small. Therefore, the IMA method may not be applicable to particles with a refractive index much greater than that of ice. This is not surprising since the shorter internal wavelength corresponding to increasing m results in increased interactions between dipoles. Thus, neglecting some of these stronger interactions by using the IMA method will have a more significant impact on the overall error. However, it has been noted in previous literature that the accuracy of DDA also decreases with increasing refractive index. Yurkin et al. [44] highlight that the DDA method using the lattice dispersion relation (LDR) for the polarisability (i.e. the formulation used in this work) is only known to

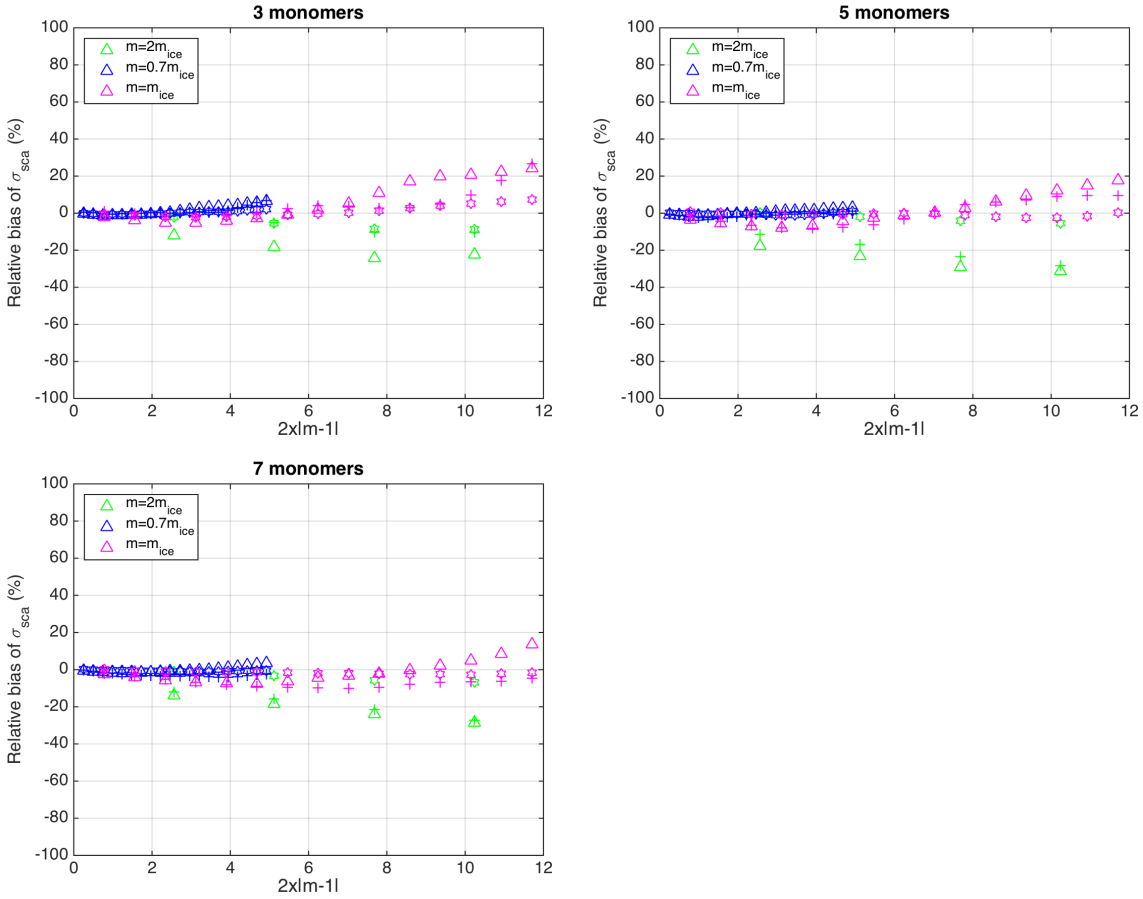

Figure 5.17: Bias in σ_s as a function of $2x|m-1|$, using three different refractive indices of $2m_{ice}$ (green), $0.7m_{ice}$ (blue), and m_{ice} (magenta). The triangles correspond to plate-like monomers, plus signs represent columns, and hexagrams represent dendrites.

be applicable if $|m-1| < 2$. For the results shown here when the refractive index is doubled, $|m-1| = 2.56$, exceeding the known range of applicability of the method. It is therefore possible that we are in a region where DDA with LDR does not perform well, making it difficult to analyse the accuracy of IMA in these cases.

This experiment shows that although the refractive index plays an important role in the validity of the IMA method, the accuracy is not determined solely by the value of $2x|m-1|$, which is referred to as the "phase shift" parameter in RGA literature. We saw in Fig. 5.4 that the effective density is also important, and it appears that the increase in refractive index has a more significant effect on accuracy for higher density plate-like and columnar aggregates, compared to the lower density dendritic particles. For that reason, it is likely that some combination of x, m, and ρ_{eff} may be used to determine the region where the IMA scattering method performs well. Further tests would be required in order to recommend generalised applicability limits. However, from the

tests performed here, we propose that the method may be applied to scattering by many ice aggregates in the microwave and sub-mm regimes, provided the particle sizes are not too large. This is explored further in the following chapter, where the method is applied to simulate measurements obtained from a case study.

5.6 Concluding remarks

In this chapter, we have developed a new scattering approximation called IMA. Overall, the method provides better results than RGA, but it is clear that some physics is not captured. As part of our future work, we plan to consider whether the phase shifts could be represented more accurately. This could be achieved by performing calculations for each monomer in sequence from the front of the aggregate to the back, and carrying a phase delay to each subsequent monomer. For example, once $\mathbf{P}$ is calculated for monomer 1 in response to the applied field, the input for monomer 2 could be calculated as $\mathbf{E}^{inc} + \mathbf{E}^{sca}_{mon1}$, and so on.

Chapter 6

Application of the IMA scattering method to radiative transfer simulations

6.1 Introduction

Experiments can be performed that incorporate several different measurement techniques and simulations. These allow errors to be identified in one or more of the methods. This type of experiment is called a closure experiment. In this chapter we discuss a comprehensive microwave closure experiment that has been performed. The study involved utilising independent datasets from a variety of in-situ and remote-sensing instruments, along with performing radiative transfer simulations using ARTS [51]. It is noted, however, that not all measurements were obtained coincidently in time. Observations from above the cloud were obtained first, with in-situ measurements obtained thereafter, thus resulting in a limitation of the experiment.

6.2 Details of the case study

The data analysed in this study was collected during the North Atlantic Waveguide and Downstream impact EXperiment (NAWDEX) campaign. Measurements of deep frontal cloud were obtained in a region off the west coast of Scotland on 14 October 2016. The instrumentation used and measurements obtained from both above and within the cloud are described in more detail in the following subsections.

6.2.1 Above-cloud measurements

Three different aircraft took coincident measurements from above the cloud during this case, at an altitude of approximately 9.5 km. Fig. 6.1a shows the flight path of the aircraft. The Facility for Airborne Atmospheric Measurements (FAAM) BAe-146 aircraft carried the ISMAR radiometer, which measured the vertical and horizontal polarised brightness temperatures upwelling from the ice cloud beneath. This was done with an off-nadir observation angle of between 51 and 52°, matching the planned configuration of ICI. Coincident data was also obtained from two different radars. The 95.04 GHz RASTA cloud radar flew on board the French Service des Avions Francais Instrumentions pour la Recherche en Environnement (SAFIRE) Falcon 20 aircraft. More information on the RASTA radar can be found in Ref. [113]. The 35 GHz radar was on board the German High Altitude and LOng Range Research Aircraft (HALO), and is part of the HALO microwave package (HAMP) [114]. Both radars operated at an observation angle of 0°, i.e. nadir. The 35 GHz radar differs from other airborne radars as it uses a high-power magnetron as a transmitting source, enabling a peak emitting power of 27 kW and an airborne sensitivity of −39.8 dBZ. The 95.04 GHz radar has a much lower peak power of 1.8 kW, and its sensitivity at 1 km is between −32 and −16 dBZ, depending on the antenna configuration.

Radiometers such as ISMAR convert measured radiation into brightness temperatures, i.e. the temperature of a theoretical blackbody that would emit an equivalent amount of radiation. Colder brightness temperatures correspond to more ice in the clouds, as

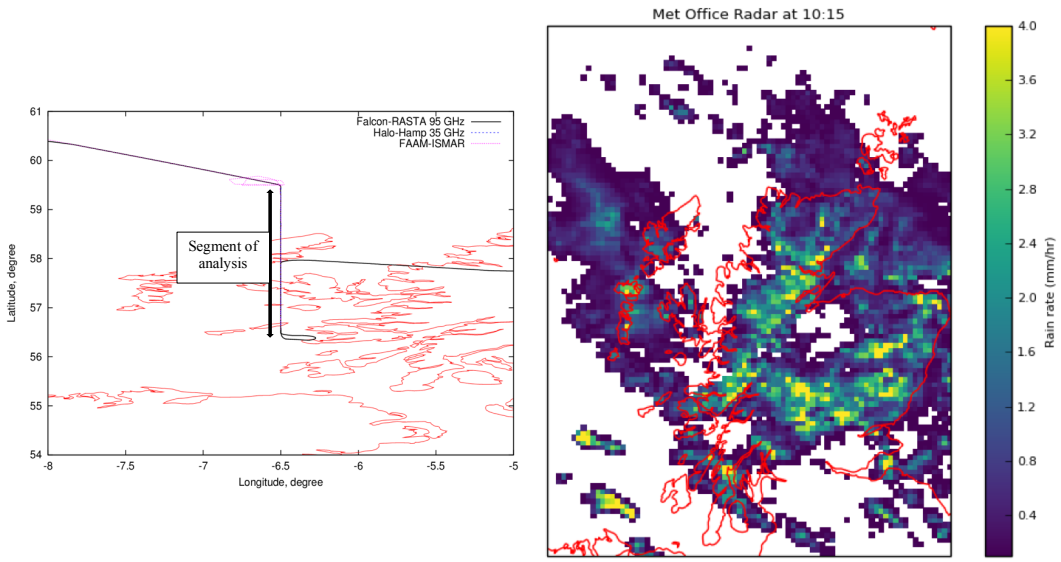

(a) Flight path (b) Rain rate

Figure 6.1: Flight path of the three aircraft during the above-cloud near-coincident run, and the rain rate estimated from the Met Office C-band radar (5.6 GHz) at Druim a Starraig in Scotland at that time.

a greater amount of radiation from the lower atmosphere is scattered on its way to the instrument's detector, as shown in Fig. 6.2. By comparing the brightness temperatures at orthogonal horizontal and vertical polarisations, i.e. TB_H and TB_V, we can gain some information about the size, shape, and orientation of ice particles within the cloud. Let us denote the polarimetric difference $TB_V - TB_H$ as V-H. If large values of V-H are measured, it is indicative of horizontally oriented particles, since more horizontally polarised radiation is scattered, resulting in $TB_V > TB_H$. Random orientation produces no clear signal. According to Gong and Wu [115], neglecting the polarimetric signal could result in errors of up to 30% in IWP retrievals.

Fig. 6.3 shows the brightness temperatures at H and V polarisations measured from ISMAR during this campaign, along with the V-H polarimetric differences. Fig. 6.3a shows that large brightness temperature depressions were measured as the aircraft flew over the thick cloud, with a decrease of approximately 30 K at a latitude of 57.3°. Fig. 6.3b shows that there were regions where a large V-H polarimetric signal was measured, reaching almost 10 K. The V-H signal is correlated with the brightness temperature depression, indicating that it is microphysical rather than being caused by the surface.

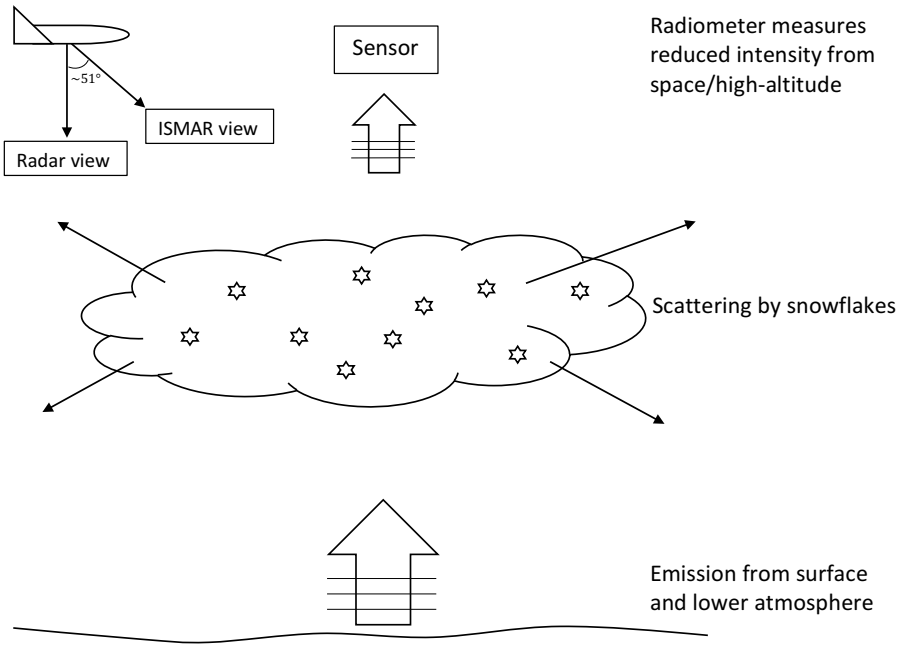

Figure 6.2: Cartoon of the scattering process, showing a reduction in measured radiation by a radiometer as a result of scattering by snowflakes in the atmosphere. The measurements used in this study from the ISMAR radiometer were taken at an off-nadir observation angle of between 51 and 52°. Both radars used here operated at an observation angle of 0°, i.e. nadir.

Fig. 6.4 shows the radar reflectivities measured at the frequencies of 35 GHz and 95.04 GHz. It is clear that the 35 GHz radar detects a signal from particles in the upper region of the cloud that are not picked up by the higher frequency radar. This is a result of the higher sensitivity of the 35 GHz radar, as described previously. Two regions of particularly high reflectivity are seen, where the 35 and 95.04 GHz radars measure values of about 20 and 10 dBZ respectively. These are located at altitudes between about $2 - 4$ km, and latitudes between approximately 58.4° and 57.9°, and 57.7° and 57.3°. These reflectivities correspond to the large brightness temperature depressions measured from ISMAR, as shown in Fig. 6.3a, and thus could be caused by large oriented ice particles. A thin melting layer is observed below 2 km, with a bright band showing in the 35 GHz reflectivity.

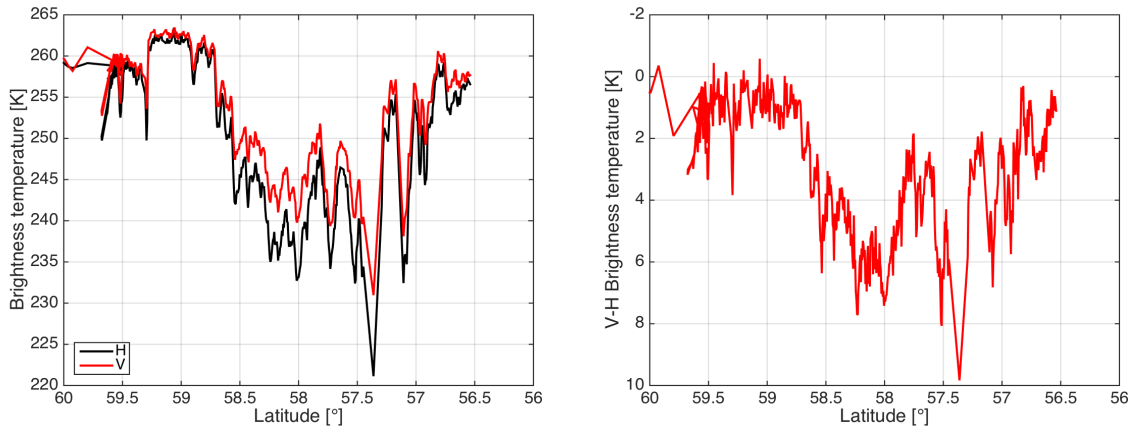

(a) Brightness temperature (b) V-H Brightness temperature difference

Figure 6.3: Brightness temperatures at V and H polarisations measured at different latitudes using the ISMAR radiometer at 243 GHz, along with the V-H brightness temperature difference.

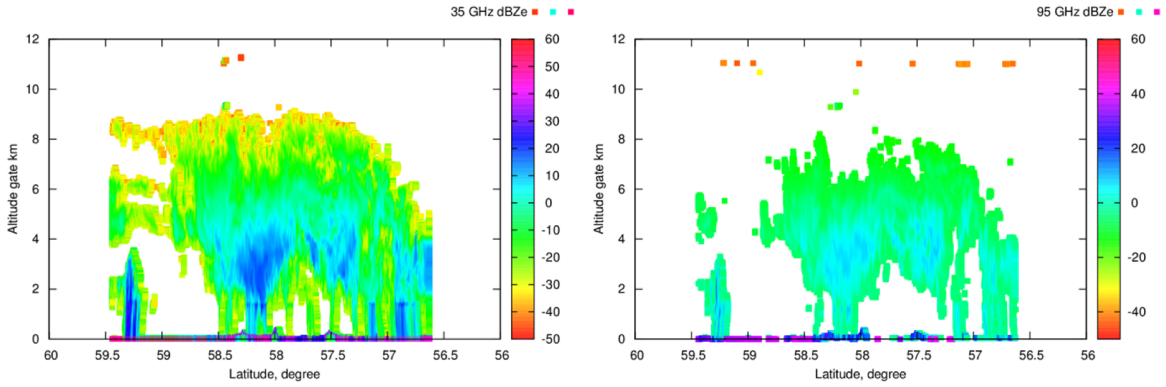

Figure 6.4: Measured reflectivities from HAMP and RASTA.

6.2.2 In-situ measurements

Following the above-cloud run of the three aircraft, in-situ measurements were obtained from the FAAM aircraft, which carried the Cloud Droplet Probe (CDP), along with the CIP-15 and CIP-100 instruments. The two CIP instruments are optical array probes (OAPs), providing 2-D images of particles measuring 15 to 930 µm, and 100 to 6200 µm, respectively. A review of the different probes is given by McFarquhar and Coauthors [116].

For a cloud comprising an ensemble of scattering particles, we need to consider a particle size distribution (PSD). The PSD is a function which gives a description of the number of particles of different sizes that are present in a cloud. For ice particles, the distribution $n(D_{max})$ is usually measured in units of $\mathrm{cm}^{-3}\mu\mathrm{m}^{-1}$. The number of parti-

cles of a given size per unit volume is then given by multiplying by the appropriate bin width $n(D_{max})dD_{max}$. The CDP, CIP-15, and CIP-100 probes provide measurements of the PSDs, along with cloud particle imagery which is useful to decide which particle habit to use for radar and mm-wave simulations. In this experiment, we model the atmosphere using multiple layers, described in more detail in section 6.4. Within each layer, the PSDs from the three instruments were composited using the method described in Cotton et al. [5], and averaged over 10 second intervals. The layer-averaged PSDs are used in this study. The deep cone Nevzorov probe provided data on the liquid and total water (ice plus liquid) contents by measuring the amount of power required to melt and evaporate particles that come into contact with the sensor. The IWC is also averaged over 10 second intervals, and layer-averaged. Due to the inhomogeneity of the cloud, there is some variability in IWC, represented by a standard deviation corresponding to each of the layer averages.

The overall plan in this chapter is to determine whether we can combine the in-situ measurements to construct an atmospheric model to replicate the large brightness temperature depressions and V-H differences measured from ISMAR. ARTS is particularly useful for this work because of its capability to handle polarised radiative transfer. Brightness temperatures are calculated using the RT4 polarised radiative transfer model within ARTS, described in Ref. [117]. RT4 assumes that particles are azimuthally random, i.e. there is some preferential polar alignment, but the particles are randomly oriented in the azimuth. Furthermore, the model assumes a plane-parallel atmosphere. Thus in all the simulations performed here, we use a 1-D plane-parallel atmosphere within ARTS, with azimuthally randomly oriented particles. The differences in brightness temperatures between those simulated using ARTS, and those measured by the airborne radiometer, ISMAR are analysed. The calculations are performed at 243 GHz, since this channel in ISMAR measures orthogonal H and V polarisations.

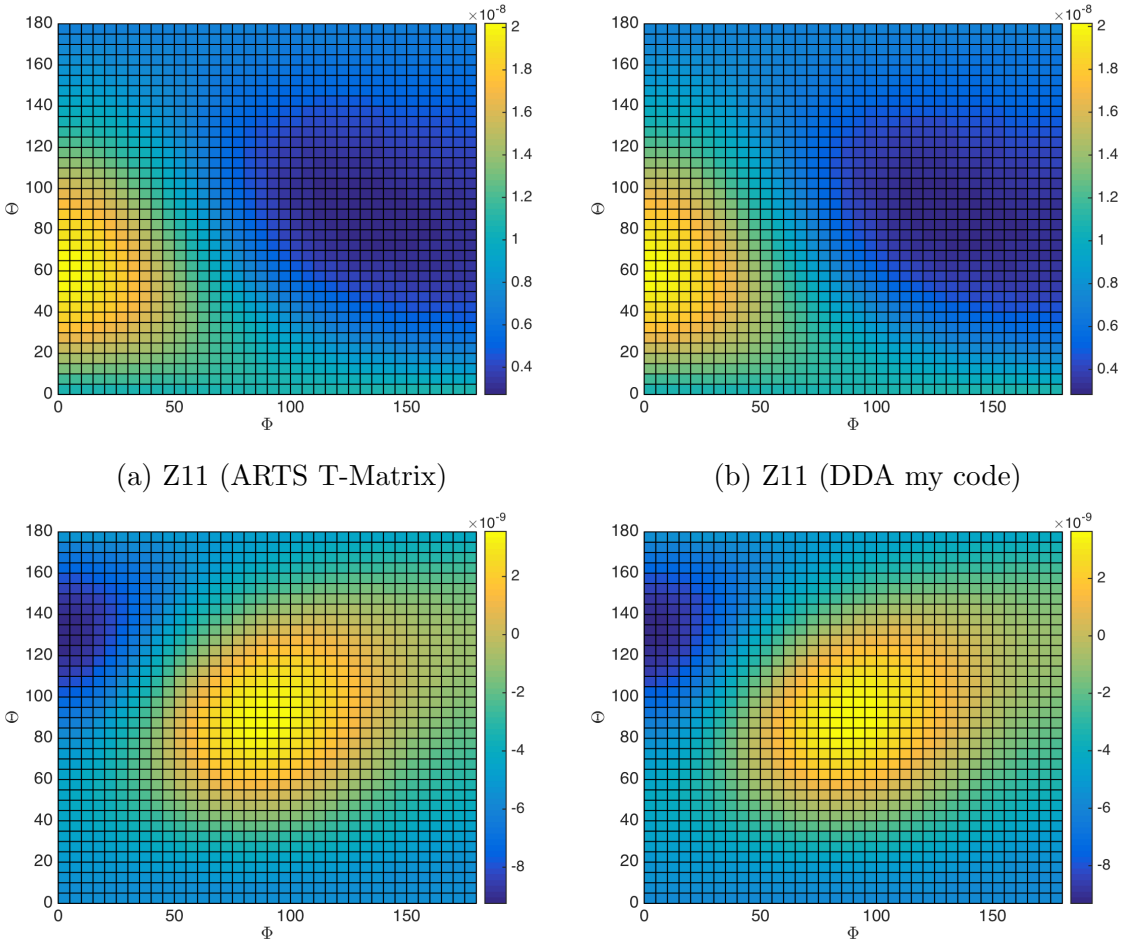

(a) Z11 (ARTS T-Matrix)

(b) Z11 (DDA my code)

(c) Z12 (ARTS T-Matrix)

(d) Z12 (DDA my code)

Figure 6.5: Z11 and Z12 elements of the phase matrix, obtained from the ARTS example which uses the T-Matrix scattering method, and calculated using my DDA implementation. These examples are for $\Theta_{inc} = 60°$. The plots show the scattered azimuth angle, Φ along the abscissa, and the scattered polar angle, Θ along the ordinate.

6.3 Validation of scattering parameters required as input into ARTS

As well as including a database of scattering calculations for realistic particle habits performed using DDA [37], ARTS also accepts externally generated scattering calculations. In the previous chapter, I described a new light scattering approximation for aggregates of ice particles, which we have named the Independent Monomer Approximation (IMA). As we wish to evaluate the usefulness of the IMA scattering method, we employ that approximation in this chapter.

As outlined in section 2.5.2, the inputs required by ARTS include the phase matrix,

Z, extinction matrix, **K**, and absorption vector, **a**, for each particle. During a three month placement at the UK Met Office, I spent time implementing the numerics to perform these single-scattering calculations for ice particles. In order to validate my implementation, comparisons were performed using different particles. Note that the tests have been performed using monomers. Recall that the basis of the IMA method is that DDA calculations are performed for individual monomers within an aggregate. This means that when single monomers are used, as in these test cases, the scattering calculations are done using the DDA method. Thus the tests described here assess the accuracy of the implementation of the scattering calculations, but do not evaluate the applicability of the IMA scattering method.

Firstly, comparisons were done using single-orientation cases. The amplitude scattering matrix elements of a spherical particle were calculated using my implementation. These results were compared with the values calculated using Mie scattering. Results within 1% were obtained for Rayleigh spheres, with errors for larger size parameters remaining within 10%. Next, a hexagonal prism geometry was tested by comparing our results with those calculated using the T-Matrix formalism of Havemann and Baran [118]. Again, results within 10% were found.

Secondly, comparisons were done using different incident and scattered angles. In order to ensure all of the matrix elements were accurately implemented in the format expected by ARTS, a test case for an azimuthally random spheroid was provided by Patrick Eriksson, one of the ARTS developers. This case allowed us to check the phase matrix, extinction matrix and absorption vector calculations, before proceeding with calculations for particles specific to this case study. The ARTS data is calculated using the T-Matrix method. A range of angles between 0° and 180° have been tested. All elements are in excellent agreement with the ARTS example, with relative errors below 4%. Fig. 6.5 shows examples of 2 of the 16 phase matrix elements obtained from the ARTS test case, and calculated using my implementation. The phase matrix elements have units of m^2. The example shown is for $\Theta_{inc} = 60°$. In this chapter, calculations are done for aggregates specific to this case, which are then implemented into ARTS to perform polarised radiative transfer simulations.

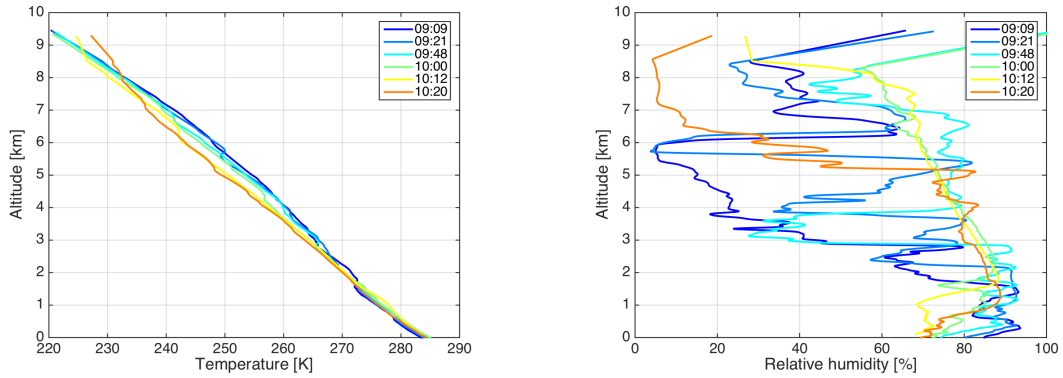

(a) Temperature [K] (b) Relative humidity [%]

Figure 6.6: Temperature and relative humidity profiles obtained from 6 different dropsondes. The time of each dropsonde release is given in the figure legend.

6.4 Construction of a model atmosphere

The first thing to do is to construct a model of the atmosphere, which will be used in the radiative transfer simulations. Prior to descending through the cloud, the aircraft released a series of dropsondes to obtain the background atmospheric state for input into ARTS. As well as providing water vapour mixing ratio profiles of the atmosphere, the dropsonde profiles provide surface properties such as temperature and wind speed that feed into the ocean surface emissivity model used within ARTS. Fig. 6.6 shows some of the measurements obtained from the dropsondes, namely the temperature and relative humidity profiles.

As a supplement to the background state, we need to input information on the cloud that was present during the study. Due to the depth of the cloud, it would not be possible to obtain an adequate representation of the atmospheric conditions using a single averaged layer. Hence we model our atmosphere based on the aircraft profiles, using 7 different layers with depths of approximately 1 km each. These layers are located between altitudes of 2 km and 9 km.

6.4.1 Mass-size relationships

The single-scattering properties will be integrated over the layer-averaged PSDs in the radiative transfer simulation, to obtain the layer-averaged single-scattering properties.

This requires that we make some assumptions about how the density of the particles varies with maximum dimension, D_{max}. These relationships are usually of the form $m = aD_{max}^{b}$, where m is the mass of the particle, and the parameters a and b are constants which depend on particle habit and atmospheric conditions such as temperature. As discussed by Mason et al. [119] and references therein, the prefactor, a, of the mass-size relationship scales the ice density, and the exponent, b, is related to the particle shape or growth mechanism. Mitchell et al. [120] presented mass-size relationships with values of b ranging from 1.7 to 2.6 for different habits. By simulating a variety of particles, Fontaine et al. [121] showed that in general $b \approx 2$ if the particle height remains constant while the length increases, and b approaches 3 for dense particles whose height and length grow at the same speed. For lower density aggregates, $b < 3$ even when the area envelope grows at the same rate. As discussed by Westbrook et al. [108], the value of b for snowflakes is usually around 2.

For the simulations performed here, it is important to do as much as possible to try and match the atmospheric state at the time of the in-situ observations. Therefore, rather than employing relationships that are commonly used in the literature, mass-size relationships specific to this case are derived using the layer-averaged PSDs, along with the bulk IWC measured using the Nevzorov probe. Two different approaches were taken to derive the relationships. Firstly, it was assumed that the prefactor of the power law was fixed at a value of $a = 0.0257\,\mathrm{kgm}^{-b}$, and the exponent b was varied until good agreement was found with the measured bulk IWC data. This was done by integrating the relationships over the layer-averaged PSDs, and varying b until the resulting IWC is within 1% of the layer-averaged bulk IWC from the Nevzorov probe. The prefactor value used in this case is equivalent to that determined from observations by Cotton et al. [5]. Secondly, a different group of relationships was derived by fixing the exponent to be the average of the b values obtained in the first case, and the prefactor was varied accordingly. The resulting parameters are given in Table 6.1. As expected, $b \approx 2$ at the bottom of the cloud where large aggregate snowflakes are present.

The relationships were used to construct two sets of particles for this study, as described in section 6.4.2. Further experiments are performed to decide upon the most suitable

Layer	b (a=0.0257)	a (b=2.12)
1	2.30	0.0051
2	2.30	0.0051
3	2.21	0.012
4	2.04	0.048
5	2.025	0.051
6	2.0	0.060
7	2.007	0.050

Table 6.1: Values of a and b for the initial mass-size relationships of each of the 7 layers. The first column shows the values obtained by fixing a at $a = 0.0257\,\mathrm{kgm}^{-b}$, and varying the exponent b. The second column shows the values obtained by fixing b at $b = 2.12$, and varying the prefactor a.

mass-size relationships for this case, thereby allowing a final model to be fixed that can then be used for the radiative transfer simulations.

6.4.2 Particle generation

To decide on which particle habits to use, imagery from the CIP-100 cloud imaging probe is used. As mentioned previously, the probe measures particles between the sizes of 100 µm and 6200 µm. This means the CIP-100 images are more useful than those from CIP-15 for visually identifying particle shapes, since the CIP-15 probe measures smaller particles of 15 µm to 930 µm. Imagery at times when there was a peak in the Nevzorov measured IWC for each of the 7 profiles is examined, and examples from each cloud layer are shown in Fig. 6.7.

Mixtures of particle habits were present throughout the cloud, but visual inspection of the imagery led us to approximate the atmospheric model using 2 different particle types. We use columnar aggregates higher up in the cloud, between 9 km and 6 km, and dendritic aggregates lower in the cloud between 6 km and 2 km (i.e. P4-P7). Mixed-phase precipitation was present below 2 km, with a thin melting layer showing as a bright band in the radar reflectivities in Fig. 6.4. However, we do not represent melting particles here, and instead just assume a Marshall-Palmer distribution of rain beneath the ice cloud base. The distribution used here corresponds to a rain rate of $1 - 2$ mm/hr, estimated from the radar data shown in Fig. 6.1b.

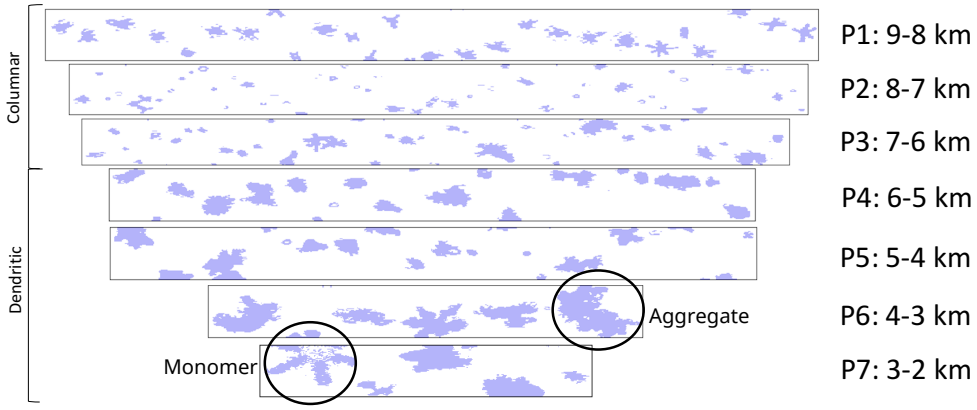

Figure 6.7: CIP-100 images from each of the 7 cloud layers profiled by the aircraft, at times of maximum IWC. The height of each frame is approximately 6.4 mm. Examples of individual monomers and aggregates are highlighted. We approximate the top 3 layers (P1-P3) as columnar aggregates, and the bottom 4 layers (P4-P7) as dendritic aggregates. The layer altitudes are given to the right of the particle imagery.

I generated particles to have masses that are specific to this case. For both sets of mass-size relationships, a range of columnar and dendritic aggregates were constructed using the particle aggregation model of Westbrook et al. [108]. Within the model, the monomer shape and size are specified at the outset, and realistic aggregates are generated via the mechanism of differential sedimentation. Those with masses that match the derived mass-size relationships to within within 20% were kept, storing a maximum of one particle per size bin. Otherwise the generated particles were discarded. As mentioned previously, we assume azimuthally random orientation for our simulations to match the assumptions made in RT4. The particles generated here have a random orientation, and hence it is necessary to re-orient them such that the largest dimension is positioned horizontally.

The particle size bins corresponding to the distribution suggest that the cloud contained particles up to approximately $D_{max} = 5.75$ mm. There are large uncertainties in the number concentrations of ice particles smaller than 100 µm, due to shattering [122]. Furthermore, Buehler et al. [123] show the sensitivity of various submillimeter channels to particles of different size. At the frequency of 243 GHz considered here, particles less than 100 µm do not influence the brightness temperatures. For particles larger than D_{max} =100 µm, I have attempted to generate a particle for the majority of the size

bins in each layer. However, this was not possible for every size bin and thus I have rebinned the measured PSDs to match the particle sizes that have been generated for this case study. The smallest particles were ignored by setting the concentrations of any measured particles below 100 µm to 0. The new bins use the generated particles to represent the bin centre, although their D_{max} values are not found exactly at the centre of the bin. The midpoints between successive particles represent the bin edges, resulting in bins of non-uniform width. The bin edges of the smallest and largest particles were calculated such that the bin is symmetrical about the first and last particles in the set, i.e. the D_{max} values of the first and last particles do lie at the central point of the bounding bins.

6.4.3 Testing the model

The 2 radar frequencies are useful for constraining the atmospheric model we are applying to the 243 GHz radiative transfer simulations, with regards to testing the in-situ derived mass-size relations in section 6.4 and the range of particles generated for each layer. The radar cross section, σ_r, of the generated particles is calculated at 95.04 GHz and 35 GHz using IMA. These calculations are used to simulate the above-cloud equivalent radar reflectivity, Z_e, in order to test the suitability of the generated particles for this case. The equation for Z_e is given by Atlas et al. [124]:

$$Z_e = 10^{18} C \int \sigma_r(D_{max}) n(D_{max}) dD_{max}, \tag{6.1}$$

where $C = \lambda^4/\pi^5 |(\epsilon_{liquid} - 1)/(\epsilon_{liquid} + 2)|^2$ is a frequency-dependent constant, and $n(D_{max})$ represents the in-situ distribution of particles. Without the factor of 10^{18}, Z_e would have units of m^3. Multiplication by 10^{18} converts the units of Z_e to conventional radar meteorology units of $mm^6 m^{-3}$. More information on the method can be found in Baran et al. [125].

Z_e was calculated using both sets of mass-size relationships derived in Table 6.1. Comparisons of the radar reflectivity simulations with the measured data allowed us to

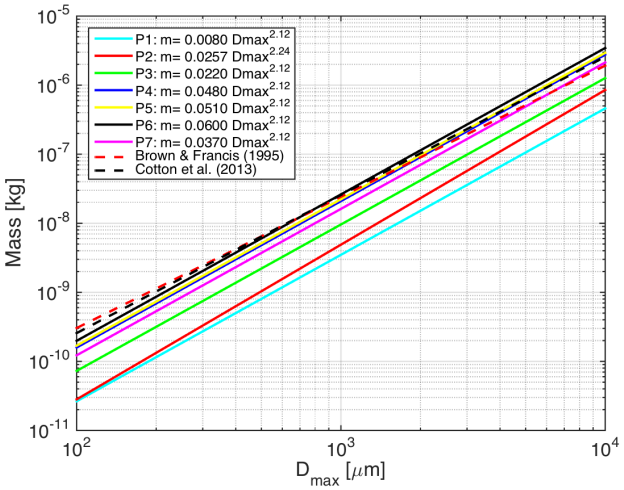

Figure 6.8: The final mass-size relationships used to model the particles for this study. Also plotted are relationships derived by Brown and Francis [4], and Cotton et al. [5].

decide on the most appropriate relationship for each layer, or alternatively iterate our model where necessary to obtain results closer to the measured reflectivities. This involved taking the variability of IWC in each layer into account by increasing or decreasing the layer averaged value by 1 standard deviation, and re-deriving mass-size relationships, along with generating new particles. The final number of aggregate realisations generated for each layer ranges from 46 to 62. The tweaked relationships mainly have $b = 2.12$ as derived in Table 6.1, except for in layer 2 where better results were found when a was fixed to 0.0257. The corresponding mass-size relationships, along with commonly used relationships of Brown and Francis [4], and Cotton et al. [5], are plotted in Fig. 6.8. The relationships derived for the lower layers of cloud are very consistent with the commonly used relationships of Brown and Francis and Cotton et al., while particles in the top layers of cloud have lower masses that would not be represented correctly by those relationships.

Fig. 6.9 shows the simulated reflectivities using the final modelled particles, with the measured reflectivities shown in red and the different coloured markers representing simulations performed using the particles generated for each of the 7 different cloud layers. Note that I performed the calculations of σ_r for the particles, but Fig. 6.9 was generated by Anthony Baran at the Met Office. Grey lines are plotted at the left side of the reflectivities, showing the estimated sensitivity of each of the radars. Below this noise level, signal is not detectable by the radar. The minimum detectable signal is

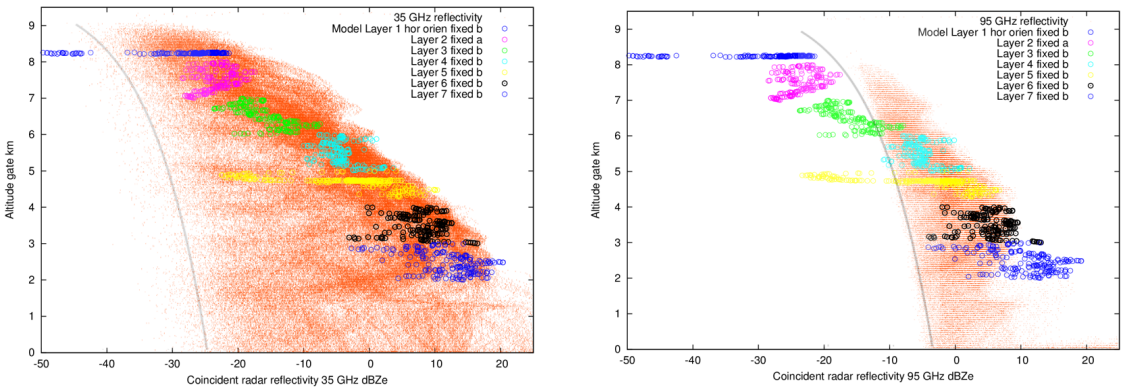

(a) 35 GHz (b) 95.04 GHz

Figure 6.9: Simulated reflectivities at 35 GHz and 95.04 GHz. The orange dots show the observed reflectivities from the HAMP and RASTA radars. The different coloured circles show the reflectivites calculated using the horizontally aligned particles generated to follow the mass-size relationships derived from measurements. Grey lines at the left edge of the reflectivities have been plotted to show the estimated noise level, below which no signal is detected.

calculated in dBZ as $10\log_{10}(r^2) + c$, where the range, r, is equivalent to the aircraft altitude minus height, and c is a constant. Simulations of the 35 GHz reflectivities in Fig. 6.9a are generally in good agreement with the measurements, with slight overestimations in bottom layer. Given by the location of the noise-level line, simulations that may initially appear as underestimations in the top layer are likely to be below the minimum detectable signal. In the case of the 95.04 GHz simulations in Fig. 6.9b, the low sensitivity of the radar means there is a very clear line in the measurements below which no signal is picked up. Moreover, considerably fewer reflectivity observation data points appear in the higher frequency case than in the lower frequency case. In layer 7, more pronounced overestimations in the reflectivities are simulated at 95.04 GHz, along with slight overestimations in layer 6. However, overall the models fit with the observations and thus these particles are used to simulate the V and H polarisation measurements from ISMAR.

6.5 Simulation of the ISMAR polarised brightness temperatures at 243 GHz

A range of particles have been generated for each of the 7 model layers to follow the in-situ measurements as closely as possible. However, prior to considering the full polydispersive distribution within each layer, two simplified cases are examined. Firstly, a single-layer cloud is modelled in order to explore the general behaviour of brightness temperatures at 243 GHz with variations in cloud IWP. Then a 7-layer cloud is constructed, but with a monodispersive distribution of particles within each layer. These cases are useful for obtaining a broad understanding of the impact of ice on retrievals. Moreover, they are useful to test different model assumptions, such as the number of streams required, along with providing the opportunity to check that the IMA scattering method gives reasonable results.

6.5.1 Single-layer, monodispersive distribution

To explore how brightness temperatures vary with IWP, a highly simplified single-layer cloud is modelled. One particle is used to represent all the cloud ice, using a monodispersive distribution between 2 km and 9 km in altitude. This involves calculating the relevant scattering properties of the particle and implementing them into ARTS, along with a corresponding number concentration to represent the density of particles. Increasing the number concentration corresponds to a higher IWP within the cloud. Fig. 6.10 shows the results for different values of IWP up to $400\,\mathrm{g\,m^{-2}}$, which is close to the value measured in this case study. The brightness temperatures are simulated using a single dendritic particle, and also using an aggregate of two dendritic monomers. Note that particle size would have important effects on the results but this has not been considered here. Thus we cannot make direct comparisons between the results of the two cases. Nevertheless, we can get a basic idea of the effect of IWP on brightness temperatures.

The brightness temperatures at H and V polarisation are seen in Fig. 6.10a, along

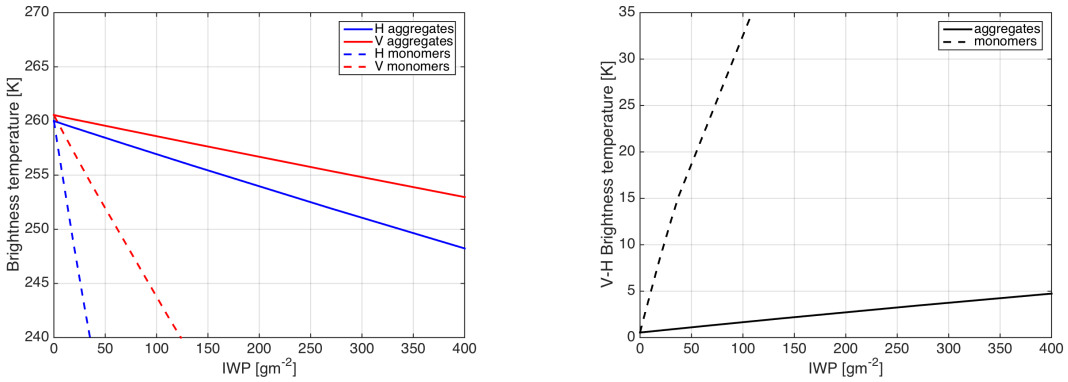

(a) Brightness temperature (b) V-H brightness temperature difference

Figure 6.10: Simulations using a single-layer cloud: Brightness temperatures at H and V polarisation simulated for different values of IWP, and the V-H brightness temperature difference. The solid lines show the results using an aggregate of two dendritic monomers, and the dashed lines show the results using a single dendritic monomer.

with the V-H brightness temperature difference in Fig. 6.10b. As described previously, a Marshall-Palmer distribution of rain is also included in the simulation between the ground and the cloud base at 2 km. Thus the value at an IWP of 0 g m^{-2} corresponds to a simulation where only rain is included. As IWP is increased, an enhanced brightness temperature depression is simulated by both particles. However, it is clear that the choice of particle hugely affects the results. A considerably larger depression and polarisation signal is simulated using the single particle than with the aggregate of two monomers. Moreover, using the single particle results in the presence of a large signal even at very low values of IWP, with the V-H brightness temperature difference reaching almost 35 K at an IWP of 100 g m^{-2}. Using the aggregate with the same IWP only results in a V-H difference of 2 K. The simulated values for the single dendrite are much larger than what was measured by ISMAR. This is unsurprising as a cloud composed of only horizontally oriented single particles is unrealistic. Nonetheless, it is interesting to note the large polarisation signature that occurs due to horizontally aligned crystals.

6.5.2 Multi-layer, monodispersive distribution

The model cloud is divided into 7 layers, with a monodispersive distribution of particles within each layer. For this setup, the measured layer averaged D_{max} is used along with

the derived mass size relationships to obtain an average mass for each layer, and one particle is generated for each layer to match that mass. Each of the model layers are given an appropriate number density using the layer averaged IWC. The single-scattering properties of the particles are incorporated into ARTS, along with their number densities.

Fig. 6.11a shows the individual brightness temperatures at H and V polarisation for each of the scenarios considered. The points along the abscissa represent the gradual increase in cloud layers used in the simulation, starting with the clear-sky case. Then a Marshall-Palmer distribution of rain is inserted between the ground and the cloud base at 2 km. This rain distribution is included in all further simulations presented here. The third point along the x-axis displays the result when the top layer of ice cloud is included, along with the rain distribution. Then the second layer of ice is added, and so on until the full 7 layers of cloud ice along with a distribution of rain below the cloud base are included. The plot is done in this way to mimic the increasing depressions measured by ISMAR as the aircraft flew over the cloud, as in Fig. 6.3a.

Fig. 6.11b shows the same results for the cases considered in Fig. 6.11a, but here the values are plotted as V-H brightness temperature differences. The red crosses show the values measured from ISMAR, and the simulations of the various scenarios are displayed using different markers. The clear-sky polarisation result of approximately 2 K is shown by the magenta circle, arising from differences in surface emissivity. The yellow circle shows the V-H temperatures simulated when rain is included, resulting in a decreased V-H compared to the clear-sky case, with a value of only 0.5 K. The V-H results when monodispersive layers of ice are included are shown by the cyan markers. Two different marker shapes are used to represent the gradual increase in the number of layers used in the simulation. The cyan triangles show the results obtained using partial cloud amounts. In other words, the points labelled "Rain + Layer 1" to "Rain + L(1-6)" along the abscissa in Fig. 6.11a. The cyan star shows the final result using all 7 of the model layers, i.e. "Rain + all layers" in Fig. 6.11a.

Note that the yellow circle is positioned at $TB_V \approx 261$ K but is overlapped by other

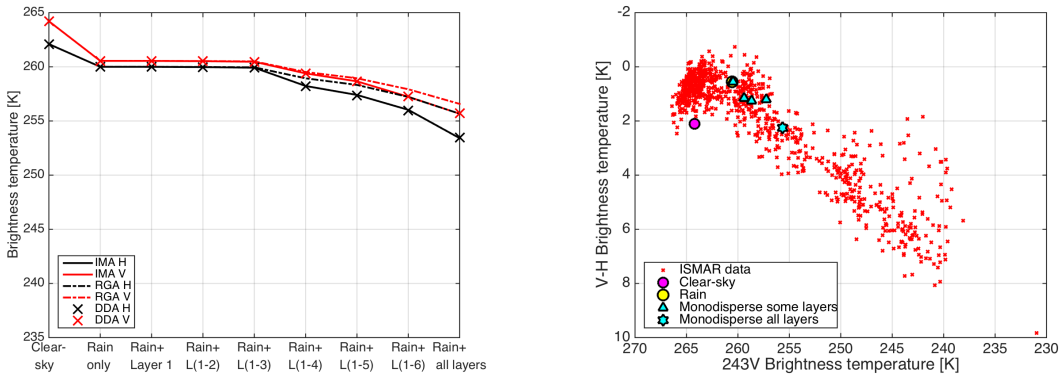

(a) Brightness temperature

(b) V-H brightness temperature difference

Figure 6.11: Results for the monodispersive case. The left panel shows TB_V and TB_H, calculated using IMA, RGA, and DDA. The points along the abscissa start with results for the clear-sky case, and each consecutive point shows results obtained by adding one more layer of cloud to the simulation. This is described fully in the main text. The right panel shows the results using IMA, plotted as V-H differences.

results. It can be seen clearly in Fig. 6.11a that three of the simulations for the monodispersive case give the same results- using only layer 1, using layers 1 and 2, and using layers 1, 2, 3. The values are also the same as the case when only the rain is included. Thus the markers corresponding to these 4 cases overlap in Fig. 6.11b. This shows that the top 3 layers of columnar aggregates do not significantly affect the brightness temperature simulations in the monodispersive case. The inclusion of layers 4-6 causes an increase in both the brightness temperature depression and the V-H difference. When layer 7 is included, V-H increases further by approximately 1 K. However, the value remains quite small at only 2.25 K, while the largest measured value from ISMAR was close to 10 K. Nonetheless, the monodispersive test case produces reasonable results that fit some of the ISMAR measurements.

It is seen in Fig. 6.11a that each of the simulations was performed using three different scattering methods to obtain the single-scattering properties. The three methods are: our new Independent Monomer Approximation (IMA), the Rayleigh-Gans Approximation (RGA), and the Discrete Dipole Approximation (DDA). The brightness temperatures simulated using DDA are within 0.05 K of the IMA results, while RGA fails to produce an equivalent depression, differing from the DDA results by up to 2.2 K. With RGA the brightness temperature depressions would be much smaller than the more accurate IMA technique, thereby resulting in erroneous retrievals. Thus we

are confident that the IMA method is sufficiently accurate to be applied to this study. The results of the polydispersive case using the IMA scattering method are presented in the next section.

6.5.3 Multi-layer, polydispersive distribution

In this section, simulations are performed using the measured PSDs and the full range of generated particle models described in section 6.4.2. As outlined above, the measured PSDs are rebinned to match the particle sizes that have been generated for this case study. The rebinned PSDs for each of the 7 layers can be seen in Fig. 6.12, with each cross representing one of the generated particles. The single-scattering properties of each of the particles are calculated using IMA, and are incorporated into ARTS along with the rebinned PSDs.

The results for the polydispersive case are shown in Fig. 6.13. In an equivalent manner to the monodispersive case, simulations are performed by adding one layer of cloud at a time, until the full model cloud is included. The individual H and V brightness temperatures are displayed in Fig. 6.13a. Similar to what was found for the monodispersive case, the top 3 layers of cloud have very little effect on the brightness temperatures. As additional model layers are included in the simulation, the brightness temperatures become more depressed at both H and V. Comparisons of Fig. 6.11a and Fig. 6.13a show that using a polydispersive distribution of particles results in greater brightness temperature depressions than the monodispersive case, and these are closer to what was measured from ISMAR. TB_V and TB_H are depressed to values below 240 K, whereas less significant depressions of approximately 255 K are simulated using the monodispersive distribution. Note that the equivalent calculations are also performed using RGA, with the results shown by the dash-dot lines in Fig. 6.13a. It is clear that the RGA scattering method underestimates brightness temperature depressions that can be simulated using IMA, by up to 9.6 K.

The V-H brightness temperature differences are shown in Fig. 6.13b. Results adding layers of ice cloud as before are shown using blue triangles, with the result using the

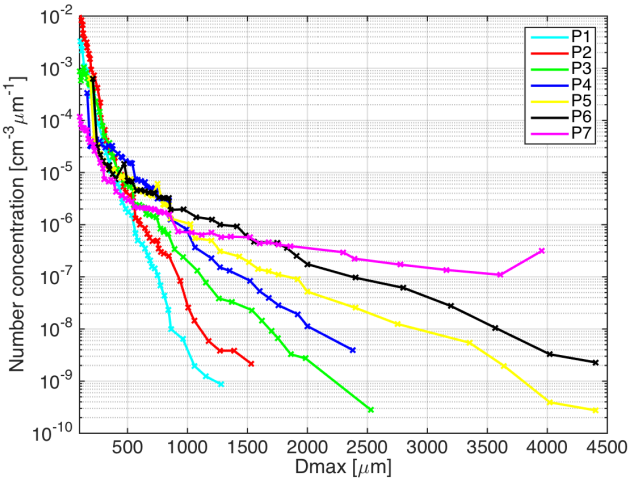

Figure 6.12: PSD number concentrations rebinned to match the particles generated for this case study.

full 7-layer cloud depicted by the blue star. The lowest blue triangle shows the result calculated using the top 6 layers of ice cloud, along with the rain distribution below 2 km. It is interesting to note that when layer 7 is included (blue star), the brightness temperature depression increases further but the polarisation signal decreases. When all 7 layers of cloud are used in the polydispersive simulations, the polarimetric V-H brightness temperature difference has a small value of slightly less than 2 K. This decrease in polarisation signal could be caused by the inclusion of too many large, lower density particles in the bottom layer of cloud, which have a weak polarisation dependence. The particle habit used in that layer of our model may not adequately represent the real cloud. Alternatively, these results may suggest that the sizes of the largest ice crystals were overestimated by the probes.

It is interesting to consider alternative reasons why the simulated polarimetric signal is not as great as that measured by ISMAR, and explore ways in which it could be increased to match the observations. One potential reason could be that there was a change in microphysics between the times of the ISMAR measurements which were made at 10-10:20 UTC and the in-situ cloud measurements taken between 10:37 and 11 UTC. Another possibility could be that we haven't taken the melting layer into account. Looking at the radar reflectivities in Fig. 6.9, the melting layer appears quite thin with a brightband depth of approximately $100 - 200$ m. Nonetheless, the melting layer has a significant polarisation signature in radar, so it is possible that neglecting

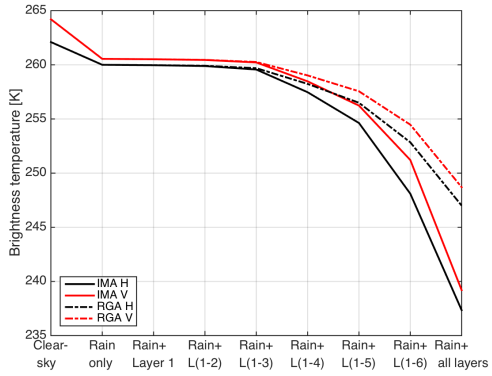

(a) Brightness temperature

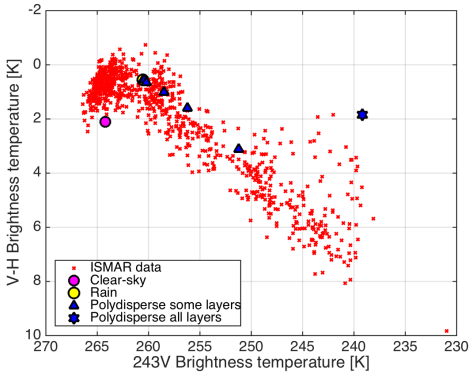

(b) V-H brightness temperature difference

Figure 6.13: As in Fig. 6.11, but for the polydispersive case.

to include it in our simulations is causing V-H to be too small.

Gong and Wu [115] showed that the V-H differences can be increased by increasing the mean size of the PSD, and by changing the particle habit or aspect ratio. Therefore, we investigate these points in the following sections. It is worth noting that a further way of increasing the polarimetric difference would be to consider habit mixture models, such as by Miao et al. [126] . Using aggregates of differing monomer shapes in our simulations may increase the V-H differences, but this is beyond the scope of the present study.

6.5.4 Changing properties of the PSD

The first method we employ in order to try and enhance the polarimetric signal is increasing the mean size of the PSD. In order to do that in a systematic way, we do the following: Using the measured PSD for each layer, D_{max} is plotted against $\ln(N)$, and straight lines are fit to the distribution. This means a parameterised exponential size distribution $N(D_{max}) = N_0 \exp(-\lambda D_{max})$ is obtained for each layer. The intercept and slope parameters, N_0 and λ, can now be tweaked in order to try and match the ISMAR measurements. For consistency with the original setup, the parameterised PSDs have been truncated using the lower and upper limits of the measured PSDs. The measured and parameterised PSDs for each layer are plotted in Fig. 6.14a. The fitted exponential PSDs are imperfect, and tend to underestimate concentrations of particles less than

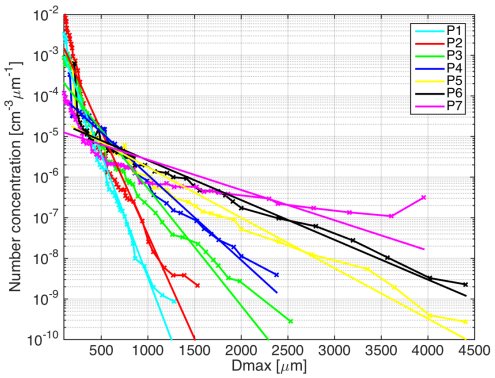

(a) Exponential fits to the PSDs

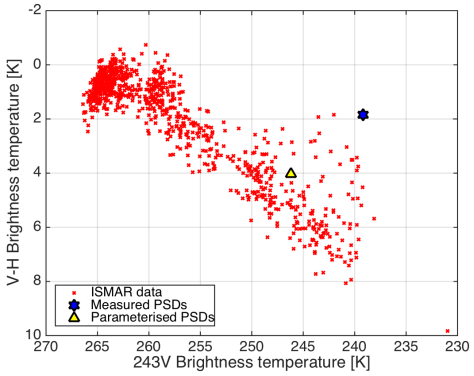

(b) V-H using parameterised PSDs and measured PSDs

Figure 6.14: (a) The lines with crosses show the rebinned measured PSDs in each of the model layers, as in Fig. 6.12, and the straight lines show the fitted exponential PSDs. (b) The blue star shows the V-H brightness temperature difference calculated using the measured PSDs, and the yellow triangle shows the result using the exponential fits.

approximately 200 µm, and also underestimate concentrations of the largest particles of the distribution, while overestimating particles of an intermediate size. However, they should be adequate for the idealised experiment that follows.

First of all, the brightness temperatures are calculated using the parameterised exponential PSDs for each layer. The result is displayed in Fig. 6.14b. It is interesting to note that this gives a V-H brightness temperature difference of 4 K that matches the ISMAR measurements more closely than the original experiment with the measured PSDs. The yellow triangle in Fig. 6.14b shows that the V-H value falls quite centrally within the ISMAR measurements. The blue star depicts the polydispersive case which gives a smaller V-H value slightly below 2K. The simulated value does not lie within the main bulk of the ISMAR measurements. In the previous section, we speculated that there were too many large particles at the cloud base that were diminishing the polarisation difference. Thus the increase in V-H as a result of using the parameterised PSDs may be due to the fact that these fits estimate fewer of the largest particles within each layer. Moreover, although fewer large particles are considered when using the parameterised fits, the fits still result an increase of the mean particle size within each layer, before any changes are made to N_0 or λ. As mentioned previously, an increased mean particle size is one possible mechanism that may increase the polarimetric signal. Therefore the larger V-H values may be a result of the increased mean

particle size.

In order to further increase the mean size of the PSD, adjustments are made to either N_0 or λ of one layer at a time. Changing N_0 alone will not achieve the goal of increasing the mean size. Thus it may be expected that the main polarimetric differences will be found by decreasing λ. However, a reduction in the number of large particles may be achieved by decreasing N_0, so it is worthwhile experimenting with changing both parameters to see if any increase to the polarimetric signal can be simulated.

6.5.4.1 Changing λ

Values of λ in each cloud layer are varied, changing only one layer at any time. λ is divided by a range of values, chosen experimentally to explore whether greater polarimetric signatures can be simulated. An example of the resulting fits for layer 3 can be seen in Fig. 6.15a. In layer 3, λ is divided by values between 1.2 and 2.1. However, it is noted that different values between 1.1 and 3.5 are used for other layers. The figure shows that changing λ in such a way increases the number of larger particles in the distribution, whilst having less of an effect of the number of smaller particles. This results in an increased mean particle size. The fits for the remaining layers have not been plotted, but possess similar properties resulting in increasing the mean size of the distribution.

The V-H brightness temperature differences obtained by varying λ in each layer individually are calculated, and the results are shown in Fig. 6.15b. It can be seen that increased V-H values may be simulated by changing λ in layers 1-6. However, changing λ in layer 7 increases the depression but does not increase the polarimetric difference. This is unsurprising as in section 6.5.3 we proposed that the V-H signal was diminished due to the presence of too many large particles in that layer. Therefore, increasing the mean size will not be beneficial in the bottom layer. The most notable results come from varying λ in the top 3 cloud layers. It is possible to simulate brightness temperatures close to the ISMAR measurements by using the successive decreases in λ, such as those outlined in Fig. 6.15a, resulting in gradual increases to the V-H values. In

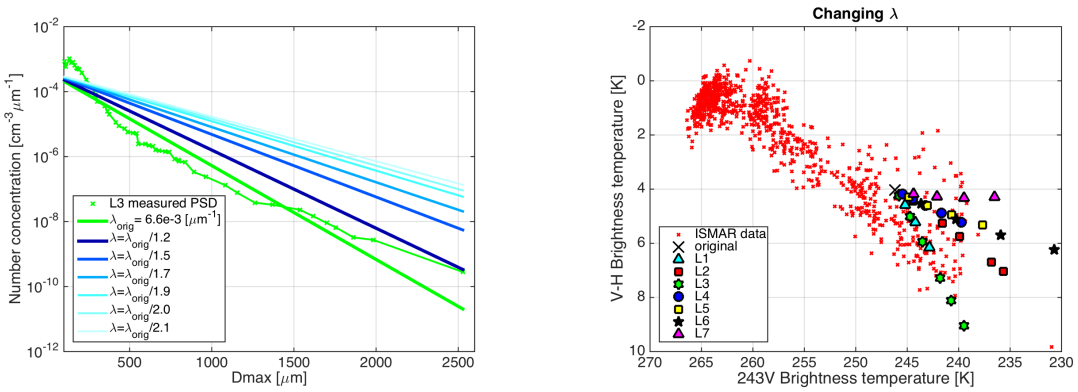

(a) Fits resulting from changing λ in layer 3 (b) V-H brightness temperature difference

Figure 6.15: An example of the changes made to the PSD by varying λ, in this case for layer 3. (b) shows the V-H results obtained for the variations in each layer.

the case of layer 3, a small increase to V-H is simulated by dividing λ by 1.2, while division by 2.1 gives a large V-H of approximately 9 K. The simulated V-H brightness temperatures fit the ISMAR results nicely. In terms of the mean size of the PSD, using the parameterised fit in that layer results in an increase from 175 µm to approximately 244 µm before making any changes to λ. The successive decreases in λ then result in further increases to the mean size, from 274 µm when λ is divided by the smallest value of 1.2, to 409 µm at the largest deviation of λ. The results from this experiment are in agreement with Ref. [115], showing that increasing the mean particle size of a distribution may increase the simulated polarimetric signal, provided that absorption by large particles does not dominate.

However, the important point to stress is that the changes made to λ in order to simulate these realistic values generally result in parameterised PSDs that do not fall within a reasonable deviation of the measured PSDs. As already mentioned, varying λ in the top 3 layers gives the most interesting results as the V-H differences tend to follow the ISMAR measurements. However, the fits applied to these layers employ large changes to λ, and as a result the parameterised PSDs deviate widely from the measurements. Of all the fits used for the three top layers, only the smallest V-H temperature simulated for layer 3 falls completely within four standard deviations of the measured PSDs. Furthermore, employing the largest deviation of λ in layer 3 means that the IWP of the layer is increased from 21 g m^{-2} to 216 g m^{-2}, which is almost half of the measured total IWP! The fits in the bottom four layers employ less

drastic changes to λ, resulting in two of the fits in layers 4 and 5, and three of the fits in layer 6 falling within four standard deviations of the measured PSDs. However, simulations of the largest V-H differences require values of TB_V to be depressed to lower values than those measured from ISMAR. Less significant polarimetric differences are simulated while remaining within a realistic brightness temperature depression. Thus, although it is interesting that realistic brightness temperature values can be simulated by changing layers 1-3, it is not useful in this case as the setup required to do so does not agree with the in-situ measurements.

6.5.4.2 Changing N_0

We now explore what happens to the V-H brightness temperature differences when N_0 is varied in the parameterised exponential PSDs. Initially, values of N_0 were decreased such that the number of large particles in the distribution would be reduced. Decreasing N_0 in the top three layers made no difference to the polarimetric signal. Interestingly, decreasing N_0 in the bottom layers resulted in a lower V-H brightness temperature difference than using the original PSD. Therefore, N_0 is increased in this section to see if the polarimetric differences are affected.

As in the case of changing λ, only the fits resulting from changing N_0 in layer 3 are shown. The fits are displayed in Fig. 6.16a. The brightness temperatures simulated by increasing N_0 in each of the seven layers are shown in Fig. 6.16b. No changes to the results are found by increasing N_0 in layers 1 and 2. Thus the results for these cases overlap the black cross showing the original result. Increasing N_0 in layers 3-7 results in enhanced V-H differences, with layer 3 showing the most significant differences. However, the main bulk of the largest V-H values measured by ISMAR fall between approximately TB_V =240 K and 245 K. The largest V-H values of approximately 8K measured within this range generally cannot be simulated without also simulating a depression that is too large. There is one single point found at approximately T_V =231 K with the largest measured V-H value of almost 10 K. A result close to this can be simulated by changing N_0 in layer 3. However, as in the case of

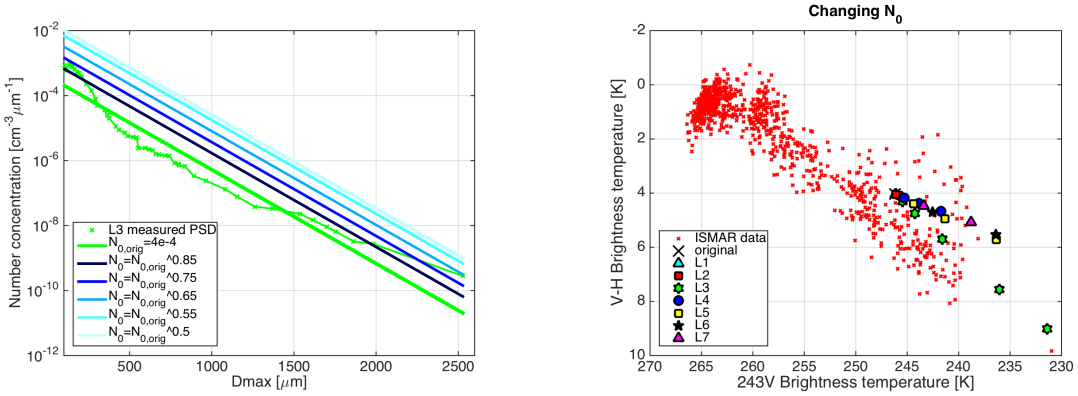

(a) Fits resulting from changing N_0 in layer 3 (b) V-H brightness temperature difference

Figure 6.16: Changes made to the PSD by varying N_0 in layer 3, along with the V-H results obtained using variations in each layer.

changing λ, the parameterised PSDs used for those simulations deviate widely from the in-situ measurements. None of the parameterised fits used for layer 3 fall completely within four standard deviations of the measured PSDs. Thus it is necessary to consider other potential reasons why the largest V-H brightness temperature differences were not simulated using the original model.

6.5.5 Changing particle habit

The second potential reason for the small polarimetric signal in the original simulations is that aggregates are not responsible for the V-H brightness temperature difference observed from ISMAR. Up until this point, monomers have not been included in our model atmosphere, and we saw in Fig. 6.10b that single dendrites have stronger polarimetric signals than aggregates. To test this hypothesis, horizontally aligned dendrites are added to the cloud base. There is evidence from the imagery in Fig. 6.7 that such particles were present at the time of interest. It is worth pointing out that since we are using single particles, the scattering calculations for these additional dendrites are done using DDA rather than IMA, as the IMA method is only applicable to aggregates.

A monodispersive distribution of horizontally aligned single dendrites is used to replace the aggregates in the lowest portion of the cloud. The dendrites have a size of approximately D_{max} =1 mm. The number concentration is chosen in such a way that the measured IWC over the 1 km-deep layer is maintained. Different heights of the

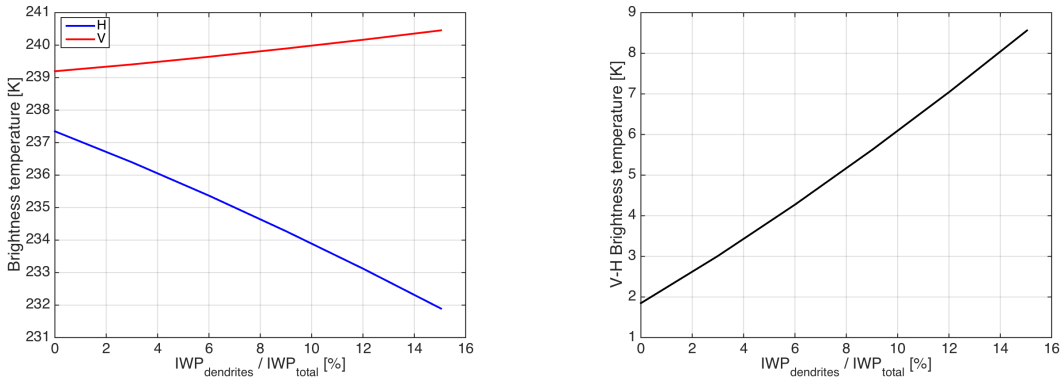

(a) TB_H and TB_V (b) V-H brightness temperature difference

Figure 6.17: Brightness temperatures at V (red line) and H (blue line) polarisations, and the difference between them (V-H). Along the abscissa, the percentage of the total IWP comprising single dendrites increases.

cloud layer are replaced by dendrites, starting with the bottom 100 m, and increasing the height by 100 m at a time, until finally the lowest 500 m of cloud is replaced with dendrites. These values correspond to dendrites comprising 3 to 15% of the total IWP. The brightness temperatures at H and V polarisations and the V-H difference for the different IWP percentages are shown in Fig. 6.17.

Fig. 6.18 shows the V-H brightness temperature differences plotted along with the values measured from ISMAR. The results from the monodispersive and polydispersive cases in sections 6.5.2 and 6.5.3 are plotted for reference in Fig. 6.18a. The V-H differences using different amounts of dendrites are plotted in Fig. 6.18b. The blue star shows the original result before the inclusion of dendrites. The square closest to the star is the result when 100 m is replaced with dendrites, and the lowest square shows the result obtained when half of the bottom layer (i.e. the lowest 500 m of cloud) is replaced. Even when no dendrites are included, the largest brightness temperature depression is captured. However, adding dendrites increases the polarisation difference, with each extra 100 m increasing V-H by approximately 1 K, while TB_V remains almost constant. A V-H value of 8.4 K is obtained when the lowest 500 m of the model cloud is replaced with single dendrites, which is very consistent with ISMAR measurements. Thus, agreement with observations is possible by including a small IWP of oriented ice crystals in the simulation.

Although the measured brightness temperature depressions can generally be repro-

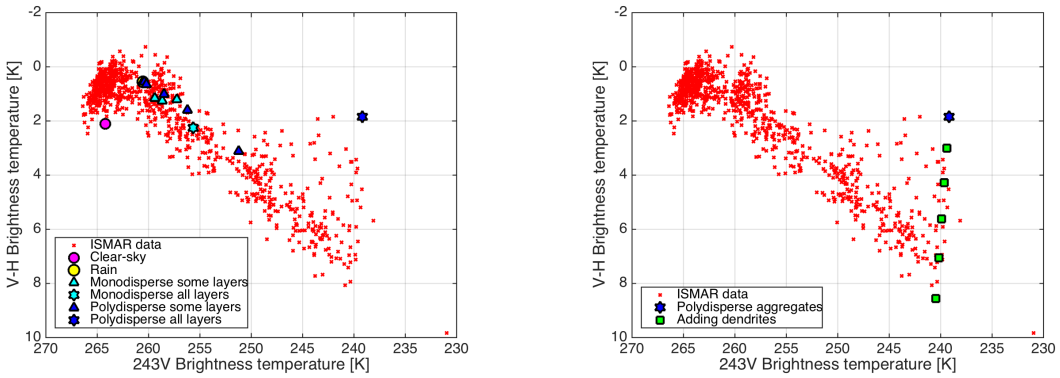

(a) Monodispersive and polydispersive results. (b) V-H when dendrites are included.

Figure 6.18: The red crosses show the measured V-H from ISMAR. Panel (a) shows scenarios considered in Figs. 6.11 and 6.13 when no dendrites are included. In panel (b), the green squares show the values simulated when the aggregates in the lowest region of cloud are replaced with horizontally aligned single dendrites. The different squares show results obtained when the amount of cloud comprising dendrites is gradually increased, as described in the text. V-H increases with increased IWP fraction.

duced using the IMA scattering method, the polarisation difference is very sensitive to the assumed particle shape for a given ice water path, specifically the presence of single crystals mixed with aggregates. Thus it is possible that these large polarimetric signals cannot be simulated using aggregates alone. Therefore, to obtain good retrievals from ICI, it is important to represent the cloud as accurately as possible. Utilising the multi-frequency polarisation information available from the instrument could provide a way to constrain this, thereby reducing the need to make unrealistic assumptions.

Chapter 7

Concluding remarks

7.1 Discussion

The research in this thesis involved analysing the internal electric fields of ice particles in order to develop new scattering approximations, one of which was applied to a case study. The results have been presented in chapters 3 to 6.

In chapter 3, the DDA numerical method was used to investigate the internal fields and scattering properties of ice particles, presenting results for size parameters of $x = 0.01$ where the particle is in the Rayleigh regime, along with larger size parameters of $x = 2$ and $x = 10$.

Exploring the magnitude of the internal electric field for different monocrystals, it was found that the field varies greatly with size parameter. For $x = 0.01$, the field is almost uniform, with a factor of 1.15 between the average and maximum field values of the hexagonal plate. The magnitude of the field is small, with an average of approximately 1.4 times the value obtained as a result of the applied wave only. For $x = 2$ the magnitude is also small with a relatively uniform field, ranging from an average of approximately 1.02 for the hexagonal prism, to approximately 1.13 for the cylindrical disk. Increasing x results in a more complex internal field with larger maximum values. Strong focussing is observed at the forward side of the monocrystals for $x = 10$. The

focussing behaviour is persistent for different orientations in the x-y plane, and occurs independently of whether the incident wave hits a flat prism facet or a sharp edge. Focussing remains when the incident wave is directed at small angles in the y-z plane, but the behaviour starts to diminish for larger angles. Such angles correspond to cases where the incident wave is approximately travelling in the direction of a basal face, rather than hitting a prism face or edge. The diminished focussing is a result of the small thickness of the plate in the direction of travel of the incident wave, as strong focussing is found when the same angles are used along with the thicker hexagonal prism of aspect ratio 1. For the single hexagonal plate, the internal field structure is a combination of 2 distinct waves. The perpendicular component of the field, P_x, takes the form of a wave extending through the centre of the particle, and the parallel component, P_y, has a structure resembling a standing wave around the perimeter.

Mitchell and co-workers developed the Modified Anomalous Diffraction Approximation ("MADA"), for the efficient prediction of the extinction of radiation by water droplets [127] and ice crystals [128] at size parameters $x \approx$ 10-1000. In addition to its speed, an attractive feature of the MADA is that physical wave scattering phenomena are explicitly represented as separate terms, and this can provide insight into their roles in the scattering process. Our results provide new data on these scattering phenomena for hexagonal ice crystals (specifically the existence and characteristics of internally-reflected surface waves and waves extending through the particle), and thus may be informative for further development and theoretical underpinning of the MADA approach.

A simple aggregate of 2 hexagonal plates sees a similar uniformity of the internal field for $x = 0.01$ and $x = 2$. However, a dramatic decrease in focussing behaviour and symmetry was found for $x = 10$, along with an overall smoothing of the field. This was even more obvious for a chain-like aggregate of 5 plates. It was found that this behaviour is partly controlled by the alignment of the plates, and the focussing patterns vary depending on the arrangement of the individual monocrystals. For example, if multiple plates are aligned such that there is a longer path length in the incident direction, there will be more enhanced coupling and a larger field magnitude at the

forward side of the particle, compared to when the plates are arranged more irregularly with respect to the incident direction.

As the complexity of the particle is increased further, the internal field continues to lose more structure, and no regions of enhanced coupling are obvious for the fluffy aggregate of 10 dendrites. The maximum value of electric field decreases significantly for aggregated dendrites, with the single hexagonal plate displaying a maximum magnitude approximately 3 times larger than the irregular aggregates for $x = 10$. Different values of x give very similar internal fields for the complex aggregate, with almost identical average and maximum values for $x = 0.01$ and $x = 2$, and slightly larger values for $x = 10$. An interesting observation is that the individual dendrites comprising the aggregate act somewhat independently of each other, as seen by calculating the field of the monocrystals in isolation from the rest of the particle. This could have important consequences for scattering calculations, suggesting that calculations for large aggregates could be done without the need for huge computer resources. Individual crystals could be solved independently and then combined to obtain approximations for complex particles.

To explore the performance of currently used approximations, the Maxwell-Garnett formula was employed to calculate the internal field of spherical or spheroidal particles of equivalent size to the different aggregates in this study. It was found that the reduced permittivity used in this method leads to the loss of internal field structure. The effective medium approximation causes the average field to be overestimated for all particles, and the maximum value to be underestimated in most cases.

The effect of the internal electric field on far-field scattering was also examined by calculating the differential scattering cross section for a number of particles in this study. For $x = 0.01$, the particles scatter equally in the forward and backward directions, and can be represented fully using only the component of the field which is perpendicular to the direction of propagation. As size parameter is increased, the amount of scattering observed becomes very dependent on scattering angle. For both single orientation and orientationally averaged cases, it was found that the component perpendicular to the

direction of propagation contributes mainly to scattering in the forward and backward directions. For size parameters of $x = 2$ and $x = 10$, a field component in the direction of propagation emerges, and this parallel component contributes to sidescatter. It is evident that for $x = 10$, the influence of the latter component is getting weaker as particle complexity is increased. The polar plot for the irregular aggregate displays very few angles where $P_{\parallel}$ dominates the total scattering. We saw for the hexagonal plate that it is the standing wave around the perimeter that leads to sidescatter. For irregular aggregates of "fernlike" dendrites, it appears that their fluffy structure is incapable of supporting such a standing wave. This may be why we see a decrease in the contribution from $P_{\parallel}$ to the total scattering.

Approximations of dendritic aggregates using Maxwell-Garnett soft spheres was explored. As discussed, this method leads to an internal field that is more uniform than the true field. In the far-field, underestimations of scattering properties were found. The far field results were also calculated using RGA, showing more accurate results than the soft sphere, but with errors persisting at some angles for $x = 10$, predominantly in the backward hemisphere.

In chapter 4, the use of a scattering-order formulation (SOF) of the DDA was explored. The method has the potential to reduce the large memory requirements associated with solving the DDA linear system, but is known to have convergence issues when coupling between the dipoles is strong. Computations of the internal field and far-field scattering properties were performed, and comparisons were done with DDA results. This was done for the hexagonal plate monomer, and also for aggregates of plates, columns, and dendrites. For each of the different habits, particles comprising 3, 5, and 7 monomers were generated. Values of x up to 10 were used.

It was found that the SOF method converges for a solid ice plate of size parameter $x < 4.5$, diverging for $x \geq 4.5$. For the aggregates, only $x = 2$ and $x = 10$ were explored. Overall, aggregates of dendrites showed good results with the method, converging in all cases examined. Aggregates of plates and columns showed convergent scattering calculations for $x = 2$ but did not show promising results for $x = 10$. When 3 or 5

monomers of plates or columns were used, none of the aggregates converged. Increasing the number of monomers resulted in improved convergence, with some of the aggregates of 7 monomers showing convergent behaviour for the backscatter cross section.

Three of the aggregates were chosen and used to examine the internal fields, including one aggregate of 7 dendrites and two aggregates of 7 plates. The two aggregates of plates were chosen as they had different backscatter behaviour, with one showing convergent results and the other showing divergence.

As discussed above, in most aggregated particles, increasing the number of monomers tends to result in the field losing the clear wave-like structure that is found in single monomers such as the hexagonal plate. Irregular arrangements make constructive interference less likely, and the fields tend to have lower magnitudes, which are easier to represent using SOF. This is why increasing the number of monomers improves convergence for the aggregates considered. Aggregates of dendritic monomers also experience weaker interactions and less coupling between monomers, resulting in lower magnitudes which can be represented accurately using SOF. Consequently, accurate far-field scattering solutions are obtained for these particles.

However, divergent behaviour is still found in some cases, which is why two different aggregates of plates were considered. As expected, it was found that divergence in the far-field scattering solution is caused when the internal field magnitude is overestimated by SOF. The aggregate of plates with the divergent far-field solution has strong interactions leading to a larger internal field magnitude than the other particles examined. As discussed above, enhanced coupling occurs when the monomers are aligned in the plane of the propagation direction of the incident wave, rather than in a more irregular alignment. SOF struggles to represent these regions of strong coupling, overestimating the field magnitudes. As a result the backscatter solution diverges with increased iterations.

Due to the convergence issues with SOF, variations of the method have been employed in the past which incorporate a relaxation parameter in an attempt to prevent divergence. In this thesis we investigated different choices of the parameter, η, to see

whether an optimal choice could be found for ice particles. Since a value of $\eta = 0.5$ has been employed in previous literature [77], we began by testing similar values of $0.1 \leq \eta < 1$, where $\eta = 1$ corresponds to SOF.

For the hexagonal plate of $x = 10$, none of the values chosen led to convergence. For the dendritic aggregate, convergence was found for all values of η. For the two aggregates of plates, the overall bias in scattering calculations decreased when many of the values of $\eta < 1$ were used, compared to the SOF case, but results oscillated around the DDA solution rather than truly converging.

An alternative approach was taken to calculate η, using a method employed by Kleinman et al. [2] to solve a Helmholtz problem. The parameter, which we call η_{Kl}, is chosen to minimise the residual error at the first iteration, and it may have a complex value. It was found that η_{Kl} does not provide good results for the hexagonal plate, overestimating the field around the particle edge, even in cases such as $x = 4$ when SOF gave good results. In the future we plan to explore this further to find out why the field is overestimated around the edge of the plate. The far-field results diverge for all values of $2 \leq x \leq 10$. However, the η_{Kl} relaxation parameter greatly improved convergence for the aggregates of 7 plates. Convergence was achieved for 9 of the 10 particles tested, but the parameter led to instability in one case. In that case the internal field magnitude was hugely overestimated, with a relative error over 3000%. It is unclear why the instability occurred. We plan to explore this further by looking at aggregates of columns, and also aggregates comprising different numbers of monomers. It is possible that although this is not a good method for single monomers, η_{Kl} may generally be useful for scattering calculations of aggregates, provided the instability is not a recurring issue. It would be interesting to explore convergence by looking at how the spectral radius changes with particle shape and size parameter.

Using ideas from the findings in chapter 3, a new scattering method specifically for aggregates called the Independent Monomer Approximation (IMA) was developed and tested in chapter 5. The method involves doing DDA calculations within monomers, while ignoring interactions between different monomers of an aggregate. This allows for

both time and memory improvements when compared to DDA. We set out to explore how the accuracy of the method changes as different parameters are tweaked, looking at the effective density ρ_{eff}, size parameter x, and monomer shape of the aggregates described above.

To change the effective density, different numbers of monomers were used, resulting in particles with more monomers having a lower value of ρ_{eff} in general. For smaller values of ρ_{eff}, there is weaker coupling so the simplifications employed in IMA have less of an impact. A decrease in the bias occurs in these cases. For small size parameters, the bias in σ_s remains approximately constant as ρ_{eff} is increased. For $x > 2$ the bias increases with ρ_{eff}, with the correlation becoming more apparent with increasing x.

In terms of the monomer shape, dendritic particles provide the best results overall, while the bias is larger for plates and columns for most scattering quantities considered. These findings are similar to what was found using SOF. We attribute this to the air gaps in the structure of dendritic particles, weakening interactions between dipoles. The weaker interactions result in a lower magnitude which is easier to reproduce with IMA. However, it is unclear whether the improved results are simply due to the dendritic particles generally having a lower effective density than the aggregates of plates and columns.

It is worth noting that although dendritic particles give the best results, the other particle shapes still exhibit a lower bias using IMA than when RGA is used. RGA underpredicts σ_s by almost 60% in some cases, while the IMA bias mainly remains within 20%, exceeding that value for only a small number of cases at larger x. The bias in σ_a is very low for all particles using IMA, and larger errors of up to 70% are calculated using RGA. The bias in σ_b is less than 20% for $x < 5$ using IMA, reaching 60% for RGA. More unpredictable errors are found for larger x. We are interested to test whether these errors are cancelled out if orientational averaging is considered, and plan to address that in future work. The asymmetry bias is small for both IMA and RGA, showing results within 10% for IMA and 20% for RGA. This result is expected as it is an integral quantity so is not as sensitive to the exact representation of the field

at each point.

Using an aggregate of 7 dendrites, it was found that increasing the percentage of mass from rime generally enhances the magnitude of the σ_s bias using IMA. Overall the bias is larger using RGA for all rime percentages considered. Histograms of the internal field magnitudes show that riming changes the distribution shape. However, the distributions are very similar using IMA and DDA, suggesting that the increased bias using IMA results from the method failing to predict the precise locations of different magnitudes within the particle.

It was found that IMA does not satisfy the optical theorem, and hence extinction should be calculated by summing the scattering and absorption cross sections. The internal phase shift is not captured correctly, since each monomer sees the incident wave only, and interactions are only considered within the individual monomers. The phase error is more prominent within higher density plate-like aggregates than in dendritic particles.

IMA was applied to a case study in chapter 6. The study involved utilising aircraft-based in-situ and remote sensing observations. In-situ measurements from cloud probes were used to construct a model atmosphere. Aggregates were generated which we believed to be representative of the atmospheric conditions close to the time of the measurements. However, it is important to note that the microwave closure experiment is imperfect in design, especially for heterogeneous scenes like the one we are examining. The time of remote sensing and in-situ measurements are different. Using in-situ data is useful, but has the distinct disadvantage that the cloud is only sampled in a small region, so particles may not be representative of the total cloud. Furthermore, measurements are limited to capabilities of the particular instruments, e.g. the limited sizes that can be measured by different probes.

The newly developed IMA method was used to perform scattering calculations of the generated particles. The calculations, along with the atmospheric model, were input into ARTS to perform polarised radiative transfer simulations. Comparisons of the simulated results with remote sensing measurements from ISMAR radiometer were

performed. It was found that IMA is capable of reproducing the brightness temperature depression and polarisation signature, but the aggregates used did not fully represent the observations. It was required that some aggregates at the cloud base were changed to horizontally aligned dendrites in order to increase the V-H polarised brightness temperature differences.

7.2 Future Work

In this thesis we have explored scattering by simple and complex particles. Analysis of their internal electric fields has given us insight into the scattering processes involved, and allowed us to propose and test approximations to the full DDA equations. It has also allowed us to unpick the strengths and weaknesses of these new approximations on a fundamental level. Our new IMA method is a promising technique for efficient estimation of scattering by aggregate snowflakes - and we have applied it successfully to a remote sensing application. We hope to further explore these new avenues of research in future, and apply them to practical radar and radiometry remote sensing problems.

The majority of the work presented in chapter 3 considers particles of fixed orientation. On one hand it is a scenario that makes sense physically, as planar crystals tend to orient themselves horizontally [129]. Hence, the fixed orientation examples for plate-like particles are similar to probing with radar at low elevation. However, we acknowledge that plates may oscillate and rotate around the axis perpendicular to their face, depending on the Reynolds number [130]. Therefore, the geometries included are unlikely to be representative of all orientations. Although we considered orientationally averaged results for the complex aggregate, it would be interesting to develop this work by looking at orientationally averaged examples for all particles. Another interesting extension to this work would be to investigate the evolution of the internal field as the size parameter is increased to much larger values, which may be possible for infinitely long, thin crystals, as described in Refs. [131, 132].

It was found that dendritic particles provide the best results with IMA, and we discussed that this may be because the effective density is lower than aggregates of plates and columns. It would be interesting to investigate this further by doing some tests keeping ρ_{eff} constant while comparing different monomer shapes. As another area of future work, we plan to explore whether the representation of the phase lag could be improved in IMA. A first step could be to include a local phase delay in the calculations, analogous to the implementation of WKB compared to RGA. We discussed that WKB allows a change of phase corresponding to the propagation of the wave from the particle penetration point to the interior location of the volume element. A similar refinement to IMA could allow improvements to the performance of the scattering approximation, with only a small increase to computational intensity. Another method could be to perform calculations for the monomers in order, starting with the first monomer in the direction of the incident wave. Performing calculations in this way means that a phase lag could be recorded and incorporated into the input for the next monomer. We are particularly interested to see if these approaches result in improved calculations of extinction using the optical theorem.

Overall, IMA is more accurate for lower values of refractive index m, size parameter x, and effective density ρ_{eff}. It is probable that some combination of these three properties provide the limits of applicability of the method. This will be developed in future work. Once the further tests of the IMA method outlined here have been performed, we plan to measure the time and memory improvements and publish the results.

We also plan to publish the findings from chapter 6, where IMA was applied to a case study. This will be beneficial to guide ICI developments. Since simulations are sensitive to particle shape, it is important to accurately represent the particles within the cloud, rather than making assumptions about shape. This may be done using the multi-frequency information available from ICI. More accurate retrievals will be made possible by utilising this information.

Appendix A

A.1 Derivation of relaxation parameter η

The generalised overrelaxation method used by Kleinman, Roach, and van den Berg [2] corresponds to the Purcell and Pennypacker [77] iterative procedure, provided we interpret their relaxation parameter in a specific way. Let's call β the relaxation parameter denoted by α in Ref. [2]. In our notation, the iterative scheme in [2] is then:

$$\mathbf{P}^{n+1} = \beta \mathbf{E}_{inc} + (\mathbf{I} - \beta \mathbf{A})\mathbf{P}^{n}. \tag{A.1}$$

Comparing equation A.1 with equation 4.6, it is clear that the parameter β is equivalent to $\eta\alpha$ in our notation, where η is our relaxation parameter and α is the polarisability.

The residual r of an iterative method provides a measure of how close we are to the correct solution, tending to 0 for the exact solution. For a linear system $Ax = b$, the residual may be defined as $r = b - Ax$ or $r = Ax - b$. Most iterative methods use the residual to measure when a sufficiently accurate solution has been reached. The idea used by Kleinman is to choose a value of β that minimises the residual after one iteration. Let us introduce a residual error $Q := \|r_1\|^2$, and define the first residual $r_1 = AP^1 - E_{inc}$. From equation 4.5 we can write $P^1 = \beta E_{inc,j}$, and thus $r_1 = \beta A E_{inc} - E_{inc}$. The goal is then to choose β such that Q is minimised after one iteration. We may separate β into real and imaginary parts, i.e. $\beta = \beta_r + i\beta_i$, and choose β_r and β_i to satisfy $\partial Q/\partial\beta_r = 0$ and $\partial Q/\partial\beta_i = 0$.

Let us now introduce an inner product of two vectors u and v, denoted (u, v) or sometimes $\langle u, v \rangle$:

$$(u, v) = u_1 \bar{v}_1 + u_2 \bar{v}_2 + \cdots + u_n \bar{v}_n.$$

We use the convention that the inner product is linear in the first argument and anti-linear in the second argument, i.e. when you take the scalar β out of the (.,.) you get a conjugation only if it comes from the second slot:

$$(\beta u, v) = \beta(u, v)$$
$$(u, \beta v) = \bar{\beta}(u, v).$$

This is more commonly used in the mathematical community, whereas physicists often use the reverse. We can now write the residual error as:

$$Q := \|r_1\|^2 = (\beta A E_{inc} - E_{inc}, \beta A E_{inc} - E_{inc}) = a|\beta|^2 - b\bar{\beta} - \bar{b}\beta + c,$$

where

$$a = (AE_{inc}, AE_{inc}) = \|AE_{inc}\|^2, \quad b = (E_{inc}, AE_{inc}), \quad c = (E_{inc}, E_{inc}) = \|E_{inc}\|^2.$$

Writing $\beta = \beta_r + i\beta_i$, we have:

$$Q = a|\beta_r + i\beta_i|^2 - b(\beta_r - i\beta_i) - \bar{b}(\beta_r + i\beta_i) + c.$$

Noting that the squared norm is: $|z|^2 = z\bar{z}$, the relationship can be written:

$$Q = a(\beta_r + i\beta_i)(\beta_r - i\beta_i) - b(\beta_r - i\beta_i) - \bar{b}(\beta_r + i\beta_i) + c = a(\beta_r^2 + \beta_i^2) - b(\beta_r - i\beta_i) - \bar{b}(\beta_r + i\beta_i) + c.$$

As mentioned above, we want to choose β_r and β_i to satisfy $\partial Q/\partial \beta_r = 0$ and $\partial Q/\partial \beta_i = 0$. Separating Q into real and imaginary parts, we may find the partial derivatives:

$$\partial Q/\partial \beta_r = 2a\beta_r - b - \bar{b}$$
$$\partial Q/\partial \beta_i = 2a\beta_i + bi - \bar{b}i.$$

To minimise, we set:

$$2a\beta_r - b - \bar{b} = 0$$

$$2a\beta_i + bi - \bar{b}i = 0.$$

Noting that $\Re(b) = (b + \bar{b})/2$ and $\Im(b) = (b - \bar{b})/2i$, we may write $\beta = \beta_r + i\beta_i = b/a$. Thus Q is minimised by:

$$\beta = b/a = \frac{(\mathbf{E}_{inc}, \mathbf{AE}_{inc})}{\|\mathbf{AE}_{inc}\|^2}. \tag{A.2}$$

It was noted above that β is equivalent to $\eta\alpha$. Thus, for the relaxation parameter η we have:

$$\eta = \beta/\alpha = \frac{(\mathbf{E}_{inc}, \mathbf{AE}_{inc})}{\alpha\|\mathbf{AE}_{inc}\|^2}. \tag{A.3}$$

The `dot` function in Matlab computes `dot(u,v)` $= \bar{u}_1 v_1 + \bar{u}_2 v_2 + \cdots + \bar{u}_n v_n$. Therefore, in order to obtain the desired result of $(\mathbf{E}_{inc}, \mathbf{AE}_{inc})$ in Matlab, we may use the `dot` function with the arguments reversed, i.e. $\eta = \texttt{dot}(\mathbf{AE}_{inc}, \mathbf{E}_{inc})/(\alpha \times (\texttt{norm}(\mathbf{AE}_{inc}))^2)$.

Bibliography

[1] K. McCusker, C. D. Westbrook, and A. Moiola, "Analysis of the internal electric fields of pristine ice crystals and aggregate snowflakes, and their effect on scattering," *Journal of Quantitative Spectroscopy and Radiative Transfer*, vol. 230, pp. 155 – 171, 2019.

[2] R. E. Kleinman, G. F. Roach, and P. M. van den Berg, "Convergent born series for large refractive indices," *Journal of the Optical Society of America A*, vol. 7, pp. 890–897, 1990.

[3] J. Tyynelä, J. Leinonen, D. Moisseev, and T. Nousiainen, "Radar backscattering from snowflakes: Comparison of fractal, aggregate, and soft spheroid models," *Journal of Atmospheric and Oceanic Technology*, vol. 28(11), pp. 1365–1372, 2011.

[4] P. R. A. Brown and P. N. Francis, "Improved measurements of the ice water content in cirrus using a total-water probe," *Journal of Atmospheric and Oceanic Technology*, vol. 12, no. 2, pp. 410 – 414, 1995.

[5] R. J. Cotton, P. R. Field, Z. Ulanowski, P. H. Kaye, E. Hirst, R. S. Greenaway, I. Crawford, J. Crosier, and J. Dorsey, "The effective density of small ice particles obtained from in situ aircraft observations of mid-latitude cirrus," *Quarterly Journal of the Royal Meteorological Society*, vol. 139, no. 676, pp. 1923 – 1934, 2013.

[6] A. V. Matus and T. S. L'Ecuyer, "The role of cloud phase in Earth's radiation budget," *Journal of Geophysical Research: Atmospheres*, vol. 122, pp. 2559–2578, 2017.

[7] Y. Zhang, A. Macke, and F. Albers, "Effect of crystal size spectrum and crystal shape on stratiform cirrus radiative forcing," *Atmospheric Research*, vol. 52, pp. 59–75, 1999.

[8] D. P. Wylie, W. P. Menzel, H. M. Woolf, and K. I. Strabala, "Four years of global cirrus cloud statistics using HIRS," *Journal of Climate*, vol. 7, pp. 1972–1986, 1994.

[9] J.-L. F. Li and Coauthors, "An observationally based evaluation of cloud ice water in CMIP3 and CMIP5 GCMs and contemporary reanalyses using contemporary satellite data," *Journal of Geophysical Research: Atmospheres*, vol. 117, p. D16105, 2012.

[10] J. Mülmenstädt, O. Sourdeval, J. Delanoë, and J. Quaas, "Frequency of occurrence of rain from liquid-, mixed-, and ice-phase clouds derived from A-Train satellite retrievals," *Geophysical Research Letters*, vol. 42, pp. 6502–6509, 2015.

[11] G. L. Stephens and Coauthors, "CloudSat mission: Performance and early science after the first year of operation," *Journal of Geophysical Research: Atmospheres*, vol. 113, p. D00A18, 2008.

[12] N. B. Wood, *Estimation of snow microphysical properties with application to millimeter-wavelength radar retrievals for snowfall rate*. PhD thesis, Colorado State University, 2011. 231 pp.

[13] O. O. Sourdeval, L. C. Labonnote, A. J. Baran, J. Mülmenstädt, and G. Brogniez, "A methodology for simultaneous retrieval of ice and liquid water cloud properties. Part 2: Near-global retrievals and evaluation against A-Train products," *Quarterly Journal of the Royal Meteorological Society*, vol. 142, pp. 3063–3081, 2016.

[14] S. Eliasson, S. A. Buehler, M. Milz, P. Eriksson, and V. O. John, "Assessing observed and modelled spatial distributions of ice water path using satellite data," *Atmospheric Chemistry and Physics*, vol. 11, pp. 375–391, 2011.

[15] A. J. Geer and F. Baordo, "Improved scattering radiative transfer for frozen hydrometeors at microwave frequencies," *Atmospheric Measurement Techniques*, vol. 7, pp. 1839–1860, 2014.

[16] H. R. Pruppacher and J. D. Klett, *Microphysics of Clouds and Precipitation*. Kluwer Academic Publishers, 2 ed., 1997.

[17] U. Lohmann, F. Lüönd, and F. Mahrt, *An Introduction to Clouds: From the Microscale to Climate*. Cambridge University Press, 2016.

[18] C. D. Westbrook, A. J. Illingworth, E. J. O'Connor, and R. J. Hogan, "Doppler lidar measurements of oriented planar ice crystals falling from supercooled and glaciated layer clouds," *Quarterly Journal of the Royal Meteorological Society*, vol. 136, pp. 260–276, 2010.

[19] C. M. Platt, N. L. Abshire, and G. T. McNice, "Some microphysical properties of an ice cloud from lidar observation of horizontally oriented crystals," *Journal of Applied Meteorology and Climatology*, vol. 17, pp. 1220–1224, 1978.

[20] A. J. Heymsfield and C. M. R. Platt, "A parameterization of the particle size spectrum of ice clouds in terms of the ambient temperature and the ice water content," *Journal of the Atmospheric Sciences*, vol. 41, pp. 846–855, 1984.

[21] J. Um, G. M. McFarquhar, Y. P. Hong, S.-S. Lee, C. H. Jung, R. P. Lawson, and Q. Mo, "Dimensions and aspect ratios of natural ice crystals," *Atmospheric Chemistry and Physics*, vol. 15(7), pp. 3933–3956, 2015.

[22] T. Takahashi, T. Endoh, G. Wakahama, and N. Fukuta, "Vapor diffusional growth of free-falling snow crystals between -3 and -23°C," *Journal of the Meteorological Society of Japan. Ser. II*, vol. 69, pp. 15–30, 1991.

[23] M. P. Bailey and J. Hallett, "A comprehensive habit diagram for atmospheric ice crystals: Confirmation from the laboratory, AIRS II, and other field studies," *Journal of the Atmospheric Sciences*, vol. 66, pp. 2888–2899, 2009.

[24] J. L. Stith, J. Dye, A. Bansemer, A. J. Heymsfield, C. A. Grainger, W. A. Petersen, and R. Ciffelli, "Microphysical observations of tropical clouds," *Journal of Applied Meteorology and Climatology*, vol. 41, pp. 97–117, 2002.

[25] J. L. Stith, J. A. Haggerty, A. Heymsfield, and C. A. Grainger, "Microphysical characteristics of tropical updrafts in clean conditions," *Journal of Applied Meteorology and Climatology*, vol. 43, pp. 779–794, 2004.

[26] P. J. Connolly, C. P. R. Saunders, M. W. Gallagher, K. N. Bower, M. J. Flynn, T. W. Choularton, J. Whiteway, and P. Lawson, "Aircraft observations of the influence of electric fields on the aggregation of ice crystals," *Quarterly Journal of the Royal Meteorological Society*, vol. 131, pp. 1695–1712, 2005.

[27] J. Latham and C. P. R. Saunders, "Experimental measurement of the collection efficiencies of ice crystals in electric fields," *Quarterly Journal of the Royal Meteorological Society*, vol. 96, pp. 257–265, 1970.

[28] C. P. R. Saunders and N. M. A. Wahab, "The influence of electric fields on the aggregation of ice crystals," *Journal of the Meteorological Society of Japan*, vol. 53, pp. 121–126, 1975.

[29] B. Vonnegut, "Orientation of ice crystals in the electric field of a thunderstorm," *Weather*, vol. 20, pp. 310–312, 1965.

[30] P. V. Hobbs, S. Chang, and J. D. Locatelli, "The dimensions and aggregation of ice crystals in natural clouds," *Journal of Geophysical Research: Oceans and Atmospheres*, vol. 79, pp. 2199–2206, 1974.

[31] A. Battaglia, C. D. Westbrook, S. Kneifel, P. Kollias, N. Humpage, U. Löhnert, J. Tyynelä, and G. W. Petty, "G band atmospheric radars: new frontiers in cloud physics," *Atmospheric Measurement Techniques*, vol. 7, pp. 1527–1546, 2014.

[32] K. F. Evans, J. R. Wang, P. E. Racette, G. Heymsfield, and L. Li, "Ice cloud retrievals and analysis with the Compact Scanning Submillimeter Imaging Radiometer and the cloud radar system during CRYSTAL FACE," *Journal of Applied Meteorology and Climatology*, vol. 44, pp. 839–859, 2005.

[33] M. Brath, S. Fox, P. Eriksson, R. C. Harlow, M. Burgdorf, and S. A. Buehler, "Retrieval of an ice water path over the ocean from ISMAR and MARSS millimeter and submillimeter brightness temperatures," *Atmospheric Measurement Techniques*, vol. 11, pp. 611–632, 2018.

[34] S. Fox and Coauthors, "ISMAR: an airborne submillimetre radiometer," *Atmospheric Measurement Techniques*, vol. 10, pp. 477–490, 2017.

[35] V. Kangas and Coauthors, "Ice cloud imager instrument for MetOp second generation," *13th Specialist Meeting on Microwave Radiometry and Remote Sensing of the Environment (MicroRad)*, pp. 228–231, 2014.

[36] K. F. Evans, J. R. Wang, D. O. Starr, G. Heymsfield, L. Li, L. Tian, R. P. Lawson, A. J. Heymsfield, and A. Bansemer, "Ice hydrometeor profile retrieval algorithm for high-frequency microwave radiometers: application to the CoSSIR instrument during TC4," *Atmospheric Measurement Techniques*, vol. 5, pp. 2277–2306, 2012.

[37] P. Eriksson, R. Ekelund, J. Mendrok, M. Brath, O. Lemke, and S. A. Buehler, "A general database of hydrometeor single scattering properties at microwave and sub-millimetre wavelengths," *Earth System Science Data*, vol. 10, pp. 1301–1326, 2018.

[38] R. P. Lawson and R. E. S. L. J. Angus, "Observations and numerical simulations of the origin and development of very large snowflakes," *Journal of the Atmospheric Sciences*, vol. 55, pp. 3209–3229, 1998.

[39] P. R. Field, A. J. Heymsfield, and A. Bansemer, "Snow size distribution parameterization for midlatitude and tropical ice clouds," *Journal of the Atmospheric Sciences*, vol. 64, pp. 4346–4365, 2007.

[40] A. J. Baran, H. Ishimoto, O. Sourdeval, E. Hesse, and C. Harlow, "The applicability of physical optics in the millimetre and sub-millimetre spectral region. Part II: Application to a three-component model of ice cloud and its evaluation against the bulk single-scattering properties of various other aggregate models," *Journal of Quantitative Spectroscopy and Radiative Transfer*, vol. 206, pp. 83–100, 2018.

[41] K.-N. Liou and P. Yang, *Light Scattering by Ice Crystals*. Cambridge University Press, 2016.

[42] P. Eriksson, M. Jamali, J. Mendrok, and S. A. Buehler, "On the microwave optical properties of randomly oriented ice hydrometeors," *Atmospheric Measurement Techniques*, vol. 8, pp. 1913–1933, 2015.

[43] C. Mätzler, *Thermal microwave radiation - Applications for remote sensing*, vol. 52. The Institution of Engineering and Technology, electromagnetic waves series ed., 2006.

[44] M. A. Yurkin, M. Min, and A. G. Hoekstra, "Application of the discrete dipole approximation to very large refractive indices: Filtered coupled dipoles revived," *Physical Review E*, vol. 82, 2010.

[45] F. M. Kahnert, "Numerical methods in electromagnetic scattering theory," *Journal of Quantitative Spectroscopy and Radiative Transfer*, vol. 79-80, pp. 775–824, 2003.

[46] J. G. V. Bladel, *Electromagnetic Fields*. Wiley, Hoboken, NJ, 2007.

[47] M. A. Yurkin and A. G. Hoekstra, "The discrete dipole approximation: An overview and recent developments," *Journal of Quantitative Spectroscopy and Radiative Transfer*, vol. 106, pp. 558–589, 2007.

[48] J. D. Jackson, *Classical Electrodynamics*, vol. 3. John Wiley and Sons, Inc., 1962.

[49] M. I. Mishchenko, L. D. Travis, and A. A. Lacis, *Scattering, Absorption, and Emission of Light by Small Particles*. Cambridge University Press, 2002.

[50] B. T. Draine, "The discrete dipole approximation and its application to interstellar graphite grains," *The Astrophysical Journal*, vol. 333, pp. 848–872, 1988.

[51] P. Eriksson, S. A. Buehler, C. P. Davis, C. Emde, and O. Lemke, "ARTS, the atmospheric radiative transfer simulator, version 2," *Journal of Quantitative Spectroscopy and Radiative Transfer*, vol. 112(10), pp. 1551–1558, 2011.

[52] C. F. Bohren and D. R. Huffman, *Absorption and scattering of light by small particles*. Wiley, New York, 1983.

[53] V. N. Bringi and V. Chandrasekar, *Polarimetric Doppler weather radar: principles and applications*. Cambridge University Press, 2001.

[54] H. C. van de Hulst, *Light scattering by small particles*. Dover Publications Inc., New York, 1981.

[55] K. F. Evans and G. L. Stephens, "Microwave radiative transfer through clouds composed of realistically shaped ice crystals. Part I. Single scattering properties," *Journal of the Atmospheric Sciences*, vol. 52, pp. 2041–2057, 1995.

[56] A. J. Baran, E. Hesse, and O. Sourdeval, "The applicability of physical optics in the millimetre and sub-millimetre spectral region. Part I: The ray tracing with diffraction on facets method," *Journal of Quantitative Spectroscopy and Radiative Transfer*, vol. 190, pp. 13–25, 2017.

[57] P. C. Waterman, "Matrix formulation of electromagnetic scattering," *Proceedings of the IEEE*, vol. 53(8), pp. 805–812, 1965.

[58] P. C. Waterman, "Symmetry, unitarity, and geometry in electromagnetic scattering," *Physical Review D*, vol. 3, pp. 825–839, 1971.

[59] S. P. Groth, A. J. Baran, T. Betcke, S. Havemann, and W. Śmigaj, "The boundary element method for light scattering by ice crystals and its implementation in BEM++," *Journal of Quantitative Spectroscopy and Radiative Transfer*, vol. 167, pp. 40–52, 2015.

[60] C. D. Westbrook, R. C. Ball, and P. R. Field, "Radar scattering by aggregate snowflakes," *Quarterly Journal of the Royal Meteorological Society*, vol. 132(616), pp. 897–914, 2006.

[61] J. Tyynelä, J. Leinonen, C. D. Westbrook, D. Moisseev, and T. Nousiainen, "Applicability of the Rayleigh-Gans approximation for scattering by snowflakes at microwave frequencies in vertical incidence," *Journal of Geophysical Research: Atmospheres*, vol. 118, pp. 1826 – 1839, 2013.

[62] J. Leinonen, S. Kneifel, and R. J. Hogan, "Evaluation of the Rayleigh-Gans approximation for microwave scattering by rimed snowflakes," *Quarterly Journal of the Royal Meteorological Society*, vol. 144(S1), pp. 77–88, 2017.

[63] Z. Chen, A. Taflove, and V. Backman, "Photonic nanojet enhancement of backscattering of light by nanoparticles: a potential novel visible-light ultramicroscopy technique," *Optics Express*, vol. 12(7), pp. 1214–1220, 2004.

[64] M. J. Mendes, I. Tobías, A. Martí, and A. Luque, "Light concentration in the near-field of dielectric spheroidal particles with mesoscopic sizes," *Optics Express*, vol. 19, pp. 16207–16222, 2011.

[65] J. F. Owen, R. K. Chang, and P. W. Barber, "Internal electric field distributions of a dielectric cylinder at resonance wavelengths," *Optics Letters*, vol. 6, pp. 540–542, 1981.

[66] J. Tyynelä, *Polarization studies in electromagnetic scattering by small Solar-system particles*. PhD thesis, University of Helsinki, 2011. 57 pp.

[67] J. Tyynelä, E. Zubko, K. Muinonen, and G. Videen, "Interpretation of single-particle negative polarization at intermediate scattering angles," *Applied Optics*, vol. 49, pp. 5284–5296, 2010.

[68] J. P. Barton, "Electromagnetic field calculations for an irregularly shaped, near-spheroidal particle with arbitrary illumination," *Journal of the Optical Society of America A*, vol. 19, pp. 2429–2435, 2002.

[69] Y. Lu, E. E. Clothiaux, K. Aydin, G. Botta, and J. Verlinde, "Modeling variability in dendritic ice crystal backscattering cross sections at millimeter wavelengths using a modified Rayleigh-Gans theory," *Journal of Quantitative Spectroscopy and Radiative Transfer*, vol. 131, pp. 95–104, 2013.

[70] D. A. G. Bruggeman, "Berechnung verschiedener physikalischer konstanten von heterogenen substanzen. I. dielektrizitätskonstanten und leitfähigkeiten der mischkörper aus isotropen substanzen," *Annalen der Physik*, vol. 416, pp. 636–664, 1935.

[71] J. C. Maxwell-Garnett, "Colours in metal glasses and in metallic films," *Philosophical Transactions of the Royal Society A*, vol. 203, pp. 385–420, 1904.

[72] B. Johnson, G. Petty, and G. Skofronick-Jackson, "Microwave properties of ice-phase hydrometeors for radar and radiometers: Sensitivity to model assumptions," *Journal of Applied Meteorology and Climatology*, vol. 51(12), pp. 2152–2171, 2012.

[73] B. T. Draine and P. J. Flatau, "Discrete-dipole approximation for scattering calculations," *Journal of the Optical Society of America A*, vol. 11(A), pp. 1491–1499, 1994.

[74] M. A. Yurkin and A. G. Hoekstra, "The discrete-dipole-approximation code ADDA: Capabilities and known limitations," *Journal of Quantitative Spectroscopy and Radiative Transfer*, vol. 112(13), pp. 2234–2247, 2011.

[75] H. DeVoe, "Optical properties of molecular aggregates. I. Classical model of electronic absorption and refraction," *The Journal of Chemical Physics*, vol. 41, pp. 393–400, 1964.

[76] H. DeVoe, "Optical properties of molecular aggregates. II. Classical theory of the refraction, absorption, and optical activity of solutions and crystals," *The Journal of Chemical Physics*, vol. 43, pp. 3199–3208, 1965.

[77] E. M. Purcell and C. R. Pennypacker, "Scattering and absorption of light by non-spherical dielectric grains," *Astrophysical Journal*, vol. 186, pp. 705–714, 1973.

[78] A. Lakhtakia, "Strong and weak forms of the method of moments and the coupled dipole method for scattering of time-harmonic electromagnetic-fields," *International Journal of Modern Physics C*, vol. 3, pp. 583–603, 1992.

[79] B. T. Draine and J. Goodman, "Beyond Clausius-Mossotti - Wave propagation on a polarizable point lattice and the discrete dipole approximation," *The Astrophysical Journal*, vol. 405, pp. 685–697, 1993.

[80] Y. Saad and M. H. Schultz, "GMRES: A generalized minimal residual algorithm for solving nonsymmetric linear systems," *SIAM Journal on Scientific and Statistical Computing*, vol. 7(3), pp. 856–869, 1986.

[81] J. J. Goodman, B. T. Draine, and P. J. Flatau, "Application of fast-fourier-transform techniques to the discrete-dipole approximation," *Optics Letters*, vol. 16, pp. 1198–1200, 1991.

[82] A. Quarteroni, R. Sacco, and F. Saleri, *Numerical Mathematics*. Springer, 2007.

[83] S. B. Singham and C. F. Bohren, "Light scattering by an arbitrary particle: a physical reformulation of the coupled dipole method," *Optics Letters*, vol. 12, pp. 10–12, 1987.

[84] S. B. Singham and C. F. Bohren, "Light-scattering by an arbitrary particle - the scattering-order formulation of the coupled-dipole method," *Journal of the Optical Society of America A*, vol. 5, pp. 1867–1870, 1988.

[85] G. W. Petty and W. Huang, "Microwave backscatter and extinction by soft ice spheres and complex snow aggregates," *Journal of the Atmospheric Sciences*, vol. 67, pp. 769–787, 2010.

[86] E. Zubko and Coauthors, "Validity criteria of the discrete dipole approximation," *Applied Optics*, vol. 49, pp. 1267–1279, 2010.

[87] B. T. Draine and P. J. Flatau, "User guide for the discrete dipole approximation code DDSCAT 7.1," 2010.

[88] A. Malinka, *Asymptotic Methods in the Theory of Light Scattering by Nonspherical Particles. In: Kokhanovsky A. (eds) Springer Series in Light Scattering.*, vol. 5. Springer, 2020.

[89] J. D. Klett and R. A. Sutherland, "Approximate methods for modelling the scattering properties of nonspherical particles: evaluation of the Wentzel–Kramers–Brillouin method," *Applied Optics*, vol. 31, pp. 373–386, 1992.

[90] M. A. Yurkin, V. P. Maltsev, and A. G. Hoekstra, "The discrete dipole approximation for simulation of light scattering by particles much larger than the wavelength," *Journal of Quantitative Spectroscopy and Radiative Transfer*, vol. 106, pp. 546–557, 2007.

[91] W. Śmigaj, T. Betcke, S. Arridge, J. Phillips, and M. Schweiger, "Solving boundary integral problems with BEM++," *ACM Transactions on Mathematical Software*, vol. 41(2), 2015.

[92] M. A. Yurkin, V. P. Maltsev, and A. G. Hoekstra, "Convergence of the discrete dipole approximation. I. Theoretical analysis," *Journal of the Optical Society of America A*, vol. 23, pp. 2578–2591, 2006.

[93] Y. Lu, *Development and analysis of an ice crystal scattering database for remote sensing applications and cloud model evaluation.* PhD thesis, The Pennsylvania State University, 2013. 125 pp.

[94] J. Tyynelä, E. Zubko, G. Videen, and K. Muinonen, "Interrelating angular scattering characteristics to internal electric fields for wavelength-scale spherical particles," *Journal of Quantitative Spectroscopy and Radiative Transfer*, vol. 106, pp. 520–534, 2007.

[95] K. Muinonen, J. Tyynelä, E. Zubko, H. Lindqvist, A. Penttilä, and G. Videen, "Polarization of light backscattered by small particles," *Journal of Quantitative Spectroscopy and Radiative Transfer*, vol. 112, pp. 2193–2212, 2011.

[96] S. Y. Matrosov, A. J. Heymsfield, and Z. Wang, "Dual-frequency radar ratio of nonspherical atmospheric hydrometeors," *Geophysical Research Letters*, vol. 32, 2005.

[97] K. McCusker, "How fast do ice crystals grow?," Master's thesis, University of Reading, 2015. 49 pp.

[98] Y. Lu, E. E. Clothiaux, K. Aydin, and J. Verlinde, "Estimating ice particle scattering properties using a modified Rayleigh-Gans approximation," *Journal of Geophysical Research: Atmospheres*, vol. 119, pp. 10,471–10,484, 2014.

[99] C. D. Westbrook, "Rayleigh scattering by hexagonal ice crystals and the interpretation of dual-polarisation radar measurements," *Quarterly Journal of the Royal Meteorological Society*, vol. 140, pp. 2090–2096, 2014.

[100] R. J. Hogan, R. Honeyager, J. Tyynelä, and S. Kneifel, "Calculating the millimetre-wave scattering phase function of snowflakes using the self-similar Rayleigh-Gans Approximation," *Quarterly Journal of the Royal Meteorological Society*, vol. 143, pp. 834–844, 2017.

[101] D. Ori, T. Maestri, R. Rizzi, D. Cimini, M. Montopoli, and F. S. Marzano, "Scattering properties of modelled complex snowflakes and mixed-phase particles at microwave and millimeter frequencies," *Journal of Geophysical Research: Atmospheres*, vol. 119, pp. 9931–9947, 2014.

[102] R. J. Hogan, L. Tian, P. R. A. Brown, C. D. Westbrook, A. J. Heymsfield, and J. D. Eastment, "Radar scattering from ice aggregates using the horizontally aligned oblate spheroid approximation," *Journal of Applied Meteorology and Climatology*, vol. 51(3), pp. 655–671, 2012.

[103] A. T. de Hoop, "Convergence criterion for the time-domain iterative Born approximation to scattering by an inhomogeneous, dispersive object," *Journal of the Optical Society of America A*, vol. 8, pp. 1256–1260, 1991.

[104] C. Acquista, "Light scattering by tenuous particles: A generalization of the Rayleigh-Gans-Rocard approach," *Applied Optics*, vol. 15, pp. 2932–2936, 1976.

[105] P. Chiappetta, "Multiple scattering approach to light scattering by arbitrarily shaped particles," *Journal of Physics A*, vol. 13, pp. 2101–2108, 1980.

[106] S. D. Druger, M. Kerker, D. S. Wang, and D. D. Cooke, "Light scattering by inhomogeneous particles," *Applied Optics*, vol. 18, pp. 3888–3889, 1979.

[107] C. Haspel and M. Tzabari, "Sensitivity tests on the convergence tendency of the scattering order formulation of the discrete dipole approximation," *Applied Optics*, vol. 56, 2017.

[108] C. D. Westbrook, R. C. Ball, P. R. Field, and A. J. Heymsfield, "A theory of growth by differential sedimentation with application to snowflake formation," *Physical Review E*, vol. 70, 2004.

[109] R. J. Hogan and C. D. Westbrook, "Equation for the microwave backscatter cross-section of aggregate snowflakes using the self-similar rayleigh-gans approximation," *Journal of the Atmospheric Sciences*, vol. 71, pp. 3292–3301, 2014.

[110] J. Leinonen and W. Szyrmer, "Radar signatures of snowflake riming: A modelling study," *Earth and Space Science*, vol. 2, pp. 346–358, 2015.

[111] L. Tsang, J. A. Kong, and K.-H. Ding, *Scattering of Electromagnetic Waves: Theories and Applications*. John Wiley and Sons, Inc., 2000.

[112] M. J. Berg, *A Microphysical model of scattering, absorption, and extinction in electromagnetic theory*. PhD thesis, Kansas State University, 2008. 276 pp.

[113] A. Protat, D. Bouniol, J. Delanoë, E. O'Connor, P. T. May, A. Plana-Fattori, A. Hasson, U. Görsdorf, and A. J. Heymsfield, "Assessment of CloudSat reflectivity measurements and ice cloud properties using ground-based and airborne cloud radar observations," *Journal of Atmospheric and Oceanic Technology*, vol. 26, pp. 1717–1741, 2009.

[114] M. Mech, E. Orlandi, S. Crewell, F. Ament, L. Hirsch, M. Hagen, G. Peters, and B. Stevens, "HAMP - the microwave package on the High Altitude and LOng

range research aircraft (HALO)," *Atmospheric Measurement Techniques*, vol. 7, pp. 4539–4553, 2014.

[115] J. Gong and D. L. Wu, "Microphysical properties of frozen particles inferred from global precipitation measurement (GPM) microwave imager (GMI) polarimetric measurements," *Atmospheric Chemistry and Physics*, vol. 17, pp. 2741–2757, 2017.

[116] G. M. McFarquhar and Coauthors, "Processing of ice cloud in situ data collected by bulk water, scattering, and imaging probes: Fundamentals, uncertainties, and efforts toward consistency," *Meteorological Monographs*, vol. 58, pp. 11.1–11.33, 2017.

[117] K. F. Evans and G. L. Stephens, "Microwave radiative transfer through clouds composed of realistically shaped ice crystals. Part II. Remote sensing of ice clouds," *Journal of the Atmospheric Sciences*, vol. 52, pp. 2058–2072, 1995.

[118] S. Havemann and A. J. Baran, "Extension of T-matrix to scattering of electromagnetic plane waves by non-axisymmetric dielectric particles: application to hexagonal ice cylinders," *Journal of Quantitative Spectroscopy and Radiative Transfer*, vol. 70, pp. 139–158, 2001.

[119] S. L. Mason, C. J. Chiu, R. J. Hogan, D. Moisseev, and S. Kneifel, "Retrievals of riming and snow density from vertically-pointing doppler radars," *Journal of Geophysical Research: Atmospheres*, vol. 123, pp. 13807–13834, 2018.

[120] D. L. Mitchell, R. Zhang, and R. L. Pitter, "Mass-dimensional relationships for ice particles and the influence of riming on snowfall rates," *Journal of Applied Meteorology*, vol. 29, pp. 153–163, 1990.

[121] E. Fontaine, A. Schwarzenboeck, J. Delanoë, W. Wobrock, D. Leroy, R. Dupuy, C. Gourbeyre, and A. Protat, "Constraining mass-diameter relations from hydrometeor images and cloud radar reflectivities in tropical continental and oceanic convective anvils," *Atmospheric Chemistry and Physics*, vol. 14, pp. 11367–11392, 2014.

[122] A. V. Korolev, E. F. Emery, J. W. Strapp, S. G. Cober, and G. A. Isaac, "Quantification of the effects of shattering on airborne ice particle measurements," *Journal of Atmospheric and Oceanic Technology*, vol. 30, pp. 2527–2553, 2013.

[123] S. A. Buehler, C. Jiménez, K. F. Evans, P. Eriksson, B. Rydberg, A. J. Heymsfield, C. J. Stubenrauch, U. Lohmann, C. Emde, V. O. John, T. R. Sreerekha, and C. P. Davis, "A concept for a satellite mission to measure cloud ice water path, ice particle size, and cloud altitude," *Quarterly Journal of the Royal Meteorological Society*, vol. 133, pp. 109–128, 2007.

[124] D. Atlas, S. Y. Matrosov, A. J. Heymsfield, M.-D. Chou, and D. B. Wolff, "Radar and radiation properties of ice clouds," *Journal of Applied Meteorology and Climatology*, vol. 34, pp. 2329–2345, 1995.

[125] A. J. Baran, R. Cotton, K. Furtado, S. Havemann, L. C. Labonnote, F. Marenco, A. Smith, and J.-C. Thelen, "A self-consistent scattering model for cirrus. II: The high and low frequencies," *Quarterly Journal of the Royal Meteorological Society*, vol. 140, pp. 1039–1057, 2014.

[126] J. Miao, K.-P. Johnsen, S. Buehler, and A. Kokhanovsky, "The potential of polarization measurements from space at mm and sub-mm wavelengths for determining cirrus cloud parameters," *Atmospheric Chemistry and Physics*, vol. 3, pp. 39–48, 2003.

[127] D. L. Mitchell, "Parameterization of the Mie extinction and absorption coefficients for water clouds," *Journal of the Atmospheric Sciences*, vol. 57, pp. 1311–1326, 2000.

[128] D. L. Mitchell, Y. Liu, and A. Macke, "Modeling cirrus clouds. Part II: Treatment of radiative properties," *Journal of the Atmospheric Sciences*, vol. 53, pp. 2967–2988, 1996.

[129] V. Noel and K. Sassen, "Study of planar ice crystal orientations in ice clouds from scanning polarization lidar observations," *Journal of Applied Meteorology and Climatology*, vol. 44, pp. 653–664, 2005.

[130] K. Cheng, P. K. Wang, and T. Hashino, "A numerical study on the attitudes and aerodynamics of freely falling hexagonal ice plates," *Journal of the Atmospheric Sciences*, vol. 72, pp. 3685–3698, 2015.

[131] P. J. Flatau and B. T. Draine, "Light scattering by hexagonal columns in the discrete dipole approximation," *Optics Express*, vol. 22(18), pp. 21834–21846, 2014.

[132] P. J. Flatau and B. T. Draine, "Fast near field calculations in the discrete dipole approximation for regular rectilinear grids," *Optics Express*, vol. 20(2), pp. 1247–1252, 2012.